Multiaxial Fatigue Response of Normalized 1045 Steel Subjected to Periodic Overloads: Experiments and Analysis

by

John Joseph Francis Bonnen

A thesis
presented to the University of Waterloo
in fulfillment of the
thesis requirement for the degree of
Doctor of Philosophy
in
Civil Engineering

Waterloo, Ontario, Canada, 1998

The University of Waterloo requires the signatures of all persons using or photocopying this thesis. Please sign below, and give address and date.

Acknowledgements

I would like express my deepest gratitude to my supervisor, Professor Tim Topper, for his guidance, expertise, and especially his patience and understanding. I wish also to express my sincere gratitude to the members of the Mechanics and Durability group at Ford – Al Conle, Chin-Chan Chu, Russ Chernenkoff, Al Krause, and Angela Hübner. They have all given their time and expertise selflessly and been invaluable to me in both the experimental and analytical portions of this work.

I would also like to thank Floyd Alberts for his help with metallography, and Warren Copple and John Lasecki for their help in the laboratory.

Lastly, I wish to thank Ford Motor Company for the support, financial and otherwise, it has given me during the course of this investigation.

Dedicated to Cindy, David and Paul

who gave me a rhyme and a reason

Abstract

During the past decade it has been observed that periodically applied overloads of yield stress magnitude can significantly reduce or eliminate crack closure under uniaxial or mode I loading. In this thesis the results of a series of biaxial tension-torsion experiments that were performed to evaluate the effects of overloads on the fatigue life of smooth tubes constructed of normalized SAE 1045 steel are presented. Constant amplitude and periodic overload experiments were conducted under five different in-phase stress ratios, including uniaxial ($\Psi = \sigma_{xy}/\sigma_{xx} = 0$), pure torsion ($\Psi = \infty$), and three intermediate ratios ($\Psi = \frac{1}{2}$, 1, and 2). In addition, under torsional loading, two different out-of-phase overloads were evaluated.

Periodically applied overloads of yield stress magnitude caused cracks to grow under crack face interference-free conditions. Strain-life curves were obtained by computationally removing the overload cycle damage from test results and calculating equivalent fatigue lives. A factor of two reduction in the fatigue limit was found at all strain ratios when these results were compared to constant amplitude results.

Another series of constant amplitude and periodic overload tests was conducted on notched axle shafts to evaluate the effects of overloads on a component. The effects of various kinds of bending overloads on torsional fatigue were found to be quite similar to those encountered in the Ψ=0 tubular testing.

Further, under in-phase loading, it was found that shear cracks initiated and grew longitudinally for Ψ=0, $\frac{1}{2}$, and 1, and for Ψ=2 loading shear cracks initiated on the maximum shear strain planes. These observations concerning the initiation plane were used to unify the constant amplitude data and to justify the use of the maximum shear criterion with the overload fatigue data. Parameter-life curves were developed using the equivalent life data and several common multiaxial damage parameters. It was found that the simple maximum shear strain criterion together with uniaxial overload data gave safe but not unduly conservative life predictions for all of these strain ratios.

Crack face interference-free crack growth curves were obtained for mode I and mode II crack growth and observations of cracking were combined with two models

which predict changes in crack growth behavior. The models used were based on crack area increment and strain energy release rate criteria. Both of these models underpredict the shear crack length at which crack growth mode changes, but they do predict the general trends observed in the data in terms of changes in crack growth mode as a function of strain amplitude and load ratio.

Several different crack growth predictions were made. These included baseline predictions wherein the strain concentration profile is determined separately for each load ratio. Predictions were then made using the crack area increment and strain energy release rate criteria. The strain concentration profiles for shear and tensile crack growth were independently determined, and they were then used in the area and energy models to predict strain life curves for all of the stress ratios. The area and energy models gave good predictions of the experimental lives for all of the stress ratios, but the best predictions were provided by the baseline predictions.

Contents

1 Introduction 1

1.1 Crack Face Interference . . . 3

1.1.1 Overloads and Uniaxial Crack Closure . . . 3

1.1.1.1 Low Level Overloads . . . 4

1.1.1.2 High Level Overloads . . . 4

1.1.2 Crack Face Interference under Multiaxial Loading . . . 5

1.1.2.1 Static Loads in the Mode I Crack Plane . . . 5

1.1.2.2 Dynamic loads in the Mode I Crack Plane . . . 6

1.1.2.3 Shear Crack Face Interference – Mode II/III . . . 7

1.1.2.4 Summary of Crack Face Interference Reduction Techniques . . . 9

1.2 Life Prediction Techniques . . . 10

1.2.1 Damage Summation and the Local Strain Approach . . . 10

1.2.1.1 Uniaxial Damage Parameters . . . 11

1.2.1.2 Critical Plane Analysis . . . 12

1.2.1.3 Multiaxial Damage Parameters . . . 12

1.2.2 Fatigue Crack Propagation . . . 13

1.2.2.1 Modelling Short Crack Growth . . . 14

1.2.2.2 Multiaxial Crack Growth Equations . . . 16

1.2.2.3 Crack Growth Directions . . . 16

1.2.2.4 Cracking Observations for Tests of SAE 1045 Steel . 17

1.3 Purpose and Objectives of This Study . . . 19

2 Materials and Procedures 21

2.1 Material . . . 21

2.2 Uniaxial Properties . . . 22

2.2.1 Monotonic Tests . . . 22

2.2.2 Constant Amplitude Tests . . . 26

2.2.3 Periodic Overload Tests . . . 27

2.2.4 Uniaxial Crack Growth Tests . . . 28

2.3 Multiaxial Tests and Techniques . . . 30

2.3.1 Bending-Torsion Tests . . . 30

2.3.1.1 Constant Amplitude Bending and Torsion Tests . . . 32

2.3.1.2 Static Bending Moment Torsion Tests . . . 32

2.3.1.3 Bending Overload Torsion Tests . . . 33

2.3.2 Axial-Torsion Tests . . . 36

2.3.2.1 Fatigue Life Tests . . . 40

2.3.2.2 Tension-Torsion Crack Growth Tests . . . 44

2.4 Specimen Stress-Strain Analysis . . . 46

2.4.1 General Stress/Strain Analysis . . . 46

2.4.2 Torsion experiments, Ψ=0 . . . 51

2.4.3 The Stress-Strain Curve and Other Material Properties . . . 53

2.4.4 Analysis of Bending-Torsion Shaft . . . 53

2.4.5 Elastic Analysis . . . 53

2.4.6 Elastic-Plastic Analysis . . . 56

2.4.6.1 Uniaxial Neuber Analysis . . . 56

2.4.6.2 Multiaxial Neuber Correction . . . 57

2.4.7 Damage Parameters and Critical Plane Analysis . . . 58

2.4.7.1 Uniaxial Parameters – Normal Stress/Strain . . . 60

2.4.7.2 Shear-Strain Based Parameters . . . 60

2.4.7.3 Energy Based Parameters . . . 61

3 The Role of Overloads in Multiaxial Fatigue 62

3.1 Uniaxial Behavior, $\Psi=\infty$ . . . 63

3.1.1 Constant Amplitude Tests . . . 63

3.1.2 Overloads and Equivalent Uniaxial Damage . . . 63

3.1.3 Uniaxial Crack Closure . . . 68

3.1.4 Anisotropy in Uniaxial Fatigue . . . 69

3.1.5 Uniaxial Stress-Strain Behavior . . . 70

3.2 Tension-Torsion Tests . . . 72

3.2.1 Torsional Behavior, $\Psi=0$ . . . 73

3.2.1.1 In-Phase Torsional Testing . . . 73

3.2.1.2 Torsion Testing with Tension Overloads (Out-of-Phase) 75

3.2.1.3 $\Psi=0$ Combined Results . . . 79

3.2.1.4 Proposed Crack Face Interaction Mechanisms under $\Psi=0$ Loading . . . 81

3.2.2 In-Phase $\Psi = \frac{1}{2}$ Overload Tests . . . 85

3.2.2.1 Proposed Crack Face Interaction Mechanisms under $\Psi = \frac{1}{2}$ Loading . . . 88

3.2.3 In-Phase $\Psi=1$ Overload Tests . . . 89

3.2.3.1 Crack Face Interaction in $\Psi=1$ Overload Tests . . . 91

3.2.3.2 Proposed Crack Face Interaction Mechanisms under $\Psi=1$ Loading . . . 91

3.2.4 In-Phase $\Psi=2$ Overload Tests . . . 91

3.2.4.1 Proposed Crack Face Interaction Mechanisms under $\Psi=2$ Loading . . . 94

3.2.5 Tension-Torsion Cyclic Stress-Strain Response . . . 98

3.3 Bending-Torsion Experiments . . . 99

3.3.1 Constant Amplitude Bending and Torsion Tests . . . 99

3.3.2 Bending Overload Tests and Equivalent Multiaxial Damage . . 99

3.3.3 Cyclic Torsion Tests with a Static Bending Moment . . . 103

3.3.4 Bending Peak Hold Periodic Overload Tests . . . 105

3.3.5 Combined Bending-Torsion and Tension-Torsion Results . . . 107
3.4 Unification of Fatigue Life Results . . . 108
3.4.1 Constant Amplitude Tests . . . 108
3.4.2 Unification of Overload Data . . . 111
3.4.2.1 Evaluation of Damage Criteria . . . 111
3.4.2.2 Initiation Plane Based Data Reduction . . . 120
3.5 Summary . . . 121

4 Crack Growth and Crack Growth Modelling **124**
4.1 Crack Growth Measurements and Crack Mode Observations . . . 125
4.1.1 Mode I Crack Growth Experiments . . . 125
4.1.2 Mode II Crack Growth Experiments . . . 126
4.1.3 Crack Growth Mode Observations . . . 130
4.2 Predictions of Cracking Behavior . . . 134
4.2.1 Crack Area Increment Criterion . . . 134
4.2.2 The Strain-Energy Release Rate Criterion . . . 136
4.2.3 Discussion of Crack Transition Predictions for a Semi-Elliptical Crack . . . 138
4.2.4 Crack Transition Predictions for Through Cracks . . . 140
4.3 Crack Growth Life Predictions . . . 145
4.3.1 Baseline Life Predictions . . . 145
4.3.2 Shear and Tensile $\frac{a}{D}$ Estimates (and Predictions) . . . 149
4.3.3 Crack Area Increment and Strain Energy Release Rate Growth Models . . . 154
4.3.4 Discussion of Predictions . . . 155
4.4 Summary . . . 162

5 Summary and Conclusions **164**

A Chu's Modified Mróz Plasticity Model **167**

B Crack Growth Geometry Factors **171**

B.1 Correction Factors for Uniaxial Specimens 171

B.1.1 Single Edge Crack With Backface Correction 171

B.1.2 Elliptical Surface Crack in a Solid Bar Under Tension 171

B.2 Integrated Mode I, Mode II and Mode III Geometry Factors 172

B.2.1 Mode I and II Stress Intensity Solutions for a Through Crack in a Tube 172

B.2.2 Elliptical Surface Crack in a Tube 174

C Crack Propagation Program **177**

List of Tables

2.1 Chemical Composition of SAE 1045 steel. (Wt. %). 21
2.2 Normalized SAE 1045 monotonic material properties. 22
2.3 Normalized SAE 1045 cyclic material properties (per ASTM E606). . 27

4.1 Initiation and propagation angles (with respect to the x-axis) for normalized 1045. 131
4.2 Observed and predicted initial shear crack lengths (ISCL) for Ψ=0 loading. 132
4.3 Observed and predicted initial shear crack lengths (ISCL) for $\Psi=\frac{1}{2}$ loading. 132
4.4 Observed and predicted initial shear crack lengths (ISCL) for Ψ=1 loading. 133
4.5 Observed and predicted initial shear crack lengths (ISCL) for Ψ=2 loading. 134

List of Figures

1.1 Example of mode III crack subjected to axial loading 8
1.2 Cracking behavior observed normalized SAE 1045 steel subjected to tension and torsion 18

2.1 Microstructure of normalized SAE 1045 steel (400X), L-T orientation. 23
2.2 Microstructure of normalized SAE 1045 steel (400X), L-S orientation. 23
2.3 Microstructure of normalized SAE 1045 steel (400X), S-T orientation. 24
2.4 Microstructure of normalized SAE 1045 steel (100X) showing banding in the L-T orientation. 24
2.5 Stringers in normalized SAE 1045 steel (125X), L-T orientation. . . . 25
2.6 Uniaxial Specimen. All dimensions in mm. 25
2.7 Uniaxial constant amplitude history. ($R_\epsilon = \frac{\epsilon_{min}}{\epsilon_{max}} = -1$). 26
2.8 Uniaxial overload history. 28
2.9 Mode I crack growth specimen. All dimensions in mm. 29
2.10 High R-ratio crack growth history. 29
2.11 Bending-torsion fixture with specimen. 30
2.12 Bending-torsion specimen. All dimensions in mm. 31
2.13 Ratchetting in a static bending moment test. 33
2.14 Static bending history used on bending-torsion rig. 34
2.15 Bending torsion standard overload history. 34
2.16 Bending torsion peak hold history. 35
2.17 Axial-torsion load frame. 36
2.18 Typical specimen installation with axial-torsion extensometer. 37
2.19 Displacement gage affixed to axial-torsion load frame. 38

2.20 Feedback plots from a constant amplitude test. 39
2.21 Axial-torsion specimen. All dimensions in mm. 40
2.22 Feedback plots from an overload test. 42
2.23 $\Psi = 0$ histories with different types of overloads. 43
2.24 Axial-torsion crack growth specimen. All dimensions in mm. 44
2.25 Example of precrack crack growth removal. All dimensions are in mm. 45
2.26 Stress/strain coordinate system for a) uniaxial and b) tension-torsion specimens. 47
2.27 Mohr circle diagrams (drawn for $\Psi = 2$) showing stress and strain paths and the definitions of ϵ_d, α, and C_Ψ. 49
2.28 Mohr's circles for in-phase torsional loading. 52
2.29 Simplified Mohr's circles for out-of-phase torsional loading. 52
2.30 Stress/strain coordinate system for bending-torsion specimens. 54
2.31 Illustration of uniaxial Neuber correction. 57

3.1 Constant amplitude $R_\epsilon = -1$ fatigue response of SAE 1045 steel. . . . 64
3.2 Periodic overload and effective strain curves for normalized SAE 1045 steel. 66
3.3 Longitudinal and transverse strain-life data for SAE Phase I normalized SAE1045 steel. 70
3.4 Stress-strain behavior of normalized SAE1045 steel. 71
3.5 Load paths shown in (a) principal stress and (b) axial-torsion axes. . 72
3.6 Fatigue response of normalized SAE1045 under in-phase torsional loading, $\Psi = \frac{\sigma_{xx}}{\sigma_{xy}}$=0 ($\psi = \frac{\epsilon_{xx}}{\epsilon_{xy}}$=0). 74
3.7 Periodic tension overload curve for torsional loading of normalized SAE1045 steel. 76
3.8 Relaxation of tension stress with application of repeated torsional cycling $(\epsilon_{xx}^{ol})_a$=0.005, $(\epsilon_{xy}^{sc})_a$=0.005, and η=10. 77
3.9 Tension peak-hold overload torsion tests on normalized SAE1045 steel. 78
3.10 The impact of various types of overloads on the torsional fatigue ($\Psi = \frac{\sigma_{xx}}{\sigma_{xy}}$=0) of normalized SAE1045 steel. 79

3.11 Torsional stress-strain responses before and after axial peak hold overloads ($\Psi = \frac{\sigma_{xx}}{\sigma_{xy}}$=0) in normalized SAE1045 steel. 80
3.12 Typical small crack growth under ($\Psi = \frac{\sigma_{xx}}{\sigma_{xy}}$=0) loading of normalized SAE1045 steel. 81
3.13 Preferential cracking through ferrite grains and along the ferrite/pearlite grain boundaries 83
3.14 Proposed crack face interference mechanism under in-phase $\Psi = \frac{\sigma_{xx}}{\sigma_{xy}}$=0 loading. 84
3.15 Appearance of asperities subjected to an in-phase $\Psi = \frac{\sigma_{xx}}{\sigma_{xy}}$=0 overload history. 84
3.16 Proposed closure mechanism under $\Psi = \frac{\sigma_{xx}}{\sigma_{xy}}$=0 loading with tension overloads. 85
3.17 Typical appearance of asperities under $\Psi = \frac{\sigma_{xx}}{\sigma_{xy}}$=0 loading with axial overloads. 86
3.18 Periodic overload and constant amplitude fatigue responses of normalized SAE 1045 for $\Psi = \frac{\sigma_{xx}}{\sigma_{xy}} = \frac{1}{2}$ ($\psi = \frac{\epsilon_{xx}}{\epsilon_{xy}} = \frac{1}{3}$). 87
3.19 Typical small crack growth under $\Psi = \frac{\sigma_{xx}}{\sigma_{xy}}$=$\frac{1}{2}$ loading of normalized SAE1045 steel. 88
3.20 Proposed closure mechanism under in-phase $\Psi = \frac{\sigma_{xx}}{\sigma_{xy}} = \frac{1}{2}$ loading. . . 89
3.21 Periodic Overload and constant amplitude fatigue responses of normalized SAE 1045 for $\Psi = \frac{\sigma_{xx}}{\sigma_{xy}}$=1 ($\psi = \frac{\epsilon_{xx}}{\epsilon_{xy}} = \frac{2}{3}$). 90
3.22 Typical small crack growth under ($\Psi = \frac{\sigma_{xx}}{\sigma_{xy}}$=1) loading of normalized SAE1045 steel. 92
3.23 Periodic overload and constant amplitude fatigue responses of normalized SAE 1045 for $\Psi = \frac{\sigma_{xx}}{\sigma_{xy}}$=2 ($\psi = \frac{\epsilon_{xx}}{\epsilon_{xy}} = \frac{4}{3}$). 93
3.24 Small cracks developed under in-phase $\Psi = \frac{\sigma_{xx}}{\sigma_{xy}}$=2 loading. 95
3.25 Crack behavior under in-phase $\Psi = \frac{\sigma_{xx}}{\sigma_{xy}}$=2 loading. 96
3.26 Asperities developed under in-phase $\Psi = \frac{\sigma_{xx}}{\sigma_{xy}}$=2 loading. 97
3.27 Cyclic stress-strain response of normalized SAE1045 steel to biaxial loading. 98

3.28 Constant amplitude and periodic overload bending-torsion fatigue curves for normalized SAE1045 100
3.29 Bending overload stress/strain behavior of notched SAE shafts. . . . 101
3.30 Constant amplitude, bending overload, and static bending bending-torsion fatigue curves for normalized SAE1045. 104
3.31 Constant amplitude, bending overload, and static bending bending-torsion fatigue curves for normalized SAE1045. 106
3.32 Combined bending-torsion and tension-torsion data. 108
3.33 Constant amplitude curves for tension-torsion and bending-torsion tests plotted on the basis of applied shear strain amplitude ($(\epsilon_{xy}^{ca})_a$). 109
3.34 Constant amplitude tension-torsion and bending torsion tests considered on the basis of initiation plane. 112
3.35 Maximum shear (ϵ_{12}) plot of constant amplitude tension-torsion and bending-torsion tests. 113
3.36 Normal stress, $\frac{\Delta\sigma_n}{2}$, plots for tension-torsion and bending-torsion overload tests. 114
3.37 Normal strain, $\frac{\Delta\epsilon_n}{2}$, plots for tension-torsion and bending-torsion overload tests. 115
3.38 Brown and Miller parameter-life plot for tension-torsion and bending-torsion overload tests. 116
3.39 Fatemi-Socie-Kurath parameter-life plot for tension-torsion and bending-torsion overload tests. 117
3.40 Smith-Watson-Topper parameter-life plot for tension-torsion and bending-torsion overload tests. 118
3.41 Parameter-life plot for Chu's parameter for tension-torsion and bending-torsion overload tests. 119
3.42 Shear strain plot of tension-torsion and bending-torsion overload tests (based on initiation plane). 121
3.43 Maximum shear strain amplitude (ϵ_{12}) curves for tension-torsion and bending-torsion overload tests. 122

4.1 Effective crack growth curve for normalized 1045 steel. 126
4.2 Effective crack growth curve for normalized 1045 and for as-received 1045 for short and long cracks. 127
4.3 Mode II effective crack growth curve for normalized 1045 steel. 128
4.4 Definition of angles β and ϕ, and and examples of crack length projection onto principle stress plane. 130
4.5 Definition of terms for a semi-elliptical crack. 135
4.6 Shear crack to tensile crack transition predictions for the area model (ξ). 141
4.7 Shear crack to tensile crack transition predictions for the energy model (χ). 142
4.8 Tensile crack to shear crack transition prediction for ξ. 144
4.9 Tensile crack to shear crack transition prediction for χ. 144
4.10 Typical algorithm for crack growth life prediction. 148
4.11 Crack growth predictions for $\Psi = \frac{\sigma_{xx}}{\sigma_{xy}}$=0 tubular overload experiments. 149
4.12 Crack growth prediction for $\Psi = \frac{\sigma_{xx}}{\sigma_{xy}}$=$\frac{1}{2}$ tubular overload experiments. 150
4.13 Crack growth prediction for $\Psi = \frac{\sigma_{xx}}{\sigma_{xy}}$=1 tubular overload experiments. 151
4.14 Crack growth prediction for $\Psi = \frac{\sigma_{xx}}{\sigma_{xy}}$=2 tubular overload experiments. 152
4.15 Crack growth prediction for $\Psi = \frac{\sigma_{xx}}{\sigma_{xy}} = \infty$ uniaxial overload experiments. 153
4.16 Flow chart for strain energy release rate crack prediction program. . . 156
4.17 Threshold conditions for shear and tensile growth for Ψ=2. 160
4.18 Threshold conditions for shear and tensile growth for Ψ=1. 160
4.19 Crack initiation types. 161

A.1 Definition of strain gage coordinates. 168

B.1 Definitions of a and W in a single edge cracked plate. 172
B.2 Definitions of a, c and W for an ellipical crack in a rod under tension. 173
B.3 Definitions of c, t, R, and β for an arbitrarily oriented through-crack in a tube. 174
B.4 Definitions of a, c, t, θ, and β for an arbitrarily oriented ellipical crack in a tube. 175

Nomenclature

A Area

a Crack depth

a_s Shear crack depth

a_t Tensile crack depth

$\frac{da}{dN}$ Crack growth rate

$\frac{\alpha}{D}$ Surface strain concentration decay factor

α Expression for third principal strain in Mohr's circle

β Angle the initiation plane makes with the specimen x-axis

c Surface half crack length

c_t Surface half crack length for shear crack

c_s Surface half crack length for tensile crack

c_{gl} Half gage length surface crack

C_Ψ Expression for diameter of Mohr's stress circle

χ Strain energy release rate ratio, G_t^c/G_s^c

D Damage to component subjected to fatigue

E Modulus of elasticity

e Nominal strain

ϵ Local strain

ϵ_d Normal strain component of largest Mohr's circle on xy plane

$\Delta\epsilon_{eff}$ Closure free effective strain range

$\Delta\epsilon^*$ Strain range based damage parameter

$\Delta\epsilon_i$ Intrinisic strain range at which crack does not propagate

$\bar{\epsilon}$ von Mises effective strain

$\underline{\epsilon}$ Strain tensor

ϵ_{xy} Tensorial shear strain

F Geometry factor for crack/specimen, also force on specimen

G Torsional modulus of elasticity

G_c Strain energy release rate

γ Engineering shear strain

η Number of small cycles between overloads

I_s Moment of inertia for notched shaft in bending

J_s Polar moment of inertia for notched shaft in torsion

K Stress intensity

K_c Critical stress intensity

ΔK_{eff} Effective stress intensity range

$\Delta K(\epsilon)$ Strain intensity range

K_t^b Stress concentration factor for notched shaft in bending

K_t^t Stress concentration factor for notched shaft in torsion

k Crack ellipticity, $\frac{a}{c}$

λ Biaxial strain ratio, $\epsilon_{xx}/\epsilon_{yy}$ or $\epsilon_{xy}/\epsilon_{xx}$

Λ Biaxial stress ratio, σ_{xx}/σ_{yy} or σ_{xy}/σ_{xx}

M_b Bending moment

M_t Torsional moment

N Number of cycles applied

n_i Number of cycles applied at amplitude i

N_f Number of cycles to failure

N_i Number of cycles to failure at amplitude i

ν Poisson's ratio

ν^* Effective Poisson's ratio

ν^p Plastic Poisson's ratio

P A parameter

Q_ϵ Metallurgical surface strain concentration factor

q Strain concentration factor at the free surface less 1

ϕ Angle the initiation plane makes with the tensile plane

r_b Bending radius for shaft

r_t Torque radius for shaft

R Radius of tubular specimen

R_σ Stress ratio, $\sigma_{min}/\sigma_{max}$

R_ϵ Strain ratio, $\epsilon_{min}/\epsilon_{max}$

R_T Torsional moment ratio, T_{min}/T_{max}

S Nominal stress

S_{op} Crack opening stress

σ Local stress

$\bar{\sigma}_y$ Cyclic yield stress

$\overline{\sigma}$ von Mises effective stress

$\underline{\sigma}$ Stress tensor

t Tubular specimen wall thickness

τ Local shear stress

θ Crack front parametric angle

ξ Crack area increment ratio, A_t/A_s

ψ Biaxial strain ratio, $\epsilon_{xx}/\epsilon_{xy}$

Ψ Biaxial stress ratio (at overload loop tips), σ_{xx}/σ_{xy}

Subscripts and Superscripts

x, y, z Orthogonal specimen coordinates

$1, 2, 3$ Orthogonal principal stress/strain coordinates

I Mode I loading

II Mode II loading

III Mode III loading

a Amplitude of the variable during the load cycle

max Maximum value of the variable in the load cycle

min Minimum value of the variable in the load cycle

m Mean value of the variable during the load cycle

f Value of variable at failure

o Initial value of variable

op Value of variable when crack is just fully open

ol Value of variable for overload cycle

sc Value of variable for small cycle

th Value of variable at fatigue threshold

e Semi-elliptical crack

t Through crack

n Normal to crack plane

s Shear crack

t Tensile crack

Operators

δ Change of variable between loading cycles

Δ Range of variable during loading cycle

Chapter 1

Introduction

Metal fatigue is a phenomenon that is caused by the repeated application of loads to a component which eventually results in the cracking and failure of that component. Over the last 150 years, the study of fatigue has been dedicated towards eliminating these failures. Modelling fatigue processes is one of the primary tools used in both understanding fatigue and eliminating failures. Current philosophy in fatigue divides the crack growth process into three stages – crack nucleation and microstructurally based growth, long (or macroscopic) crack growth, and final or cataclysmic failure. There are two basic categories of fatigue prediction models.

The first category is the continuum damage model. This approach models the crack nucleation process and determines the damage contributed from each load cycle; once the accumulated damage reaches a certain level, a fatigue crack is assumed to have nucleated and the component to have failed. The second category is the crack growth model where a small flaw is assumed to pre-exist in the material, and cycle by cycle the crack growth is calculated and accumulated. When the crack length reaches the failure length the number cycles accumulated is taken as the fatigue life.

In the ground vehicle industry, uniaxial continuum damage models are used almost exclusively for the evaluation of the fatigue performance of chassis, suspension, body, and powertrain structures. A uniaxial model assumes that the component is subjected to loading which is predominantly in a single direction. However, there may be multiple force inputs which act on the component and result in multiaxial fatigue. Uniaxial fatigue analysis is satisfactory in most cases, but it is estimated that it

produces seriously non-conservative life estimates in 5-10% of the cases involving multiaxial loading [1].

Another problem with uniaxial continuum damage fatigue analysis is that vehicle structures are subjected to variable amplitude loading more often than constant amplitude loading. In a severe variable amplitude load history, large overload cycles can cause significant changes in fatigue crack closure levels which, in turn, can cause substantial changes in the damage done by subsequent load cycles. Most models do not track these changes and thereby make predictions which can be in error by as much as a factor of 20 [2] when compared with observed component lifetimes. The constant amplitude, fully reversed laboratory tests, which are usually used as a basis for estimating component fatigue life, typically have higher levels of crack closure than the same stress-strain cycles experienced in service loadings.

Crack closure is caused by a number of mechanisms that reduce the energy available at the crack tip for cracking and result in slowed or arrested crack growth and longer component lifetimes. An understanding of the behavior of closure at high stress levels was delayed because compact tension specimens, which are typically used in closure investigations, do not allow the use of loads that approach the net section yield stress. Stresses of this magnitude arise in many notched engineering components at high load levels. In fact, these high levels, often termed overload levels, can completely eliminate crack closure [3]. Once crack closure-free uniaxial crack growth and strain-life curves were developed, safe fatigue life predictions for severely loaded structures could be made. However, similar extensions of these concepts into multiaxial loading (called crack face interference) were not made until recently [4].

In this study, crack face interference-free multiaxial fatigue behavior was investigated, multiaxial fatigue damage parameters were evaluated, and fatigue crack growth life predictions were made using the crack growth data. This chapter is devoted to the following reviews:

- observations of crack face interference under uniaxial and multiaxial fatigue,
- life prediction techniques including

1. damage prediction and damage parameters,
2. uniaxial and multiaxial fatigue crack growth predictions,
3. prediction of changes in crack growth direction,

- observed cracking behavior in SAE 1045 steel, and
- the motivation for, and an outline of the research performed.

1.1 Crack Face Interference

A decade ago Schijve [5] stated that fatigue crack closure (crack face interference) was so pervasive that no fatigue crack problem could be solved without first considering it.

The influence of mean stress on both fatigue damage and fatigue crack growth rates has been linked to changes in crack closure [3, 6, 7]. Thus, mean stress corrections in damage parameters are corrections for changes in closure with mean stress. This implies that, once closure has been eliminated, the crack growth rate for a given stress or strain range will not vary with the mean stress level (as long as the mean stress level does not lead to fast fracture).

1.1.1 Overloads and Uniaxial Crack Closure

Several different mechanisms causing crack closure have been defined, including plasticity induced closure [8, 9], roughness induced closure [10], and debris induced closure [11, 12, 13]. All of these processes affect the the load at which the crack tip opens, S_{op}. Plasticity induced closure is generated by the plastic wake of the crack tip which increases S_{op} and causes the crack tip to be closed for a portion of the loading cycle, but only when the opening stress exceeds the minimum stress in the load cycle, $S_{min}(S_{op} > S_{min})$. Roughness induced closure has the same effect, but it is caused by faceted growth of a crack along crystallographic planes in the near-threshold growth regime. A third mechanism is debris induced closure, which is produced either by

the accumulation of fretting debris [11, 12] or corrosion products [13] between the fracture surfaces.

In variable amplitude loading, overloads can be divided into two categories which have markedly different effects – those which are below approximately one-half of the cyclic yield stress (low level) and those which exceed this level (high level).

1.1.1.1 Low Level Overloads

Observations made over the course of the past 40 years regarding the influence of low level overloads on crack growth indicate two general effects: tensile overloads retard crack growth and compressive overloads accelerate crack growth [9, 14, 15]. A tensile overload increases the plastic zone size of a crack growing under constant amplitude loading and it sets up a compressive residual stress field. Crack growth rates are briefly accelerated due to a temporary reduction in S_{op}, but this acceleration is quickly replaced by retardation when the crack tip penetrates the residual stress field. As the crack grows into the field, compressive stresses build up in its wake and increase S_{op} above its steady state constant amplitude value for the lower level stresses which follow the overload. This increase in S_{op} may either retard or arrest crack growth. If the crack grows through this field then S_{op} returns to its steady-state value for the smaller constant amplitude cycles and crack growth rates again return to their previous level. On the other hand, compressive overloads reduce S_{op} by crushing asperities behind the crack tip and reducing the height of the plastic wake, thereby increasing crack growth rates. Again the decrease in S_{op} is temporary and crack growth rates return to normal once new asperities are formed and the plastic wake is re-established.

1.1.1.2 High Level Overloads

Under high level overload conditions, the elastic constraint around the plastic zone is no longer effective because of the large increase in plastic zone size. Studies by DuQuesnay [3, 16] demonstrated that high stress overloads, both compressive and tensile, accelerated short fatigue crack growth rates by reducing closure levels. DuQuesnay [3] ranked the various kinds of uniaxial overloads of a given peak stress level in order of increasing severity (decreasing S_{op}):

- Large compressive overloads which increased crack growth rates by flattening surface asperities. Crack opening stresses were thus lowered, and, depending on the load level, there was a tensile residual stress in front of the crack which kept it open;
- Large tensile overloads on smooth specimens left the crack open and hence lowered the crack opening stress level;
- A tensile overload followed by a compressive overload employed both mechanisms but the tensile plasticity ahead of the crack was partly reversed by the compressive component of the cycle;
- A compressive overload followed by a tensile overload which decreased S_{op} by the largest amount.

DuQuesnay [17, 18] developed the following empirical model to describe steady state crack closure

$$S_{op} = \alpha S_{max}\left[1 - \left(\frac{S_{max}}{\bar{\sigma}_y}\right)^2\right] + \beta S_{min}, \tag{1.1}$$

where α and β are material constants. Equation 1.1 was proposed after he measured crack opening levels on smooth specimens with strain gages placed across the crack mouth. The results were then confirmed with a small number of observations using replica techniques. This purely empirical equation describes crack closure behavior for a range of nominal cyclic stresses up to and slightly exceeding the cyclic yield stress.

1.1.2 Crack Face Interference under Multiaxial Loading

1.1.2.1 Static Loads in the Mode I Crack Plane

Closure can also be affected by loads applied in various fashions across a growing mode I crack. Hopper and Miller [19] tested two cruciform specimens, one with a center drilled hole and spark machined starter cracks, and the other with a center

drilled hole and starter notches. A static load was applied on one axis while the other was cyclicly loaded. Strain ratios, $\lambda_{max} = \frac{\epsilon_x}{\epsilon_y}$, of -1, 0, and 1 were selected for testing. The results indicated clearly that the application of a compressive stress applied parallel to plane of the crack and along its length (hereafter referred to as a "P-stress") increased mode I crack growth rates while a tensile P-stress slowed mode I crack growth.

Hourlier and Pineau [20] studied tubes made of alloyed steels, mild steels, and titanium which were precracked under mode I tensile loading. When they applied static torsion and simultaneous cyclic tension they found that mode I fatigue crack growth rates were severely reduced. The reduction in ΔK_{eff} was attributed to fracture surface mismatch caused by shear displacements. This indicated that the static shear loads increased crack face interference levels and reduced ΔK_{eff}.

1.1.2.2 Dynamic loads in the Mode I Crack Plane

Brown and Miller [21], in a series of tests on cruciform specimens with a central starter slit, observed that a compressive P-stress increased crack growth rates. For the same tensile stress range across the crack they applied equal compressive stresses in the plane of the crack (shear loading, $\Lambda = \frac{\sigma_x}{\sigma_y} = -1$), equal tensile stresses in the plane of the crack (equibiaxial, $\Lambda = 1$), and no stresses in the plane of the crack (uniaxial, $\Lambda = 0$). The results indicated that fully reversed tests in shear had faster growth rates than the uniaxial tests which, in turn, had faster growth rates than the equibiaxial tests. However, at lower stresses, these tests showed no significant effect of Λ. In fact, the authors maintained that for normal stress amplitudes which are much less than the cyclic yield stress, the effect of stress biaxiality was negligible. They further comment that previous researchers who found no effect of stress biaxiality had tested, in all probability, at loads too low to discern its effects. Youshi et al. [22], testing at larger stress amplitudes, found similar results for strain controlled tests and further determined that the slowest growth rates occurred for $\lambda = \frac{\epsilon_x}{\epsilon_y} = 0.5$ because plastic deformation at the crack tip was minimized in this configuration – they maintained that plastic zone size strongly influences fatigue crack growth rates. Finally, Smith

and Pascoe [23] confirmed the P-stress effect in their tests on a cruciform specimen. These studies indicate that mode I crack face interference is reduced by the application of compressive P-stresses when they are of the order of the cyclic yield stress, but substantially lower P-stresses do not reduce interference significantly.

1.1.2.3 Shear Crack Face Interference – Mode II/III

Socie [24] performed a series of experiments which demonstrated that, for shear cracks growing in Inconel 718 tubes, both shear systems must have increased crack face interference to lengthen fatigue life. Compression applied across a single set of shear planes has little or no effect on life. On the other hand, tensile loads on either shear system have deleterious results.

Tschegg [25] observed that, as crack lengths increased in AISI C1018 steel, crack face interference under mode III loading consumed an increasing part of the crack driving force, especially at lower crack driving force levels. For a constant crack driving energy level applied to a mode III crack, increased crack lengths led to dramatic increases in crack face interference which, in turn, substantially reduced the crack driving force seen by the material at the crack tip. Tschegg performed these experiments on circumferentially notched cylindrical steel specimens. Wang and Miller [26, 27] documented the onset of crack face interference through a series of torsion fatigue experiments with varying mean torsion levels on a ferritic stainless steel. They found that short crack faces slipped freely until crack lengths of $150\mu m$ were reached, and that increasing both torsional mean levels and amplitudes increased short crack growth rates. They attributed the sudden increase in closure after $150\mu m$ of growth to a microstructural barrier encountered there.

One method of reducing crack face interference under shear is to separate the crack faces via a static tensile load. Static tensile loads applied across mode III cracks can substantially increase growth rates [28, 29, 30]. Data from Brown, et al. [28] is replotted in Figure 1.1 and demonstrates this effect dramatically. A static 2kN end load (40MPa nominal stress) was applied axially to circumferentially notched specimens of 316 stainless steel which were then cycled torsionally. A DC potential drop system

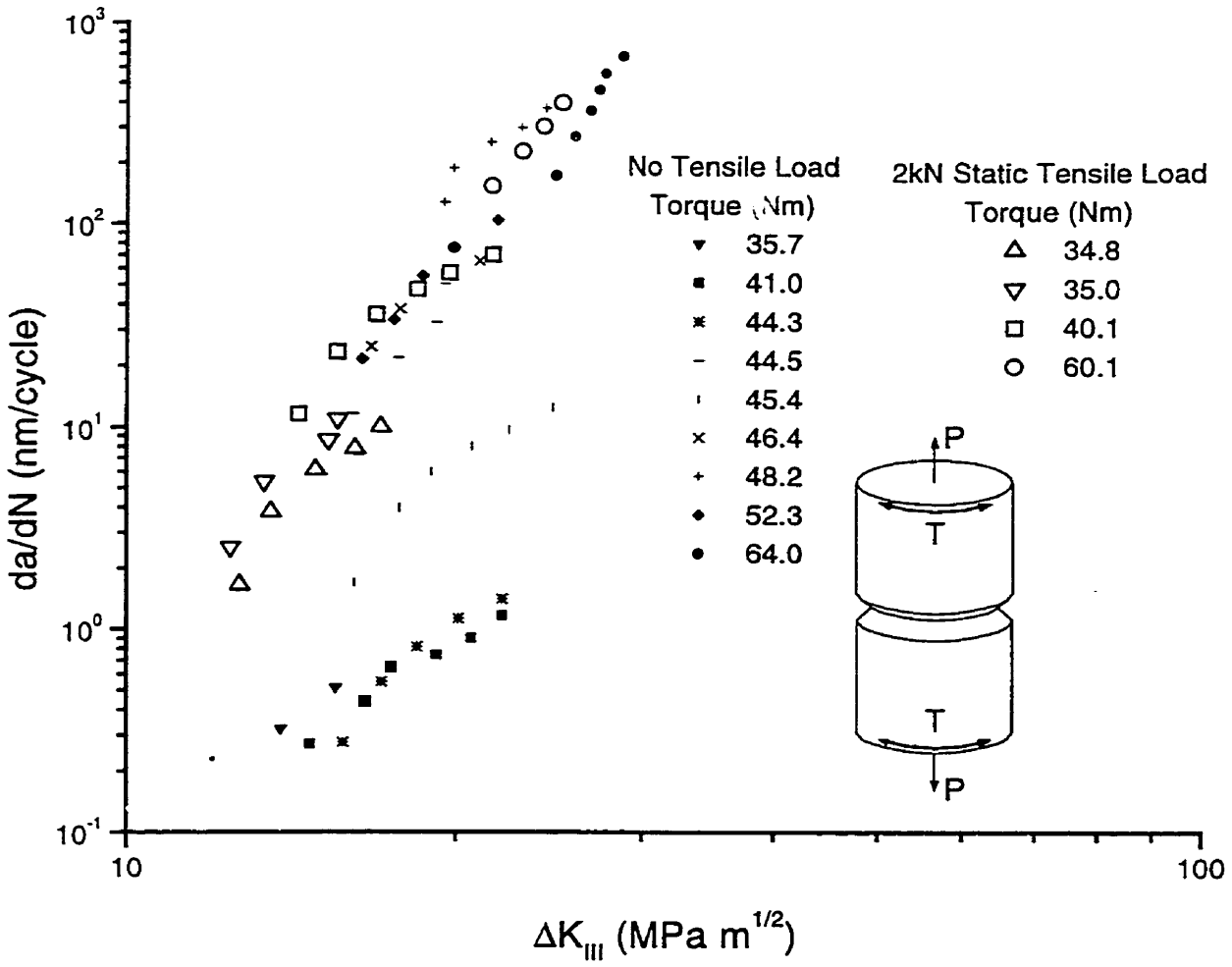

Figure 1.1: Example of mode III crack subjected to axial loading, from [28].

was then used to track mode III crack growth into the specimen interior. As seen in Figure 1.1, the axial load increased crack growth rates by an order of magnitude. However, even without the static tensile load the highest torsional moment levels reach the same limiting crack growth curve established by the specimens with tensile loads. Tschegg [25] observed that the crack growth rates at the highest torsional moment levels were least affected by the onset of crack face interference.

Another method of reducing closure is by applying mode III overloads during mode III crack growth. Ritchie et al. [31] applied mode III overloads to circumferentially

notched cylindrical ASTM A439 steel specimens during a mode III crack growth test. Crack length was monitored with a DC potential drop system; it was found that mode III overloads accelerated mode III crack growth. In this case the behavior was attributed to a decrease in "rubbing and abrasion between sliding crack surfaces," which presumably means that asperity heights were reduced by smearing and thereby led to reduced levels of crack face interference. In an in-phase biaxial study on IMI 834 cruciform specimens, Trautmann et al. [32] combined high mean stress overloads with short blocks of small constant amplitude cycles. Two tests were conducted with an identical overload cycle and the same small cycle stress range, but each test had a different small cycle mean stress level. For the smallest small cycle stress range tested, the crack growth curves for the two mean stress levels were almost identical and this implied similar small cycle crack growth rates – independent of mean stress. Hence, they appeared to have achieved crack face interference-free crack growth for these small constant amplitude cycles. Varvani-Farahani [4] removed crack face interference by applying large compressive (mode I) overloads across shear cracks growing under various strain ratios ($\lambda = +1,\ -\nu,\ -0.625$, and -1) and obtained accelerated crack growth rates.

1.1.2.4 Summary of Crack Face Interference Reduction Techniques

Most overloads with macroscopic plasticity (shear, compressive, and tensile) accelerate tensile mode cracks. Conversely, tensile overloads which result in only localized plasticity hinder crack growth. However, a static or cyclic tensile load applied parallel to the plane of a mode I crack (P-stress) slowed mode I crack growth while a compressive load applied in the same fashion accelerated the mode I crack growth. Static shear loads also slowed mode I crack growth.

A mode II or III crack with a compressive load applied across the crack faces resulted in arrested or slowed growth, but unless compressive loads were applied across both shear planes overload fatigue life was unaffected. However, a tensile load applied across either shear plane system caused cracks on that plane to grow at an increased rate. Finally, either compressive overloads applied across the crack or shear overloads applied in the crack plane cause shear cracks to grow at increased rates.

1.2 Life Prediction Techniques

There are two methods by which estimates of component fatigue life have been traditionally made. The first is a damage (or initiation) based life prediction which determines the number of load applications until a crack of a certain size is observed. The second method, crack propagation based life prediction, computes the crack extension for a flaw of known size after each load application until the component undergoes structural failure.

1.2.1 Damage Summation and the Local Strain Approach

As mentioned before, damage summation techniques estimate the number of cycles to reach a predetermined crack size [33]. Damage analysis usually employs strain-life curves to estimate the damage for any given cycle. The fractional damage is calculated for a given cycle by

$$D = \frac{n_i}{N_i} \tag{1.2}$$

where N_i is the number of cycles to failure at strain amplitude i, and n_i is the number of cycles the component spends at strain amplitude i.

The Palmgren-Miner rule [34, 35] used to estimate fatigue life is expressed as

$$\sum_i \frac{n_i}{N_i} = 1. \tag{1.3}$$

This equation defines failure to be at the point where the damage from all of the damaging events sum to unity. This technique can be used with any damage parameter.

The local strain approach [36] assumes that the fatigue life of any given location on a component is governed by the strain history of the material at that location. The fatigue life at this location is further assumed to be equivalent to a smooth laboratory specimen subjected to the same history. This technique allows designers to pick the local areas or "hot-spots" where the component is most likely to fail.

1.2.1.1 Uniaxial Damage Parameters

Although the descriptions in the previous section used strain amplitude as a fatigue damage parameter, other parameters have been used to assess fatigue damage. The following are common damage parameters which have been used to analyze component life for multiaxial fatigue:

Maximum normal strain amplitude

$$P_{\epsilon_n} = \Delta\epsilon_n/2. \tag{1.4}$$

This parameter stipulates that the maximum normal strain amplitude is the dominant factor in fatigue damage accumulation.

Maximum normal stress amplitude

$$P_{\sigma_n} = \Delta\sigma_n/2. \tag{1.5}$$

This parameter stipulates that the maximum principal stress amplitude is the dominant factor in fatigue damage accumulation.

Maximum shear strain amplitude

$$P_{\gamma} = \Delta\gamma/2. \tag{1.6}$$

This parameter stipulates that the maximum shear stress amplitude is the dominant factor in fatigue damage accumulation.

Smith-Watson-Topper parameter This parameter [37] is a mean stress corrected damage parameter, and it takes the form

$$P_{SWT} = \sigma_{max}\Delta\epsilon \tag{1.7}$$

where σ_{max} refers to the maximum stress during the cycle. This parameter stipulates that the combination of the maximum normal stress and normal strain range describes the damage accumulation.

1.2.1.2 Critical Plane Analysis

One way to extend continuum uniaxial damage techniques to multiaxial fatigue is via critical plane analysis. In critical plane analysis, a damage parameter, whether uniaxial or multiaxial, is computed on a number of planes which have orientations that are distributed around the points of the compass, (e.g., every 10°). The plane which has the largest value of the parameter is presumed to be the one on which failure will occur. For a single damage event, this technique finds the largest value of a damage parameter and the plane upon which it occurs. For in-phase loading (loading in which the ratio of the orthogonal stresses or strains remains constant) this plane remains constant; for constant amplitude loading the damage accumulation rate on that plane remains constant.

1.2.1.3 Multiaxial Damage Parameters

These are damage parameters in which more than a single axis loading is considered.

Brown and Miller parameter Originally the the Brown and Miller parameter [38] was expressed as

$$(\epsilon_{11} - \epsilon_{33})/2 = f\left((\epsilon_{11} + \epsilon_{33})/2\right), \tag{1.8}$$

where f is an arbitrary function. However, this formula is usually expressed [39, 40] as

$$P_{BM} = \Delta\epsilon_{xy}/2 + K(\Delta\epsilon_{xx}/2), \tag{1.9}$$

where the empirical factor K is usually taken as 1/2 for steels. The shear strain amplitude is the most important factor, and the next most important is the tensile strain amplitude normal to the plane of shear – it contributes half as much (for steel) to the total damage accumulation. The second term represents the influence that the normal strain range can have on crack face interference. The Brown and Miller parameter is only defined on the maximum shear strain plane.

Fatemi-Socie-Kurath parameter A parameter of this form was originally proposed by Findley [41]. Later, Fatemi et al. [29, 30] and Socie et al. [42] developed somewhat similar parameters which can be generalized into a single parameter [39, 40] and are termed, for the purpose of this document, as the Fatemi-Socie-Kurath parameter. This parameter takes the form of

$$P_F = \frac{\Delta\gamma}{2}\left(1 + K_F\frac{(\Delta\sigma_n/2)}{\bar{\sigma}_y}\right) \tag{1.10}$$

where $\bar{\sigma}_y$ is the cyclic yield stress and K_F is a factor usually taken somewhere between 0.3 and 0.6. In this parameter, the shear strain amplitude is the primary source of damage, but the amplitude of the tensile stress normal to the shear plane strongly influences the damage that the shear strain amplitude can create – in other words the impact of normal stress on crack face interference.

Chu's parameter Chu's parameter [43] is a multiaxial extension of the Smith-Watson-Topper parameter [37] and is represented by

$$P_C = \tau_{max}\Delta\gamma + (\sigma_n)_{max}\Delta\epsilon_n/2. \tag{1.11}$$

The second term in the equation is that of the Smith-Watson-Topper parameter and represents the tensile damage contribution normal to the crack plane while the first term represents the damage contribution by shear.

1.2.2 Fatigue Crack Propagation

Successful efforts to model stable crack propagation began in the 1950's when Paris [44] first introduced ΔK as a crack driving parameter and correlated it with crack growth rate data (da/dN). Typically K is used in the form

$$\Delta K = F\Delta S\sqrt{\pi a}, \tag{1.12}$$

where the factor F incorporates crack geometries, component geometries and loading mode, ΔS is the applied positive stress range and a is the crack length. Elber [8, 9] introduced the concept of crack closure to explain the variation in crack growth rate

with mean stress for a constant ΔK value. Schijve [5] described closure as the process whereby the uncracked material at a crack tip is shielded from the full range of remotely applied stress by plasticity at the crack tip, interference between the crack faces, and other effects. Elber [9] developed the concept of the crack tip opening stress (S_{op}) which describes the first point upon increasing loading at which the crack is entirely open. Above S_{op}, any increase in the applied load is seen immediately by the material at the crack tip. Using this concept Elber [9] then proposed an effective stress intensity,

$$\Delta K_{eff} = (S_{max} - S_{op})\sqrt{\pi a} \quad \text{where } S_{max} > S_{op}. \tag{1.13}$$

When it became apparent that the small scale yielding assumption built into ΔK was frequently violated, fatigue researchers began using a strain intensity factor [45] where

$$\Delta K(\epsilon) = \Delta \epsilon E F \sqrt{\pi a}. \tag{1.14}$$

Several researchers [46, 47, 48, 49] have employed this technique in applications where plasticity was significant.

1.2.2.1 Modelling Short Crack Growth

Short cracks are those cracks, typically smaller than a single grain diameter in size, whose growth rates are much faster than that of a significantly longer crack with the same applied ΔK level. Small cracks are usually a few grain diameters in size but still have a faster growth rate than that of a long crack. A long crack is one which is several grain diameters in length and which is unaffected by local variations in microstructure. It has been generally observed that short crack growth occurs in favorably oriented grains which have a slip system (nearly) aligned with a maximum shear plane. Small crack behavior typically involves more than a single grain but, in a fashion similar to short cracks, small cracks are strongly affected by their interaction with microstructural features.

Abdel-Raouf et al. [50] presented a short crack model that describes the strain concentration profile for a small edge crack in a favorably oriented grain intersecting the free surface. The strain concentration profile is expressed by

$$Q_\epsilon = \frac{\Delta\epsilon}{\Delta e} = 1 + q \exp\left(-a\frac{\alpha}{D}\right) \quad \text{for } a > 3\mu m, \tag{1.15}$$

where $\Delta\epsilon$ is the strain range, Δe is the nominal section strain range, a is the crack length, and q is the strain concentration factor at the surface less 1 ($Q_\epsilon^{a=0} - 1$), D is the grain size and α is a constant dependent upon the "deformation character." They determined that a typical value of q for a polycrystal with randomly oriented grains would be approximately 5. This approach has been successfully applied in short crack/long crack growth simulations using strain intensity factors [51].

Socie [47, 52] found that small crack growth rates for a given stress intensity range in modes I, II, and III were all similar for Inconel 718 and aluminum 7075-T6 for crack lengths up to 1mm. He determined that the error would be small if, under tensile loading, shear cracks growing on maximum shear planes were presumed to be mode I cracks growing on the maximum principal strain amplitude plane. Wang et al. [53] determined that, for a given stress intensity range, shear and tensile cracks grow in Waspalloy at roughly equivalent rates. Lastly, torsional fatigue data on an alloy steel from Wang, et al. [27] and uniaxial fatigue data on the same steel from Wang, et al. [54] have very similar growth rates.

Given that several widely differing materials (an aluminum, a steel and two nickel based superalloys) exhibit nearly equal tensile and shear growth rates, it is possible that many materials share this behavior. Hence, in the region of stage I crack growth, the analysis of cracks growing under multiaxial loading may potentially be modelled with reasonable accuracy by a single pre-existing short crack model such as the Q_ϵ model.

1.2.2.2 Multiaxial Crack Growth Equations

For multiaxial loading Socie et al. [47] suggested the following equations (modified in this thesis with Q_ϵ) for all of the cracking modes

$$\Delta K_I(\epsilon) = F_I E \Delta\epsilon Q_\epsilon \sqrt{\pi c}\,, \tag{1.16}$$

$$\Delta K_{II}(\epsilon) = F_{II} G \Delta\gamma Q_\epsilon \sqrt{\pi c}\,, \tag{1.17}$$

$$\Delta K_{III}(\epsilon) = F_{III} G \Delta\gamma Q_\epsilon \sqrt{\pi c}\,, \tag{1.18}$$

where c is the surface half crack length. The geometry factors F_I, F_{II}, and F_{III}, derived from Irwin [55] and Kassir and Sih [56], are all dependent on crack aspect ratio, Poisson's ratio, nominal loading condition, and the location of the calculation along the crack front.

1.2.2.3 Crack Growth Directions

Unlike uniaxial fatigue, cracks subjected to variable amplitude multiaxial loading are rarely confined to a single growth plane. Thus, predicting the direction and plane upon which a crack will grow is a significant aspect of modelling multiaxial crack growth.

Crack growth rate criterion Hourlier and Pineau [20] were the first to demonstrate that, for a given ΔK, cracking will occur in the mode in which the crack growth rates are the highest. Their experiments on titanium, aluminum, and steel alloys demonstrated that cracks grow in the fastest growth rate mode available to the material. Since that time, other researchers have duplicated their findings in AISI4340 steel [57] and ferritic stainless steels [28]. In fact, in both of these works, the researchers were able to demonstrate macroscopic differences in crack growth features which resulted from different growth modes, and they demonstrated that the crack growth rate followed a compound curve constructed of the mode I and III growth curves.

Strain energy release rate criterion Another set of researchers proposed that the direction of crack propagation will be that in which the strain energy release rate is greatest. Originally proposed by Griffith [58] to predict the onset of fracture, it was extended by Palaniswamy [59] and Nuismer [60] to predict both the crack growth direction and the likelihood of a crack branching off in another direction.

1.2.2.4 Cracking Observations for Tests of SAE 1045 Steel

For a stainless steel, a superalloy, and a low carbon steel Socie [24] observed that cracks nucleate on shear planes regardless of material type, loading amplitude, and loading type (torsion vs. uniaxial). Fash [61] noted that crack nucleation always began on shear planes over a range of ratios of torsion to tension for SAE1045 steel.

Perhaps the best review of cracking behavior observed in normalized SAE1045 steel (the material used in this study) was provided by Socie [24] where he provided crack growth maps for loading in tension and torsion, Figures 1.2a and 1.2b respectively. These maps chart the kind of crack growth that can be anticipated in 1045 steel as a function of specimen fatigue life (N_f) and life fraction (N/N_f). Socie groups behavior into three areas: shear crack growth (Region A), tensile crack growth (Region B), and crack nucleation (Region C). The lowermost line denotes the life to reach a crack of 0.1mm. Hence, a specimen with a failure life of 30,000 cycles to failure undergoing tension loading would reach a crack length of 0.1mm at $N/N_f \approx 0.2$ (or 6000 cycles). At $N/N_f \approx 0.7$ (or 21,000 cycles) the crack growth would move onto tensile planes and continue in this way until failure.

As the loading moves from tensile to torsion the dominance of shear cracking (Region A) moves from roughly 10,000 to 500,000 cycles to failure. As can be seen in Figure 1.2b a transition was observed in shear cracking behavior from the multiple initiation of shear cracks at low lives (high strain amplitudes) and rapid linking at failure to a single dominant crack which grows to failure at long lives (low strain amplitudes). These cracking observations will be compared with similar observations made in this investigation.

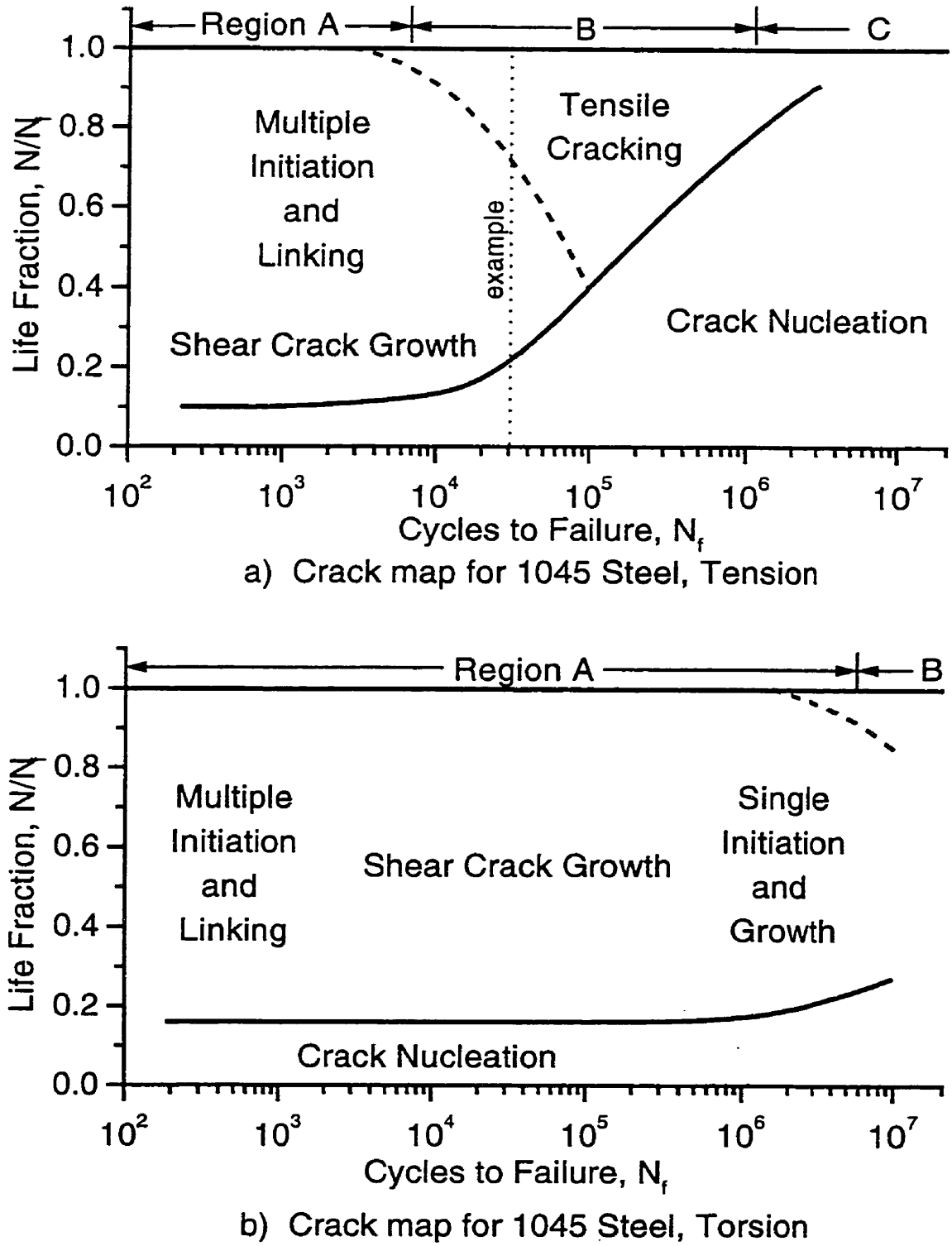

Figure 1.2: Cracking behavior observed normalized SAE 1045 steel subjected to (a) tension and (b) torsion, taken from [24].

1.3 Purpose and Objectives of This Study

As demonstrated in the foregoing review, much knowledge has been gained concerning the nature of crack face interference. DuQuesnay [3] demonstrated that life tests which were conducted under closure-free conditions (i.e. overload tests) gave the lowest fatigue lives, and under multiaxial loading others [19, 21, 22, 23] have shown that mode I crack growth could be accelerated by compressive stresses applied in the crack plane. Further, researchers found that shear crack growth was accelerated by static tensile loads applied across the crack [28, 29, 30], compressive overloads [4] applied across the crack, or shear overloads [31] applied in the plane of the crack.

The main objective of this study was to obtain crack face interference-free growth over a range of multiaxial loading conditions and to determine the usefulness of this data for predicting service load fatigue (chapter 3). The elimination of crack face interference was achieved in several ways for several different loading conditions. Initially three sets of tests which involved constant amplitude torsional cycles were conducted on tubular specimens. In order to eliminate crack face interference, two test conditions had periodic axial overloads (with and without mean stress) and the third had torsional overloads. These test conditions were duplicated in notched axle-shaft specimens to investigate the effects of overloads in a component-like structure. Constant amplitude torsion tests were conducted for both specimen types to provide data for a comparison with crack face interference-free tests. A number of other test conditions were investigated under in-phase loading. In these tests, the phase angle between the torsion and tension strains was held constant throughout the entire test. In other words, the ratio between axial and torsional strains is rigidly maintained. Five different strain ratios were investigated ranging from torsion to tension loading, and, in each of these ratios, both periodic overload and constant amplitude fatigue curves were obtained.

The results of the periodic overload tests were used to compare various damage criteria and to select those which were appropriate for biaxial loading. Observations of cracking under each kind of loading were used to select criteria.

Another principal objective of this work was to model the cracking behavior observed in the periodic overload tests (chapter 4). In order to do this, two crack face interference-free crack growth curves were developed for the principal cracking modes observed in the specimens – one each for tensile cracking and shear cracking. The crack growth rate and strain energy release rate criteria were used to predict the length of initial shear cracks in the specimens.

The second part of the crack growth modelling involved making crack growth-based life predictions for crack face interference-free fatigue life tests. Initial predictions were made using the models described in section 1.2.2, and, for each strain ratio, the value of $\frac{a}{D}$ from equation 1.15 (section 1.2.2.1) was determined. A final set of predictions was made using the crack growth rate and strain energy release rate criteria. In this case the value of $\frac{a}{D}$ was determined separately for shear crack growth (torsional loading) and tensile crack growth (tensile loading), and crack face interference-free fatigue life predictions were made for all of the strain ratios.

Chapter 2

Materials and Procedures

In this chapter, the materials, test equipment, and techniques used in this research are outlined.

2.1 Material

The material used in this study was an SAE 1045 steel in the normalized condition. The steel was hot rolled into 63.5mm diameter bar and normalized to produce a Brinell hardness of 203BHN. The chemical composition of this steel is given in Table 2.1. SAE 1045 is one of the most common grades of steel used in the automotive industry because of its combination of good hardenability and low cost. A large number of components such as suspension parts, chassis parts, powertrain parts and bracketry are fabricated from SAE 1045. It is, however, unusual to use this material in a state as soft as that employed in this study – the lowest hardness typically encountered in an application is 250BHN. Normalized steels are intended for fabrication and subsequent

Table 2.1: Chemical Composition of SAE 1045 steel. (Wt. %).

C	Mn	P	S	Si	Cu	V	B
0.47	0.80	0.016	0.016	0.22	0.08	<0.005	<0.0005
Al	**Ti**	**Nb**	**Ta**	**Ni**	**Cr**	**Pb**	**Fe**
<0.005	<0.005	0.036	<0.005	0.04	0.05	<0.005	bal

heat treating to final hardness. This particular lot of steel has been the focus of a large SAE multiaxial fatigue study [62], and the hardness was chosen to conform with the SAE study so that comparisons with data from it can be made. It should be noted that current production steels have fewer impurities and are more microstructurally homogenous than the steel used in this work.

Figures 2.1, 2.2, and 2.3 present the microstructure of the steel in the Longitudinal-Transverse (L-T), Longitudinal-Short (L-S), and Short-Transverse (S-T) orientations, respectively. It has a pearlitic/ferritic microstructure and, because of the normalization procedure, has equiaxed grains of roughly $25\mu m$. A lower magnification of the L-T orientation, shown in Figure 2.4, shows the banding characteristic in this lot of material. Figure 2.5 shows MnS stringers which, in this steel, range in length from 0.1 to 2mm. These features are aligned with the rolling direction.

2.2 Uniaxial Properties

2.2.1 Monotonic Tests

The uniaxial hourglass specimens used in this research (Figure 2.6) were first turned in a lathe, low stress ground to final dimensions, and subsequently polished longitudinally to remove machining marks. This approach minimizes the residual stresses introduced into the specimen as a result of manufacturing [63].

Tensile tests were performed in stroke control on a 25kN MTS 810 servohydraulic test system with a 6.35mm extensometer. Five specimens were strained to failure. A Masscomp 5450 Unix workstation provided the input signal and acquired strain, load and stroke data via the program discussed in section 2.3.1 [64]. The values shown in

Table 2.2: Normalized SAE 1045 monotonic material properties.

Hardness	203 BHN	Yield Stress, Upper	476MPa
Engineering Strain at Failure, e_f	0.432	Yield Stress, Lower	397MPa
Reduction in Area, %RA	48.2	Ultimate Stress	703MPa
Strength Coefficient, K	1370MPa	Young's Modulus, E	203GPa
Strain Hardening Exponent, n	0.261		

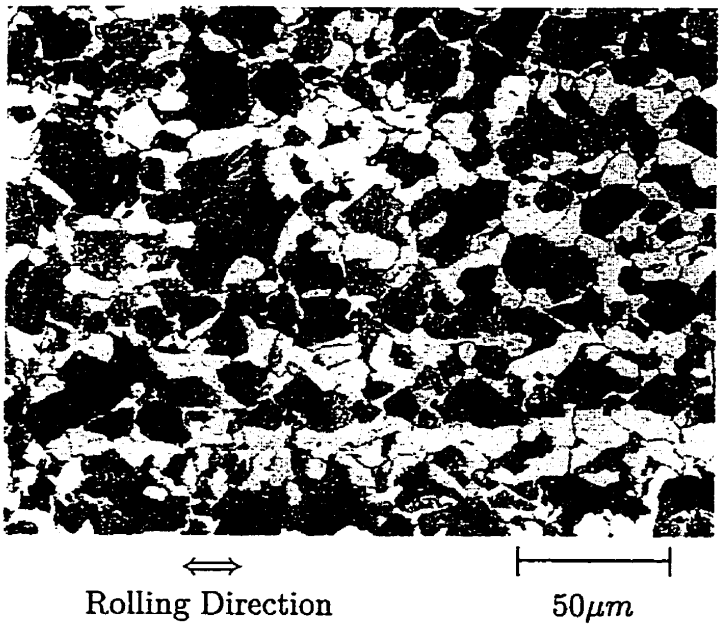

Figure 2.1: Microstructure of normalized SAE 1045 steel (400X), L-T orientation.

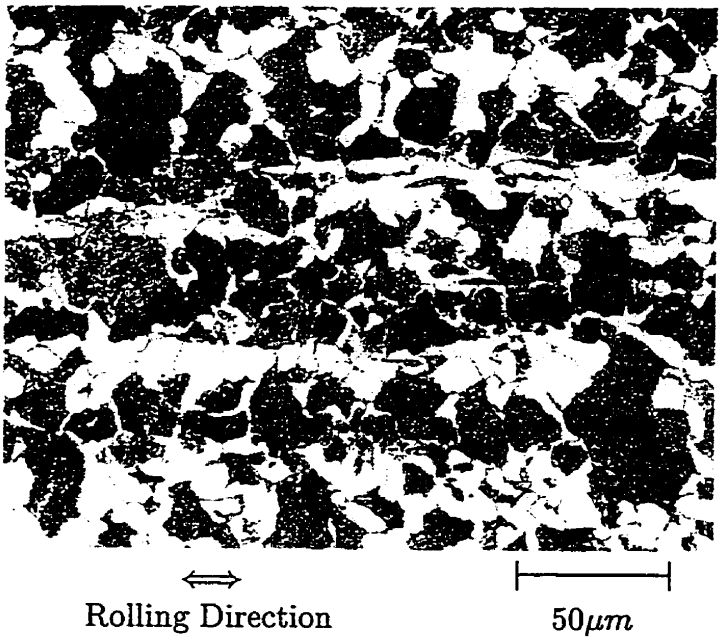

Figure 2.2: Microstructure of normalized SAE 1045 steel (400X), L-S orientation.

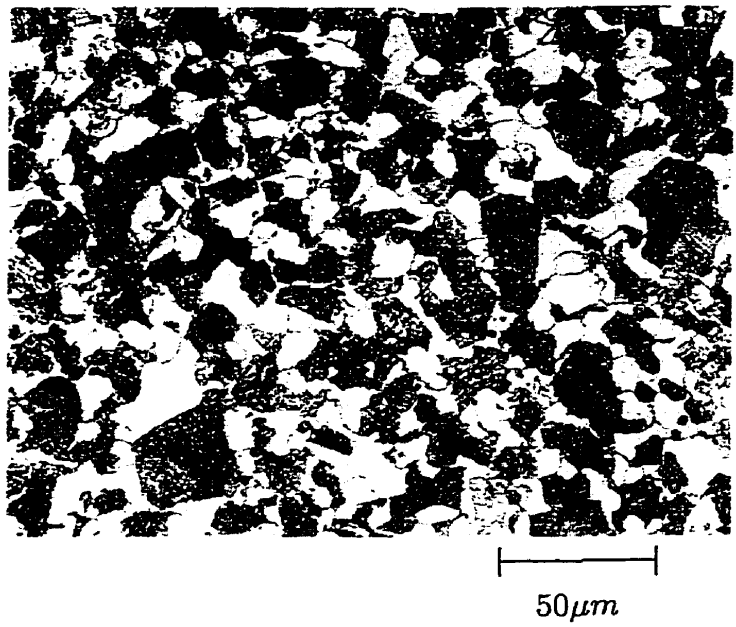

Figure 2.3: Microstructure of normalized SAE 1045 steel (400X), S-T orientation.

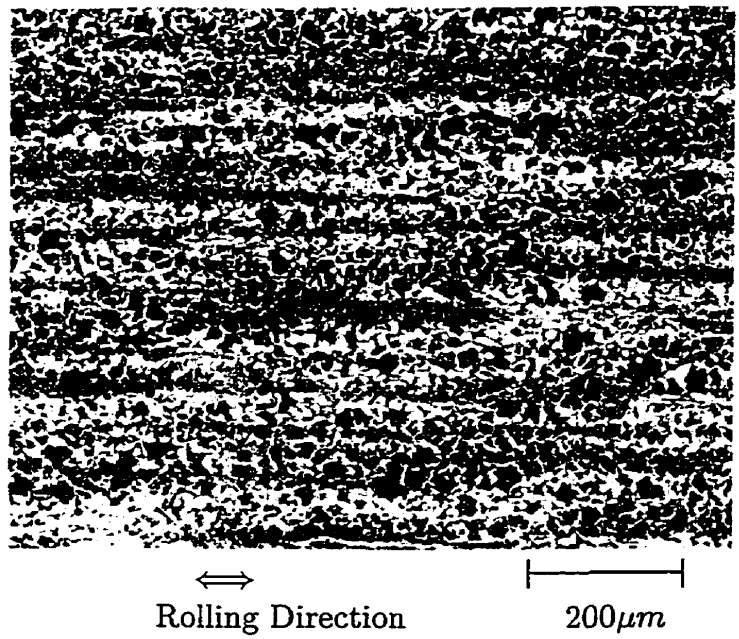

Figure 2.4: Microstructure of normalized SAE 1045 steel (100X) showing banding in the L-T orientation.

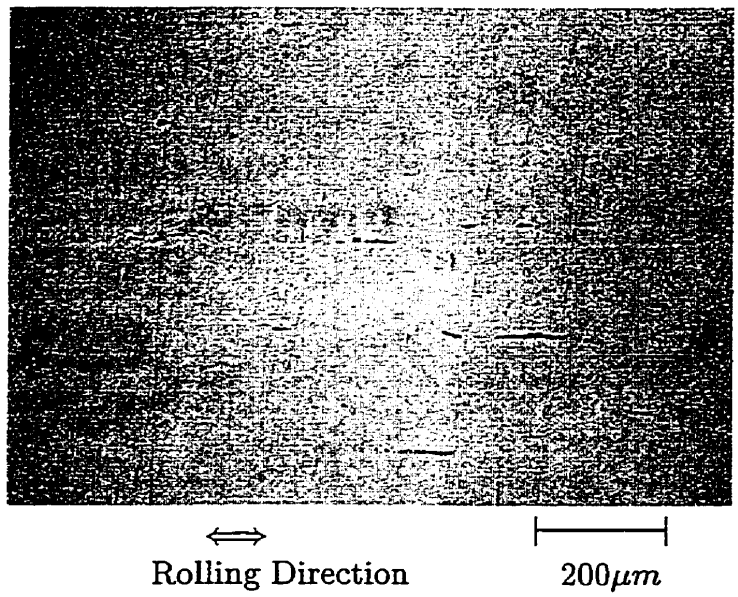

Figure 2.5: Stringers in normalized SAE 1045 steel (125X), L-T orientation.

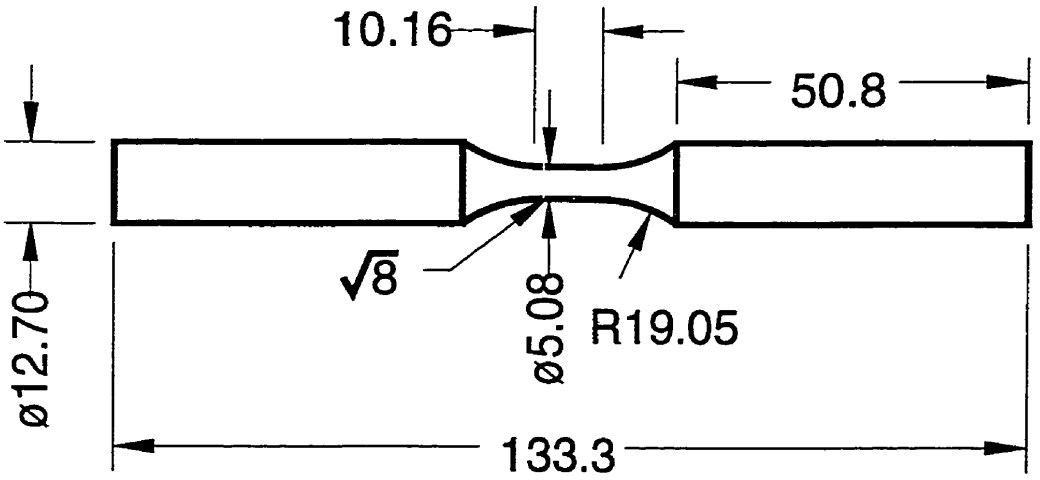

Figure 2.6: Uniaxial Specimen. All dimensions in mm.

Table 2.2 are the average of the results from the five tensile tests. Initial specimen diameter, reduction in area and strain at failure measurements were made with the aid of a shadowgraph.

2.2.2 Constant Amplitude Tests

The fully reversed ($R_\epsilon = \epsilon_{min}/\epsilon_{max} = -1$) tests presented in Figure 2.7 were conducted in strain control, and conformed to ASTM E606 [63]. Specimen diameters were measured with a shadowgraph. A 7.62mm gage length extensometer was used, and its knife edges were set into epoxy dots on the specimen surface to avoid premature initiation of a crack. Specimens were prepared as discussed in section 2.2.1.

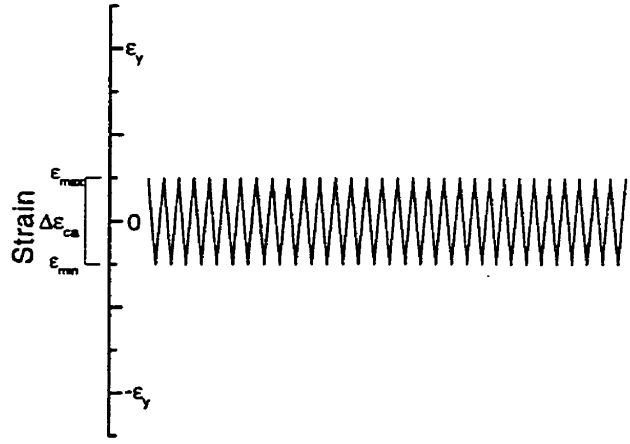

Figure 2.7: Uniaxial constant amplitude history. ($R_\epsilon = \frac{\epsilon_{min}}{\epsilon_{max}} = -1$).

The same servohydraulic system used in section 2.2.1 was also used for the uniaxial constant amplitude tests. The system load train, which included hydraulic grips, was aligned with an instrumented specimen. This procedure was performed in order to reduce premature initiation due to grip-induced bending. It was determined that the maximum specimen strain due to load frame misalignment was 20 microstrain in bending at zero applied load. Subsequent examination of the initiation sites of failed specimens indicated that the sites were randomly oriented around the circumference and along the gage length of the specimen using the load frame as reference. A consistent initiation location would have indicated that bending was present in the specimen; thus, it may be concluded that the uniaxial tests were not unduly influenced by misaligned grips.

Waveform control was provided by a pc-based programmable controller [65] which adaptively adjusted the output to ensure that the peak error was less than one percent.

Table 2.3: Normalized SAE 1045 cyclic material properties (per ASTM E606).

Young's Modulus, E	203GPa
Yield Stress, Proportional Limit	155MPa
Yield Stress, 0.2% Offset	379MPa
Cyclic Strength Coefficient, K'	1480MPa
Cyclic Strain Hardening Exponent, n'	0.221
Fatigue Strength Coefficient, σ'_f	1580MPa
Fatigue Strength Exponent, b	-0.136
Fatigue Ductility Coefficient, ϵ'_f	0.7325
Fatigue Ductility Coefficient, c	-0.566

The maximum frequency used in these tests was 40Hz, and stress-strain data was collected in logarithmic increments on an analog X-Y recorder. Failure was defined as a 5% load drop.

Uniaxial cyclic properties for this material appear in Table 2.3.

2.2.3 Periodic Overload Tests

Overload tests were conducted in strain control. The histories used in the uniaxial overload tests consisted of a single compression-tension overload cycle followed by a series of smaller cycles whose peak tensile strains were the same as the peak tensile strain of the overload cycle, see Figure 2.8. The amplitude of the overload cycle itself was selected to be 0.5% strain which corresponded roughly to 10,000 cycles to failure under conventional constant amplitude testing. A number of smaller constant amplitude cycles (η) followed the overload cycle, and the smaller cycle amplitude was set, depending on the test, at a value between 0.2% strain and 0.06% strain. Finally, the number of smaller cycles, η, placed between the overload cycles was chosen such that the overload cycles constituted no more than approximately 25% of the total damage. As discussed in [3], the effect of the overloads is to reduce as much as possible the crack closure level and thus yield a conservative strain life curve. In this document the term "small cycles" (sc) is used when referring to overload tests to indicate the smaller cycles in the overload history.

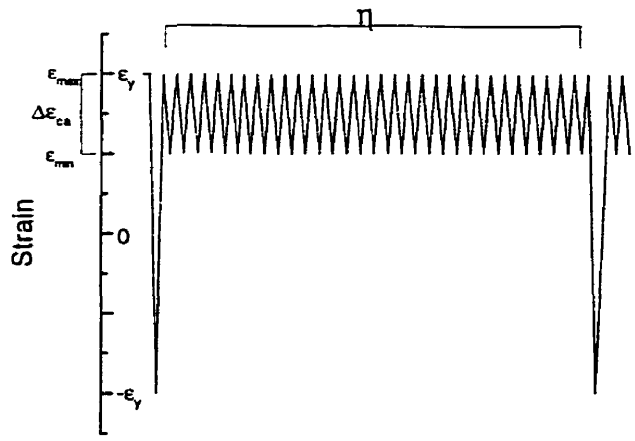

Figure 2.8: Uniaxial overload history.

2.2.4 Uniaxial Crack Growth Tests

These tests were performed in order to obtain a ΔK_{eff} vs. da/dn curve. This curve is a closure-free crack growth curve which requires the entire loading cycle be above the crack opening level. Overload cycles and high R-ratio tests were used to accomplish this task. A larger, 50kN servohydraulic system was necessary in order to test the specimen shown in Figure 2.9, and these tests were performed in load control with no extensometer. A Questar QM-100 long focal length microscope (set to 900x magnification) attached to a measurement stage was used to obtain crack growth measurements to within an accuracy of $2\mu m$.

The specimens were precracked to a crack length of 2.5mm using a constant amplitude (R_σ=-1) stress of 276MPa. Each crack length measurement was made twice to reduce measurement error. Stress intensity was calculated using the stress intensity function for long cracks and can be expressed by

$$\Delta K_I = \Delta S_I F_{cgI}\left(\frac{a}{W}\right)\sqrt{\pi a} \tag{2.1}$$

where ΔS_I is the nominal section stress, a is the crack length, and W is the specimen width. The geometry factor, $F_{cgI}\left(\frac{a}{W}\right)$, for this specimen is detailed in Appendix B, section B.1.1.

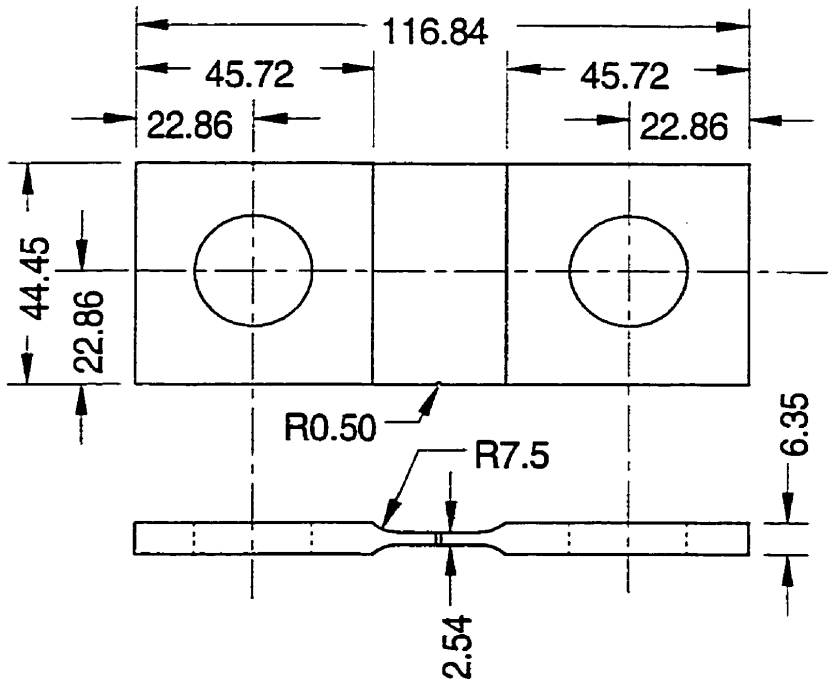

Figure 2.9: Mode I crack growth specimen. All dimensions in mm.

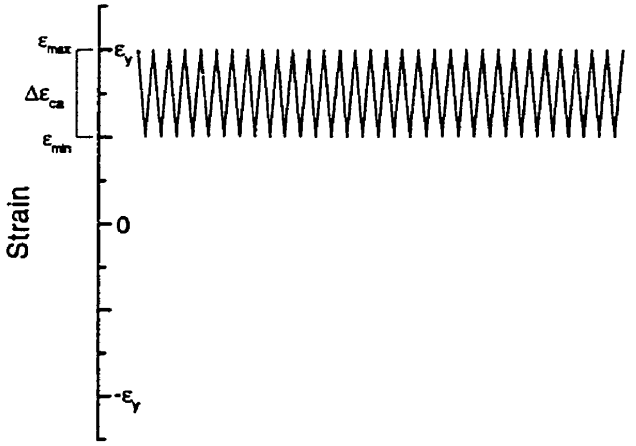

Figure 2.10: High R-ratio crack growth history.

Measurements made below 10MPa$\sqrt{\text{m}}$ were taken using a high R-ratio loading cycle, see Figure 2.10. Measurements at stress intensities above this level employed a periodic overload history as in Figure 2.8 because of the increasing crack opening

load. In these tests, the maximum nominal stress was set to 276MPa regardless of the load history employed, and the minimum of the overload cycle was -276MPa. Only in cases where the required stress intensity caused the peak stress to approach these values were they increased. Crack opening level was verified optically as in [51].

2.3 Multiaxial Tests and Techniques

2.3.1 Bending-Torsion Tests

The bending-torsion test frame pictured in Figure 2.11 was developed by the Fatigue Design and Evaluation Committee of SAE to study the effect of notches on multiaxial fatigue. The test specimen, in Figure 2.12, is clamped rigidly at one end and compressed into a yoke, by means of a collet, at the other. The yoke is then connected to two 25 kN actuators. With this frame a maximum bending moment (at the notch) of 6700Nm can be applied when the actuator loads are of the same sign, and a maximum torsional moment of 9000Nm can be applied when the actuator loads are of opposite sign. When a mixed loading is desired, the histories used to generate the desired torsion and bending responses are a linear combination, where the left actuator command signal is given by bending–torsion and the right by bending+torsion.

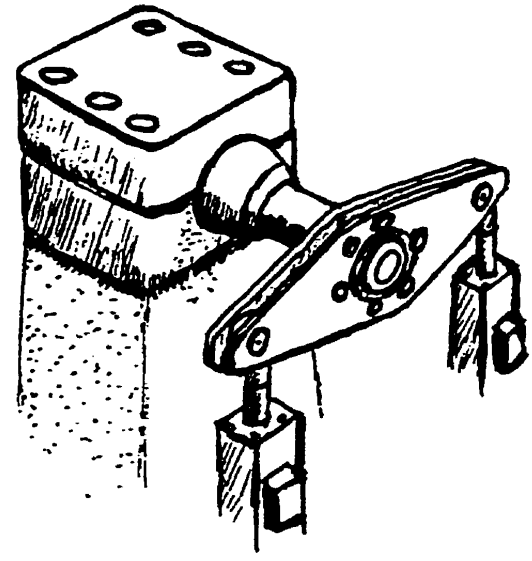

Figure 2.11: Bending torsion fixture with specimen.

The nature of this test frame couples bending and torsional loads, hence the maximum achievable moment in torque, for instance, is correspondingly decreased when a bending moment is applied, and vice-versa. The centerline to centerline distance between the actuators is 203mm, with the specimen center located halfway between the actuators. The distance from the yoke load application point to the

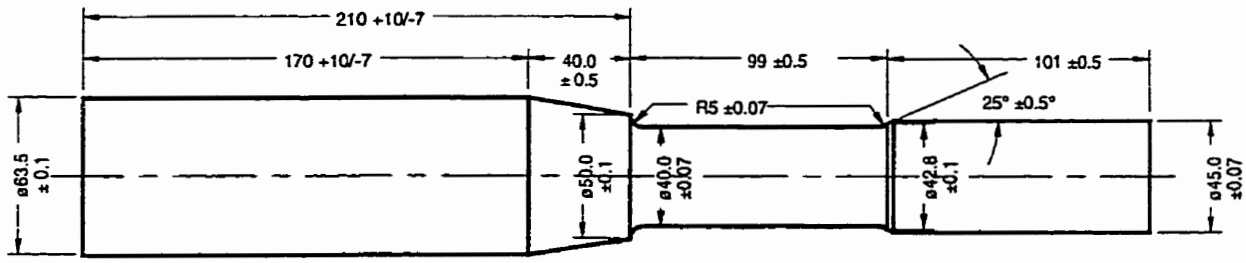

Figure 2.12: Bending-torsion specimen. All dimensions in mm.

specimen notch root is approximately 150mm – this distance was measured for each specimen and the bending loads adjusted accordingly. The advantage of this test geometry is that, in torsion, crack nucleation is confined to a small circumferential area near the notch, and, if bending is superimposed it is further reduced to a narrow strip on the top and bottom of the shaft.

The adaptive control program used in the bending-torsion tests [64] was different from that used in the uniaxial tests because of the need to synchronize the two input channels and to record feedback with the computer, but the accuracy of control was identical to the uniaxial program. These tests generally employed a maximum torsional test frequency of 8Hz (some high strain amplitude tests were slowed down to minimize section heating) and a maximum bending frequency of 2Hz. Specimen failure was defined as the first discernible compliance change – typically a 5% increase in compliance, and this resulted in an estimated failure crack length of one to three millimeters (as determined from replicas taken at logarithmic increments throughout the life of each specimen). High and low values of load (command and feedback) and displacement were periodically logged to a datafile on the control computer for later use in compliance calculations. Specimen compliance as a function of cycles during the test was presented graphically, and the determination of cycles to "failure" was made from these plots.

Surface replicas were taken of each shaft using dental impression material. These replicas were taken in logarithmic increments throughout the life of each specimen, labeled and stored. They were later used for crack measurements.

On some bending-torsion tests, small strain rosettes (MM EA-06-015RJ-120E) were laid in the notch to measure the material strain response. Each rosette was mounted with its 45° leg oriented parallel to the specimen axis with the gage center 1.5mm removed from the notch root in the reduced section.

2.3.1.1 Constant Amplitude Bending and Torsion Tests

In a torsion test history the torsion history appears as in Figure 2.7 (in Nm rather than strain), and the bending history is a flat line at 0Nm. The converse is true in constant amplitude bending histories. All constant amplitude tests were subjected to $R_T = \frac{T_{min}}{T_{max}} = -1$ loading, where the T indicates torque.

These histories are resultant histories – the actual actuator histories are a superposition of the bending and torsion components. As mentioned in the previous section, the actuators move in concert in a simple bending test, and move in exactly opposite directions for a simple torsion test. Although both actuators are moving in both torsion and bending constant amplitude tests, the resultant bending moment on the shaft is zero in the torsion tests, and the resultant torsional moment is zero in the bending tests. A graphical example of how actuator and resultant histories are interrelated is given in section 2.3.1.3.

2.3.1.2 Static Bending Moment Torsion Tests

In these tests a static bending moment was maintained throughout the test while fully reversed (R_T=-1) torsional cycles were applied. The magnitude of the static bending moment used was inversely proportional to the magnitude of the torsional moment for torsional moments above 1500Nm. Since the static bending moment combined with the torsional cycling caused bending ratchetting, the ratchetting had to be kept to a sustainable level throughout the tests; hence the reduction in the static load. Ratchetting is a result of cyclic creep, and under multiaxial loading if a cyclic stress is placed on one axis and a constant tensile stress on the other, the axis with the constant stress will experience a cycle by cycle increase in inelastic strain. In the bending-torsion tests this was evidenced by a downward drift of the end of the

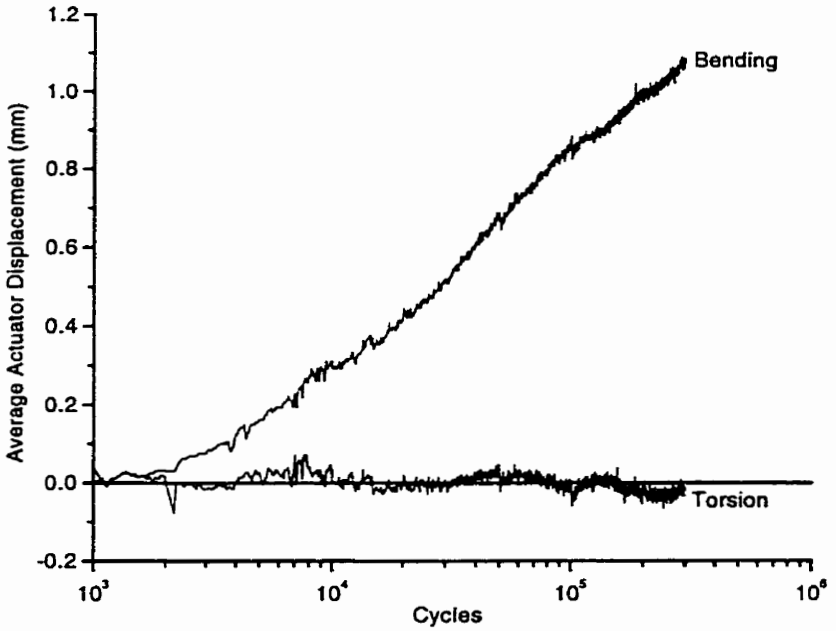

Figure 2.13: Ratchetting in a static bending moment test.

specimen, and it implies increasing bending strain throughout the test. An example of ratchetting can be found in Figure 2.13, where it is shown that through the course of the test the specimen end moves vertically due to ratchetting in bending. In this case there is no rotation and therefore no appreciable ratchetting in torsion.

Below 1500Nm torsion the shaft did not ratchet, and the full static bending moment of 2600Nm was used. See Figure 2.14.

2.3.1.3 Bending Overload Torsion Tests

Two different types of bending overload tests were used – a standard overload test in which the bending moment on the shaft is zero through the course of torsional cycling, and the peak hold test in which the bending moment is maintained at 2600Nm during torsional cycling. An example of the standard overload history is given in Figure 2.15. Figure 2.16 depicts a typical peak hold overload history with both actuator and resultant specimen histories. Ratchetting occurred in the peak hold tests, but the ratchetting strain was reversed by the periodic bending overload, and this allowed a full static moment of 2600Nm to be applied.

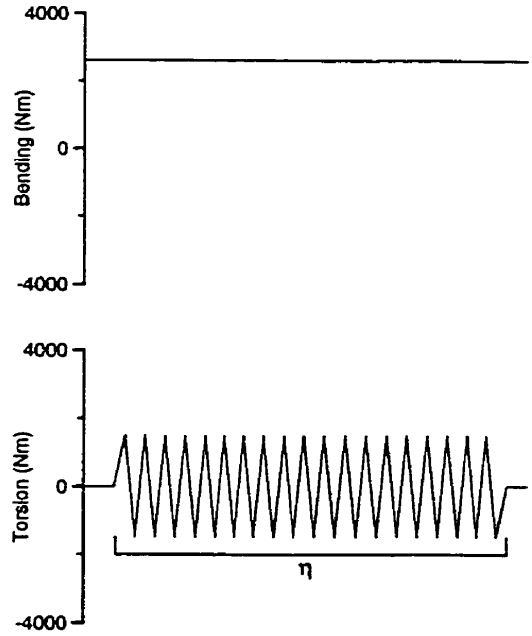

Figure 2.14: Static bending history used on bending-torsion rig.

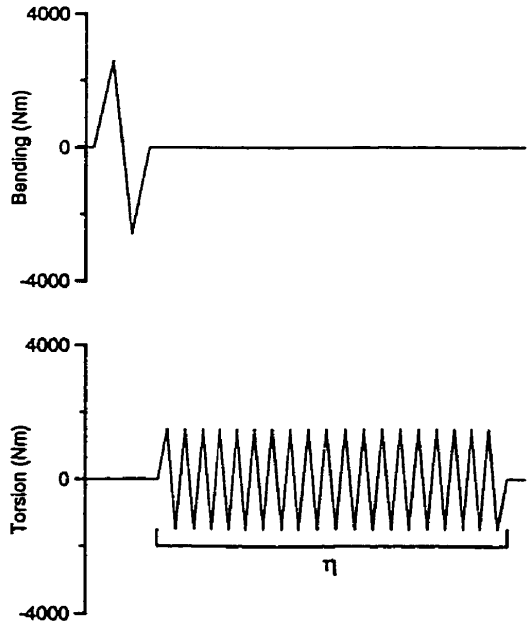

Figure 2.15: Bending torsion standard overload history.

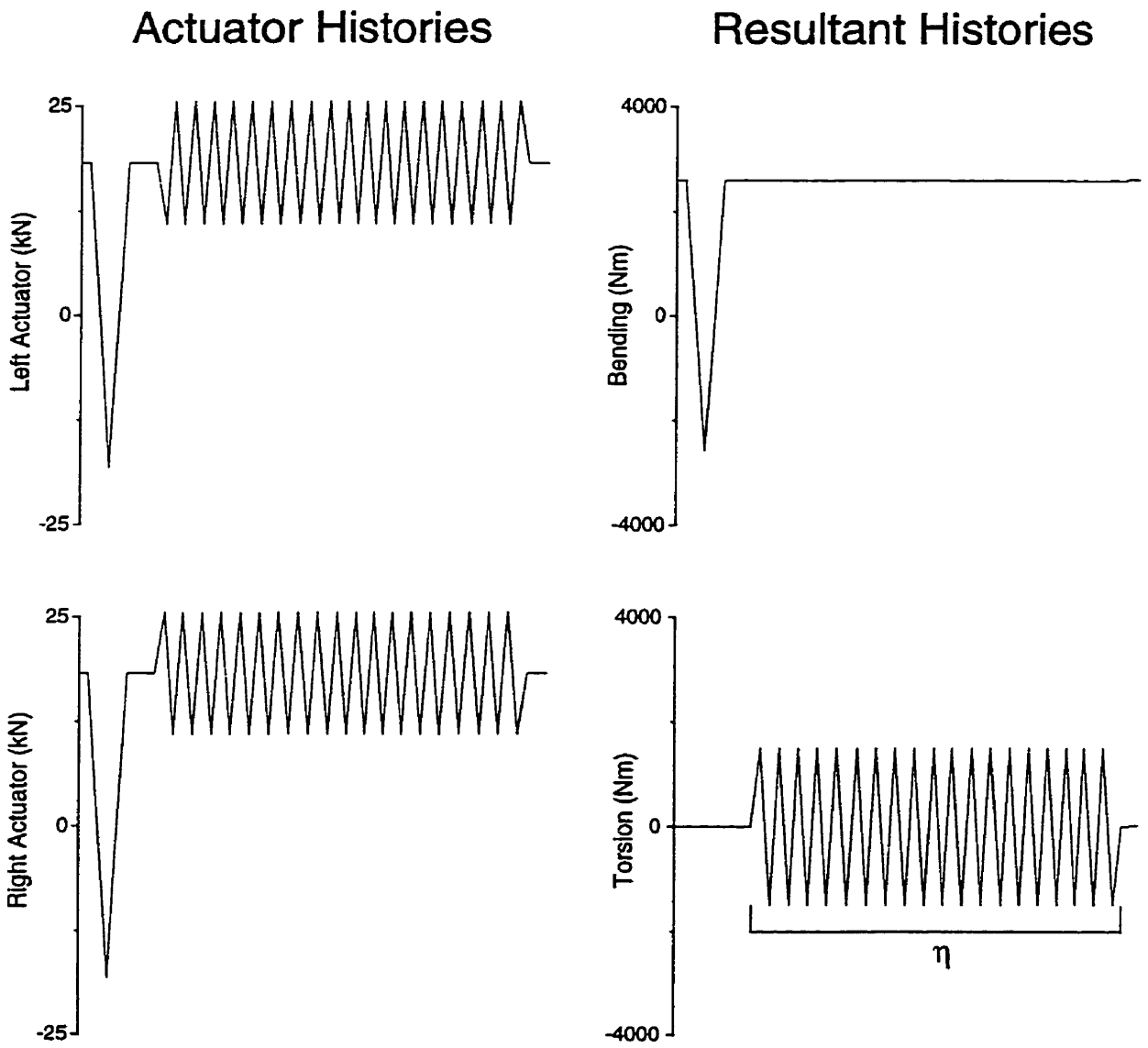

Figure 2.16: Bending torsion peak hold history showing relationship between actuator histories and resultant moment histories.

The number of small cycles between overloads (η) in both the standard and peak hold overload tests is set using the same criterion as used in the uniaxial overload tests – that overloads constitute no more than 25% of the total damage.

2.3.2 Axial-Torsion Tests

The axial-torsional tests were conducted with the load frame depicted in Figure 2.17. It is capable of exerting a 250kN axial force and a 2250Nm torque on test specimens. The load train was aligned in a fashion similar to that in section 2.2.2, with the result that the maximum bending induced by the grips was no greater than 25 microstrain.

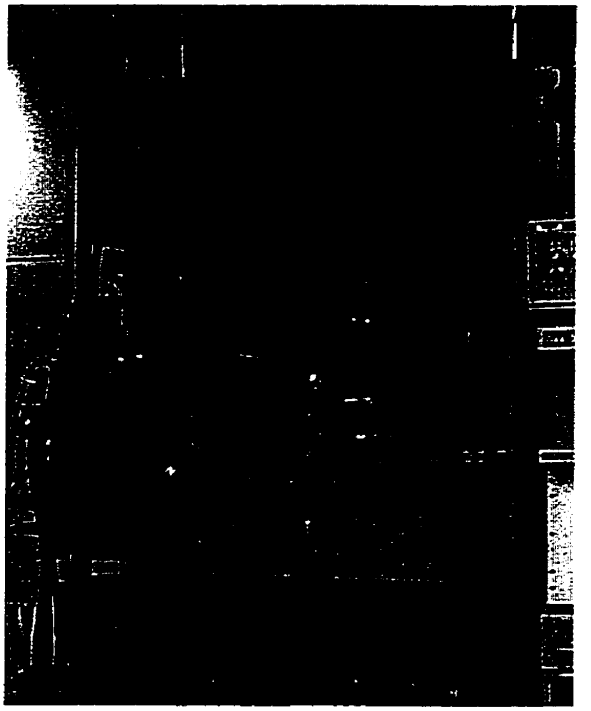

Figure 2.17: Axial-torsion load frame.

The hydraulic grips, developed at the University of Illinois [66], employ a standard 41.275mm machining collet. Because of the torsional loading component, the grip ends on the specimens were sanded with #60 emery cloth in a cross-helical pattern to improve friction between the collet and specimen. Further, the specimen was "locked" into the grips by a one-time axial preload of 44kN. This load represents a stress of 64% of the cyclic yield stress on the tubular specimens used in this study.

Strains were measured with an axial-torsion extensometer obtained from Epsilon Technology [1550-0100-010-002 ST]. A typical experimental setup with this extensometer is pictured in Figure 2.18. This extensometer has the advantage of sensing directly the shear strain at the specimen surface rather than measuring specimen twist. However, due to the large sprung mass connecting the two sides of the gage it can only be used in torsional strain control at frequencies below 1Hz. Any frequency higher than this

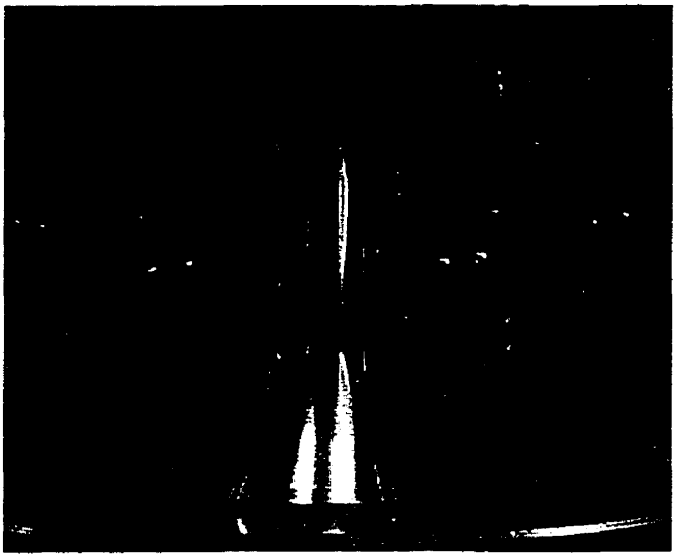

Figure 2.18: Typical specimen installation with axial-torsion extensometer.

excited the 120Hz natural resonance of the gage. When the gage is not in the control loop its maximum torsional frequency is 8Hz. The axial channel had a maximum useful control frequency of 10Hz.

Because of the need to run a large number of tests to 10^5 to 10^7 cycles, this instability problem forced a switch from strain control to rotation control. This change caused difficulties in maintaining the phase relationship between axial and torsional strain, and, as a result, the axial control was switched over to displacement. Since the LVDT installed in the load frame did not have the resolution necessary to control the strain endpoints, a displacement gage (and an additional control channel) was installed on the torsional reaction yoke, see Figure 2.19, and was calibrated to a displacement range of $\pm$0.4mm. Once installed, this new gage solved all strain phasing problems.

Tests were then conducted in displacement/rotation control while axial/torsional strain was controlled parametrically by a computer. Strains were controlled to an accuracy of one percent by the adaptive parametric control program used in section 2.3.1 [64]. A complete set of feedback signals, including strain, stress, and displacement/rotation, are shown in Figure 2.20 for a constant amplitude test. This

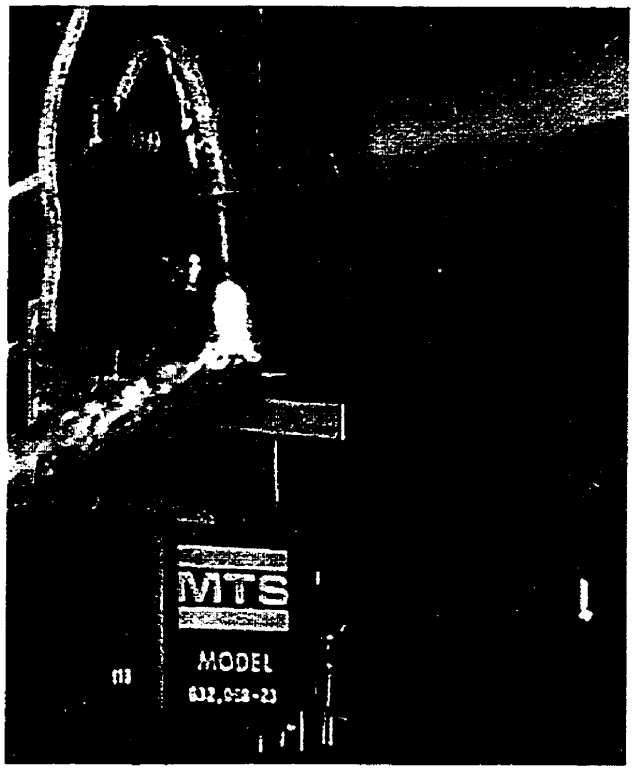

Figure 2.19: Displacement gage affixed to axial-torsion load frame.

figure shows that the phasing in the strain control is reasonably linear. The perturbation in the axial channel arises not from the control scheme, but from teflon debris in the hydrostatic bearings in the linear actuator; shortly after this test the actuator was rebuilt. This perturbation shows up most dramatically in the shear versus normal stress plot because of the plasticity it causes.

A maximum test frequency of 40Hz was employed for some high cycle tests while slower frequencies were used in tests where specimen heating or phase control were issues – at frequencies above 10Hz the hydraulic lines to the grips were disconnected to avoid fatigue failure of the fittings. At frequencies above 8 Hz load control was used on both axes. Specimen failure was defined as the first discernible compliance change. This change was determined from graphs of both load and compliance plotted as a function of cycles during the test. These calculations resulted in an estimated failure crack length of one to three millimeters. High and low values of load, strain, and

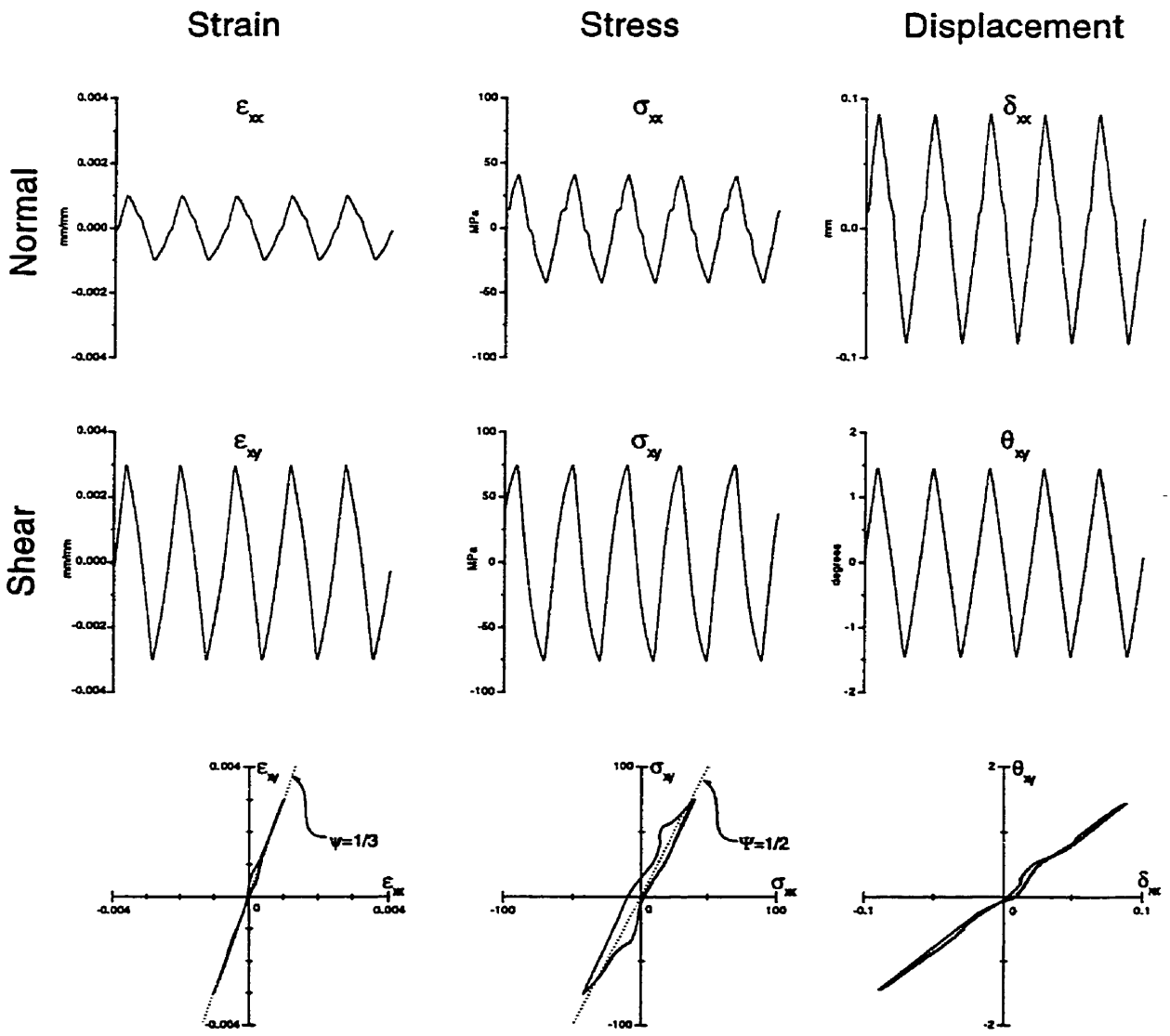

Figure 2.20: Feedback plots from a constant amplitude test including strain, stress and displacement, $\Psi = \frac{\sigma_{xx}}{\sigma_{xy}} = \frac{1}{2}, \psi = \frac{\epsilon_{xx}}{\epsilon_{xy}} = \frac{1}{3}, (\epsilon_{xy})_a = 0.003, (\epsilon_{xx})_a = 0.001$, test 34. All plots are taken from the same time slice.

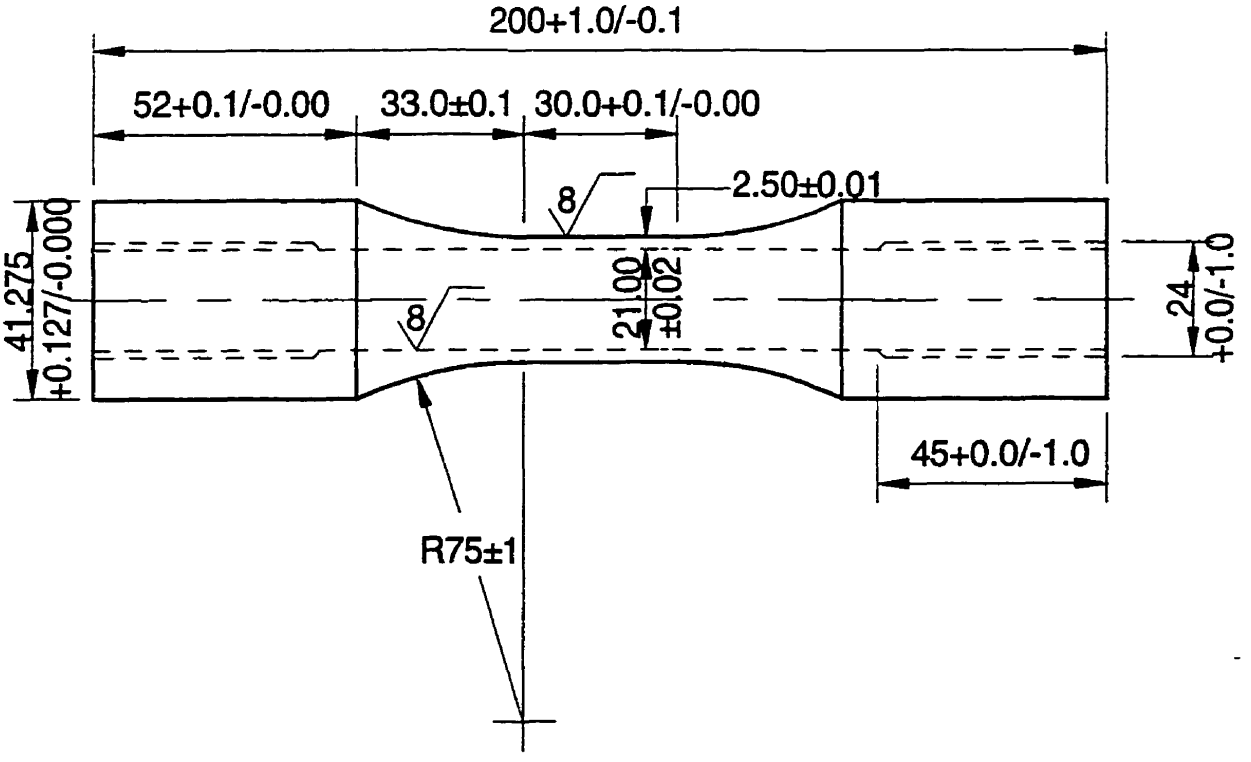

Figure 2.21: Axial-torsion specimen. All dimensions in mm.

displacement were periodically logged to a datafile on the control computer for later use in determination of failure life.

2.3.2.1 Fatigue Life Tests

A tension-torsion machine performed multiaxial fatigue life tests on the tubular specimens shown in Figure 2.21. Rough machining of the specimen consisted of lathe turning on the outer surface and boring the inside. Finish machining consisted of low-stress grinding and sanding on the outer surface and honing the inner surface with successively finer stones. The final surface finish on both the inner and the outer diameters was $\sqrt{8}\mu m$. The outer surface was polished to $1\mu m$ for the purpose of observing cracking behavior. Occasionally, if scoring was observed on the inner diameter of the tube, oversized buffing pads coated with $30\mu m$ diamond polishing compound were driven through the center of the tube using a lathe. This

pad removed the scoring, and it was followed by pads coated with successively finer compound until a $5\mu m$ finish was reached.

Four strain ratios were explored in this test series – $\psi = \epsilon_{xx}/\epsilon_{xy} = 0, \frac{1}{3}, \frac{2}{3}$, and $\frac{4}{3}$. These ratios were used because, at the overload strain level, they yield stress ratios $\Psi = \sigma_{xx}/\sigma_{xy} = 0, \frac{1}{2}, 1$, and 2. These tests were conducted so that the stress ratio produced at the endpoint of the overload cycle matched the desired stress ratio. Experimental hystersis loops in both tension and torsion (taken at the tips) indicated a relation between the strain and stress ratios of $\psi = \frac{2}{3}\Psi$. However, the stress ratio was not constant throughout an entire strain cycle. The actual stress ratios achieved at the overload loop tips in tests lie within 5% of the target ratio.

Constant amplitude The history inputs used in Figure 2.20 are typical of those used for $\psi = \frac{1}{3}$ constant amplitude tests. Strain ratios of $\psi = \frac{2}{3}$ and $\psi = \frac{4}{3}$ have normal strain histories which are 2, 3, and 4 times the size, respectively, of that pictured in the figure. For $\psi = 0$ the axial component is left in load control at 0 load for the duration of the test.

Overload tests Examples of the histories used in the multiaxial overload tests are depicted in Figure 2.22. The stress/strain ratios used in these tests were the same as those used in the constant amplitude tube testing. In this case the stress ratio depicted in the figure is $\Psi = 2$ ($\psi = \frac{4}{3}$) and there are 5000 small cycles ($\eta = 5000$) for every applied overload. Both the strain amplitude of the overload cycle and η were chosen to restrict overload damage to 25% of the total damage as in the uniaxial overload histories.

However, one stress ratio, $\Psi = 0$, provided an opportunity to use an overload which was normal to the eventual crack plane. As a result, this stress ratio had three different types of overload applied to the specimens – torsional overload, tension-compression overload with zero applied mean stress, and a tension-compression overload with the peak tensile strain held constant. Examples of each of these overloads are given in Figure 2.23.

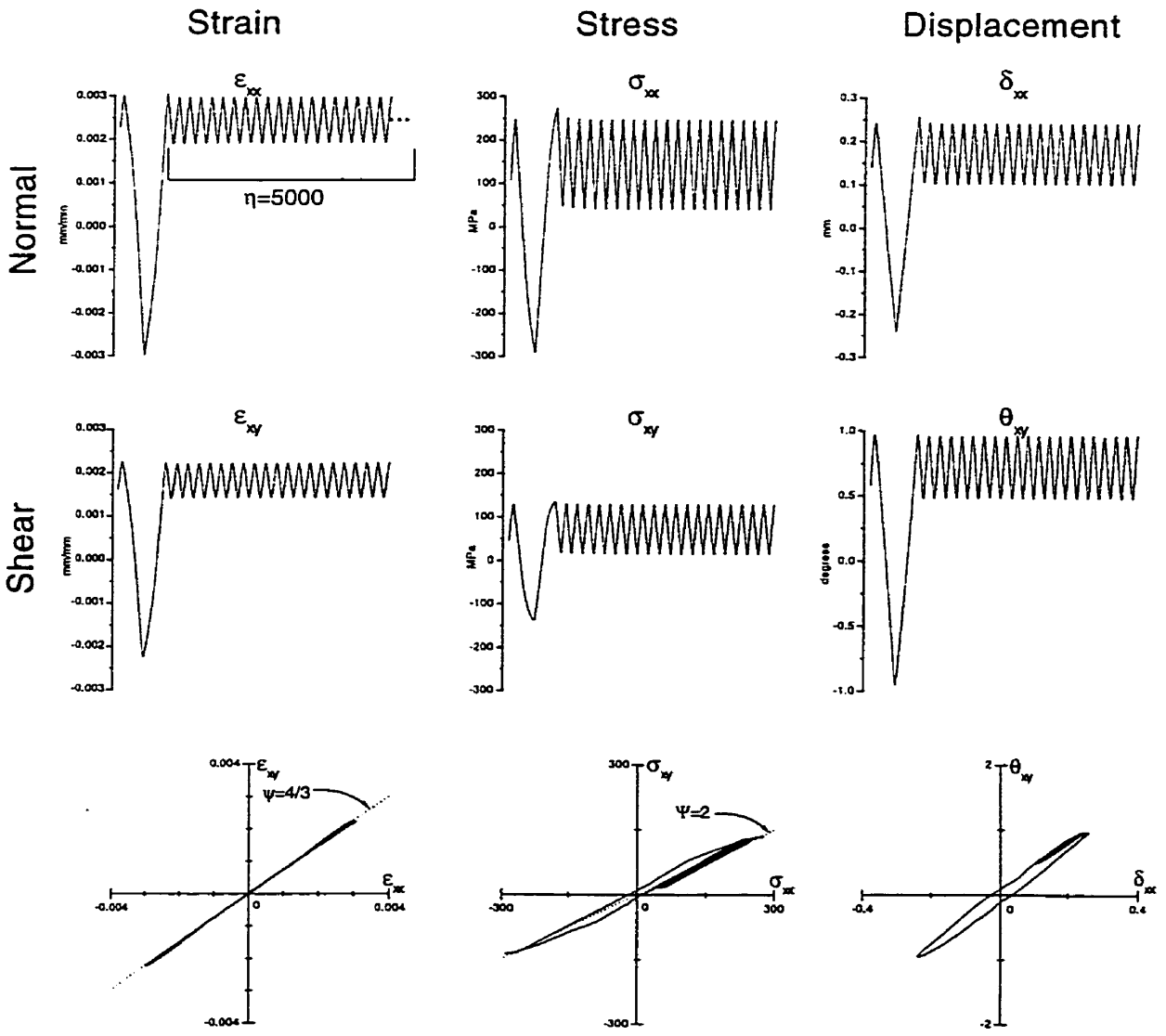

Figure 2.22: Feedback plots from an overload test including strain, stress and displacement, $\Psi = 2$, $\psi = \frac{4}{3}$, $\frac{\Delta\epsilon_{xx}^{ol}}{2} = 0.003$, $\frac{\Delta\epsilon_{xy}^{ol}}{2} = 0.00233$, $\frac{\Delta\epsilon_{xx}^{ca}}{2} = 0.000533$, $\frac{\Delta\epsilon_{xy}^{ca}}{2} = 0.0004$, $\eta = 5000$, test 50. All plots are taken from the same time slice.

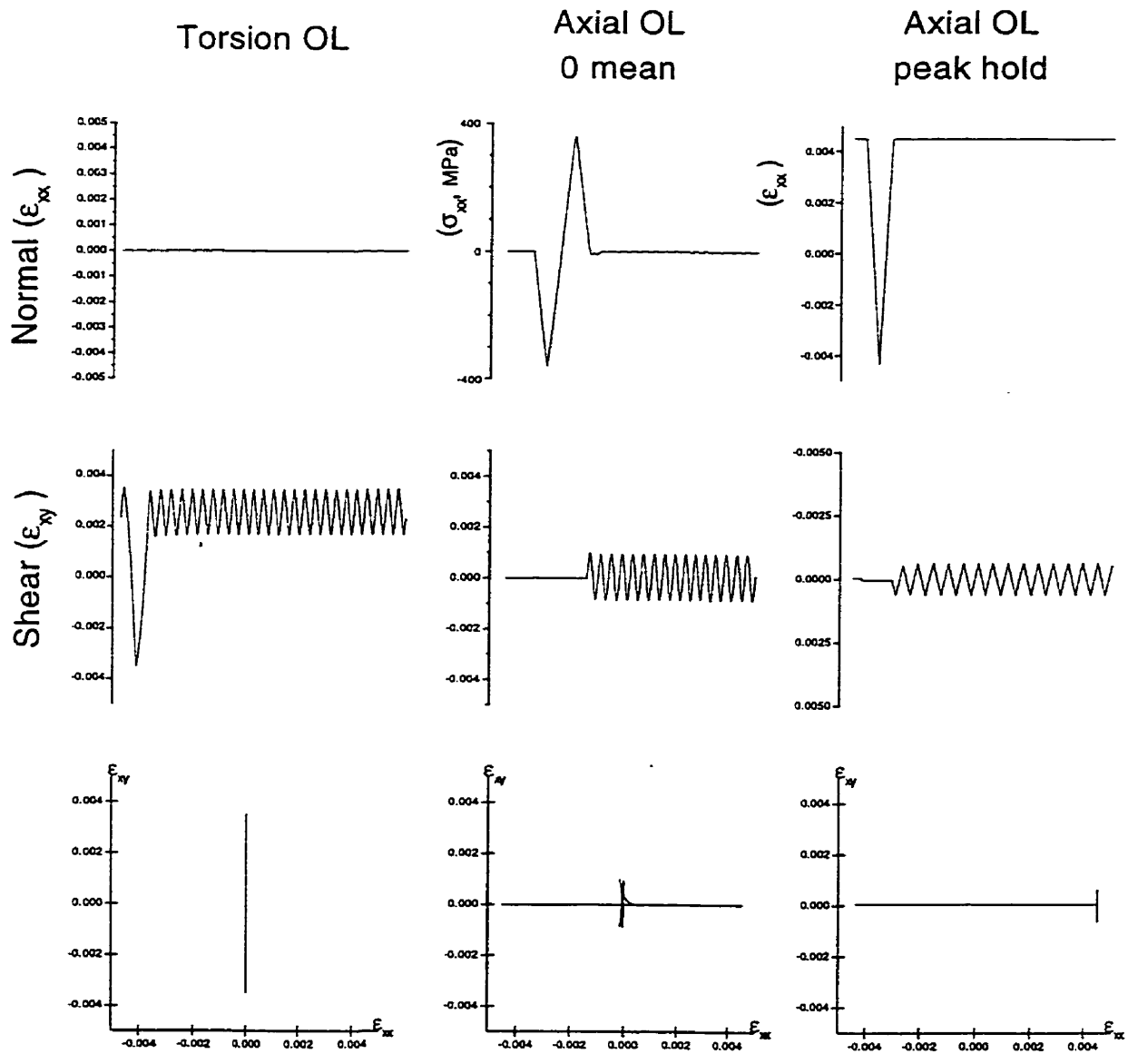

Figure 2.23: $\Psi = 0$ histories with different types of overloads.

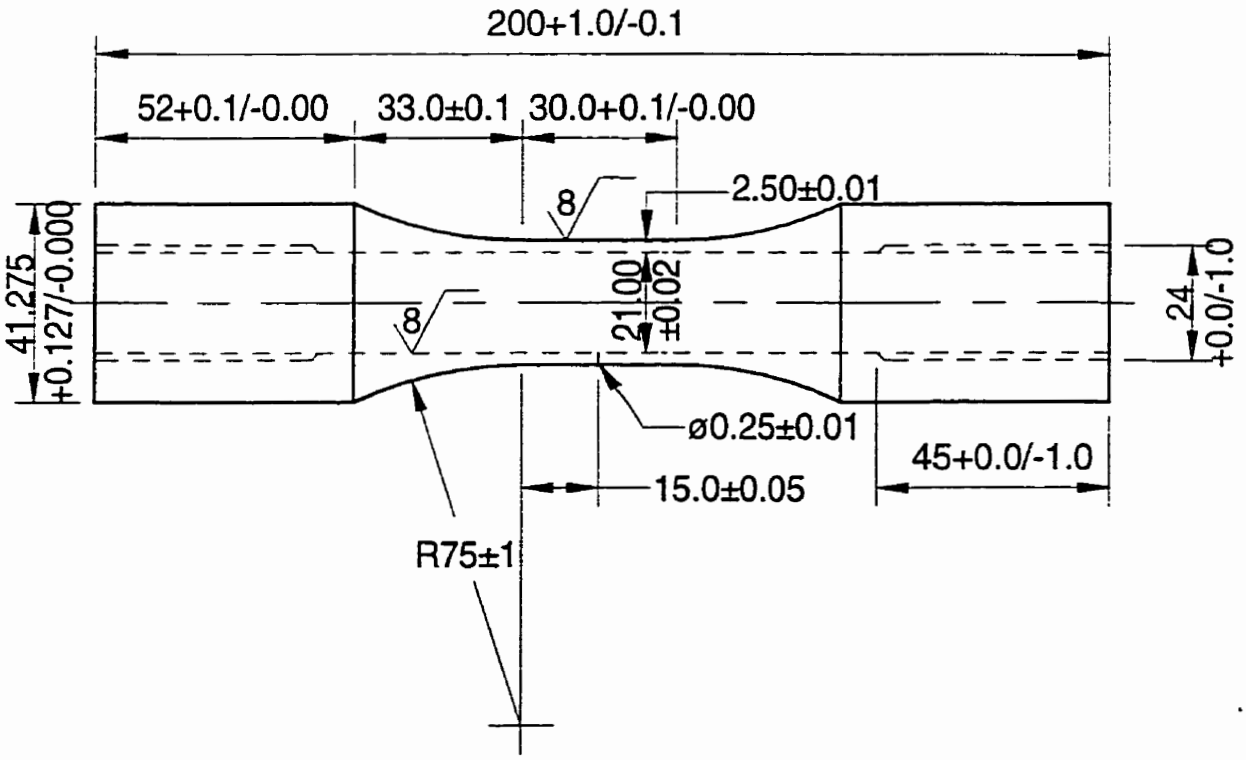

Figure 2.24: Axial-torsion crack growth specimen. All dimensions in mm.

2.3.2.2 Tension-Torsion Crack Growth Tests

Multiaxial fatigue life tests were performed on the tubular specimens shown in Figures 2.18 and 2.24. The only difference between this specimen and the one depicted in Figure 2.21 is a small 0.25mm hole drilled through the wall which acts as a crack starter. Preparation of these tubes was the same as that described in the previous section.

The tubes were precracked under the stress ratio in which they were to be tested. Precracking was conducted under parametric strain control, and an overload history was used which had $\eta = 100$ small cycles of the amplitude of the constant amplitude fatigue limit. Once the crack had grown out of the starter notch and stabilized into its normal growth direction, the crack was mapped using the Questar crack measurement system, and the sample was removed from the machine. Dental impression material was used to verify that the crack had stabilized both on the inside and outside surfaces

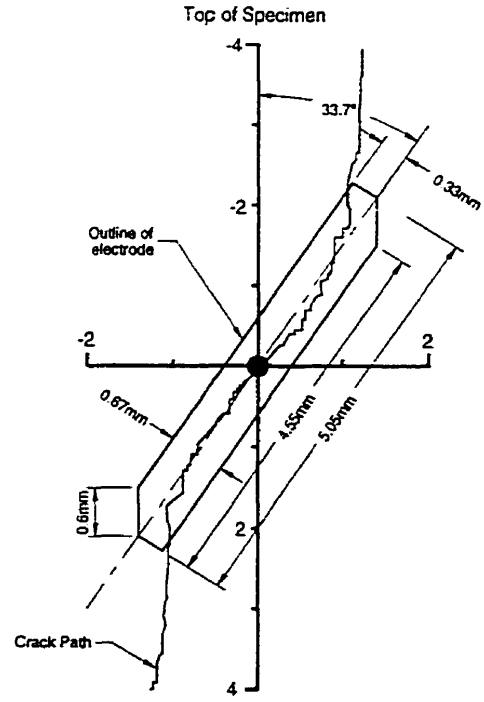

Figure 2.25: Example of precrack crack growth removal. All dimensions are in mm.

and that the crack lengths were similar. If there was a portion of the crack in the notch locale which did not conform to the regular growth pattern, that portion was removed via plunge electron discharge machining (EDM) using an electrode which was specifically designed for each specimen. The electrode was taken all the way through the wall of the tube to completely eliminate that section of crack, and the removal was verified via dental impressions taken from both surfaces. An example of a crack grown under $\Psi = 0$ with torsional overloads is given in Figure 2.25. In unnotched specimens subjected to this kind of loading, the crack tends to grow in mode II along the longitudinal axis of the specimen – hence the portion of the crack which grew out of the notch in mode I/II needed to be removed because of asymmetric load transfer across the crack. In the figure the outline of the electrode is overlaid on the undesirable section of the crack.

Unlike the uniaxial crack growth tests where high R-ratio histories were used to maintain crack closure free growth for stress intensities less than $10\text{MPa}\sqrt{\text{m}}$, it was

inappropriate to use this technique under mode II loading. High R-ratio shear loading histories do not necessarily eliminate crack face interference. Hence, tension-torsion experiments instead use only overload histories, such as described in section 2.3.2.1, to develop crack face interference-free growth. The number of small cycles between overloads, η, was set such that the damage from the overload cycles constituted no more than the 25% of the total damage in the specimen.

2.4 Specimen Stress-Strain Analysis

The purpose of this section is to document analytic techniques used on the various specimens employed during the course of this work.

2.4.1 General Stress/Strain Analysis

The coordinate systems used in referencing both uniaxial and tension-torsion specimen stresses and strains throughout this document are presented in Figure 2.26. Boundary conditions which both geometries share are

$$\sigma_{\alpha y} \equiv 0 \qquad \alpha = y, z \tag{2.2}$$

$$\sigma_{iz} \equiv 0 \qquad i = x, y, z, \tag{2.3}$$

which means that

$$\epsilon_{\alpha z} \equiv 0 \qquad \alpha = x, y. \tag{2.4}$$

Since the uniaxial specimen has only a single force imposed along the x-axis, it has a further boundary condition which is

$$\sigma_{xy} \equiv 0 \tag{2.5}$$

and results in

$$\epsilon_{\alpha y} \equiv 0 \qquad \alpha = z, x. \tag{2.6}$$

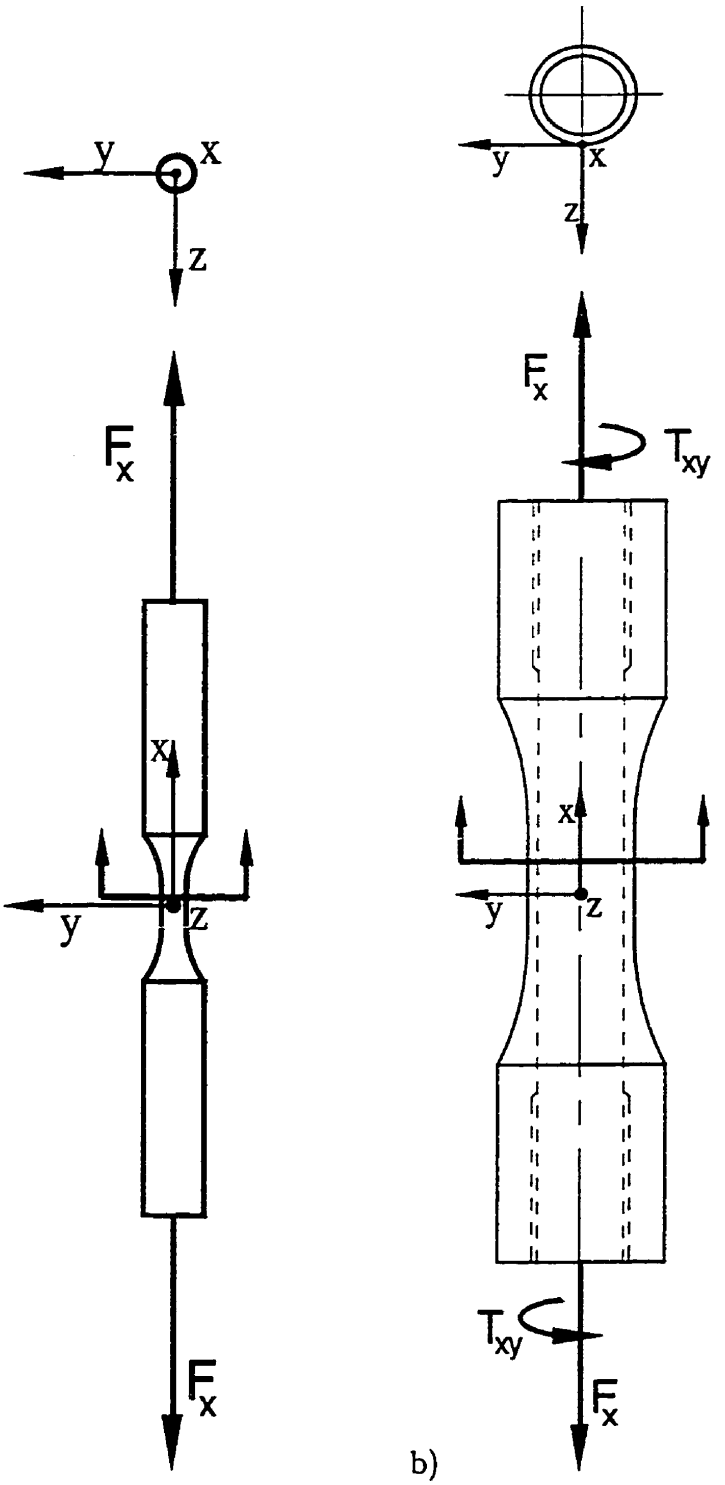

Figure 2.26: Stress/strain coordinate system for a) uniaxial and b) tension-torsion specimens.

Hooke's Law for uniaxial loading yields the elastic strains,

$$\epsilon^e_{xx} = \frac{\sigma_{xx}}{E} \tag{2.7}$$

$$\epsilon^e_{yy} = \epsilon^e_{zz} = \frac{-\nu}{E}\sigma_{xx}, \tag{2.8}$$

where ν is (elastic) Poisson's ratio and E is Young's Modulus. The plastic strain may then be defined from the total strain, ϵ_{xx}, as

$$\epsilon^p_{xx} = \epsilon_{xx} - \epsilon^e_{xx} \tag{2.9}$$

The total y- and z- axis strains are

$$\epsilon_{yy} = \epsilon_{zz} = -\nu^* \epsilon_{xx} \tag{2.10}$$

where

$$\nu^* = \frac{\nu\epsilon^e_{xx} + \nu^p\epsilon^p_{xx}}{\epsilon_{xx}} \tag{2.11}$$

and the plastic Poisson ratio is

$$\nu^p = \frac{1}{2}. \tag{2.12}$$

The stress and strain ratios, Ψ and ψ, are defined as

$$\Psi = \frac{\sigma_{xx}}{\sigma_{xy}}, \tag{2.13}$$

$$\psi = \frac{\epsilon_{xx}}{\epsilon_{xy}}. \tag{2.14}$$

As mentioned in section 2.3.2.1, the relation

$$\psi = \frac{2}{3}\Psi, \tag{2.15}$$

can be used to describe roughly the relationship between the stress and strain ratios at the overload loop tips with roughly 5% error.

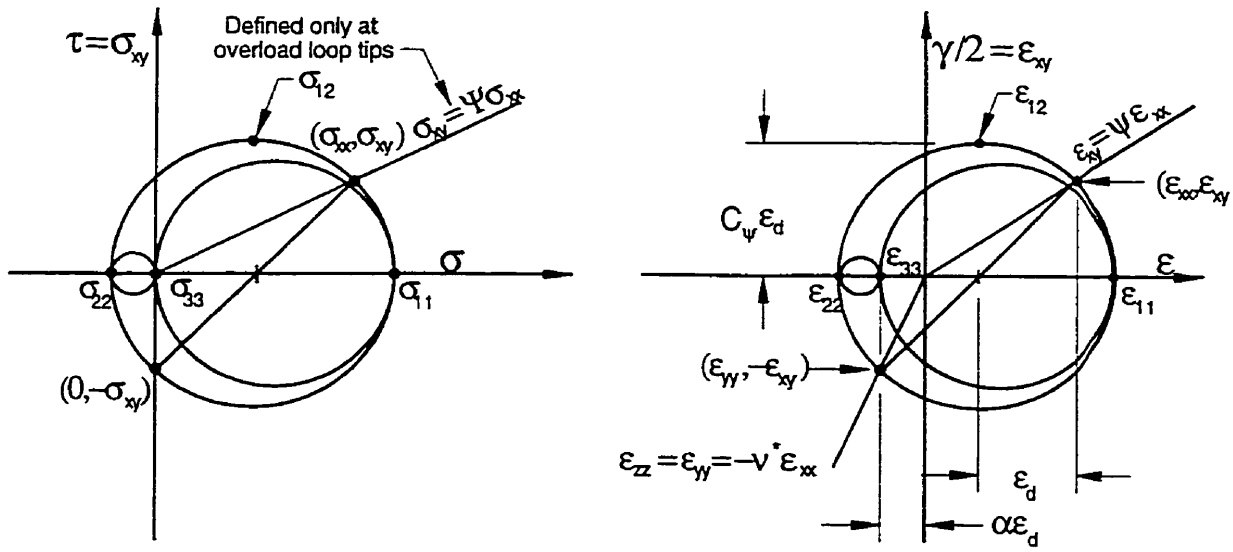

Figure 2.27: Mohr circle diagrams (drawn for $\Psi = 2$) showing stress and strain paths and the definitions of ϵ_d, α, and C_Ψ.

The von Mises equations for equivalent stress and plastic strain, considering the above boundary conditions (equations 2.2-2.4), may be defined for these specimens as

$$\bar{\sigma} = \sigma_{xx}\sqrt{1 + \frac{3}{\Psi^2}} \tag{2.16}$$

$$\bar{\epsilon}^p = \epsilon^p_{xx}\sqrt{1 + \frac{4}{3\psi^2}}. \tag{2.17}$$

The equations for elastic and total strain are

$$\bar{\epsilon}^e = \frac{\bar{\sigma}}{E}, \tag{2.18}$$

$$\bar{\epsilon} = \bar{\epsilon}^e + \bar{\epsilon}^p. \tag{2.19}$$

Other terms, taken from [39, 40], should be introduced at this juncture; Figure 2.27, which shows the Mohr's circles for stress and strain, is instructive in their definition. The following terms are only defined for in-phase loading. The normal strain component of the largest circle, ϵ_d, is defined as

$$\epsilon_d = \frac{\epsilon_{xx}}{2}(1 + \nu^*), \tag{2.20}$$

and

$$\epsilon_{zz} = \alpha\epsilon_d, \tag{2.21}$$

where

$$\alpha = \frac{-2\nu^*}{1+\nu^*}. \tag{2.22}$$

The radius of Mohr's circle r (and the maximum shear strain, ϵ_{12}) is defined as

$$r = \epsilon_{12} = C_\psi \epsilon_d \tag{2.23}$$

where

$$C_\psi = \sqrt{1 + \left(\frac{2}{(1+\nu^*)\psi}\right)^2}. \tag{2.24}$$

A similar stress term is also defined as

$$C_\Psi = \sqrt{1 + \frac{4}{\Psi^2}}. \tag{2.25}$$

The tensors for general in-phase loading (and which apply to all load ratios except pure torsion, Ψ=0) are

$$\underline{\sigma} = \sigma_{xx}\begin{pmatrix} 1 & \Psi^{-1} & 0 \\ \Psi^{-1} & 0 & 0 \\ 0 & 0 & 0 \end{pmatrix}, \qquad \underline{\epsilon} = \epsilon_{xx}\begin{pmatrix} 1 & \psi^{-1} & 0 \\ \psi^{-1} & -\nu^* & 0 \\ 0 & 0 & -\nu^* \end{pmatrix}, \tag{2.26}$$

and the principal stresses become

$$\underline{\sigma} = \frac{1}{2}\sigma_{xx}\begin{pmatrix} 1+C_\Psi & 0 & 0 \\ 0 & 1-C_\Psi & 0 \\ 0 & 0 & 0 \end{pmatrix} \qquad \underline{\epsilon} = \epsilon_d\begin{pmatrix} [1+\alpha+C_\psi] & 0 & 0 \\ 0 & [1+\alpha-C_\psi] & 0 \\ 0 & 0 & \alpha \end{pmatrix}. \tag{2.27}$$

2.4.2 Torsion experiments, Ψ=0

Torsion requires special treatment because many of the equations from the previous section become undefined.

The equivalent von Mises equations for torsion become

$$\bar{\sigma} = \sqrt{3}\sigma_{xy} \tag{2.28}$$

$$\bar{\epsilon}^p = \frac{2}{\sqrt{3}}\epsilon^p_{xy}, \tag{2.29}$$

where ϵ^p_{xy} is defined by

$$\epsilon_{xy} = \epsilon^e_{xy} + \epsilon^p_{xy} \tag{2.30}$$

and

$$\epsilon^e_{xy} = \frac{\sigma_{xy}}{2G}. \tag{2.31}$$

Under the special case of pure torsional loading ($\sigma_{xx} = 0, \sigma_{xy} \neq 0$), as represented by Figure 2.28, the stress/strain state for torsion is

$$\underline{\sigma} = \sigma_{xy}\begin{pmatrix} 0 & 1 & 0 \\ 1 & 0 & 0 \\ 0 & 0 & 0 \end{pmatrix} \qquad \underline{\epsilon} = \epsilon_{xy}\begin{pmatrix} 0 & 1 & 0 \\ 1 & 0 & 0 \\ 0 & 0 & 0 \end{pmatrix}, \tag{2.32}$$

which when rotated to principal axes becomes

$$\underline{\sigma} = \sigma_{xy}\begin{pmatrix} 1 & 0 & 0 \\ 0 & -1 & 0 \\ 0 & 0 & 0 \end{pmatrix} \qquad \underline{\epsilon} = \epsilon_{xy}\begin{pmatrix} 1 & 0 & 0 \\ 0 & -1 & 0 \\ 0 & 0 & 0 \end{pmatrix}. \tag{2.33}$$

One type of torsional experiment involved holding a static tension level while torsional cycles were applied. The Mohr circle diagrams for this situation are shown in Figure 2.29 where only the largest circles are shown for clarity. The application of torsion while holding a static tension has two results: the first is that the circle's diameter grows but remains centered at the same location, and the second is that the stress/strain state on the x-y plane changes from position A to position B (as marked on the figure). The tensors for this situation (at position B) are the same as those in equations 2.26 and 2.27.

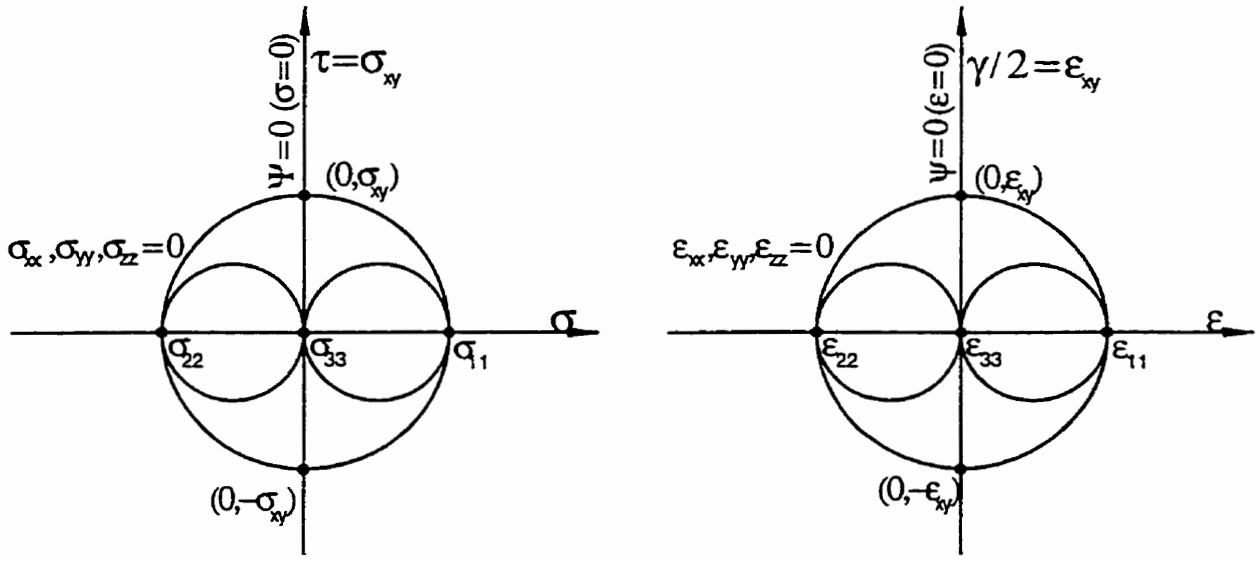

Figure 2.28: Mohr's circles for in-phase torsional loading.

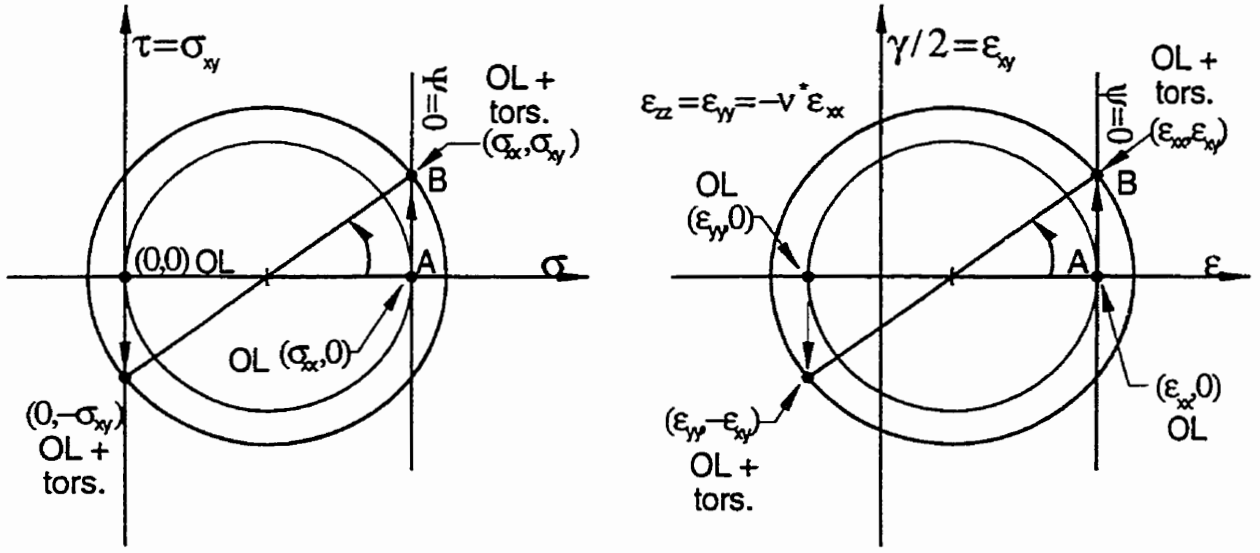

Figure 2.29: Simplified Mohr's circles for out-of-phase torsional loading.

2.4.3 The Stress-Strain Curve and Other Material Properties

Traditionally a Ramberg-Osgood type of power law relationship is used to describe the relationship between plastic strain and stress, but in recent years analysts have begun to move to digitized properties [67] wherein material curves are a set of best fit points which describe the material characteristic. In part, this approach is taken because fatigue analysis programs take the equation and its parameters and develop internal look-up tables, and in part, because the basic equations in fatigue are over-described (more equations than unknowns). Hence it is usually the cyclic stress-strain curve which suffers a poor fit to benefit the strain-life diagram and the the Basquin-Coffin-Manson equation system.

The analyses performed in this document employ these digitized curves, not only for the stress-strain curve, but for parameter-life and crack growth curves.

2.4.4 Analysis of Bending-Torsion Shaft

The coordinate system used in referencing the SAE axle shaft [68] is given in Figure 2.30. Stress analysis of this shaft is somewhat more problematical than that of either the uniaxial or tension-torsion specimens.

Loading that does not plasticize the notch can be analyzed with stress concentration factors and the analyses set forth in the previous section, but those situations where plasticity does occur in the notch require a treatment different than that used in tension-torsion analysis.

2.4.5 Elastic Analysis

Given the geometry of the SAE shaft (see Figure 2.12) Peterson's Handbook [69] yields a bending stress concentration factor of

$$K_t^b = 1.60 \tag{2.34}$$

and a torsion stress concentration factor for the notch of

$$K_t^t = 1.25 \tag{2.35}$$

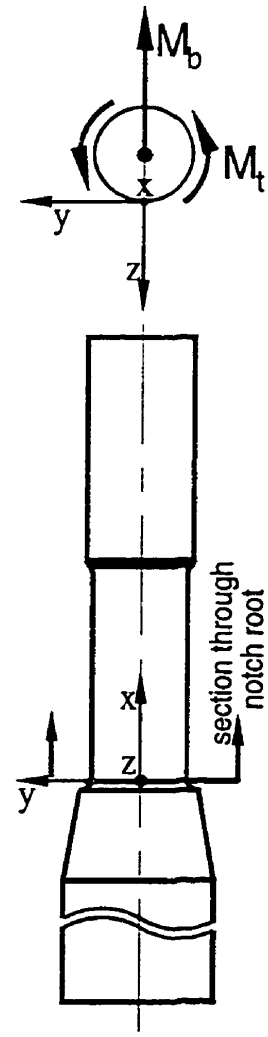

Figure 2.30: Stress/strain coordinate system for bending-torsion specimens.

These were the values employed in both the elastic and elastic-plastic analyses of the shaft. However, another source [61] has variously put the stress concentration factors at 1.61 and 1.39, respectively.

Under elastic loading the maximum nominal section stress (S_{xx}, at the top surface of the shaft) is calculated by

$$S_{xx} = \frac{M_b r_b}{I_s} \tag{2.36}$$

where

$$I_s = \frac{\pi r_s^4}{4} \qquad (= 1.26 \times 10^{-7} m^4), \tag{2.37}$$

r_s is the nominal section radius (20mm) and M_b is the applied moment, given by

$$M_b = -r_b(F_{z1} + F_{z2}). \tag{2.38}$$

The forces in the z-direction from the left and right actuators (as viewed from the small shaft end and in Figure 2.11) are given by F_{z1} and F_{z2}, respectively, and r_b is the distance along the x-axis between the notch root and the load application point (typically about 150mm).

Under elastic notch conditions the local bending stress in the notch is

$$\sigma_{xx} = K_t^b S_{xx}. \tag{2.39}$$

Torsional loading is quite similar, and the nominal section stress at the shaft surface is

$$S_{xy} = \frac{M_t r_t}{J_s} \tag{2.40}$$

where

$$M_t = -r_t(F_{z1} - F_{z2}), \tag{2.41}$$

and

$$J_s = \frac{\pi r_s^4}{2} \qquad (= 2.51 \times 10^{-7} m^4), \tag{2.42}$$

where r_t is the distance from the shaft centerline to the load application point on the yoke (203.2mm).

The local torsional stress in the notch under elastic conditions then becomes

$$\sigma_{xy} = K_t^t S_{xy}. \tag{2.43}$$

2.4.6 Elastic-Plastic Analysis

Short of finite element modelling, the best way to predict notch behavior in the shaft is through Neuber's equation.

2.4.6.1 Uniaxial Neuber Analysis

For an applied moment that produces plastic accommodation in the notch, using the above equations (2.39,2.43) it is possible to make an elastic calculation and use Neuber's equation [70, 71, 72, 73] to calculate the notch stress and strain. Usually Neuber's equation is expressed (in bending) as

$$(K_t^b)^2 = K_\sigma^b K_\epsilon^b \tag{2.44}$$

which becomes

$$(K_t^b)^2 = \frac{\sigma_{xx}}{S_{xx}} \frac{\epsilon_{xx}}{e_{xx}} \tag{2.45}$$

or

$$\sigma_{xx}\epsilon_{xx} = \frac{(K_t^b S_{xx})^2}{E}, \tag{2.46}$$

where K_σ^b and K_ϵ^b are the inelastic stress and strain concentrations in the notch expressed by

$$K_\sigma^b = \frac{\sigma_{xx}}{S_{xx}} \tag{2.47}$$

$$K_\epsilon^b = \frac{\epsilon_{xx}}{e_{xx}}. \tag{2.48}$$

The individual components of the product of $\sigma_{xx}\epsilon_{xx}$ can be determined by using the material stress-strain curve as shown in Figure 2.31.

Unfortunately, this technique is insufficient for a notch loaded in a multiaxial fashion.

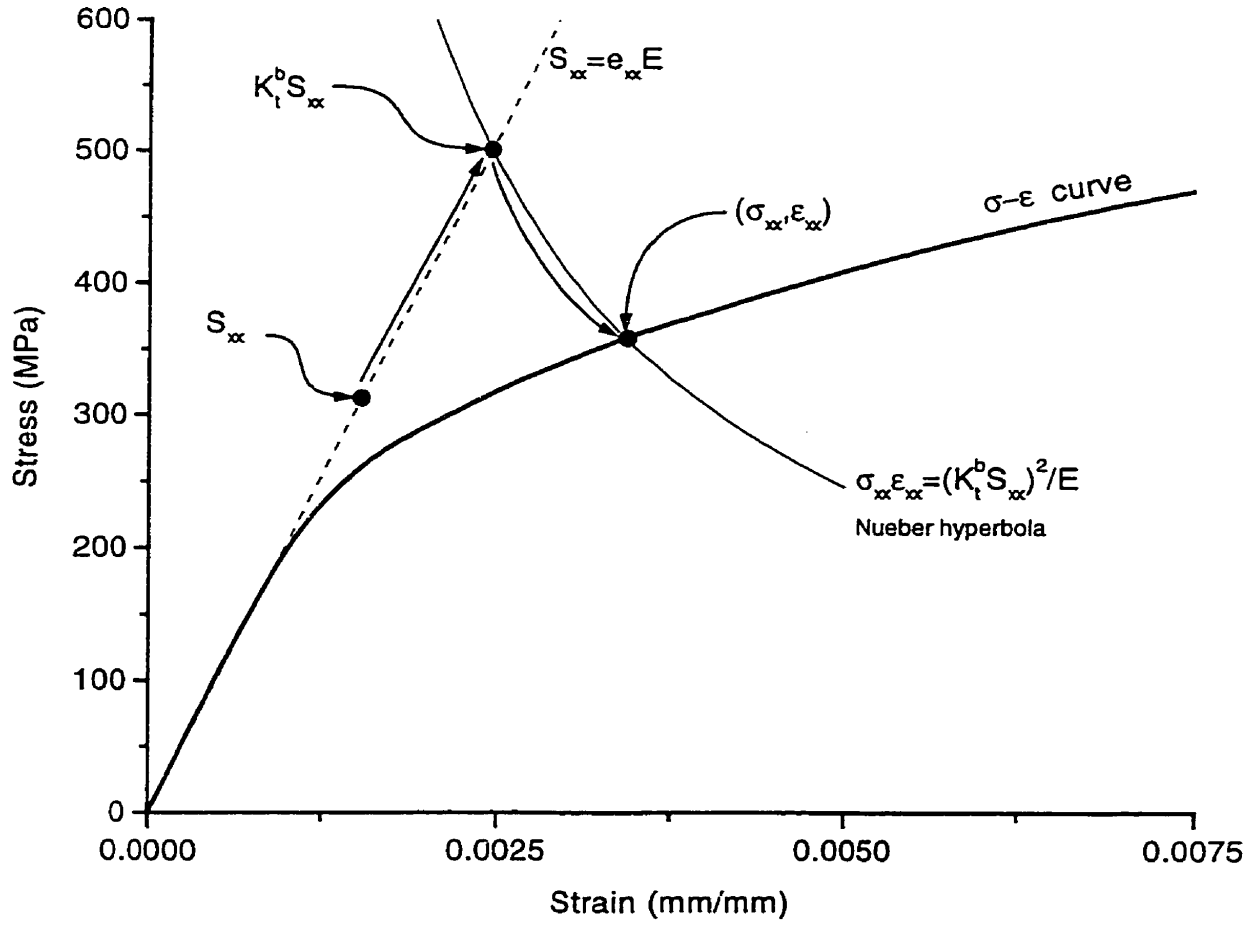

Figure 2.31: Illustration of uniaxial Neuber correction [70, 71].

2.4.6.2 Multiaxial Neuber Correction

Chu [74, 75] has developed an incremental Neuber style correction for use in multiaxial cyclic loading situations. A brief introduction is given here.

The basic tenet of this work is that if under uniaxial loading Glinka's elastic notch solution [73] can be expressed as

$$\int \sigma_{xx} d\epsilon_{xx} = \int K_{\sigma_{xx}} S_{xx} K_{\epsilon_{xx}} de_{xx} = \int K_{t,xx}^2 S_{xx} de_{xx} \tag{2.49}$$

where $K_{\sigma_{xx}}$ and $K_{\epsilon_{xx}}$ are the inelastic stress and strain concentration factors in the x-direction, and $K_{t,xx}$ is the elastic stress concentration in the x-direction. As in

equation 2.44, the product of the stress and strain concentration factors can be related to the elastic stress concentration factor by the following equation,

$$K_{\sigma_{xx}} K_{\epsilon_{xx}} = K_{t,xx}^2. \tag{2.50}$$

However, under multiaxial loading

$$S_{ij}^k = K_{ij}^{\sigma} S_{ij},\ e_{ij}^k = K_{ij}^{\epsilon} e_{ij}, \qquad i,j = x,y,z, \tag{2.51}$$

and equation 2.49 becomes

$$\int \underline{\sigma} \bullet d\underline{\epsilon} = \int \underline{S}^k \bullet d\underline{e}^k. \tag{2.52}$$

Taking this new relation in differential form,

$$\underline{\sigma} \bullet d\underline{\epsilon} = \underline{S}^k \bullet d\underline{e}^k, \tag{2.53}$$

for a surface element in the shaft notch, this energy equation becomes

$$\sigma_{xx} d\epsilon_{xx} + \sigma_{yy} d\epsilon_{yy} + 2\sigma_{xy} d\epsilon_{xy} = K_{t,xx}^2 S_{xx} de_{xx} + K_{t,yy}^2 S_{yy} de_{yy} + 2K_{t,xy}^2 S_{xy} de_{xy}. \tag{2.54}$$

The definition of the stress-strain path used needs to be set, and although Chu defined three alternatives, the proportional strain path is used in this work:

$$d\epsilon_{xx} : d\epsilon_{yy} : d\epsilon_{xy} = de_{xx} : de_{yy} : de_{xy}. \tag{2.55}$$

In order to implement this incremental form, a material constitutive model is necessary. Chu [76, 77] has extended the yield surface field concept developed by Mróz [78] into an incremental isotropic-kinematic hardening model for use in cyclic loading. While a full treatment of the plasticity model is beyond the scope of this document, a cursory introduction is given in Appendix A.

2.4.7 Damage Parameters and Critical Plane Analysis

The parameters ϵ_d, α, and C_Ψ used in section 2.4.1 (see equations 2.20, 2.22, and 2.25) in expressing the stress-strain states are also useful in evaluating multiaxial damage parameters, but it must be noted that the analyses presented in this section are only defined for in-phase load paths. All of the damage parameters require evaluation of either an amplitude, a maximum or a minimimum of a quantity throughout a loading cycle, and these transforms are denoted by $()_a$, $()_{max}$, and $()_{min}$ respectively.

Specifically, with respect to equations presented later,

$$(\epsilon_d)_a \mapsto \epsilon_{da}, \tag{2.56}$$

and the strain term in the definition of ϵ_d, ϵ_{xx}, is also taken as an amplitude.

In critical plane analysis, a damage parameter is computed on a number of planes which have orientations that are distributed around the points of the compass, (i.e., every 10°). The plane which has the largest value of the parameter is presumed to be the one on which failure will occur. This process finds the maximum value of the parameter. For some parameters such as the Brown and Miller parameter [38], the plane given by a critical plane search is not necessarily that designated by the parameter's authors [67]. This leads to a situation where the basic strain-life curve is not predicted by the parameter-life curve derived from it.

Again, the Brown and Miller parameter is used as an example. Programs initially take the strain-life curve as the input necessary for converting the calculated damage parameter back into a fatigue life. In order to do this, programs take the value of the parameter on the maximum shear plane and create a parameter-life look-up table for later use. The strain levels from the strain-life curve are then given to the program to predict. The program finds the maximum value of the parameter for each strain level, and this value happens to be about 10% higher than that calculated on the maximum shear plane. When the program returns to the look-up table it returns a life which can be in error by as much as an order of magnitude. Whether or not any given parameter is impacted by this problem is entirely dependent on the treatment given by the programmer.

As a result of this problem, the parameters presented here are designed to properly maximize the parameter life curves – so that a critical plane analysis will properly predict the original strain-life curves, regardless of parameter used. In the following sections, closed form solutions of both uniaxial and multiaxial parameters, taken from [39, 40], are presented. However, a closed form solution is only possible for these parameters when the loading is confined to a single linear path emanating from the origin. These solutions are invalid for cases such as neutral loading, but they can be used in place of a critical plane analysis to reduce most ordinary laboratory test data.

2.4.7.1 Uniaxial Parameters – Normal Stress/Strain

Normal strain amplitude as a damage parameter is one of the most common, and it is normally expressed [39, 40] as

$$P_{\epsilon_n} = (\epsilon_n)_a \tag{2.57}$$

and when changed to reflect critical plane analysis it is

$$(P_{\epsilon_n})_{max} = \epsilon_{da}[1 + C_\Psi + \alpha], \tag{2.58}$$

where the terms in these equation are defined in section 2.4.7.

Normal stress amplitude is given by

$$P_{\sigma_n} = (\sigma_{xx})_a \tag{2.59}$$

which becomes

$$(P_{\sigma_n})_a = \frac{(\sigma_{xx})_a}{2}[1 + C_\Psi]. \tag{2.60}$$

2.4.7.2 Shear-Strain Based Parameters

Among the parameters included in this set are the Brown and Miller [38], Fatemi-Socie-Kurath [30, 42], and maximum shear strain amplitude parameters.

For in-phase loading the Brown and Miller parameter can be expressed [39, 40] as

$$P_{BM} = (\epsilon_{xy})_a + 0.5(\epsilon_{xx})_a, \tag{2.61}$$

which becomes

$$(P_{BM})_{max} = \frac{\epsilon_{da}}{2}\left[1 + \alpha + \sqrt{5}C_{\Psi}\right], \tag{2.62}$$

The Fatemi-Socie-Kurath parameter takes the form of

$$P_F = \gamma_a \left(1 + K_F \frac{(\sigma_n)_a}{\bar{\sigma}_y}\right) \tag{2.63}$$

which, in critical plane format, becomes

$$(P_F)_{max} = \epsilon_{da} C_{\Psi} \sin 2\theta_c' \left[1 + \beta - C_{\Psi}\beta \cos 2\theta_c'\right]. \tag{2.64}$$

where

$$\beta = \frac{K_F(\sigma_{xx})_a}{\bar{\sigma}_y} \tag{2.65}$$

and the angle which the critical plane makes with the x-axis, θ_c', is defined by

$$\cos 2\theta_c' = \frac{1}{4}\left[\beta + 1 - \sqrt{(\beta+1)^2 + 8}\right]. \tag{2.66}$$

Finally, maximum shear strain amplitude,

$$P_\gamma = (\epsilon_{12})_a, \tag{2.67}$$

takes the form

$$(P_{\gamma_a})_{max} = \epsilon_{da} C_{\Psi}. \tag{2.68}$$

2.4.7.3 Energy Based Parameters

The last set of parameters are the Smith-Watson-Topper parameter [37], and Chu's parameter [43]. The Smith-Watson-Topper parameter [37] takes the form [39, 40] of

$$P_{SWT} = \sigma_{max}\epsilon_a \tag{2.69}$$

and becomes

$$(P_{SWT})_{max} = \frac{(\sigma_{xx})_{max}\epsilon_{da}}{2}[1 + C_{\Psi}][1 + C_{\Psi} + \alpha] \tag{2.70}$$

after critical plane analysis. Lastly, Chu's parameter is typically represented by

$$P_C = 2\tau_{max}(\epsilon_{xy})_a + (\sigma_n)_{max}(\epsilon_n)_a, \tag{2.71}$$

and it becomes

$$(P_C)_{max} = (\sigma_{xx})_{max}\epsilon_{da}\left[1 + C_{\Psi}^2 + \alpha + \frac{\alpha^2}{8}\right]. \tag{2.72}$$

Chapter 3

The Role of Overloads in Multiaxial Fatigue

During the past decade it has been observed that periodically applied overloads of yield stress magnitude can significantly reduce or eliminate crack closure under uniaxial or mode I loading. In this chapter results are presented for a series of biaxial tension-torsion experiments that were performed to evaluate the effects of overloads on the fatigue life of smooth tubes constructed of normalized SAE 1045 steel. Constant amplitude and periodic overload experiments were conducted under five different in-phase stress ratios, including uniaxial ($\Psi = \sigma_{xx}/\sigma_{xy} = \infty$), pure torsion ($\Psi = 0$), and three intermediate ratios ($\Psi = \frac{1}{2}$, 1, and 2). In addition, under torsional loading, two different out-of-phase overloads were evaluated.

Periodically applied overloads of yield stress magnitude caused cracks to grow under crack face interference free conditions. Strain-life curves were obtained by computationally removing the overload cycle damage from test results and calculating equivalent fatigue lives. A factor of two reduction in the fatigue limit was found at all strain ratios when these results were compared to constant amplitude results.

Another series of constant amplitude and periodic overload tests was conducted on notched axle shafts to evaluate the effects of overloads on components. The effects of various kinds of bending overloads on torsional fatigue was found to be quite similar to that encountered in the Ψ=0 tubular testing.

Further, it was found that, under in-phase loading, shear cracks initiated and grew longitudinally for Ψ=0, $\frac{1}{2}$, and 1, and for Ψ=2 loading shear cracks initiated on the

maximum shear planes. These observations concerning the initiation plane were used to unify the constant amplitude data and to justify the use of the maximum shear criterion with the overload fatigue data. Parameter-life curves were developed using the equivalent life data and several common multiaxial damage parameters. It was found that the simple maximum shear strain criterion together with uniaxial overload data gave safe but not unduly conservative life predictions for all of these strain ratios.

3.1 Uniaxial Behavior, $\Psi=\infty$

3.1.1 Constant Amplitude Tests

Constant amplitude tests were used in all of the stress ratios as a baseline for comparison with the overload fatigue data.

The uniaxial constant amplitude fatigue curve for normalized SAE 1045 steel is shown in Figure 3.1 where the circle data points are specimens failed under $R_\epsilon = -1$ loading. The curve is fairly typical of a medium carbon steel, and it has an endurance limit at a strain amplitude of 0.0017.

3.1.2 Overloads and Equivalent Uniaxial Damage

DuQuesnay [3] discovered that the application of a yield stress level overload reduces crack closure levels enough that subsequent cycles whose amplitudes are below the fatigue limit (small cycles) are able to advance a crack. This effect has been successfully used to describe the observation of increased small cycle damage in the presence of variable amplitude or random loading spectra [79, 80]. Although DuQuesnay was primarily interested in crack growth approaches to these phenomena, he was able to use this knowledge to develop a technique which provided a strain-life curve which could be used in continuum damage models [81]. In the paper he demonstrated a downward translation of the endurance limit to one-third of its original value. He suggested that this curve could be used for making life predictions for structures which experience variable amplitude loading.

The effect of a reduction in crack closure stress on the fatigue strength can be seen by examining a few simple tests. A constant amplitude test at ϵ_a=0.005 for this

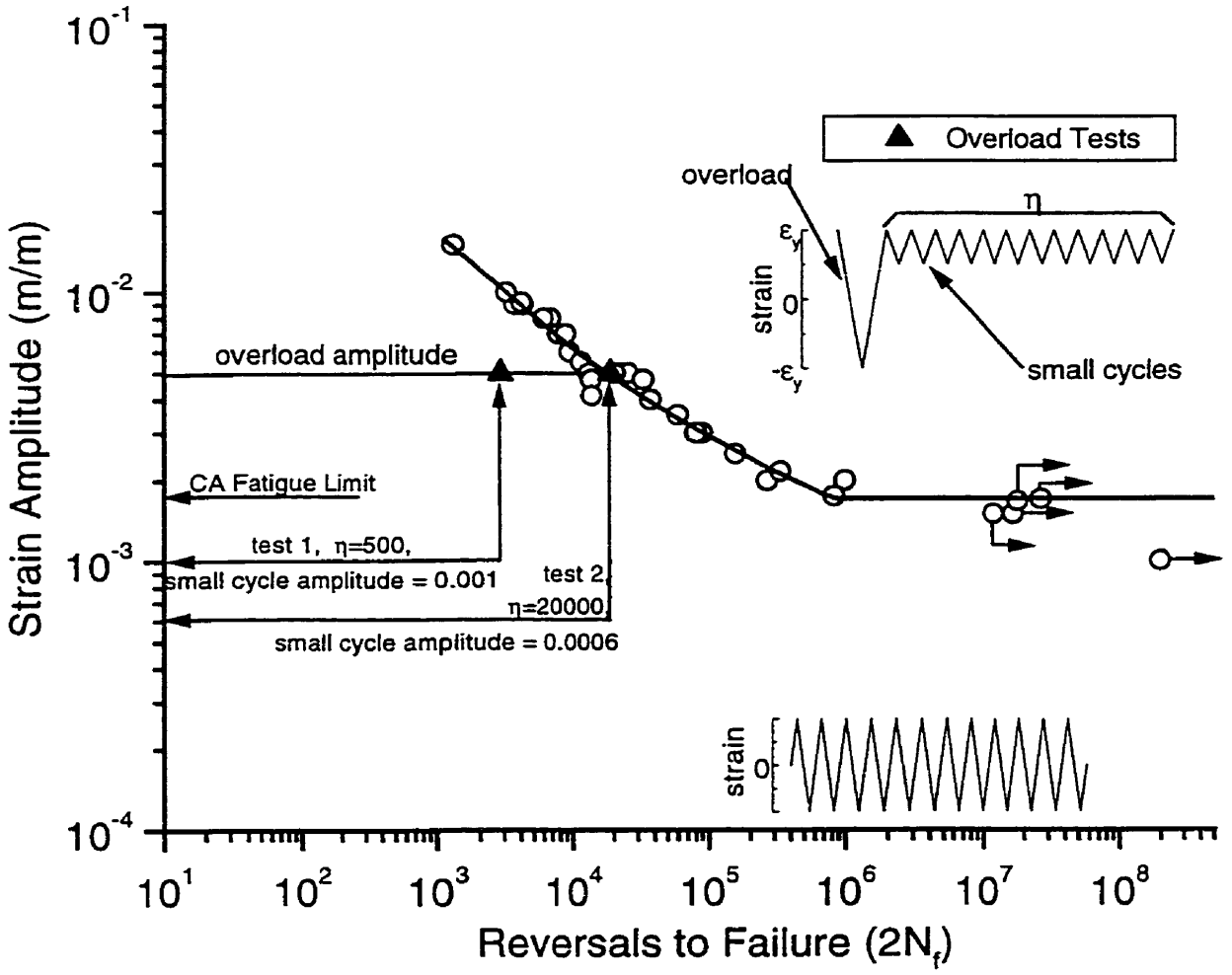

Figure 3.1: Constant amplitude $R_\epsilon = -1$ fatigue response of SAE 1045 steel.

material will result in a specimen fatigue life of roughly 20,000 reversals to failure. If, in between each cycle of ϵ_a=0.005, are placed five hundred cycles (η=500) of amplitude ϵ_a=0.001 – an amplitude which is roughly one-half of the fatigue limit – the result, plotted in Figure 3.1, is that the life of the test now falls at 2,824 large cycle reversals to failure. This result is far short of the 20,000 reversals required to cause failure in tests which consist of just the ϵ_a=0.005 cycle. However, if the smaller cycle amplitude is reduced further to one-third of the fatigue limit (ϵ_a=0.0006), and the number of smaller cycles between the larger cycles is increased to twenty thousand (η=20,000),

no effect of the smaller cycles is observed – the resulting specimen life is once again 20,000 large cycle reversals to failure. This return to the constant amplitude curve is an indication that small cycles below a certain strain amplitude will no longer contribute to the total specimen damage [3, 18, 82]. Half of the constant amplitude data in this figure is from Chernenkoff [83], and the other half was produced during this research.

The Palmgren-Miner relation indicates that, on the basis of the original strain-life curve, cycles below the endurance should have no effect, but clearly there is damage being performed by these smaller cycles from the endurance limit down to $\epsilon_a = 0.001$. At $\epsilon_a = 0.0006$ the small cycles no longer contribute substantially to damage. As one would expect, this phenomenon is observable in tests with smaller cycles which have amplitudes both below and above the fatigue limit. In order to determine the damage done by the small cycles in the overload histories, we may subtract the damage done by the overload cycles from unity using the Palmgren-Miner rule given by equation 3.2.

$$\sum_i \frac{n_i}{N_i} = 1 \tag{3.1}$$

$$\frac{n_{ol}}{N_{ol}} + \frac{n_{sc}}{N_{sc}} = 1 \tag{3.2}$$

$$n_{ol}\left(\frac{1}{N_{ol}} + \frac{\eta}{N_{sc}}\right) = 1, \tag{3.3}$$

where n_i is the number of cycles at amplitude i, N_i is the expected constant amplitude life at amplitude i, "*ol*" indicates overload cycle, "*sc*" indicates smaller cycle, and η is the number of smaller cycles between overload cycles. If the Palmgren-Miner rule is used to eliminate the fraction of damage due to the large cycles then the equivalent number of small cycles to fail the specimen should be

$$N_{sc} = n_{sc} / \left(1 - \frac{n_{ol}}{N_{ol}}\right) \tag{3.4}$$

$$N_{sc} = n_{sc} / \left(1 - \frac{n_{sc}}{\eta N_{ol}}\right) \tag{3.5}$$

$$N_{sc} = \frac{1}{\frac{1}{n_{sc}} - \frac{1}{\eta N_{ol}}}, \tag{3.6}$$

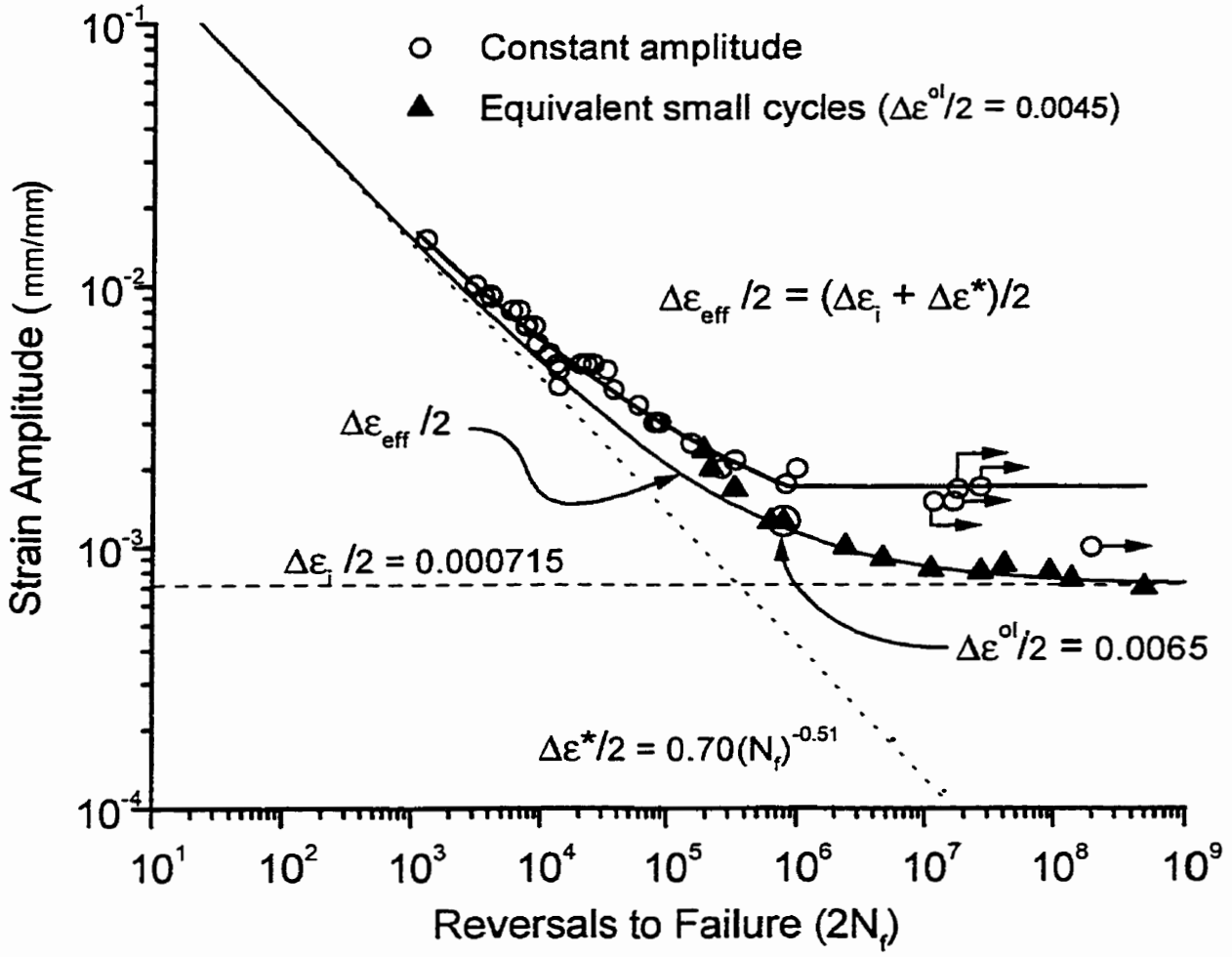

Figure 3.2: Periodic overload and effective strain curves for normalized SAE 1045 steel.

where N_{ol} is taken from the constant amplitude strain life curve. Using this equivalent small cycle life and plotting the overload tests on the basis of the amplitude of the small cycles gives the equivalent strain-life curve of Figure 3.2.

Once the damage due to overloads has been removed and the small cycle life is normalized, the equivalent strain life curve in Figure 3.2 (plotted as triangles) is obtained. The fatigue limit is reduced from a strain amplitude of 0.0017 to 0.000715 – a reduction to two-fifths of its original value. At lives below 200,000 reversals to failure, the overload curve falls close to the constant amplitude curve. The overload

curve joins the constant amplitude curve at this point because the overloads, which are set at a life of 20,000 reversals, are unable to maintain a fully open crack. In most other materials the transition point is closer to the selected overload life than an order of magnitude, but in soft SAE1045 steel it appears that this transition point is fairly typical [84, 81]. If the overload strain amplitude is increased in proportion to the increase in the smaller cycles strain amplitude at lives below 200,000 then a strain-life curve can be obtained in which the entire dataset is fully open. However, at these high strain amplitudes specimens may buckle during the overload cycle. A curve which approximates such behavior for a fully open crack is also presented in Figure 3.2 and labelled as $\Delta\epsilon_{eff}/2$. This curve is developed as follows.

DuQuesnay, et al. [81], have proposed an effective strain-life curve for use in fatigue damage calculations. The effective strain range, $\Delta\epsilon_{eff}$, which is the range of strain for which a fatigue crack is open during a cycle, is given by the difference between the maximum strain and the greater of the minimum strain or the crack opening strain. They relate effective strain range to fatigue life by the following equation,

$$\Delta\epsilon_{eff} = \Delta\epsilon^* + \Delta\epsilon_i \tag{3.7}$$

where

$$E\Delta\epsilon^* = A(N_f)^b, \tag{3.8}$$

and $\Delta\epsilon_i$ is an intrinsic strain range below which strain cycles do no damage, akin to the crack growth threshold, ΔK_{th}. The material constants A and b in equation 3.8 behave in a similar fashion to the constants in the Coffin-Manson equation. An estimate of the effective strain range at a total strain range of two percent is made by subtracting one-half of the absolute value of the minimum stress divided by the modulus of elasticity from the total strain range. This assumes that the minimum stress in the cycle is negative, and that the crack opening stress at this strain level falls halfway between the minimum stress in the cycle and zero [85]. This datum and the long life overload data for which the fatigue crack is expected to remain open

throughout the stress-strain cycle are used to obtain the $\Delta\epsilon^*$ vs. N_f curve shown in Figure 3.2. A value of $\Delta\epsilon_i$ which causes calculated $\Delta\epsilon^*$ values to fall on a linear curve when plotted versus N_f on log-log coordinates is obtained by trial and error – a first estimate of it obtained from the lower bound of the test results. The resulting linear $\Delta\epsilon^*$ versus N_f curve provides a good fit to the long life data where the crack is fully open [81, 85]. At intermediate lives the effective strain falls below the data, since the crack opening stress is above the minimum stress and the effective strain range is less than the total strain range. At the shortest lives, the effective curve once again follows the constant amplitude data because the portion of the strain cycle which is closed constitutes only a small fraction of the total strain range.

3.1.3 Uniaxial Crack Closure

DuQuesnay [3] determined that overloads which are of the order of the section yield stress reduce crack closure. Compressive overloads drastically reduce closure by flattening asperities and eliminating the interaction between crack faces. Tension overloads stretch the crack mouth open – separating the crack faces and eliminating closure. He was able to determine, with the aid of acetate replicas and with strain gages laid across the crack that overloads of sufficient amplitude and frequency can maintain a fully open crack throughout the life of a specimen. Later researchers [86, 51] were able to corroborate these observations via direct optical measurements. Varvani-Farahani, et al. [87] obtained similar results for stage I cracks using a confocal scanning laser microscope.

In the uniaxial tests in this study two methods were used to determine whether the cracks were growing under fully open conditions. The first was direct observation of the opening of a long crack at its tip in the experiments on uniaxial crack growth described in section 4.1.1. Overload and small cycle amplitudes similar to those used in smooth bar tests were applied to the notched flat crack growth specimen geometry from Figure 2.9, and the result was observed using a microscope. Initially, the overloads used during these tests were of the same strain amplitude as the smooth bar tests, but it was found that at this amplitude K_{max} rapidly approached the K_{Ic}

value of the material, hence the overload amplitude was reduced to 60% of the original. The resulting crack was observed to be growing under fully open conditions – at no time during the stress cycle was the crack seen to close at the crack tip.

A second method involved performing an overload test with an overload amplitude considerably larger than the one typically used in uniaxial tests. The circled data point in Figure 3.2 represents the test which was subjected to an overload strain amplitude ϵ_a=0.0065, a small cycle amplitude ϵ_a=0.00125, and η=250. With the exception of the overload amplitude, the adjacent point and the the circled datapoint share the same test conditions. In the presence of a larger overload it is expected that closure would be further reduced, if possible, and result in a substantially shorter fatigue life. A higher strain will further reduce crack opening stress, but if this is already below the minimum stress ($S_{op} \leq S_{min}$) the effective strain range will not change. Since no significant difference was found in the equivalent lives of these two tests it was concluded that the former was already open throughout the test, and hence the ϵ_a=0.0045 overload amplitude produced fully open crack growth.

3.1.4 Anisotropy in Uniaxial Fatigue

Although the effects of anisotropy on the fatigue strength of steels is not typically strong [88, 89], a series of longitudinal and transverse tests were conducted at a single laboratory during the SAE Fatigue Design and Evaluation Committee (FD&E) Phase I multiaxial round robin program[68], and the results from these tests are presented in Figure 3.3. The figure clearly shows a factor of three difference in fatigue lives between longitudinal and transverse specimens, indicating that there is an influence of anisotropy in this particular material. The data, taken from [62, 61], are comprised of specimens cut from Phase I normalized SAE1045 steel bar stock. The researchers believed that the anisotropy arose from the large inclusion content in this material. The material used in the current study also comes from the SAE FD&E study – in this case the raw material is Phase II normalized SAE1045 steel bar. The principal difference is that the Phase II material is a much cleaner steel with a much lower inclusion content. However, there is evidence, presented in section 3.2.1.4, which indicates that in the Phase II material there is a banding of pearlite and ferrite grains in the microstructure which leads to anisotropy under torsional loading. It is possible that this was also the cause of the anisotropy in the earlier study.

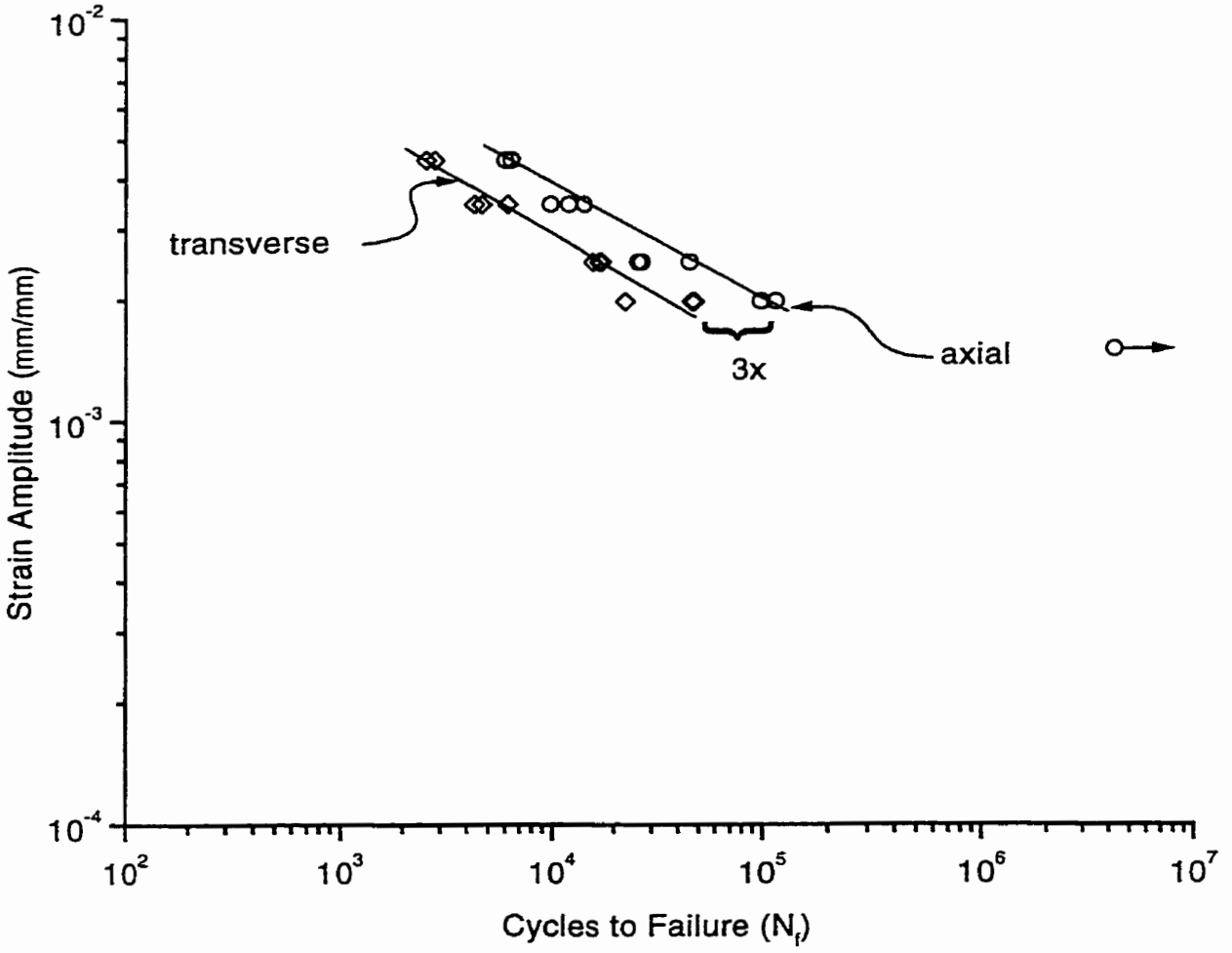

Figure 3.3: Longitudinal and transverse strain-life data for SAE Phase I normalized SAE1045 steel [62, 61].

3.1.5 Uniaxial Stress-Strain Behavior

The uniaxial monotonic and cyclic stress-strain behavior of normalized SAE1045 steel is presented in Figure 3.4. The inset graph in Figure 3.4 shows a typical monotonic test together with the constant amplitude cyclic stress strain curve for strains up to 2.5%. The curve fit to the constant amplitude data was slightly modified from the digitized curve provided in [67] which, in turn, was fit from this data set plus that found in [62]. Also plotted in this graph are periodic overload datapoints which

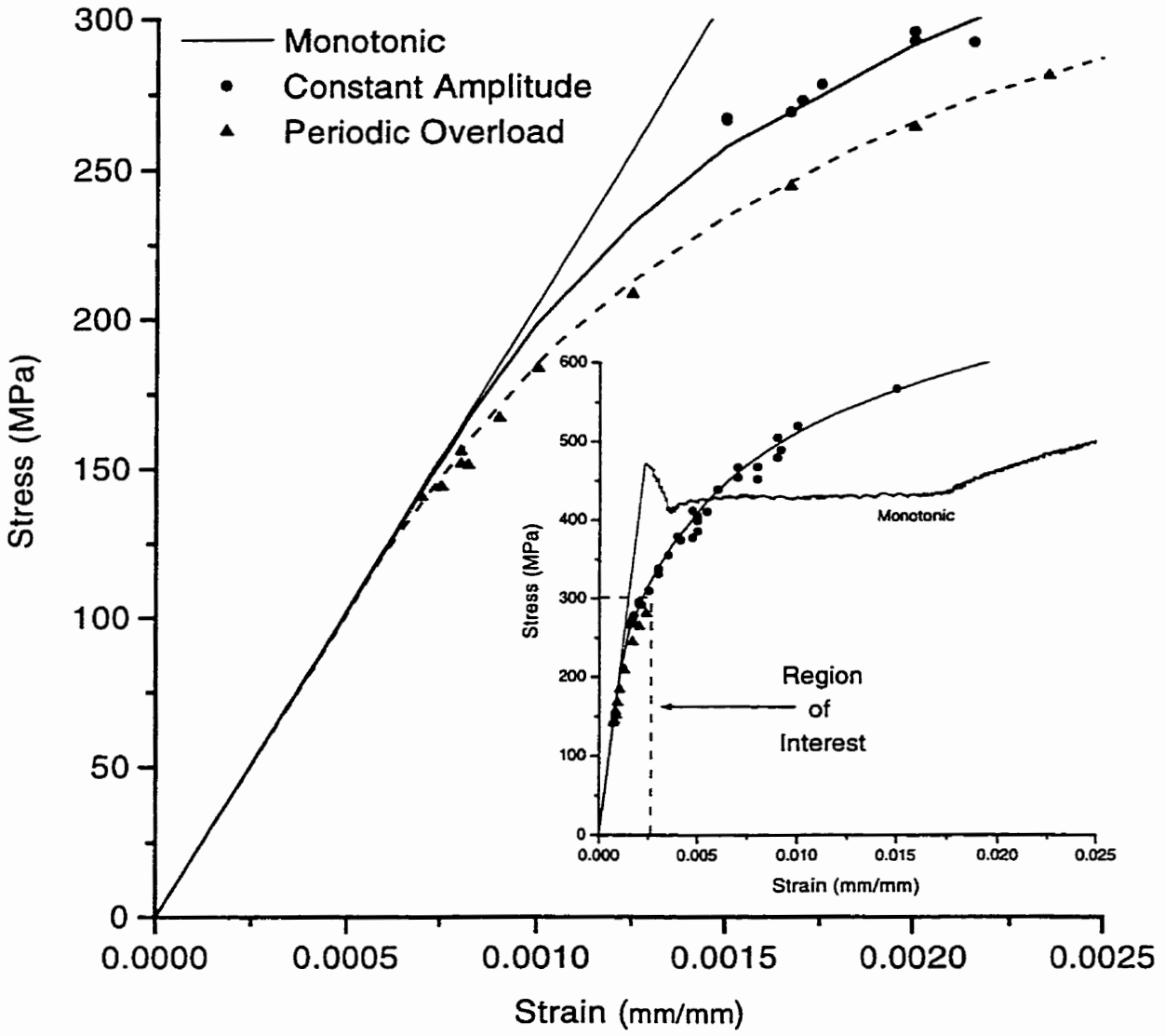

Figure 3.4: Stress-strain behavior of normalized SAE1045 steel.

are taken from the stabilized small cycles. These points can be more clearly seen in the expanded graph taken from the "Region of Interest" marked in the inset. The periodic overload datapoints diverge early from the constant amplitude curve and proceed along a different and lower path. Other researchers have observed a reduction in stress under variable amplitude loading when compared to the constant amplitude curve – Dowling [90] noted that this phenomena occurred in SAE4340 steel

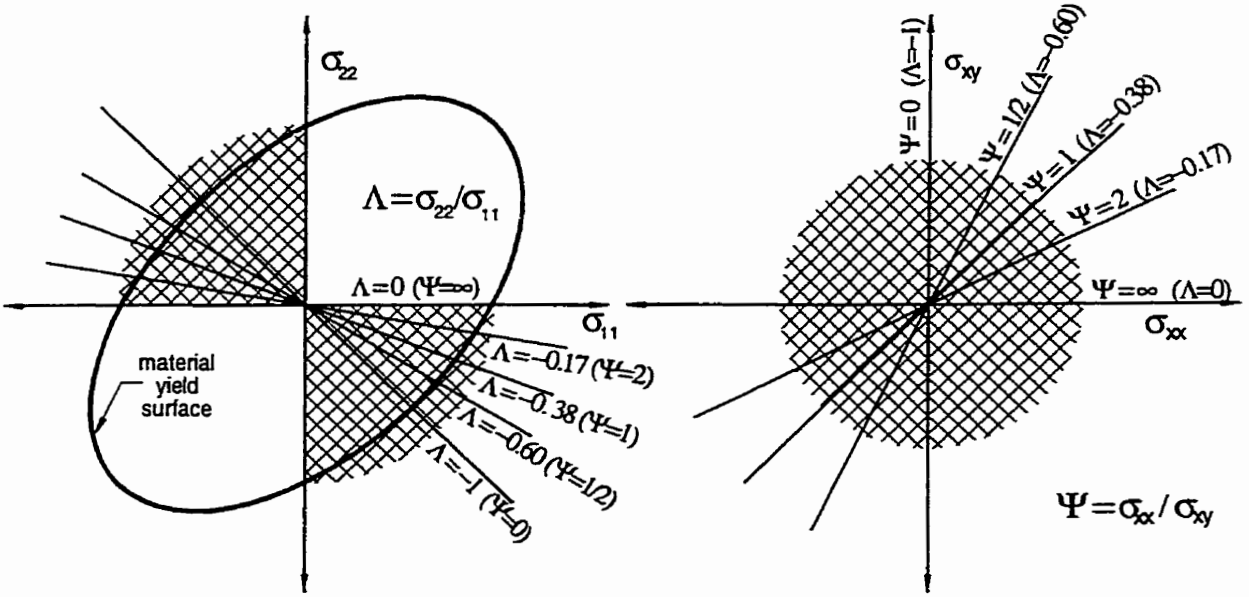

a) Principal stress axes. b) Axial-Torsion axes.

Figure 3.5: Load paths shown in (a) principal stress (with material yield surface) and (b) axial-torsion axes. Crosshatched regions indicates the stress ratios possible with bending-torsion and tension-torsion systems.

when subjected to periodic overloads, and the effect that these overloads had was to eliminate the effects of strain aging for smaller cycles. The net result was that, for the same small cycle strain amplitude, lower stresses and larger amounts of plasticity were observed for a given strain amplitude.

The periodic overload stress-strain curve is used in evaluating multiaxial damage and crack growth models.

3.2 Tension-Torsion Tests

Experiments were performed at the stress ratios shown in Figure 3.5a-b. Figure 3.5a shows the principal stress axes with a crosshatched region indicating the possible range of stress ratios which can be attained with tension-torsion and bending-torsion

systems. In this range five stress ratios (uniaxial, torsion, and three biaxial stress ratios) were selected ranging from $0 \geq \Lambda = \sigma_{22}/\sigma_{11} \geq -1$. These coordinates have been remapped in Figure 3.5b to a system that is more convenient for analyzing data obtained from the test equipment used in this investigation. In this coordinate system the ratios range from uniaxial to torsion, $\infty > \Psi = \sigma_{xx}/\sigma_{xy} \geq 0$, respectively.

The aim of the overload tests in this section was to find conditions under which a biaxially loaded fatigue crack would grow free of crack face interference. This maximizes the damage done by each small cycle and yields the shortest specimen fatigue lives. As with the uniaxial overload tests, an overload cycle was selected that would yield a life of roughly 10,000 cycles to failure. This overload level is typical of notch strains during large cycles encountered in severe loading.

3.2.1 Torsional Behavior, Ψ=0

Two kinds of periodic overload torsion tests were performed: those in which both overload and small cycles were in torsion (in-phase) and those in which the small cycles were applied in torsion but the overload cycle was applied in the tension axis (out-of-phase).

3.2.1.1 In-Phase Torsional Testing

Fatigue life data sets for both constant amplitude and periodic overload torsion tests are presented in Figure 3.6. This and subsequent fatigue life data sets are presented in tensorial shear strain, ϵ_{xy}. Tensorial shear strain is denoted by ϵ_{xy} while γ_{xy} is used to indicate engineering shear strain ($\gamma_{xy} = 2\epsilon_{xy}$). The periodic overload tests were conducted using the shear strain history shown in the figure. The torsional overload cycle, maintained at $(\epsilon^{ol}_{xy})_a$=0.0035 in all tests, was applied first and then followed by torsional small cycles (ψ=0). Calculations to determine the equivalent cycles to failure were made in the same way as for uniaxial loading (ψ=∞), described in section 3.1.2.

The introduction of overloads caused a reduction of the constant amplitude endurance limit from $(\epsilon^{ca}_{xy})_a$= 0.0016 to $(\epsilon^{sc}_{xy})_a$= 0.0007 at 10^7 cycles – a little less than one-half of its original value. The superscript *sc* indicates small cycle and the superscript *ol* indicates overload cycle.

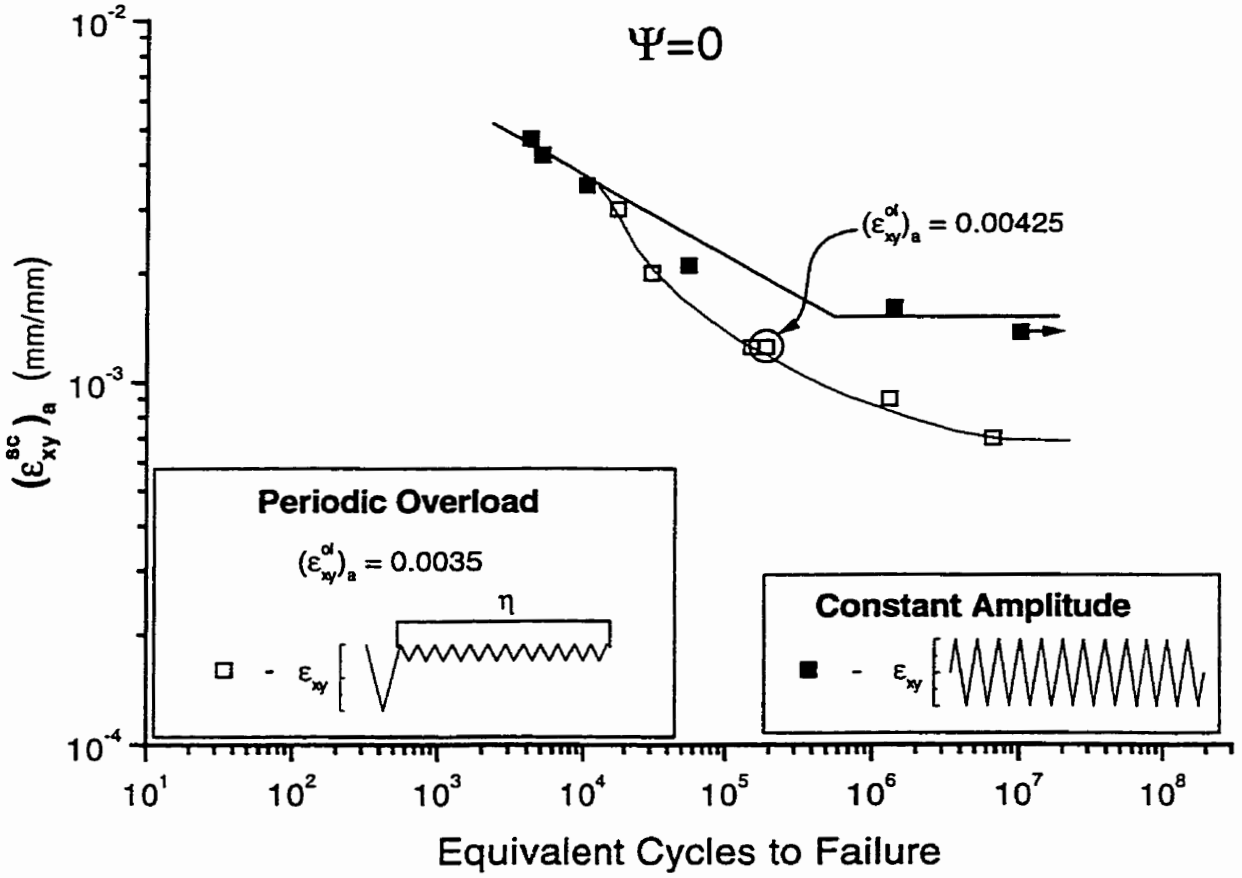

Figure 3.6: Fatigue response of normalized SAE1045 under in-phase torsional loading, $\Psi = \frac{\sigma_{xx}}{\sigma_{xy}}$=0 ($\psi = \frac{\epsilon_{xx}}{\epsilon_{xy}}$=0). Circled datapoint indicates special overload level $(\epsilon^{ol}_{xy})_a$=0.00425, $(\epsilon^{ca}_{xy})_a$=0.00125, and η=50.

In-phase Ψ=0 crack face interference Two tests were performed in order to determine whether the cracks faces under in-phase ψ=0 loading were growing free of interference with each other. The first test is indicated in Figure 3.6 by a circle around the datapoint. This test has an overload strain level of $(\epsilon^{ol}_{xy})_a$=0.00425 (constant amplitude life of 4985 cycles to failure), $(\epsilon^{sc}_{xy})_a$=0.00125, and η=50. The rest of the overload datapoints were subjected to $(\epsilon^{ol}_{xy})_a$=0.0035, including the point adjacent to the circled datapoint. This datapoint shared the same small cycle amplitude, $(\epsilon^{sc}_{xy})_a$=0.00125, but had η=20. The two tests have similar lives and it is presumed

that if the larger overload is more effective at reducing crack face interference then the calculated life of the test would fall short of the test with $(\epsilon_{xy}^{ol})_a$=0.0035, hence it is assumed that the $(\epsilon_{xy}^{ol})_a$=0.0035 overload cycle has reduced crack face interference as much as possible in these tests.

3.2.1.2 Torsion Testing with Tension Overloads (Out-of-Phase)

Zero tension mean stress In these tests the overload was first applied in strain control in the tension direction. The tension strain was then brought to a point where the tension stress was zero and held; see Figure 2.23. During the tension strain hold period small cycles were applied in torsion. In this case a fully reversed axial (Ψ=∞) overload cycle of $(\epsilon_{xx}^{ol})_a$=0.0045 was applied.

The results of these tests are presented in Figure 3.7 along with constant amplitude data. The 10^7 cycle endurance limit for periodic overload cycles is reduced to a little less than one-half of the constant amplitude endurance limit.

As with the in-phase tests an experiment was conducted to investigate the effectiveness of the $(\epsilon_{xx}^{ol})_a$=0.0045 overload. In this case the overload test, marked with a circle in Figure 3.7, consisted of $(\epsilon_{xx}^{ol})_a$=0.0075 (constant amplitude life of 3100 cycles to failure), $(\epsilon_{xx}^{ca})_a$=0.0015, and η=20. The result of this test conforms with the trend for the $(\epsilon_{xx}^{ol})_a$=0.0045 overloads and indicates that the lower overload level reduces crack face interaction to the greatest degree possible in this type of test.

Tension peak hold overload In this series of tests, a tension overload was first applied to the specimen, then the peak tension strain level was held static while small cycles were applied on the torsion axis, as illustrated in Figure 2.23. The application of torsion cycles led to stress relaxation in the tension axis as illustrated in Figure 3.8. Eventually the tension stress reaches a steady-state value, and this value depends on the amount of plasticity in the torsional stress-strain loop. At one extreme is the test shown in the figure ($(\epsilon_{xy}^{sc})_a$=0.005), in which only 7% of the tension stress generated by the tension overload remained after the torsional "small" cycles were applied, and at the other, under $(\epsilon_{xy}^{sc})_a$=0.000625 (minimal plasticity), 75% of the tension stress remained after torsional cycling.

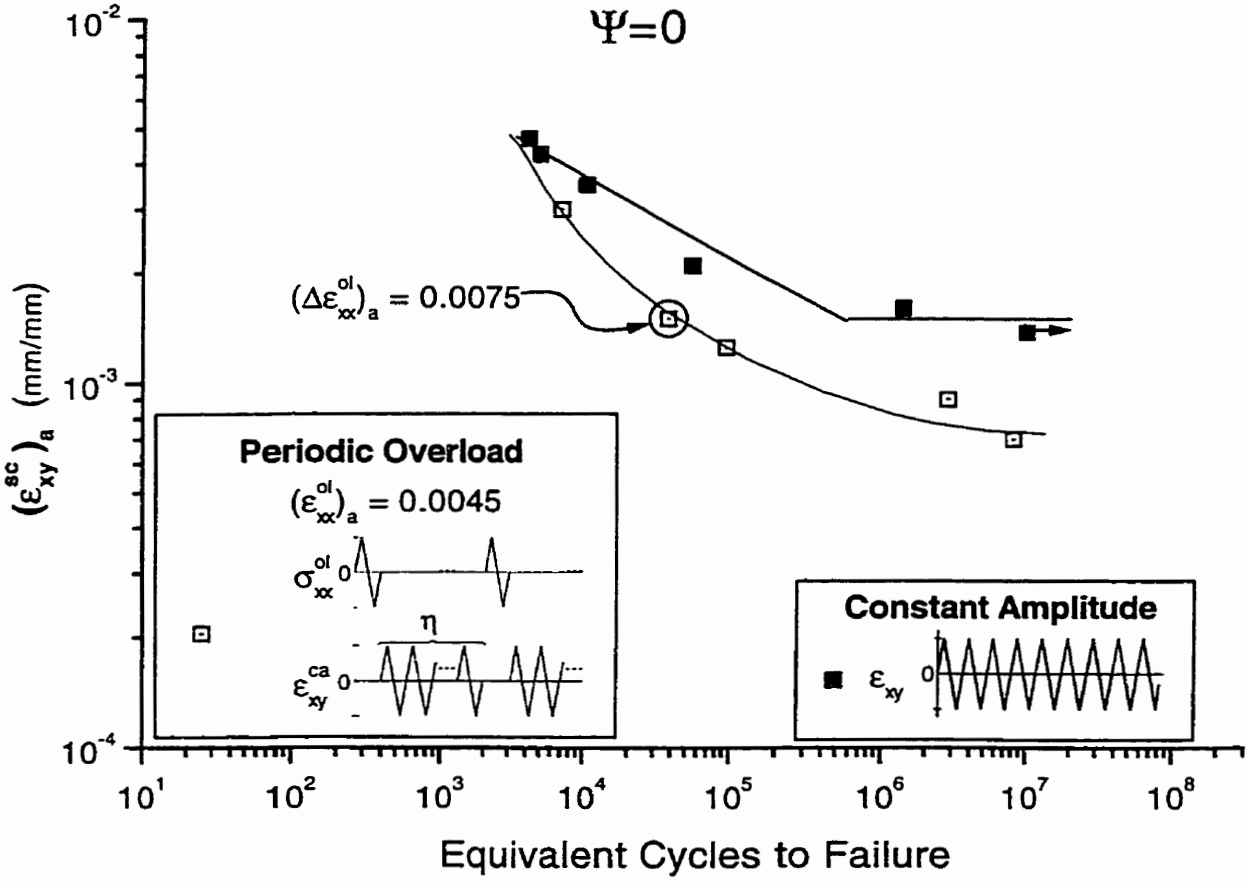

Figure 3.7: Periodic tension overload curve for torsional loading of normalized SAE1045 steel. Circled datapoint indicates special overload level $(\epsilon_{xx}^{ol})_a$=0.0075, $(\epsilon_{xy}^{ca})_a$=0.0015, and η=20.

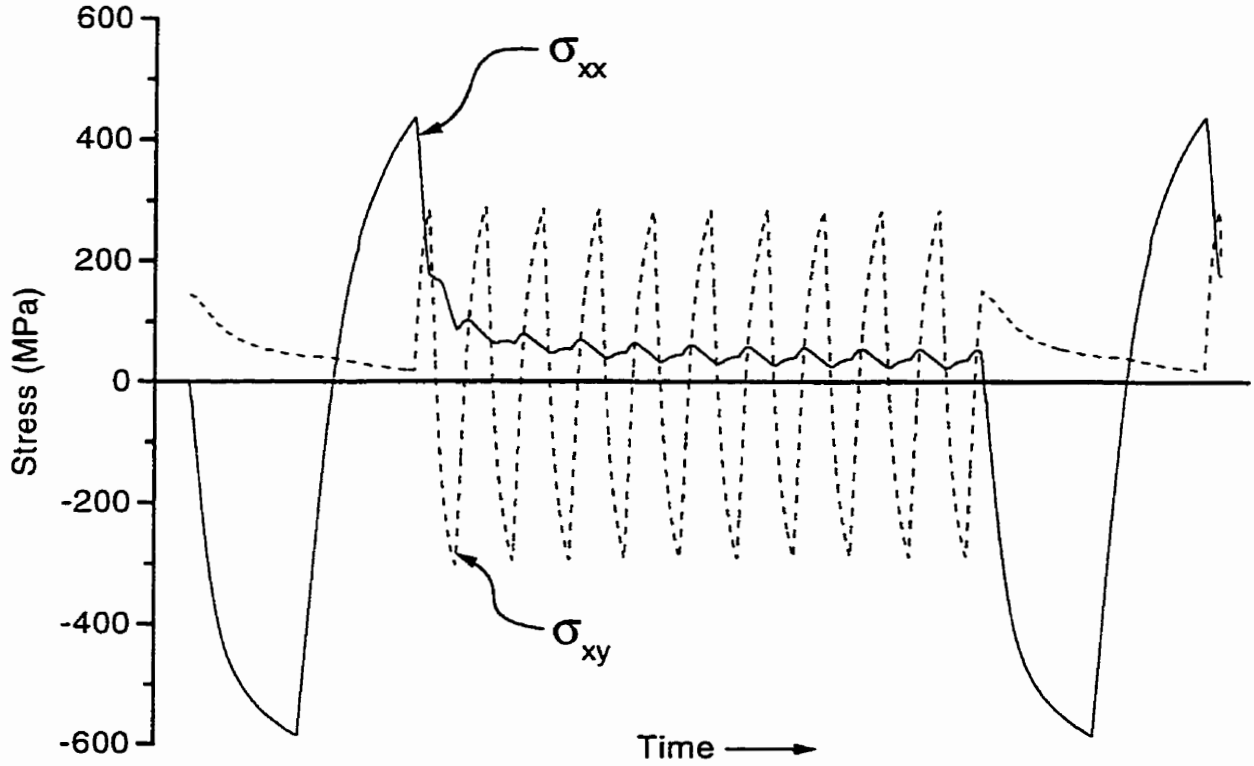

Figure 3.8: Relaxation of tension stress with application of repeated torsional cycling $(\epsilon_{xx}^{ol})_a$=0.005, $(\epsilon_{xy}^{sc})_a$=0.005, and η=10.

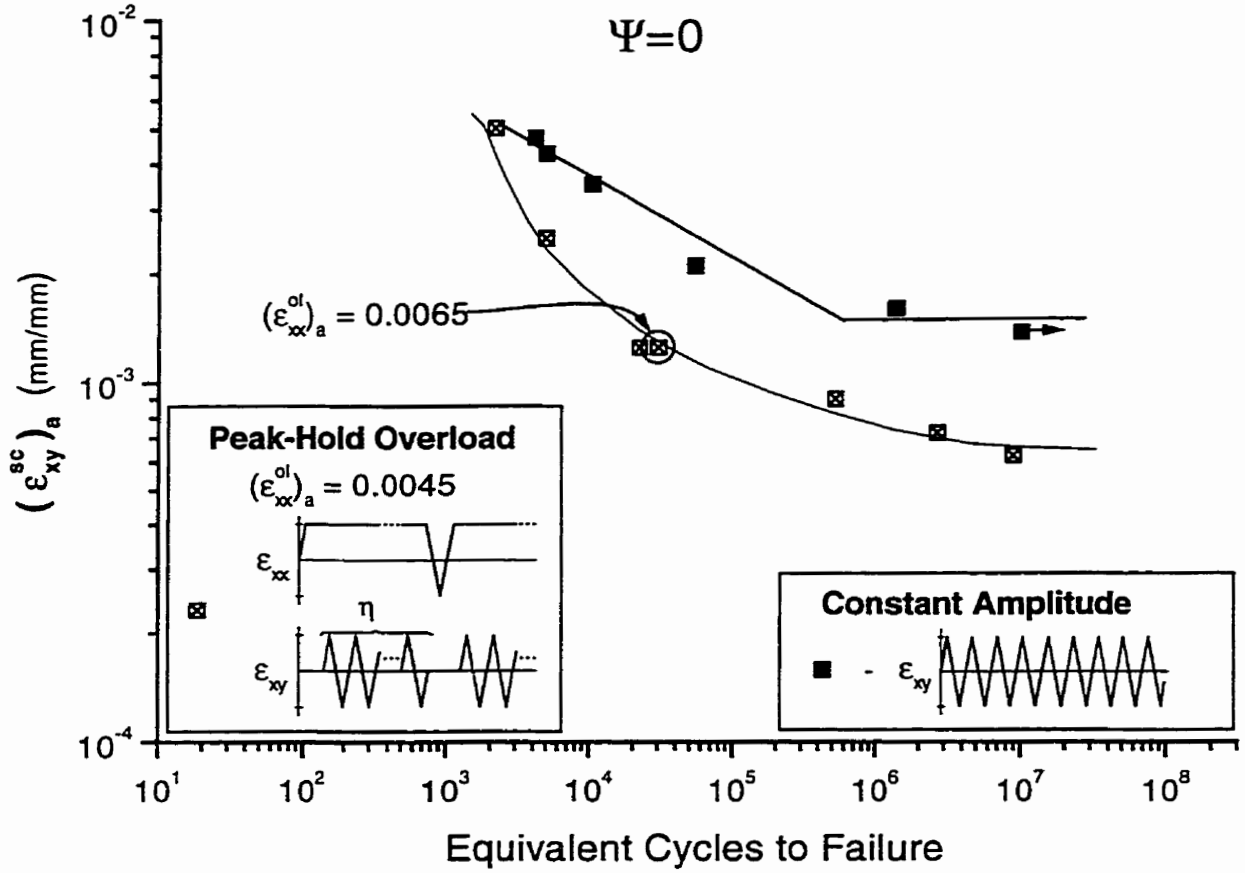

Figure 3.9: Tension peak-hold overload torsion tests on normalized SAE1045 steel. Circled datapoint indicates special overload level $(\epsilon_{xx}^{ol})_a$=0.0065, $(\epsilon_{xy}^{ca})_a$=0.00125, and η=20.

The fatigue results for this test series are presented in Figure 3.9. The 10^7 endurance limit for periodic overload tests is reduced to two-fifths of the constant amplitude endurance limit (from $(\epsilon_{xy}^{ca})_a$=0.0016 to $(\epsilon_{xy}^{sc})_a$=0.000625). At all lifetimes the peak strain hold tension overload cycle clearly reduces the fatigue resistance of this material.

As in the previous sections, a single test was performed in order to determine the efficacy of the overload cycle used in these tests. This test was identical to the adjacent data point in all respects except for the overload strain amplitude, which was $(\epsilon_{xx}^{ol})_a$=0.0065 (a constant amplitude life of 5000 cycles to failure). The standard

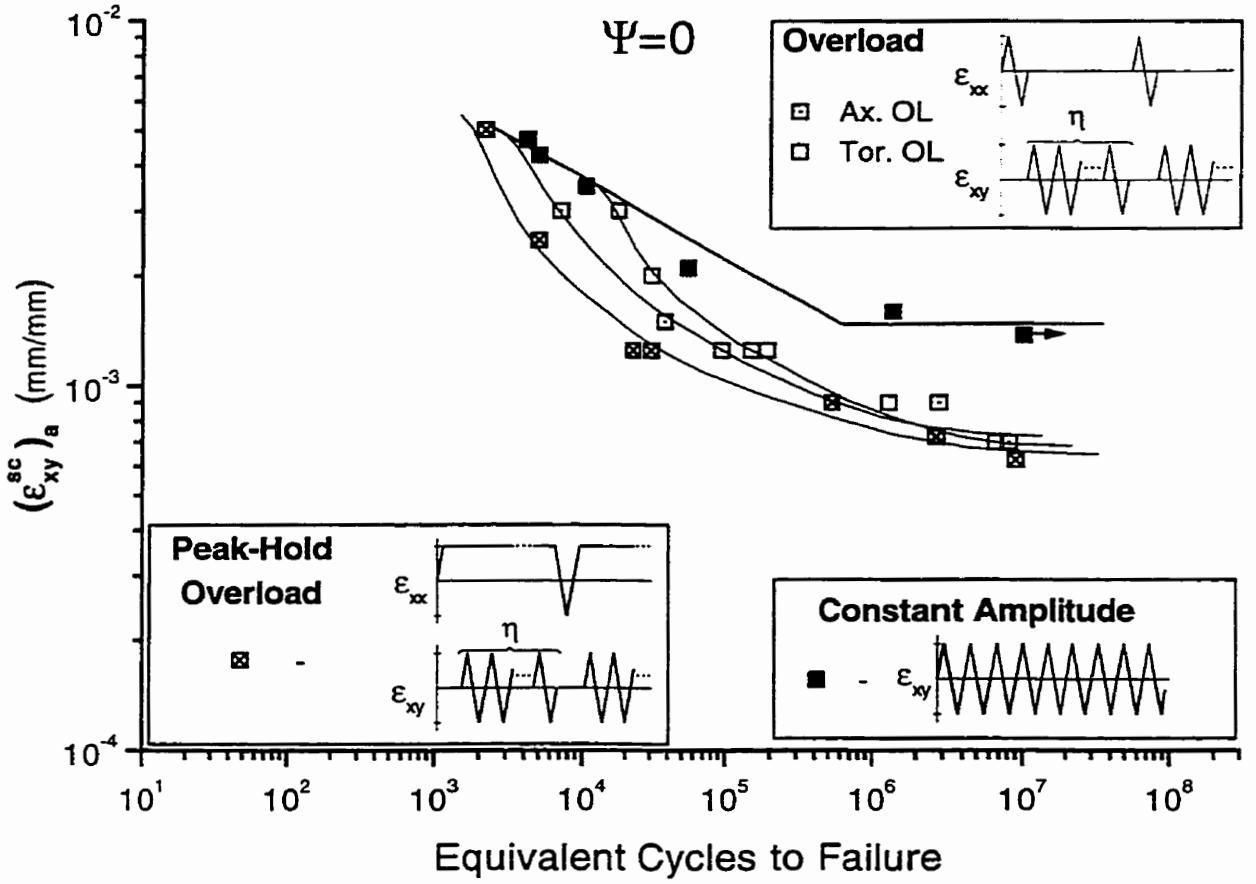

Figure 3.10: The impact of various types of overloads on the torsional fatigue ($\Psi = \frac{\sigma_{xx}}{\sigma_{xy}}$=0) of normalized SAE1045 steel.

overload strain amplitude used in the tension peak hold tests was $(\epsilon_{xx}^{ol})_a$=0.0045. Both tests share, within experimental error, the same life. This indicates that the smaller overload cycle is just as effective in reducing crack face interaction as the larger overload, and it indicates that, for this particular type of overload, the smaller overload has removed crack face interaction.

3.2.1.3 Ψ=0 Combined Results

All of the fatigue results from sections 3.2.1.1 and 3.2.1.2 are plotted in Figure 3.10. In the high life region all three datasets merge, suggesting that for small torsional

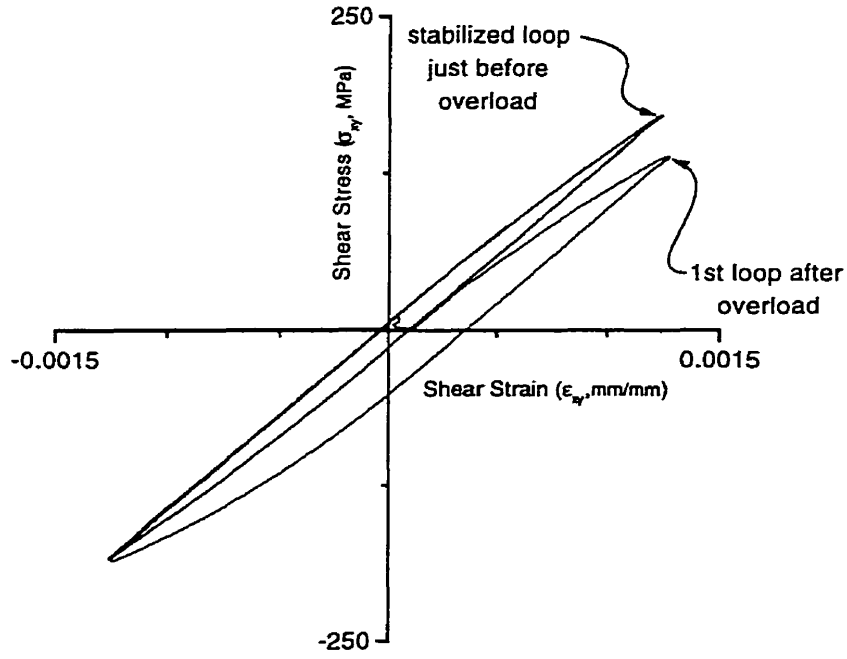

Figure 3.11: Torsional stress-strain responses before and after axial peak hold overloads ($\Psi = \frac{\sigma_{xx}}{\sigma_{xy}}$=0) in normalized SAE1045 steel.

amplitudes, all overloads eliminate crack face interference. At shorter lives, data for the peak-hold overload tests show a lower fatigue resistance than data for the other two overloads, and it is believed that, at these higher torsional strain levels, the actual overload cycle is not represented by just the tension overload, but by the tension overload and the first torsional cycle.

Figure 3.11 shows that the first torsion cycle differs substantially in appearance from subsequent torsion cycles in that it exhibits a much larger amount of plasticity. During this first torsional cycle the axial stress was observed to relax significantly. This behavior may indicate a difference between the damage increment from that lone cycle and subsequent torsional cycles. However, at lower torsional strain levels where torsional plasticity is reduced, the peak-hold data rejoin the other two datasets, and, at the same time, the difference between the first and subsequent cycles following an overload vanishes.

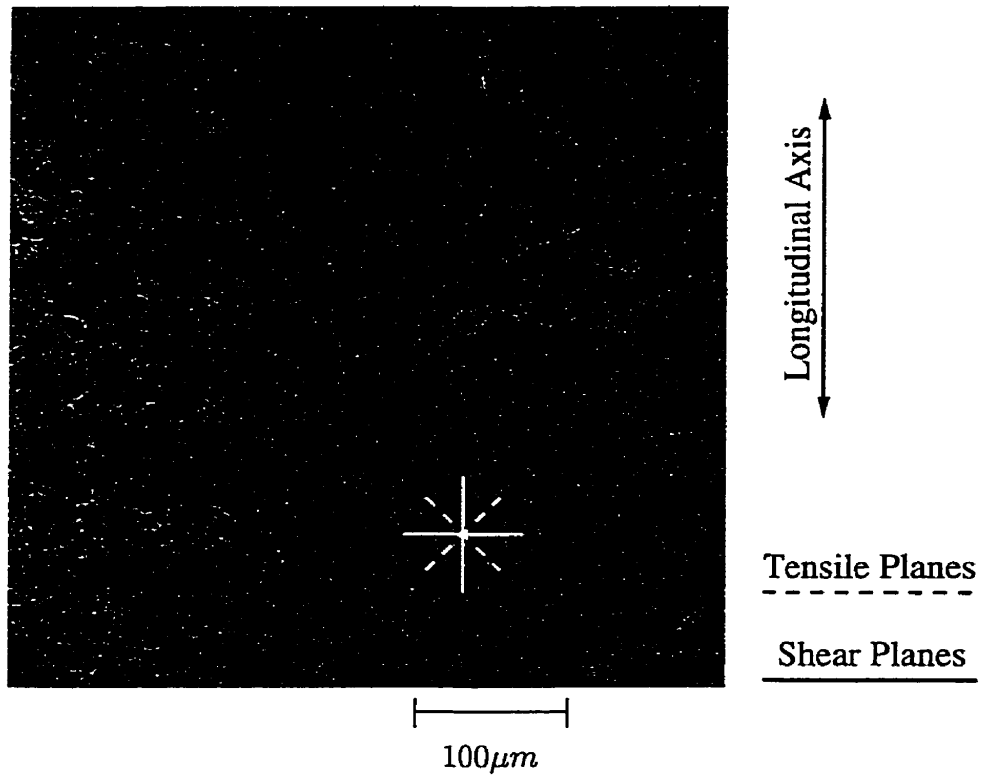

Figure 3.12: Typical small crack growth under ($\Psi = \frac{\sigma_{xx}}{\sigma_{xy}}$=0) loading of normalized SAE1045 steel. Specimen subjected to $(\epsilon_{xy}^{ol})_a$=0.0035, $(\epsilon_{xy}^{ca})_a$=0.003, η=10.

3.2.1.4 Proposed Crack Face Interaction Mechanisms under Ψ=0 Loading

In-phase torsional loading The development of cracks in both the constant amplitude and in-phase torsional overload tests was similar. Small cracks less than 50μm in length nucleate on maximum shear planes (in the longitudinal (x-axis) and circumferential (y-axis) directions). An example of the typical appearance of these cracks is given in Figure 3.12.

However, the microstructure is strongly banded into alternating regions of dense pearlite and dense ferrite grains, and cracks tend to grow in ferrite rich regions or along ferrite-pearlite grain boundaries. As a result, the longitudinal cracks become dominant and grow to failure. This behavior was observed in in-phase $\Psi = 0$, $\frac{1}{2}$ and 1 tests. Examples of the influence of microstructure on cracking for both long

and short cracks can be seen in Figures 3.13. The preference that cracks show for growth in ferrite rich regions may also explain the fatigue behavior differences between transverse and longitudinal uniaxial fatigue data observed in Figure 3.3. A crack in a transversely oriented specimen could grow along the length of the ferrite bands as opposed to a longitudinally oriented specimen where a crack would have to cross both ferrite and pearlite regions.

At longer crack lengths (0.5mm and greater) shear-crack crack faces have been observed to slide back and forth across each other, and it is believed that this is also true of shorter crack lengths. Under this kind of motion (mode II and III crack growth) the energy available at the crack tip is reduced by the interaction of asperities as shown at the left side of Figure 3.14.

In-phase overloads also follow this kind of motion, but because the translation of the crack faces is greater, the smearing of asperities is greater (as shown at the right side of Figure 3.14). Once smeared, the asperities do not impede the crack face motion to the extent they did before the overload cycle, and it is suggested that this allows more of the energy formerly expended in rubbing asperities across each other to reach the crack tip. Figure 3.15 shows an asperity smeared during a torsional periodic overload experiment.

Zero axial mean stress and peak-hold overload tests The development of early cracks in these tests is similar to that described in the previous section in that cracks form in both the x- and y- directions, but since the overload is applied in the tension (x) axis, those cracks growing on the x-plane (or in the y-direction) have less crack face interaction and eventually grow to fail the specimen. The appearance of these early cracks is identical to that in Figure 3.12.

The motion of the crack faces during the application of torsional small cycles is also identical to that in Figure 3.14. However, the motion of the crack faces during the overload, shown in Figure 3.16, differs since the faces move together and apart. In this model it is presumed that the action of the compressive overload in crushing asperities is identical to that in uniaxial loading described in [4]. The reduced height

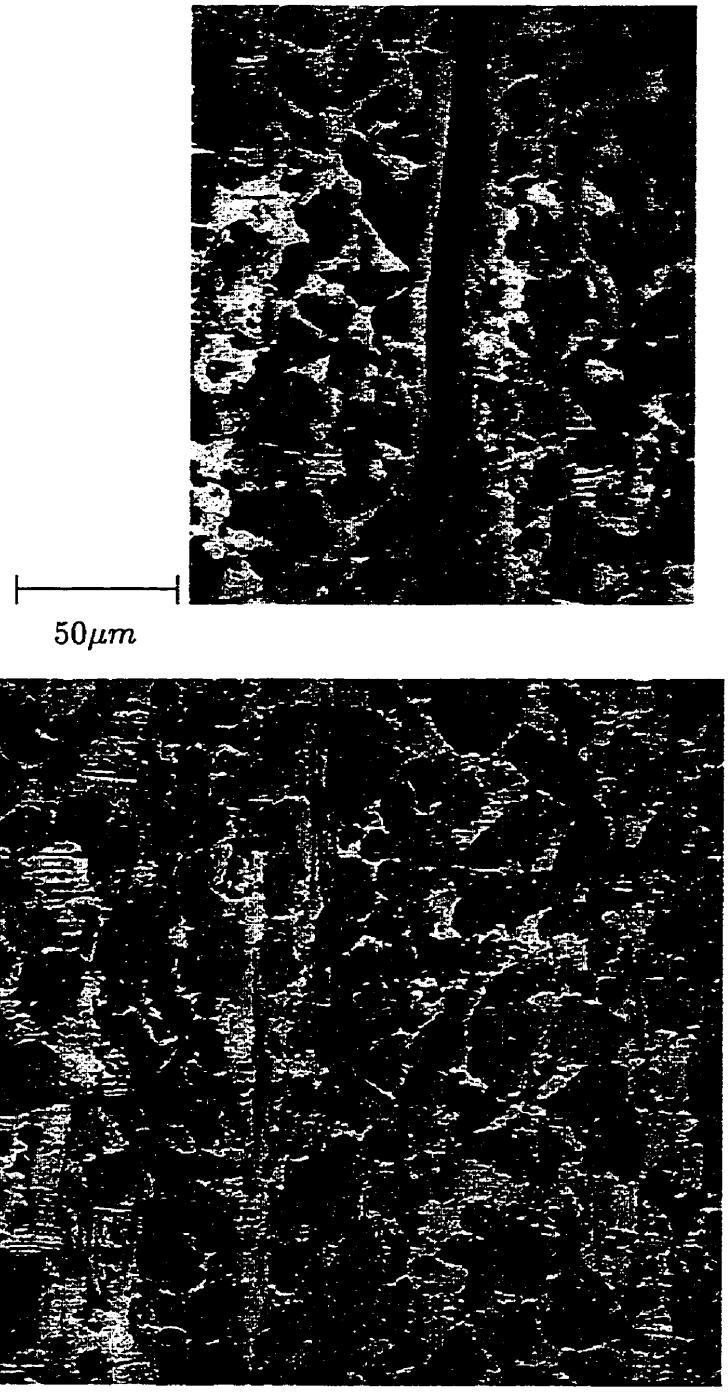

Figure 3.13: Preferential cracking through ferrite grains and along the ferrite/pearlite grain boundaries for both long (top) and shorter crack lengths (bottom). Specimen subjected to $(\epsilon_{xy}^{ol})_a$=0.00425, $(\epsilon_{xy}^{ca})_a$=0.00125, and η=50

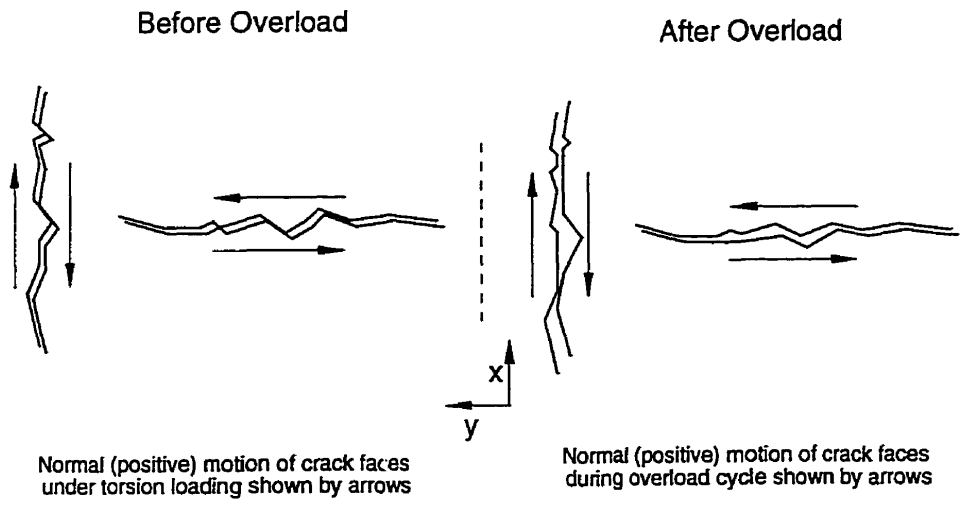

Figure 3.14: Proposed crack face interference mechanism under in-phase $\Psi = \frac{\sigma_{xx}}{\sigma_{xy}}=0$ loading.

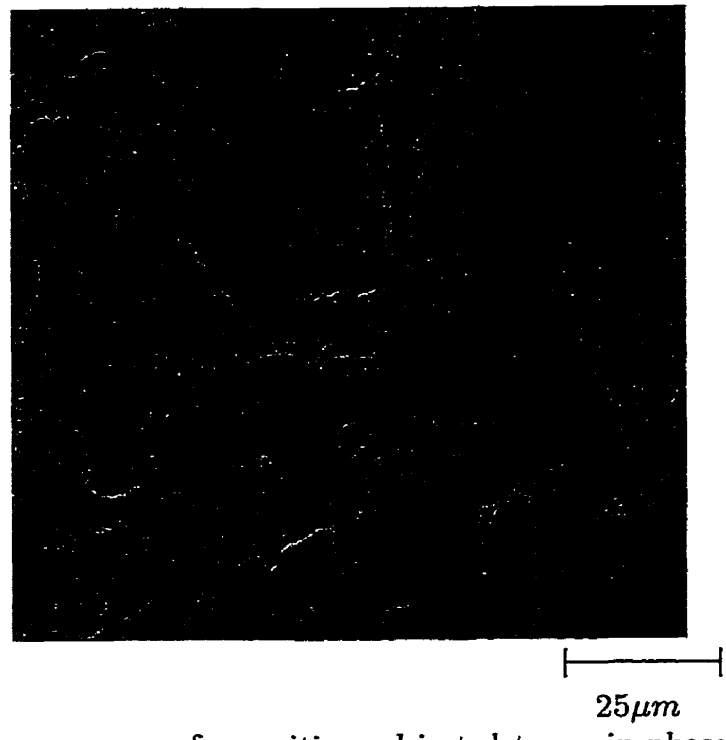

Figure 3.15: Appearance of asperities subjected to an in-phase $\Psi = \frac{\sigma_{xx}}{\sigma_{xy}}=0$ overload history. Note smearing of asperities and secondary cracking. ($(\epsilon^{ol}_{xy})_a$=0.0035, $(\epsilon^{ca}_{xy})_a$=0.003, η=10)

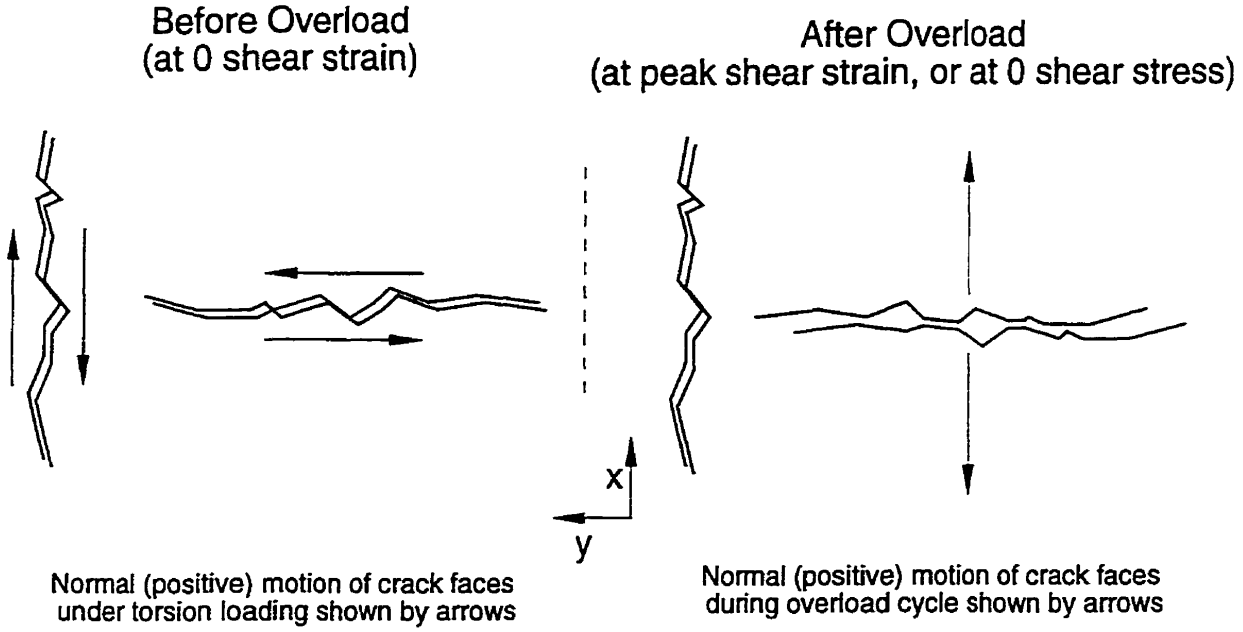

Figure 3.16: Proposed closure mechanism under $\Psi = \frac{\sigma_{xx}}{\sigma_{xy}}$=0 loading with tension overloads.

of the asperities allows easier translation of the crack faces during torsional loading and, it is presumed, that more of the crack driving energy reaches the crack tip. Figure 3.17 shows an asperity from a Ψ=0 axial peak-hold overload test which has been crushed.

In both zero mean stress and peak-hold overloads the tensile portion of the overload pulls apart the crack faces. However, in the peak-hold overload the peak separation of the crack faces is maintained during torsional cycling, but in a zero mean stress overload test the stress separating the crack faces is reduced to zero. Observations show that the crack faces are still separated because of the mean strain imposed by the overload. Hence both of these overloads reduce crack face interference.

3.2.2 In-Phase $\Psi = \frac{1}{2}$ Overload Tests

In these tests the phasing between tension and torsion strain was strictly maintained. An example of the strain histories used in these tests is shown in Figure 3.18 along

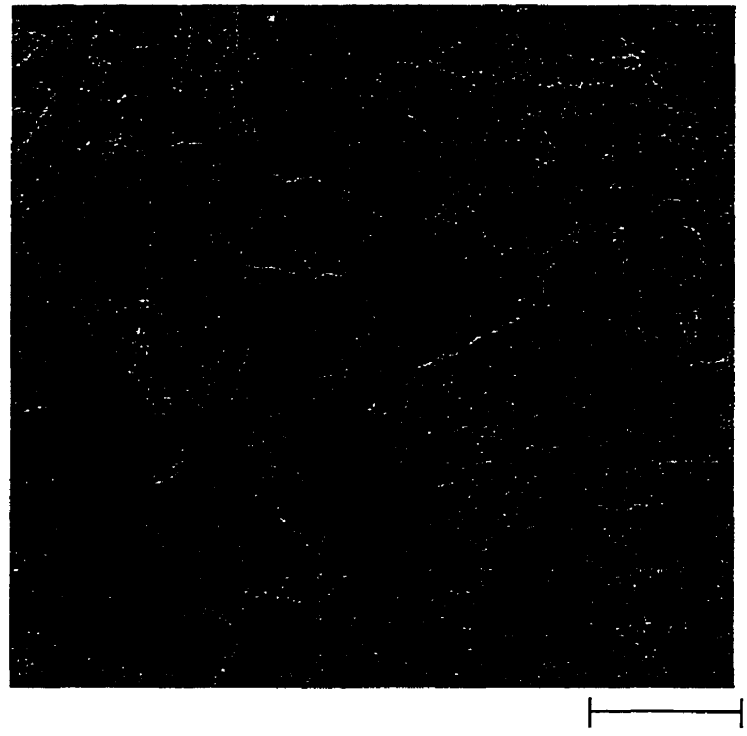

Figure 3.17: Typical appearance of asperities under $\Psi = \frac{\sigma_{xx}}{\sigma_{xy}}$=0 loading with tension peak-hold overloads. Note presence of crushed asperities and relative lack of lateral rub marks. Holes arise from stringers broken by torsional cycling. Specimen subjected to $(\epsilon_{xx}^{ol})_a$=0.0065, $(\epsilon_{xy}^{sc})_a$=0.00125, and η=50.

with the fatigue results for this strain ratio. An overload cycle was applied in both axes so that the peak negative strain in the tension axis occurred at the same instant as the peak "negative" strain in the torsion axis. The overload cycle ends at the peak positive strain on both axes, and then the small cycles are applied. The application of the small cycles follows the same ratio: the positive peaks and negative peaks occur at the same time in both axes, and the peak value of these cycles match that of the peak from the overload cycle. The ratio of the tension to the torsion strain ($\psi = \frac{\epsilon_{xx}}{\epsilon_{xy}}$) is maintained at $\frac{1}{3}$ throughout the strain histories. The term Ψ refers to the stress ratio of the overload loop tips, $\frac{\sigma_{xx}}{\sigma_{xy}}$, and is close to 1/2 during these strain controlled tests.

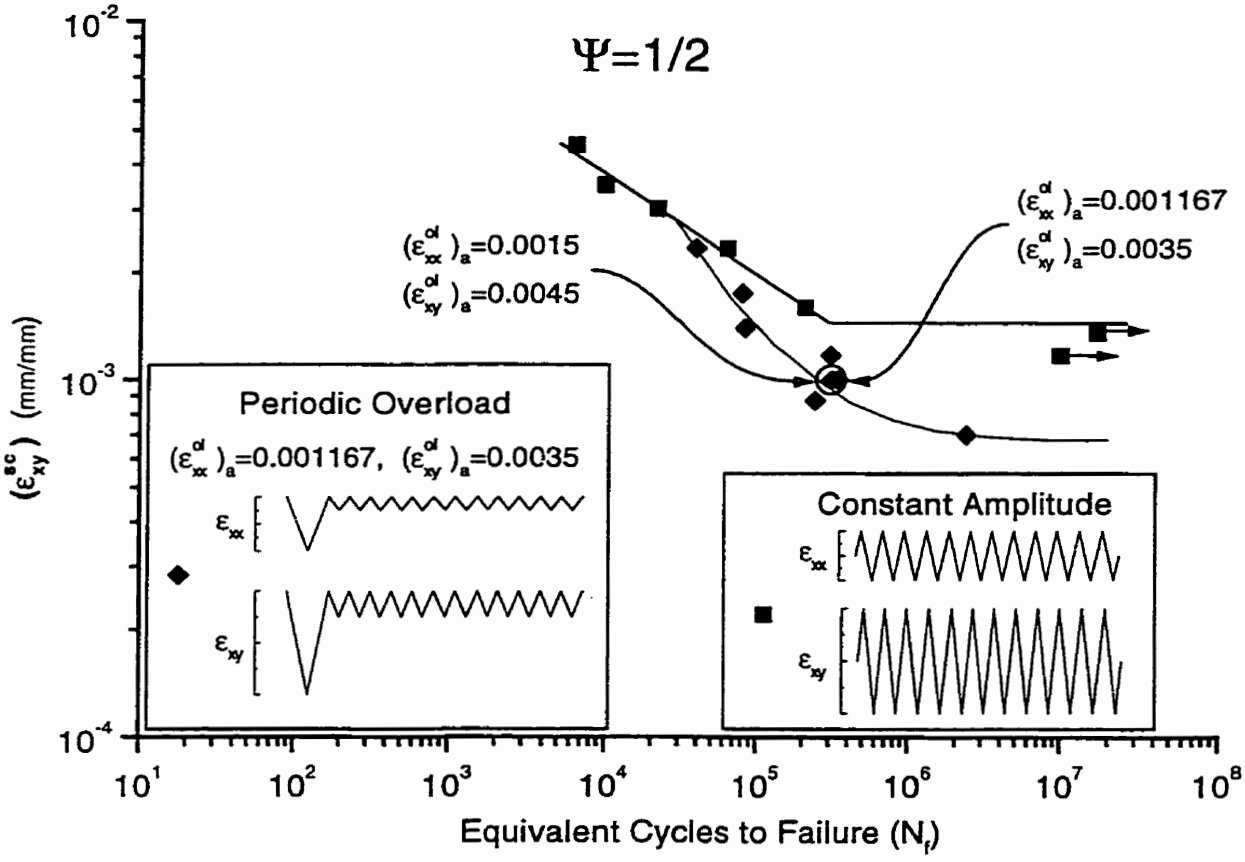

Figure 3.18: Periodic overload and constant amplitude fatigue responses of normalized SAE 1045 for $\Psi = \frac{\sigma_{xx}}{\sigma_{xy}} = \frac{1}{2}$ ($\psi = \frac{\epsilon_{xx}}{\epsilon_{xy}} = \frac{1}{3}$). Circled datapoint indicates special overload level $(\epsilon_{xy}^{ol})_a$=0.0045, $(\epsilon_{xx}^{ol})_a$=0.0015, $(\epsilon_{xy}^{ca})_a$=0.001, $(\epsilon_{xx}^{ca})_a$=0.00033, and η=20.

Data for fatigue tests at this strain ratio are shown in Figure 3.18 plotted as tensorial shear strain amplitude vs. equivalent cycles to failure. The constant amplitude 10^7 endurance limit is $(\epsilon_{xy}^{ca})_a$=0.0014 while that of the periodic overload tests is $(\epsilon_{xy}^{sc})_a$=0.00068, which is a reduction over one-half of the original fatigue limit.

The circled datapoint in Figure 3.18 represents a test with an overload strain level which was larger than the standard ($(\epsilon_{xy}^{ol})_a$=0.0035,$(\epsilon_{xx}^{ol})_a$=0.0012). With the exception of the large overload cycle ($(\epsilon_{xy}^{ol})_a$=0.0045,$(\epsilon_{xx}^{ol})_a$=0.0015 – 6493 constant amplitude cycles to failure), this test is identical to the adjacent test: $(\epsilon_{xy}^{sc})_a$=0.001,

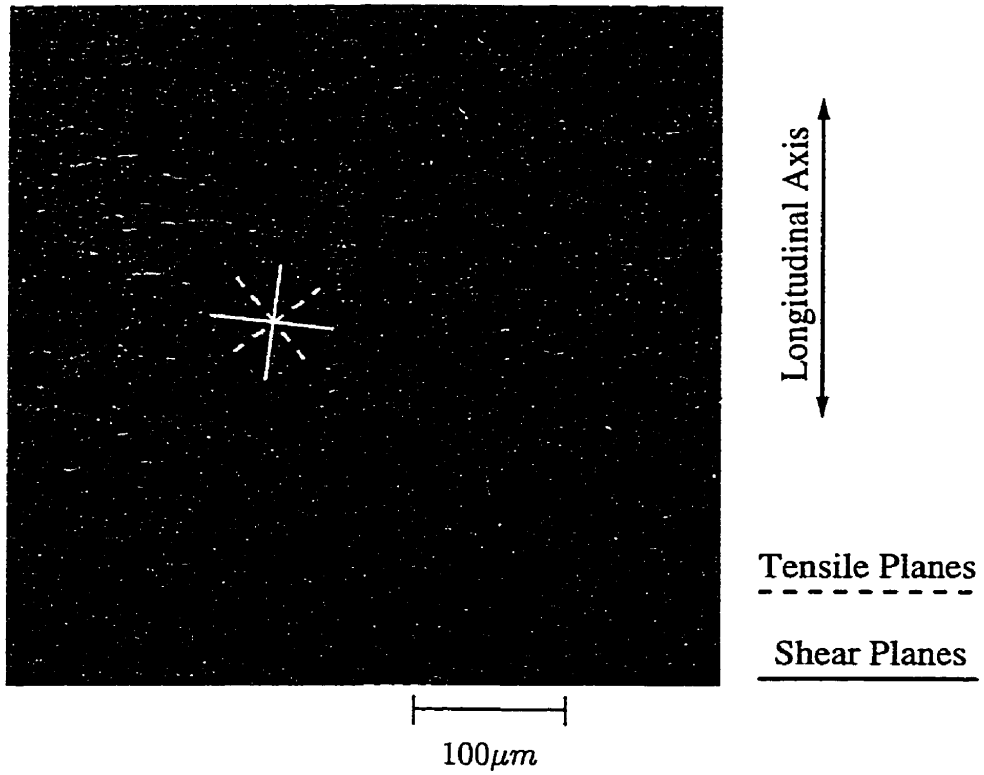

Figure 3.19: Typical small crack growth under $\Psi = \frac{\sigma_{xx}}{\sigma_{xy}} = \frac{1}{2}$ loading of normalized SAE1045 steel.

$(\epsilon_{xx}^{sc})_a$=0.0003, and η=20. Since this point does not significantly depart from the general trend, it is presumed that the smaller overload cycle allows the smaller cycles to grow under fully effective conditions.

3.2.2.1 Proposed Crack Face Interaction Mechanisms under $\Psi = \frac{1}{2}$ Loading

The early crack growth observed in this stress ratio is similar to that seen in section 3.2.1.4. The addition of tension loading to the torsional loading causes a slight rotation of the maximum shear planes (crack initiation direction), but longitudinal cracks still grow and eventually become dominant. An example can be found in Figure 3.19, which shows cracks forming on both maximum shear and longitudinal planes. The preference for the longitudinal planes is again due to the banded microstructure. As mentioned in section 3.2.1.4, cracks tend to grow through ferrite

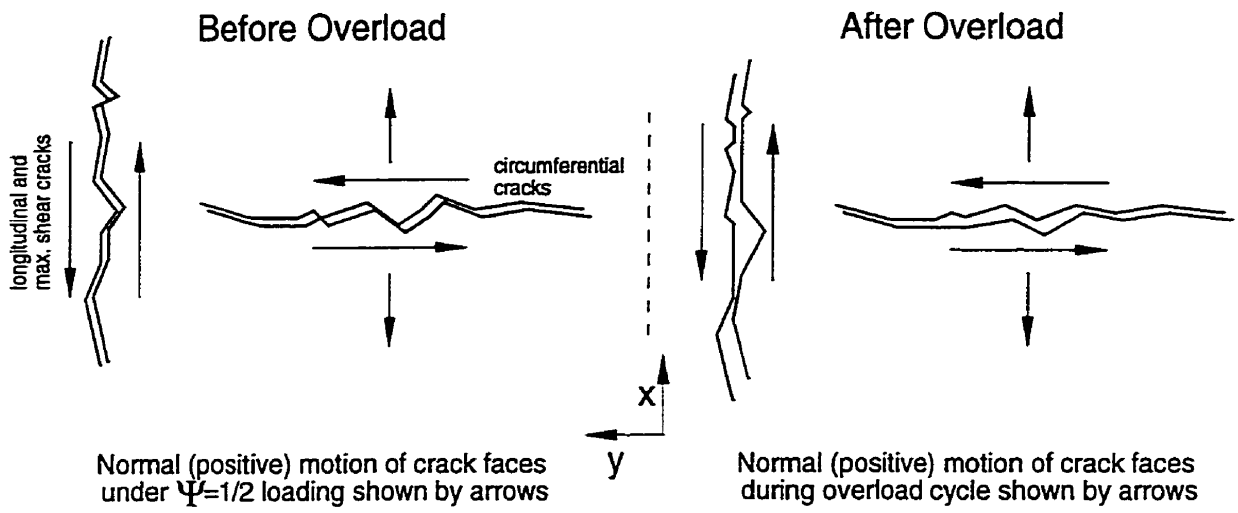

Figure 3.20: Proposed closure mechanism under in-phase $\Psi = \frac{\sigma_{xx}}{\sigma_{xy}} = \frac{1}{2}$ loading.

or along ferrite-pearlite grain boundaries, and so, at longer crack lengths, the cracks aligned with the x-axis are favored, and it is these cracks which, under constant amplitude loading, grow to failure. When subjected to periodic overload histories, cracks initiate and grow along the x-axis, but, once crack lengths reach 1-2mm, they often move onto the maximum tensile plane which is inclined 52° clockwise from x-axis.

Since the early cracking is oriented (or nearly so) along the x- and y- axes, then the stresses applied to the crack are as indicated in Figure 3.20. The cracks aligned with either the x-axis or shear planes are loaded in shear, and y-axis cracks have a combination of both tension and torsion applied to them.

3.2.3 In-Phase Ψ=1 Overload Tests

Akin to section 3.2.2, the phasing of the the tension to torsion strain is maintained rigidly in this ratio at $\psi=\frac{2}{3}$ ($\Psi=1$). Example strain histories are given in Figure 3.21 along with the the fatigue response of normalized SAE 1045 under $\Psi=1$ loading. As shown in the figure the peaks in both histories occur at the same time, and the peak positive strain level in the overload is equal to the peak positive strain in the small

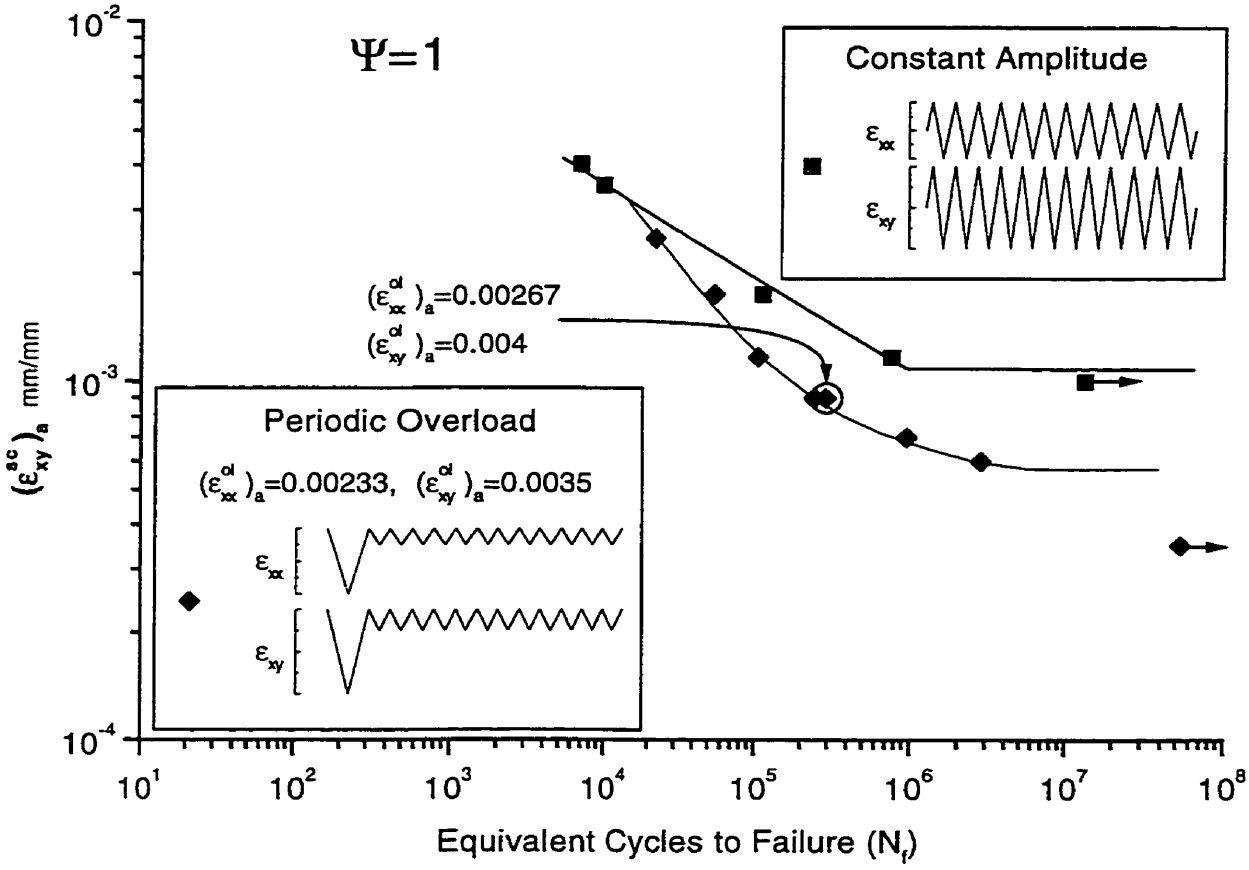

Figure 3.21: Periodic Overload and constant amplitude fatigue responses of normalized SAE 1045 for $\Psi = \frac{\sigma_{xx}}{\sigma_{xy}}$=1 ($\psi = \frac{\epsilon_{xx}}{\epsilon_{xy}} = \frac{2}{3}$). Circled datapoint indicates special overload level $(\epsilon^{ol}_{xy})_a$=0.004, $(\epsilon^{ol}_{xx})_a$=0.00267, $(\epsilon^{ca}_{xy})_a$=0.0009, $(\epsilon^{ca}_{xx})_a$=0.0006 and η=200.

cycles. The only difference between the histories employed in this and the previous section is the value of ψ.

The fatigue response of this material to $\psi=\frac{2}{3}$ loading shows a reduction of the constant amplitude 10^7 endurance limit from $(\epsilon^{ca}_{xy})_a$=0.0011 to a periodic overload endurance limit of $(\epsilon^{ol}_{xy})_a$=0.00057 – a reduction of one-half.

3.2.3.1 Crack Face Interaction in Ψ=1 Overload Tests

A large overload cycle ($(\epsilon_{xx}^{ol})_a$=0.00267, $(\epsilon_{xy}^{ol})_a$=0.004) was used as a check to determine whether the regular overload cycle ($(\epsilon_{xx}^{ol})_a$=0.0023, $(\epsilon_{xy}^{ol})_a$=0.0035) had maximized the damage done by the small cycles. In Figure 3.21 the circled datapoint and adjacent datapoint share, excepting the overload amplitude, the same test conditions – $(\epsilon_{xx}^{sc})_a$=0.0006, $(\epsilon_{xy}^{sc})_a$=0.0009, and η=200. Since there is no significant difference in the equivalent lives of the tests it is assumed that the smaller overload amplitude was sufficient to produce crack face interference free crack growth.

3.2.3.2 Proposed Crack Face Interaction Mechanisms under Ψ=1 Loading

The observations with regard to cracking are almost identical to those presented in section 3.2.2.1 on Ψ=$\frac{1}{2}$ loading. Cracking does occur on maximum shear planes, but it also occurs (as can be seen in Figure 3.22) along the x- and y- axes. Just as discussed in section 3.2.2.1 the longitudinal cracks become dominant as a result of anisotropy. Since this is the case, the crack model which applies is that pictured in Figure 3.20 and described in section 3.2.2.1. The cracking in specimens under both constant amplitude and periodic overload Ψ=1 histories is the same. After a period of growth along the x-axis to 50μm-2mm the crack tends to rotate onto the principal stress plane (which forms an angle of roughly 32° with the y-axis).

3.2.4 In-Phase Ψ=2 Overload Tests

As in tests with stress ratios of $\frac{1}{2}$ and 1 the phasing of tension and torsion strains is maintained at all times. In this case the strain ratio (ψ) is $\frac{4}{3}$. Strain histories are given in Figure 3.23 along with the fatigue curve for normalized SAE1045 steel for Ψ=2 loading.

One result that can be seen from the figure is that the 10^7 endurance limit is reduced one-half (from $(\epsilon_{xy}^{ca})_a$=0.0008 to $(\epsilon_{xy}^{sc})_a$=0.0004) by the overloads.

As a check on the assumption that small cycle damage was maximized by the chosen overload, a test with a high overload level was performed. The standard overload level at this strain ratio is $(\epsilon_{xx}^{ol})_a$=0.003, $(\epsilon_{xy}^{ol})_a$=0.00225. The higher overload

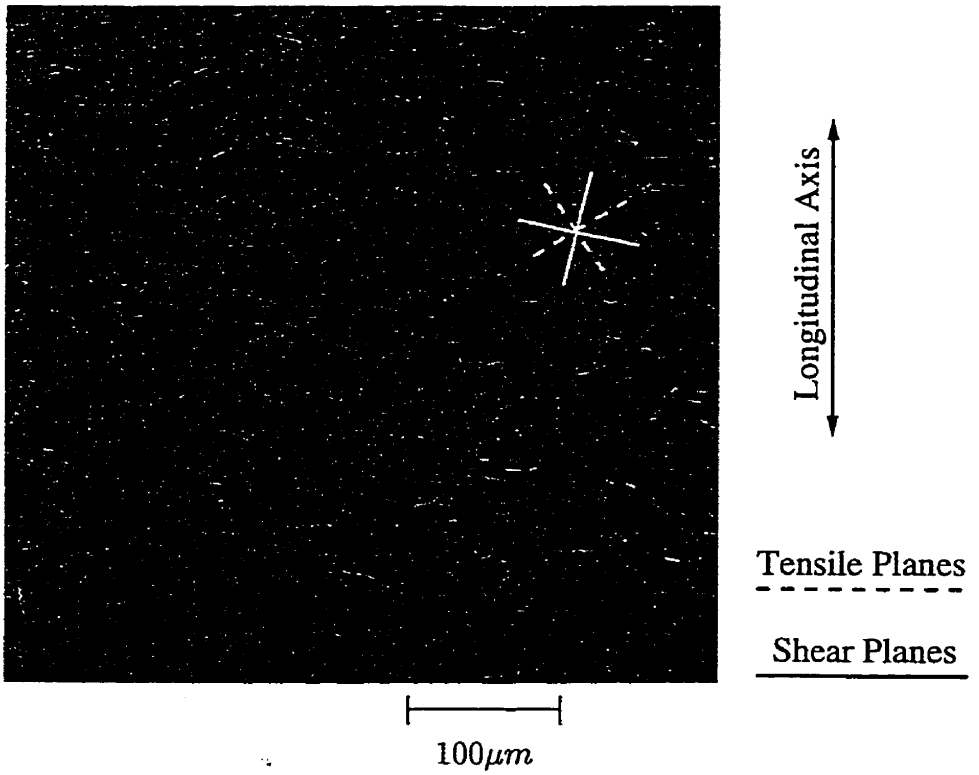

Figure 3.22: Typical small crack growth under ($\Psi = \frac{\sigma_{xx}}{\sigma_{xy}}$=1) loading of normalized SAE1045 steel.

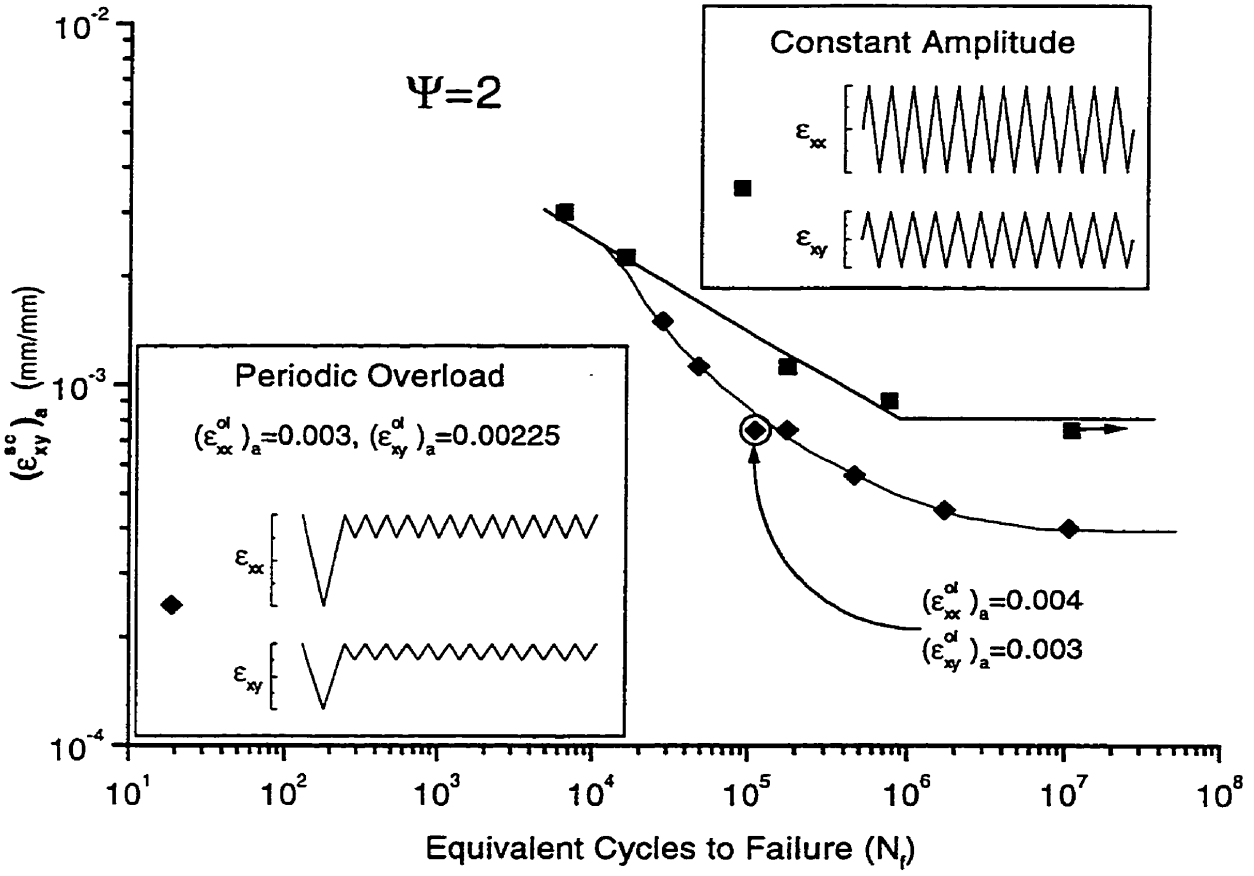

Figure 3.23: Periodic overload and constant amplitude fatigue responses of normalized SAE 1045 for $\Psi = \frac{\sigma_{xx}}{\sigma_{xy}}$=2 ($\psi = \frac{\epsilon_{xx}}{\epsilon_{xy}} = \frac{4}{3}$). Circled datapoint indicates special overload level $(\epsilon_{xy}^{ol})_a$=0.004, $(\epsilon_{xx}^{ol})_a$=0.003 with $(\epsilon_{xy}^{sc})_a$=0.001, $(\epsilon_{xx}^{sc})_a$=0.00075, and η=50.

level selected was $(\epsilon_{xx}^{ol})_a$=0.004, $(\epsilon_{xy}^{ol})_a$=0.003. This higher overload test (circled datapoint in Figure 3.23) was subjected to $(\epsilon_{xx}^{sc})_a$=0.001, $(\epsilon_{xy}^{sc})_a$=0.00075, and η=50 – identical to the point adjacent to it on the fatigue curve. Although there is a small difference in life between it and the adjacent point, the elevated overload amplitude data point does not depart significantly from the curve, and it can be concluded that the standard overload level for these tests was sufficient to maximize the small cycle damage.

3.2.4.1 Proposed Crack Face Interaction Mechanisms under Ψ=2 Loading

Cracking under Ψ=2 loading follows a pattern similar to that for previously discussed load ratios in that cracks form on maximum shear planes, but in this case cracks do not form along the x- and y- axes. Figure 3.24 demonstrates that the cracking occurs on planes close to the maximum shear planes. Once cracks grow to about 50μm in length, crack growth usually shifts onto maximum tensile (σ_{11}) planes.

Figure 3.25 shows examples of these cracks oriented on the σ_{11} and σ_{22} planes. Calculations were made of the relative stresses on each plane, and the stress arrows in the figure are scaled appropriately. During the positive portion of the overload cycle, a crack oriented along σ_{11} plane is favored because it has a larger tensile stress across it when it is open than the crack on a σ_{22} plane, and during the negative portion of the stress cycle it also receives a larger compressive overload. As a result it is anticipated that the crack aligned with the σ_{11} plane will be favored, and crack angle data taken from fracture surfaces support this assertion. Since no lateral motion of the crack faces occurs, it is suggested that the predominant mechanism of crack face interaction is identical to that seen under uniaxial loading. Asperities are crushed during the compressive portion of the loading across the crack and the crack is left open after unloading from the tensile peak.

Note that the asperities shown in Figure 3.26 show that little or no lateral motion (or rubbing) of the fracture surface occurs under this loading – indicating that the cracks are oriented close to the principal stress axis. Also note that asperities appear to be crushed rather than smeared, suggesting that mode I loading is dominant rather than either mode II or III loading.

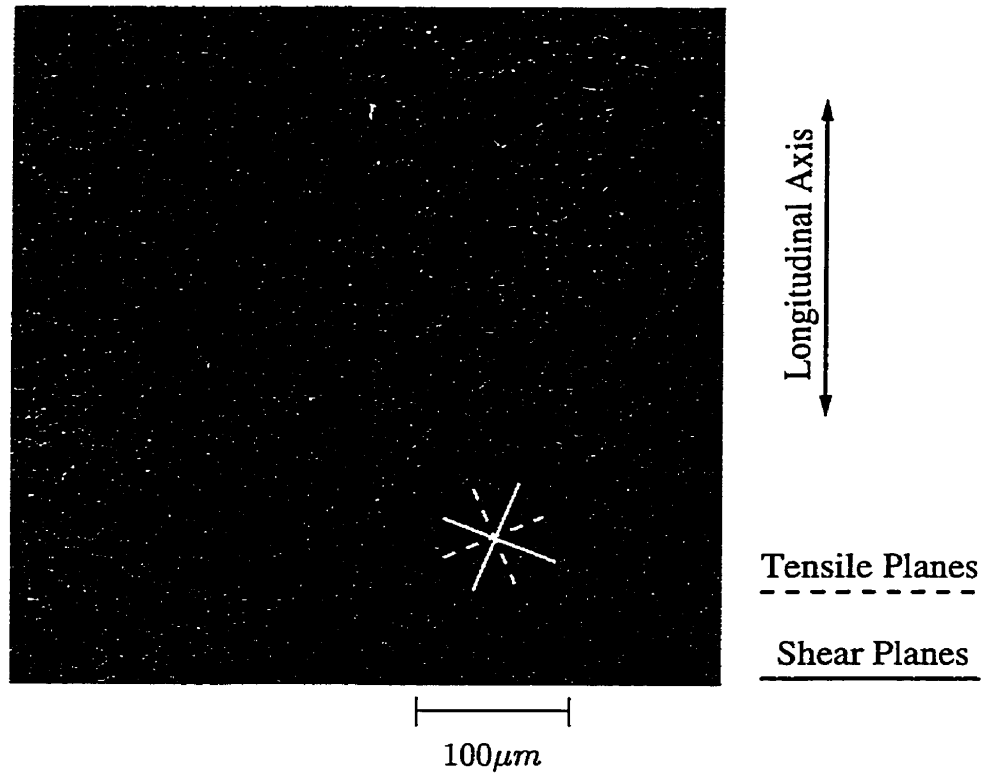

Figure 3.24: Small cracks developed under in-phase Ψ=d loading. Specimen subjected to $(\epsilon_{xx}^{ca})_a$=0.004 and $(\epsilon_{xy}^{ca})_a$=0.003.

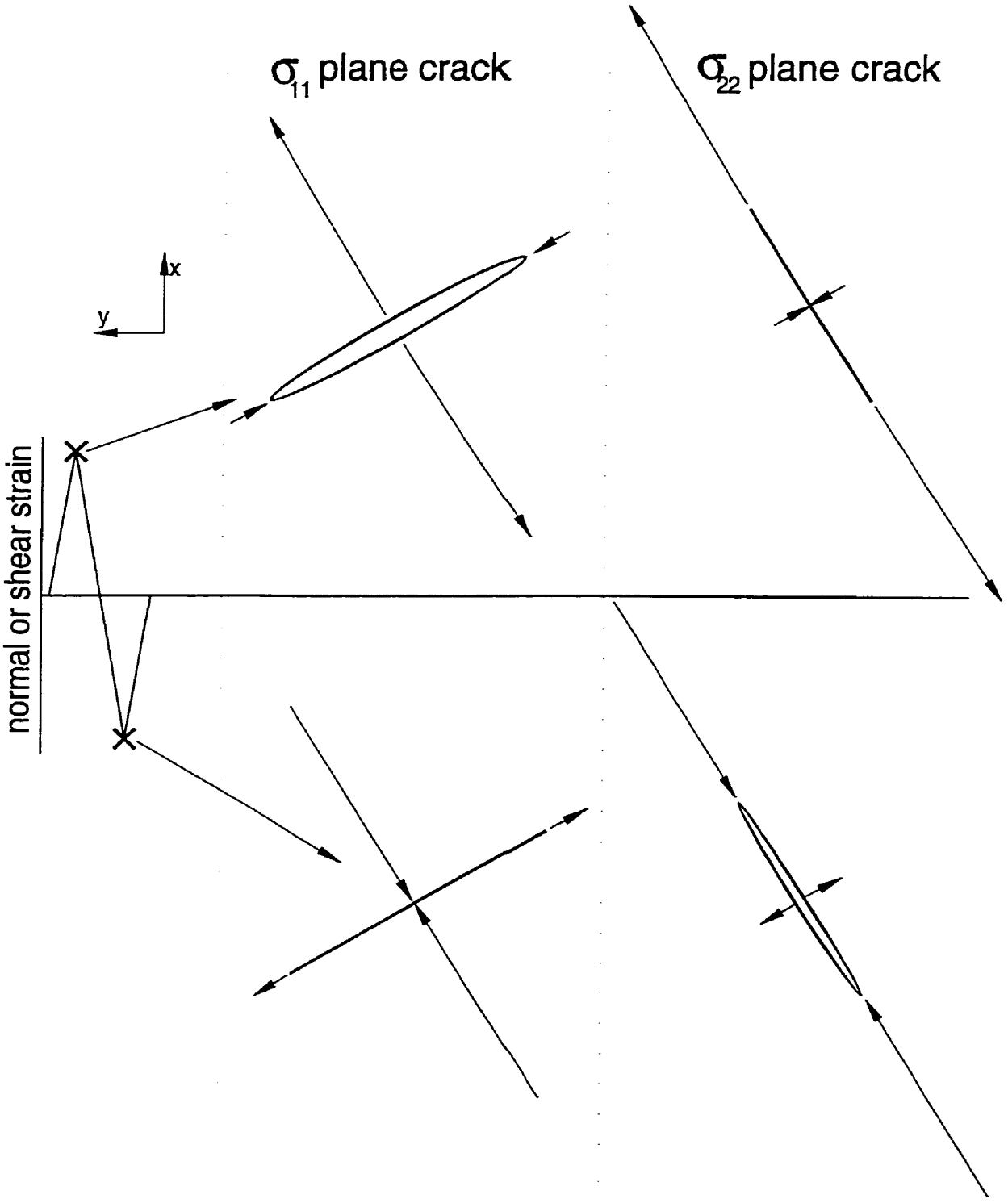

Figure 3.25: Crack behavior under in-phase $\Psi = \frac{\sigma_{xx}}{\sigma_{xy}}$=2 loading.

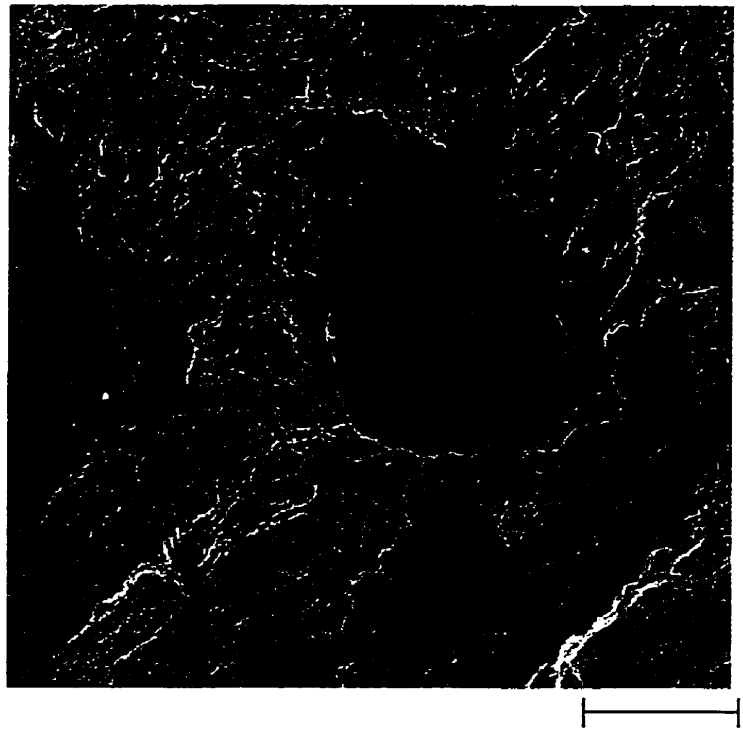

Figure 3.26: Asperities crushed during in-phase $\Psi = \frac{\sigma_{xx}}{\sigma_{xy}}$=2 loading. Specimen subjected to $(\epsilon^{ol}_{xx})_a$=0.003, $(\epsilon^{ol}_{xy})_a$=0.00225, $(\epsilon^{sc}_{xx})_a$=0.0053, $(\epsilon^{sc}_{xy})_a$=0.004, η=5000

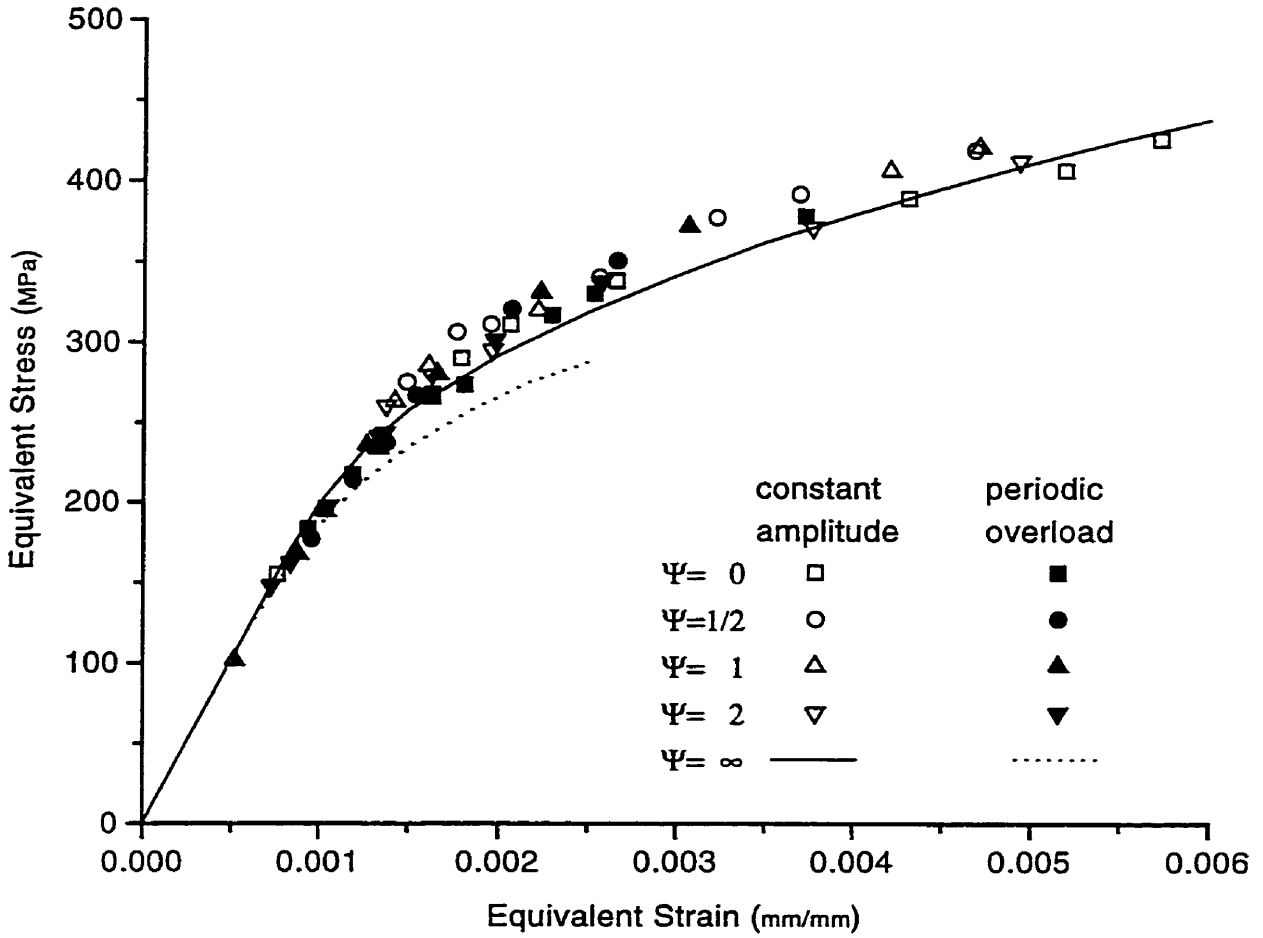

Figure 3.27: Cyclic stress-strain response of normalized SAE1045 steel to biaxial loading. Monotonic constant amplitude and periodic overload trend lines are also plotted

3.2.5 Tension-Torsion Cyclic Stress-Strain Response

The cyclic stress strain response of all of the tension-torsion tests, constant amplitude and periodic overload alike, are presented in Figure 3.27. These points are presented on von Mises effective stress - effective strain ($\bar{\sigma} - \bar{\epsilon}$) coordinates.

Also plotted in this figure are the trend lines for the uniaxial constant amplitude and overload stress-strain data, represented by the solid and dashed curved respectively. The biaxial data, for both overload and constant amplitude tests, falls into

a fairly narrow band. The uniaxial constant amplitude trend tends to fall near the bottom edge of the multiaxial band, and the uniaxial overload trend line lies outside the band. It can be seen that, with the exception of the uniaxial overload data, a single curve can be reasonably drawn for both the overload and constant amplitude tests in any given in-phase stress ratio. By extension, unlike the uniaxial dataset, no real distinction can be made between the biaxial constant amplitude and overload stress-strain data. However, the uniaxial constant amplitude trend line provides an adequate prediction of biaxial stress-strain behavior.

3.3 Bending-Torsion Experiments

The results of the bending-torsion experiments are somewhat more difficult to analyze than those of the axial-torsion experiments because neither the notch strains nor the notch stresses are measured experimentally.

3.3.1 Constant Amplitude Bending and Torsion Tests

A baseline set of torsion-only tests were performed using the SAE bending-torsion fixture and the notched axle shaft. This test series, marked by solid squares, and the load history used are depicted in Figure 3.28. Also, a single fully reversed bending-only test was conducted at a moment level of 2600Nm (notch root strain of approximately 0.6%) had a life of 8500 cycles.

3.3.2 Bending Overload Tests and Equivalent Multiaxial Damage

The aim of the bending overload tests, as in the uniaxial and axial-torsion overload tests, was to obtain, if possible, test conditions in which fatigue cracks grow free of crack face interference. This condition is expected to yield the shortest fatigue lives and represent the greatest possible damage for a given strain range.

Strains due to a fully reversed bending overload cycle of 2600Nm which caused limited notch root plasticity (a notch root strain of approximately 0.6%) are representative of those at notch roots during large cycles in service load histories. This cycle

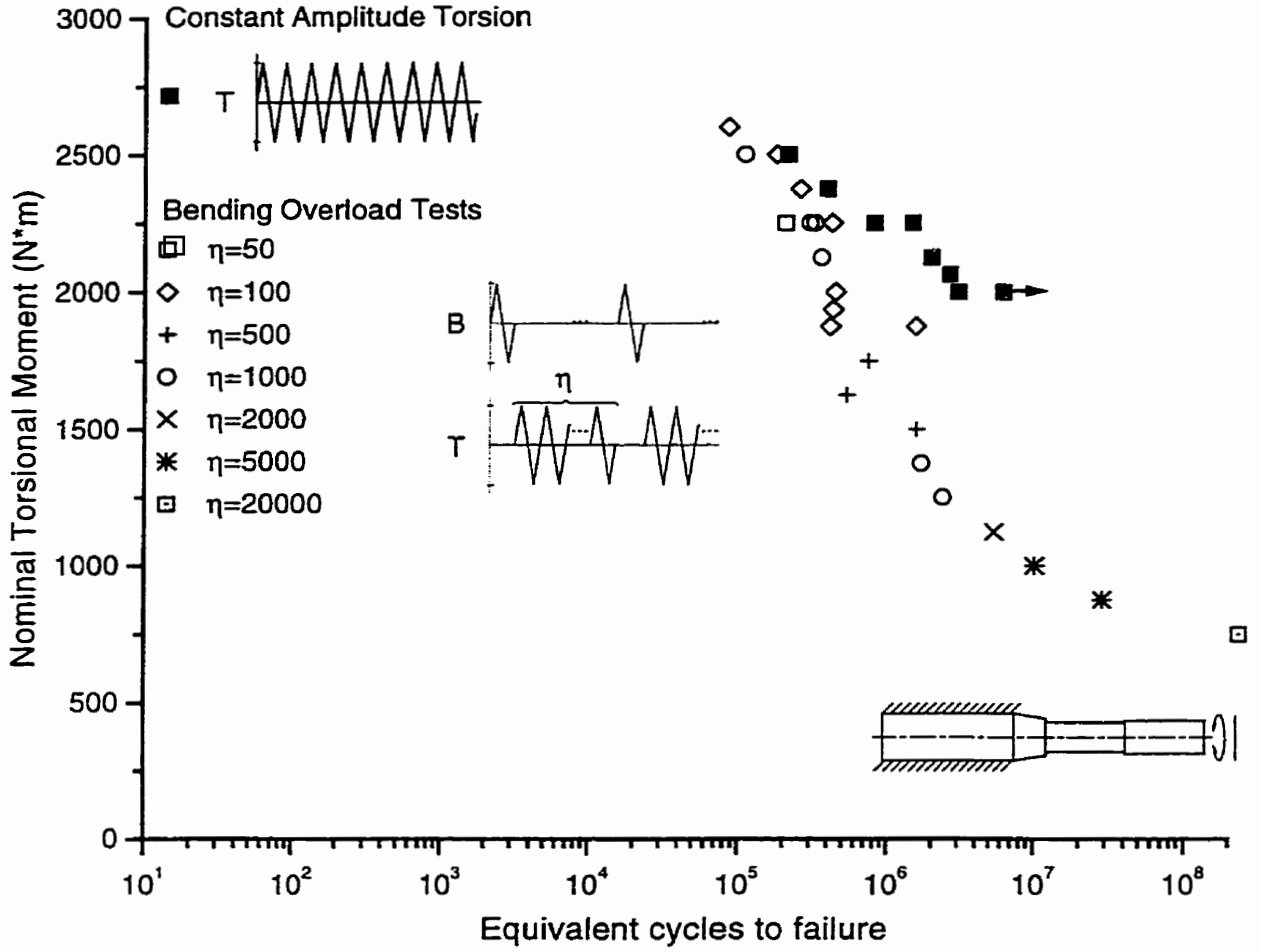

Figure 3.28: Constant amplitude and periodic overload bending-torsion fatigue curves for normalized SAE1045

results in the notch root stresses and strains depicted in Figure 3.29. On one surface a tensile inelastic notch root strain, which stretches open the crack, is followed by a compressive inelastic strain which flattens crack face asperities and leaves a negative residual strain. In the notch there is a tensile residual stress in the material ahead of the crack. On the opposite surface the material is first strained inelastically in compression, flattening the crack face asperities, and then in tension leaving a positive residual strain which separates the faces of the crack, but a compressive residual stress in the material ahead of the crack. In both cases the asperities have been

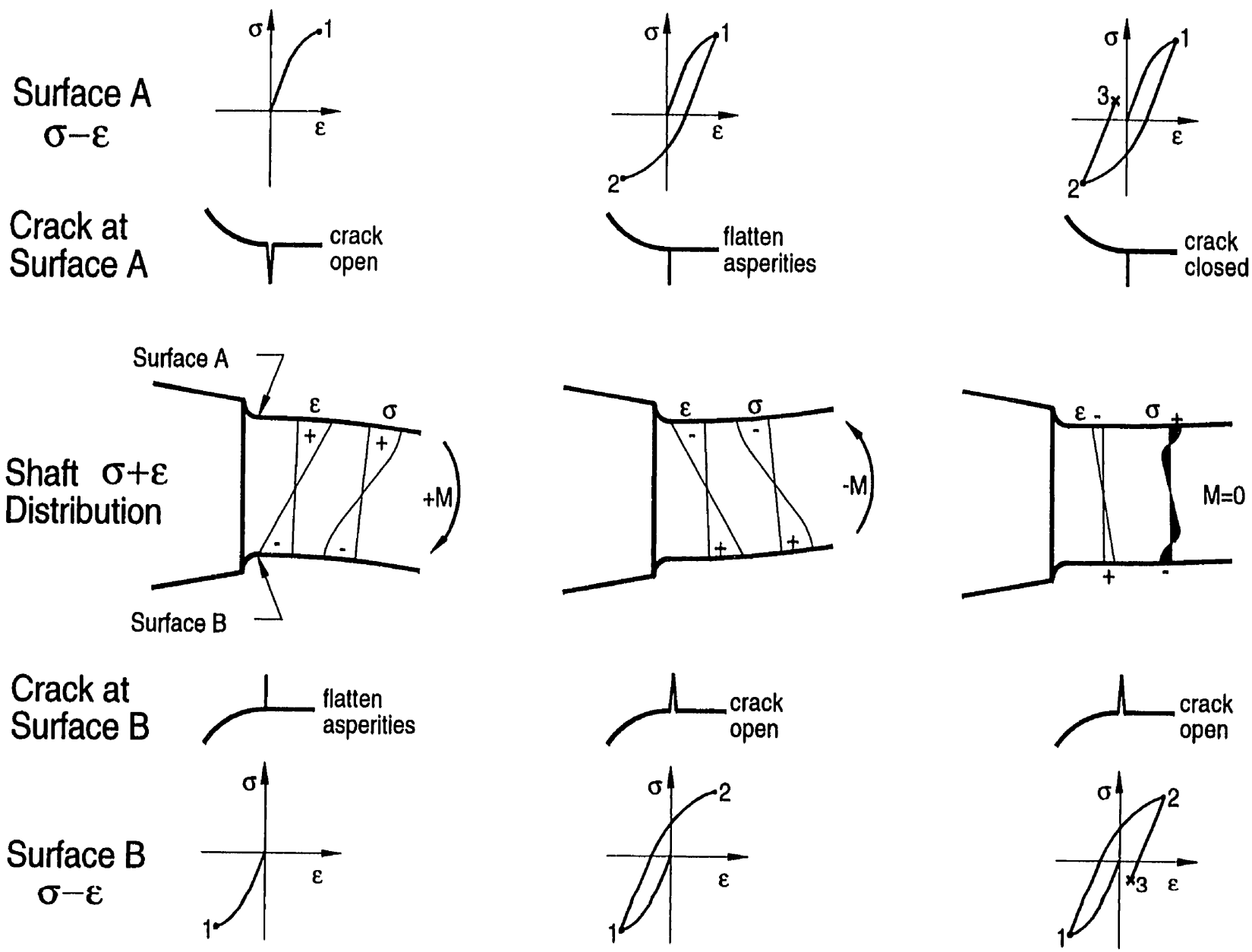

Figure 3.29: Bending overload stress/strain behavior of notched SAE shafts.

flattened during the compressive portion of the cycle so that there will be less crack face interference. The initial interference should be less for surface B in which the residual strain is positive and the crack face separation is greater than for surface A in which the residual strain is negative. However, as the crack propagates, in location A it grows into a tensile residual stress field which will tend to separate the crack faces and reduce crack face interference. On the other hand, in location B the crack will grow into a compressive residual stress field which will force the newly formed crack faces together and increase crack face interference. It is expected that in both locations, because the asperities have been crushed, crack face interference will be reduced and crack growth rates will be increased leading to shorter lives than for constant amplitude torsion tests.

After the bending overload cycle was applied, the bending moment was held constant at zero while η constant amplitude torsional cycles (R_T=-1) were applied. The value of η was varied as in the uniaxial tests so that the damage from the overloads represented no more than 25% of the total damage. The bending overload test data presented in Figure 3.28 were treated in the same fashion as the uniaxial overload datapoints in Figure 3.2 – with the assumption that the per cycle damage contribution of a bending (mode I) overload in a torsion test was the same as in the constant amplitude bending test at the overload moment level.

At the 10^7 cycle fatigue limit this reduction is one-half and is estimated to be one-third at 2×10^8 cycles. In the overload tests cracking occurred at both surfaces A and B (described above) at all stress levels above 1500Nm. However, the cracks always started first at surface A, and the cracks in this location propagated faster throughout the entire fatigue life. This observation can be explained by the residual stress-strain state in the notch following an overload. Using strain rosette histories taken from shaft notches, the notch residual stress-strain state was predicted using a multiaxial plasticity model [43]. An average initial residual longitudinal tensile stress of 340MPa was found – this is close to the 0.2% offset cyclic yield stress of 379MPa for this material.

A multiaxial Neuber model [74, 75] coupled with a multiaxial plasticity model [76, 77, 43] was used to estimate the notch strains, and through these simulations it

was determined that the 1500Nm torsional moment level marked the onset of cyclic torsional plasticity in the notch. Cyclic plasticity has a tendency to relax residual stresses; and the greater the degree of cyclic plasticity, the greater the degree of relaxation. The experimental notch strain data support this analysis – those tests with strain gage readings below 1500Nm do not exhibit any change in the bending strain level following the overload while a test above 1500Nm shows a slow continuous reduction in the mean bending strain following the overload. It is apparent that below 1500Nm torque no reduction in residual bending stresses was found, and, as a result, no cracking of surface B took place. Undoubtedly, the sustained residual bending stresses at torsional levels below 1500Nm helped reduce crack face interaction on surface A and aided crack growth. However, above 1500Nm torque, the residual bending stresses at surface B are sufficiently reduced by torsional plasticity to allow torsional cracking of surface B to proceed, and this must also have the effect of increasing crack face interaction somewhat on surface A.

3.3.3 Cyclic Torsion Tests with a Static Bending Moment

A series of constant amplitude torsion tests was run in which a constant static bending moment was applied to the shaft. The magnitude of the static bending moment was chosen to give a slow, controlled ratcheting of the shaft in bending. The static bending moment had to be continuously increased as the torsional moment level was decreased. The reason for inducing this ratcheting was that, at lower bending moment levels, the tensile stress at the notch root induced by the bending moment was relaxed by the cyclic torsion. It is this tensile stress that holds the crack open and prevents crack face interference. However, during ratcheting this relaxation is offset by the increase in stress due to the slowly increasing notch root strain. Below a 1500Nm torsional moment level the actuators lacked sufficient force capacity to cause sustained ratcheting, and, as a result, no failures were obtained because the tensile stress in the notch was insufficient to keep the crack open.

Because the bending moment was static and therefore did not add to specimen cumulative damage the raw test lives were used. The results of these experiments

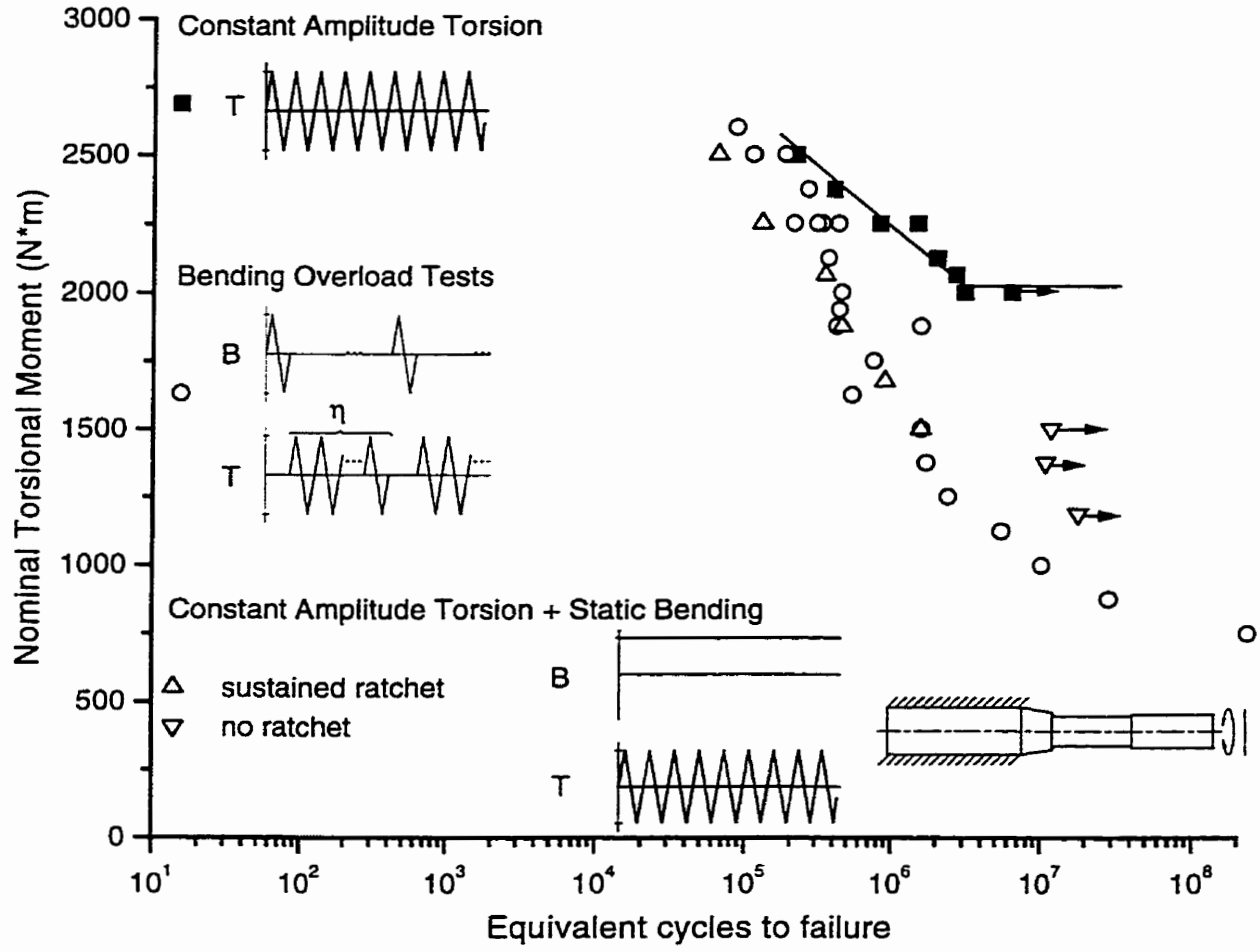

Figure 3.30: Constant amplitude, bending overload, and static bending bending-torsion fatigue curves for normalized SAE1045.

are given in Figure 3.30 with the tests with sustained ratcheting as open triangles, and the tests in which sustained ratcheting could not be obtained marked as open inverted triangles. In the regime in which sustained ratcheting was obtained the static bending results lie close to those for bending overloads. At the highest stress levels they even appear to be slightly more severe than the overload tests. At levels below a torsional moment of 1500Nm no failures occurred – all tests were stopped as runouts at 10^7 cycles.

In tests in which ratcheting occurred, the crack faces are pulled apart thus lowering

crack face interaction. In Figure 3.30 tests in which bending overloads were applied yield similar lives to those in which a static bending moment was imposed. This similarity suggests that the overloads and static bending loads both reduce crack face interference to the same extent. Crack surface evidence also supports this assertion. Surface A, which has a static tensile stress resulting from a static bending moment showed the only visible cracking. Cracks were not detectable in surface B which was subjected to static compressive stresses. This behavior is expected since, under compressive loading, the crack faces are pushed together and, presumably, crack face interference is increased.

In static bending tests below 1500Nm, the test equipment had insufficient force capacity to keep the crack open, and the tests below this level all ran out to 10^7 cycles. Above 2250Nm only small bending moments were necessary to maintain slow sustained ratcheting. If the test equipment had larger force capacities, it is believed that the static bending curve would continue to match the overload curve below 1500Nm.

3.3.4 Bending Peak Hold Periodic Overload Tests

These tests, which share characteristics of both the overload and the static bending tests, are also similar to those reported for tension-torsion tests in section 3.2.1.2. In these tests the peak bending moment was held constant at 2600Nm while the torsional cycles were applied, and then, once the torsional cycles had been applied the torsional moment was held at 0 while the bending moment was moved from 2600Nm down to -2600Nm and back. The histories applied during these experiments are depicted in Figure 3.31 along with the fatigue results. In these tests, as in the static bending moment tests, the specimen exhibited bending ratcheting during torsional cycling. However, the ratcheting strain was for the most part recovered during the bending overload cycle. This meant that, for the portion of the history during which the bending moment is held constant and while the torsional moment is cycled, it was unnecessary to reduce the positive bending moment level.

At intermediate to lower torsional moment levels, the peak hold test results coincide with those of the bending overload tests. At higher torsional moment levels

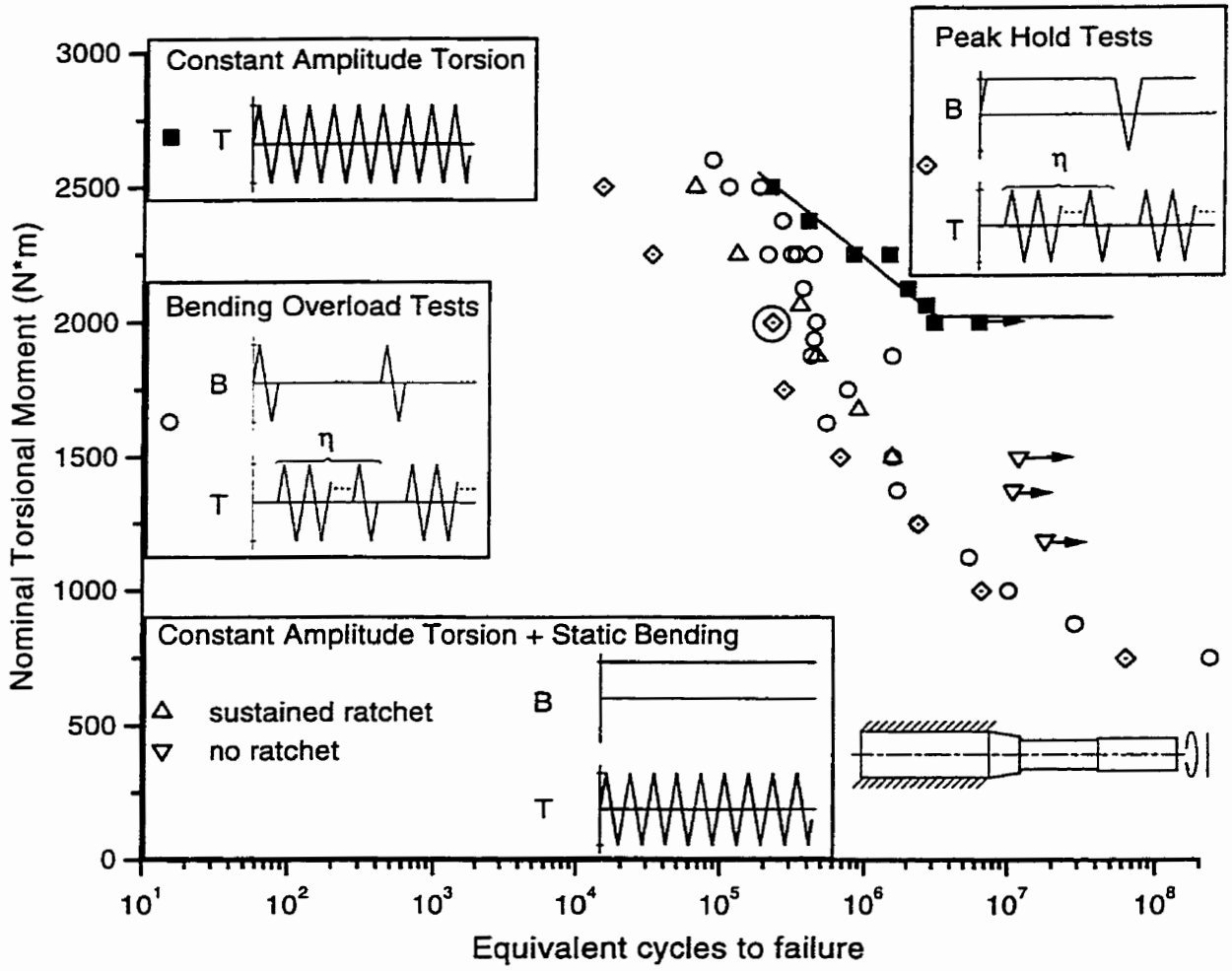

Figure 3.31: Constant amplitude, bending overload, and static bending bending-torsion fatigue curves for normalized SAE1045. Circled datapoint is one in which the value of η was too large.

the peak hold tests have lives which are clearly shorter than either overload, static bending, or constant amplitude tests. This reduction in fatigue life at high torsional moment levels is similar to that found in section 3.2.1.2.

The circled datapoint in the figure indicates a test (T_m=2000Nm, η=5000) in which insufficient overloads were applied to keep the crack growing at the higher rate. In this case η should have been 100 in order to maintain the overload damage contribution at 25%, and at η=5000 the overload damage contribution was far too

low (0.5%) to maintain crack interference free crack growth. Hence the datapoint has a longer life than the trend of the peak hold tests would indicate. It is presumed that crack face interference was eliminated immediately following the overload but returned during the prolonged torsional cycling and thus led to a longer life.

The same mechanisms which are operative in the bending overload and static bending moment tests are believed to be operative in reducing crack face interaction in these tests. In this case the negative portion of the bending moment cycle results in a large compressive stress in the surface A of the shaft and this, in turn, results in crushed asperities. Further, the positive portion of the bending moment cycle (held during the torsional cycles) pulls the crack faces apart thereby reducing crack face interaction. This is further borne out when specimen cracking is considered.

Surface A, as in the overload and static bending tests, always contained the crack which grew to failure. No visible cracks were detected in Surface B in any of the test specimens. This indicates that, while the static bending component of the history presumably reduces crack face interference and thereby accelerates crack growth on Surface A, it increases crack face interference and retards the growth of cracks on surface B.

3.3.5 Combined Bending-Torsion and Tension-Torsion Results

As mentioned in section 3.3.2 a multiaxial Neuber model [74, 75] and a multiaxial plasticity model [76, 77, 43] were used to estimate shear strain amplitudes in the notch for all of the bending-torsion tests mentioned so far. The notch strain estimates are combined with the tension-torsion results for Ψ=0 in Figure 3.32, and the data falls into a single band. At strains below $(\epsilon_{xy}^{ca})_a$=0.001 where elastic behavior dominates and the Neuber correction to the bending-torsion data is small all curves fall into a narrow band. Above this level the bending-torsion data tends to fall above the tension-torsion data. There may be two reasons for this. The first is that the Neuber conversion is known to overestimate the strains, and the second is that the shaft data above $(\epsilon_{xy}^{ca})_a$=0.001 may not be fully crack face interference free – causing the data to shift to higher strains and longer lives, respectively. Of particular interest is the peak-hold data which, in both shafts and tubes, falls at shorter lives and forms a unique band itself at high strains. The static bending data closely follows the overload data.

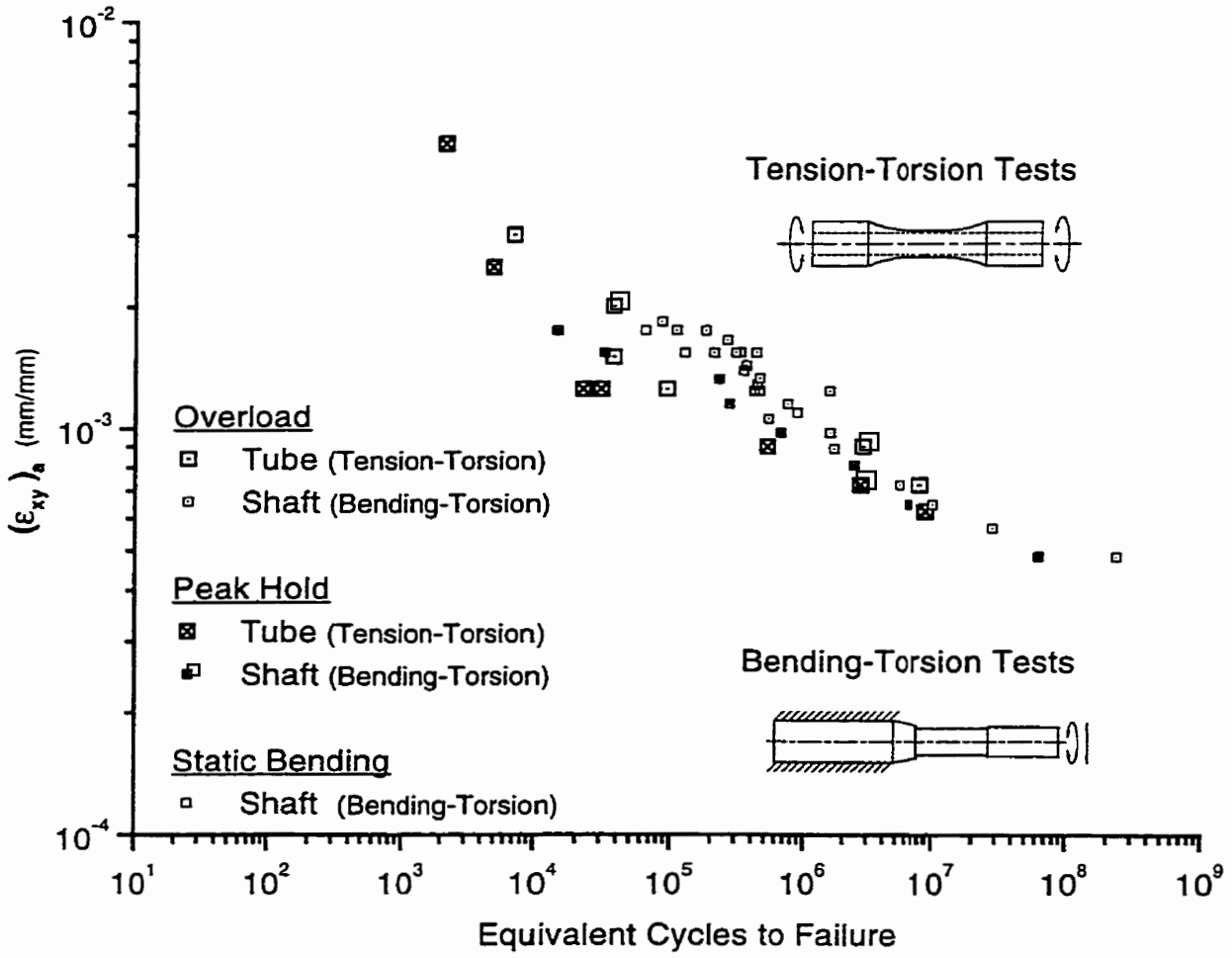

Figure 3.32: Combined bending-torsion and tension-torsion data.

3.4 Unification of Fatigue Life Results

The purpose of this section is to determine the degree to which various multiaxial damage parameters unify the various test results.

3.4.1 Constant Amplitude Tests

Because the cracking found in the constant amplitude tube tests was dominated by the cracks aligned with the x-axis and, presumably, these cracks are not greatly influenced by tension loading then it follows that the life of these tests would be

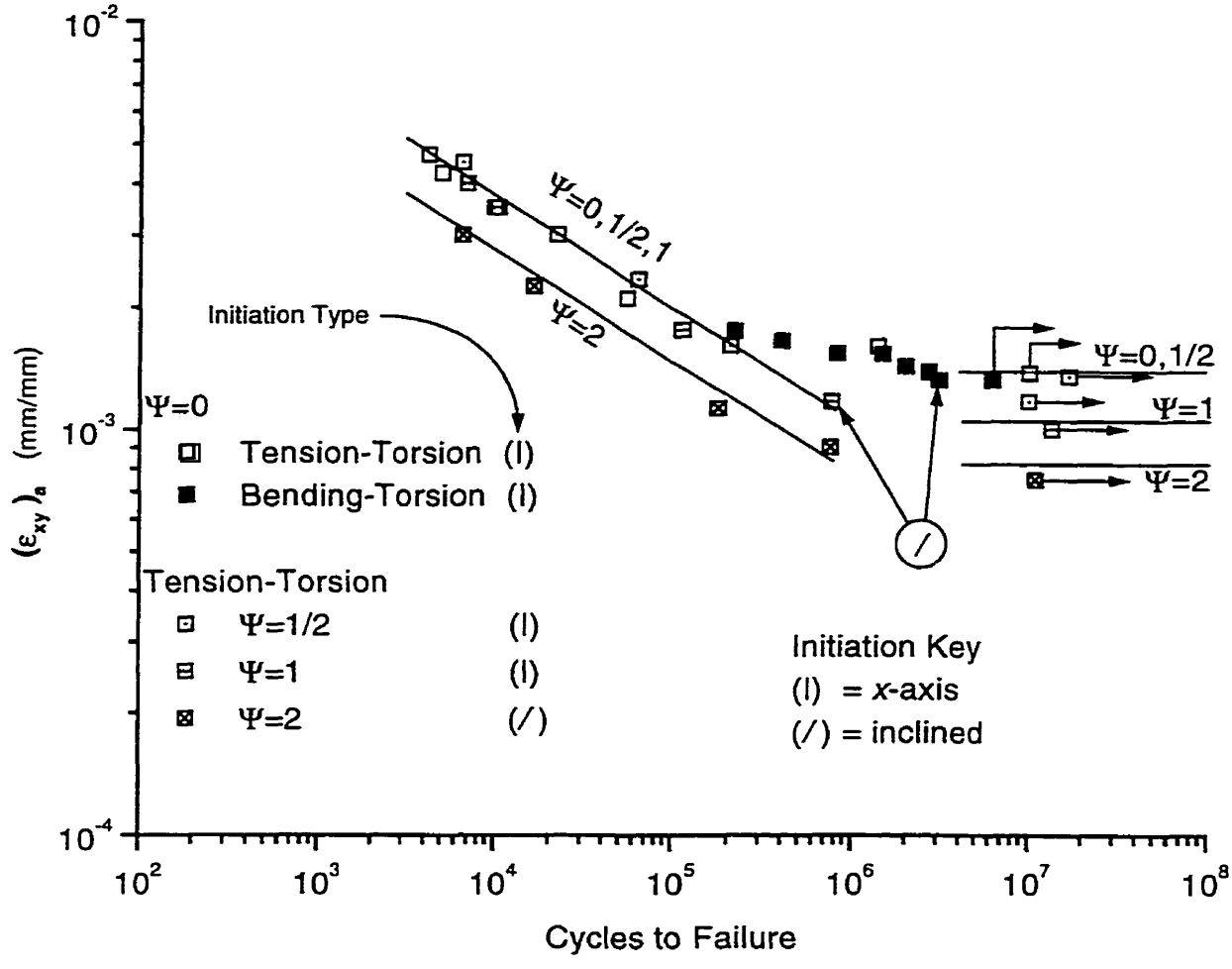

Figure 3.33: Constant amplitude curves for tension-torsion and bending-torsion tests plotted on the basis of applied shear strain amplitude ($(\epsilon_{xy}^{ca})_a$).

controlled by the applied shear strain, $(\epsilon_{xy}^{ca})_a$. However, in order to use the shaft data it had to be first converted from nominal elastic stress to local stress-strain as discussed in the previous section. Figure 3.33 shows all of the constant amplitude data from tube and shaft tests plotted against the applied shear strain (ϵ_{xy}). The figure clearly demonstrates that, in all regions except those points at the endurance limit, applied shear strain as a fatigue parameter reduces data for Ψ=0, $\frac{1}{2}$, and 1 into a single characteristic curve. The data for Ψ=2 falls on a separate but parallel line

below that of the other data.

At the fatigue limit the Ψ=0 and Ψ=$\frac{1}{2}$ data, including both tension-torsion and bending-torsion data fall into a single narrow band. The bending-torsion data fall in the gap between the runout and regular fatigue data, and, while Ψ=1 data initially follows the trend of the other data, it then departs from the trend at the Ψ=0 endurance and proceeds along an extension of the trend curve to a lower level.

Also shown in the figure is the initiation angle observed for each stress ratio. The individual tests which differed from the rest in the stress ratio are also noted on the figure. The reason behind the commonality in response to applied shear strain of load ratios Ψ=0, $\frac{1}{2}$, and 1 is the fact that, as discussed in section 3.2, crack initiation and early growth for these ratios takes place on planes aligned with the x- and y- axes, and those cracks on the x-axis are favored and become dominant. Even though, for Ψ=1/2 and 1, there is an applied axial load which would reduce crack face interference for cracks on the y-axis, the x-axis aligned cracks, which are not influenced by axial loading, grew to failure. It is suggested that the material anisotropy mentioned earlier is responsible for this effect.

A single failure at Ψ=1 lies below the Ψ=0/$\frac{1}{2}$ endurance limit, and this failure did not initiate on the x-axis; its initiation was inclined relative to y-axis. Although more data is necessary in this region, it is presumed that this change in initiation type is responsible for the endurance limit shift in the Ψ=1 data.

The Ψ=2 data lies below all of the rest of the data in this figure, and this is presumably because the initiation plane is no longer aligned with either the x- or y- axes but now lies aligned with the maximum shear planes – oriented about 20° clockwise from these axes. The influence of the strains applied on the tension axis was minimal, as was seen in Figure 3.33, since there was essentially no difference in the fatigue response between Ψ=0, 1/2 and 1 loading – for the same applied torsional strain the life is the same regardless of load ratio. This behavior is corroborated by the initiation observations. Under Ψ=2 loading the influence of tension loading is seen in the fatigue response of the material – for the same applied torsional strain amplitude the Ψ=2 life is shorter than the other stress ratios. The difference between

Ψ=2 and the other load ratios exists because, in this material, tension loading now contributes significantly to crack initiation and growth.

Since the bulk of the life in Ψ=2 and uniaxial (∞) loading is spent initiating and growing a crack along planes of maximum shear these data are plotted in Figure 3.34 against the maximum shear amplitude, $(\epsilon_{12})_a$, while the rest of the data is plotted against the applied torsional shear strain amplitude (resolved shear strain on along the x-axis), $(\epsilon_{xy})_a$. This graph demonstrates that, once the initiation plane is considered, the fatigue response of the material subjected to various stress ratios is quite similar.

Figure 3.35 presents all of the data of Figure 3.34 in terms of maximum shear amplitude, $(\epsilon_{12})_a$. The adjustment for Ψ=2 and ∞ is relatively minor – increases of 3% and 10% respectively. As can be seen, the differences between Figures 3.34 and 3.35 are not great, and the latter figure is easier to employ for the purposes of life assessment.

3.4.2 Unification of Overload Data

3.4.2.1 Evaluation of Damage Criteria

The mean stress corrections found in most damage criteria are corrections for the presence of closure/crack face interference. In the case of uniaxial loading the value of a mean stress corrected parameter typically increases with increasing tensile mean stress. If the value of the parameter is larger this implies that the life is shorter and hence the fatigue crack must be propagating faster. When an increasing tensile mean stress is applied to a growing crack, the actual stress range which reaches the crack tip increases because the crack opening stress increases less rapidly than the maximum stress. In other words $S_{max} - S_{op}$ increases because S_{max} increases more than S_{op}. The increased effective stress range causes the crack to grow faster. The converse is true for lowering the mean stress – the crack growth rate reduces as the closure stress decreases more slowly than the maximum stress.

If crack face interference has been eliminated from these tests then no mean stress correction is necessary, and the fatigue life of a specimen is governed by the amplitude

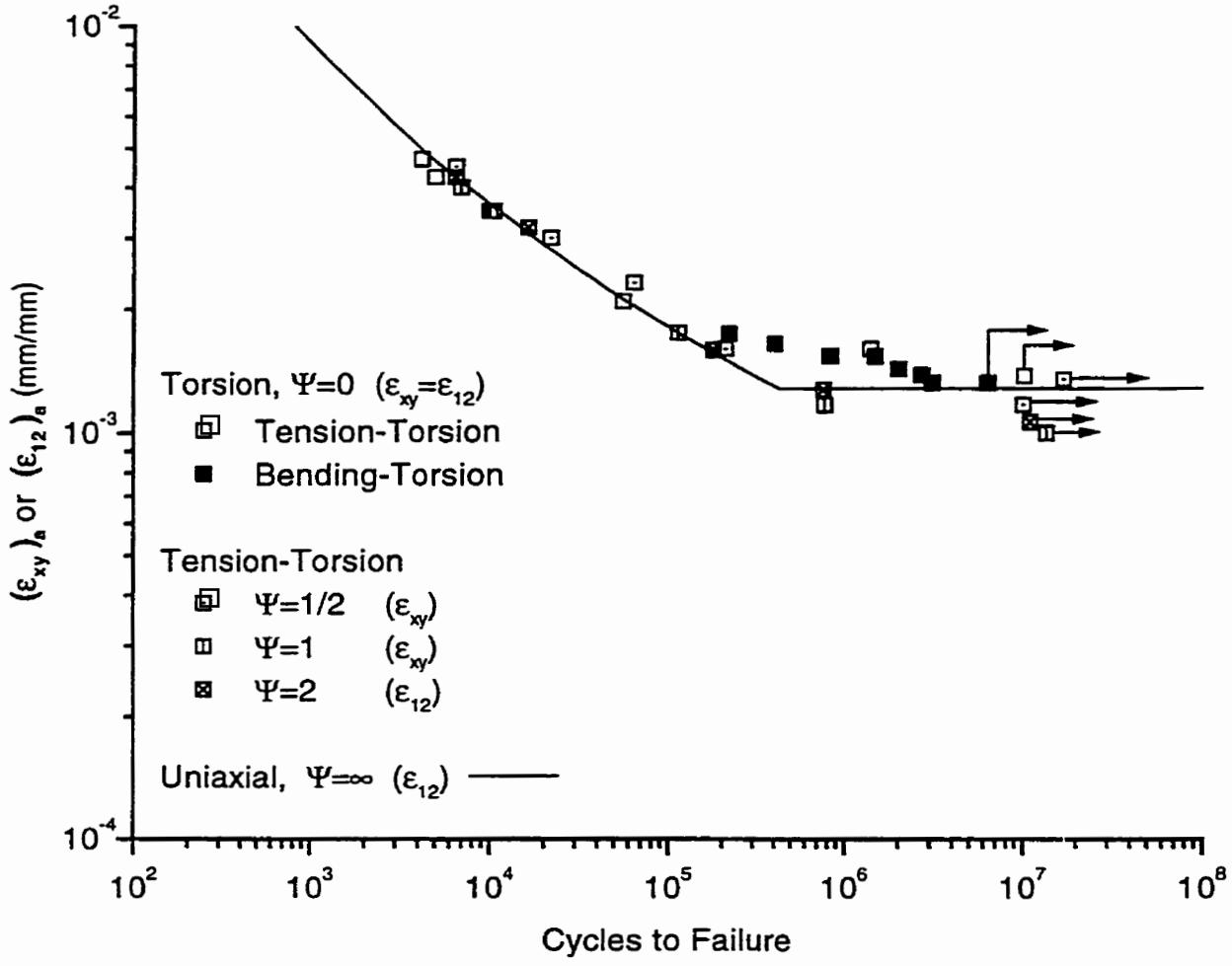

Figure 3.34: Constant amplitude tension-torsion and bending torsion tests considered on the basis of initiation plane.

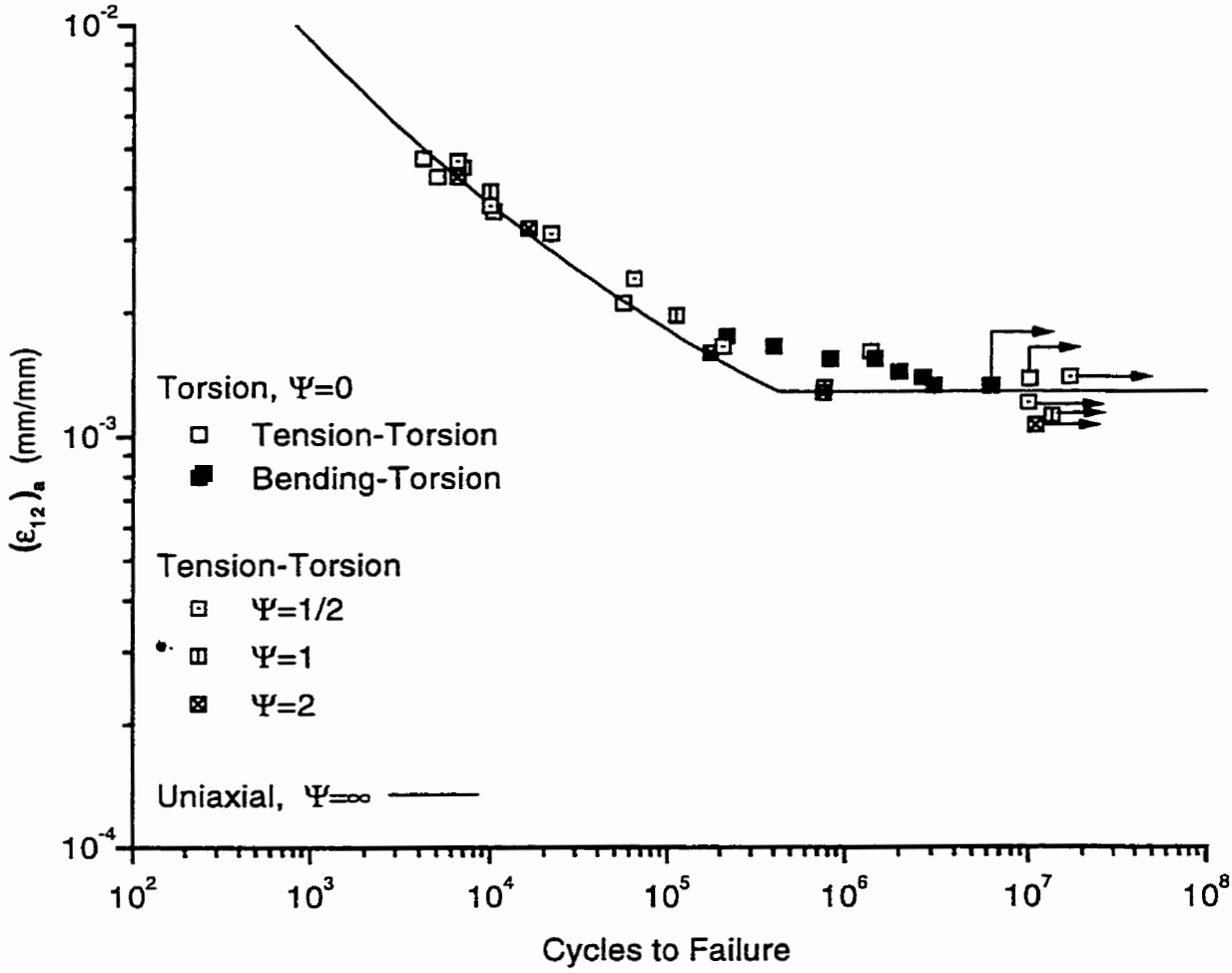

Figure 3.35: Maximum shear (ϵ_{12}) plot of constant amplitude tension-torsion and bending-torsion tests.

of deformation. Hence, for all of the damage criteria small cycle amplitudes are used in evaluating the data.

The formulae used to generate the graphs in the following sections may be found in section 2.4.7.

Uniaxial parameters – normal stress/strain The parameter life curve for the normal stress amplitude (equation 2.60) and the normal strain amplitude (equation 2.58), are presented in Figures 3.36 and 3.37, respectively. In each of the figures

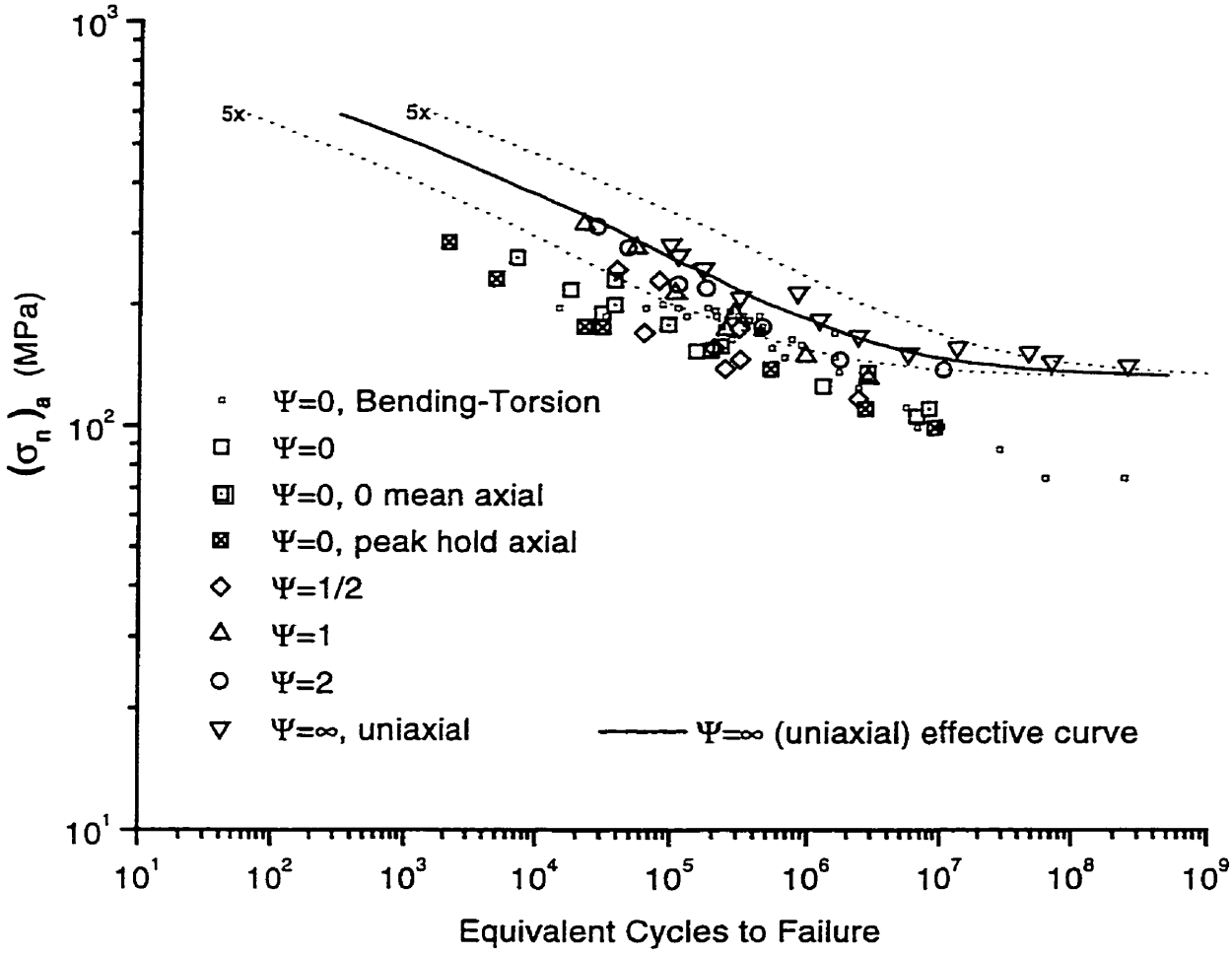

Figure 3.36: Normal stress, $\frac{\Delta\sigma_n}{2}$, plots for tension-torsion and bending-torsion overload tests.

presented in this section a uniaxial trend line, which is derived from the effective strain-life curve (presented in section 3.1.2), are provided along with bands indicating a factor of two and a factor of five in life on each side of the uniaxial effective trend line. The uniaxial data are used as a baseline for comparison for the rest of the multiaxial data.

Of all of the parameters presented here normal stress ($P_\sigma = \Delta\sigma_n$) does the poorest job of condensing the test data. Half of the multiaxial data does not fall within the 5x bands, and the condensation is especially poor at the fatigue limit. At the fatigue

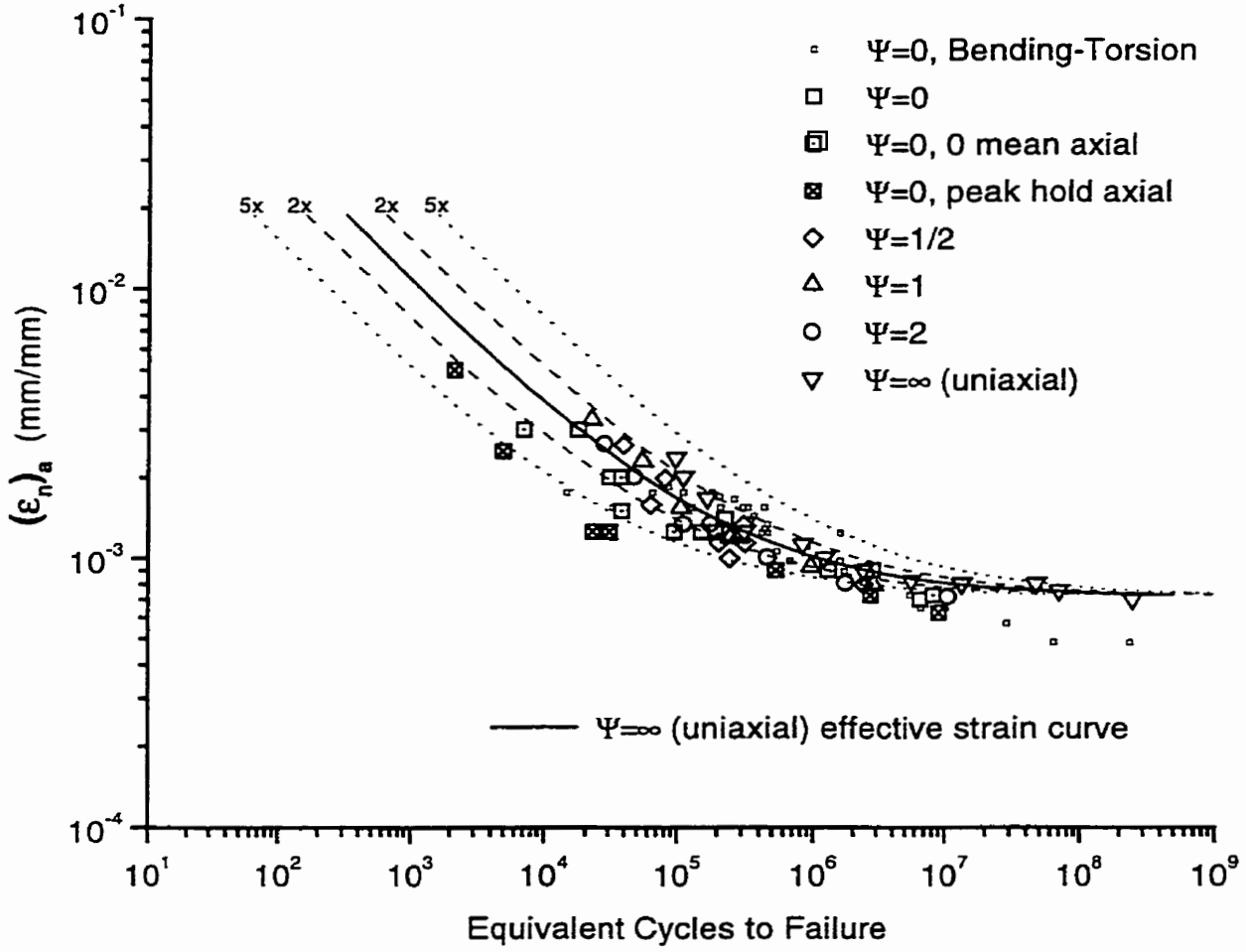

Figure 3.37: Normal strain, $\frac{\Delta\epsilon_n}{2}$, plots for tension-torsion and bending-torsion overload tests.

limit the uniaxial and bending-torsion data have over factor of two vertical separation.

The normal strain parameter ($P_\epsilon = \Delta\epsilon_n$) does a reasonable job with all of the data. Most of the multiaxial data falls well within the factor of 5 bands, and the vertical spread in the data at the fatigue limit is less than a factor of two.

Shear-strain based parameters Parameters included in this group are maximum shear strain amplitude (presented in section 3.4.2.2), Brown and Miller's parameter [38], and the Fatemi-Socie-Kurath parameter [30, 42].

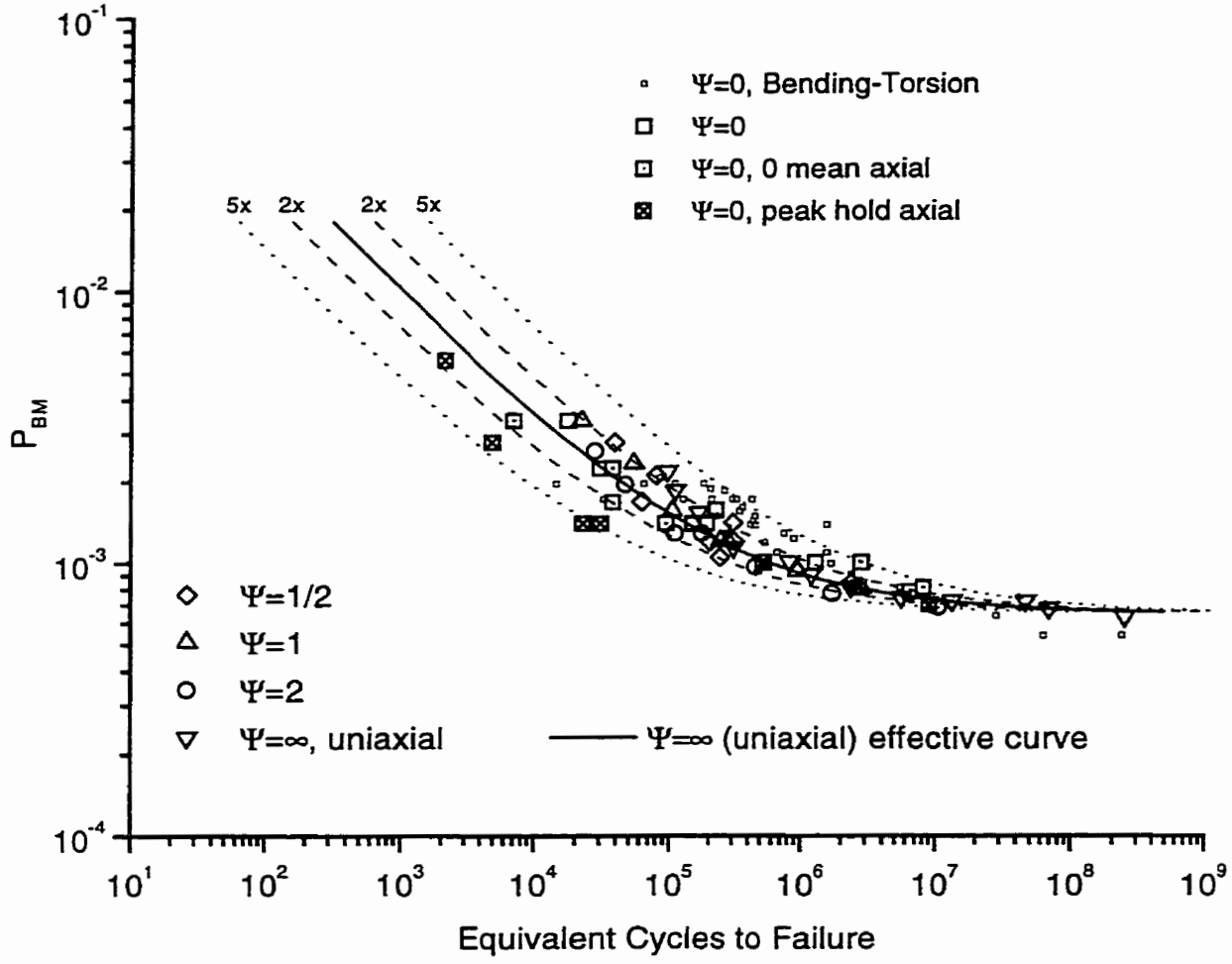

Figure 3.38: Brown and Miller [38] parameter-life plot for tension-torsion and bending-torsion overload tests.

Brown and Miller's parameter (equation 2.62), when applied to the experimental data, results in the plot in Figure 3.38. This parameter provides a good condensation of the overload data. Almost all of the tension-torsion and uniaxial data points fall within the 2x bands, and the 5x bands contain all of the rest of the tension-torsion data and most of the bending-torsion data. At the fatigue limit the vertical spread in the data is much better than that in previous parameters, roughly ±20%.

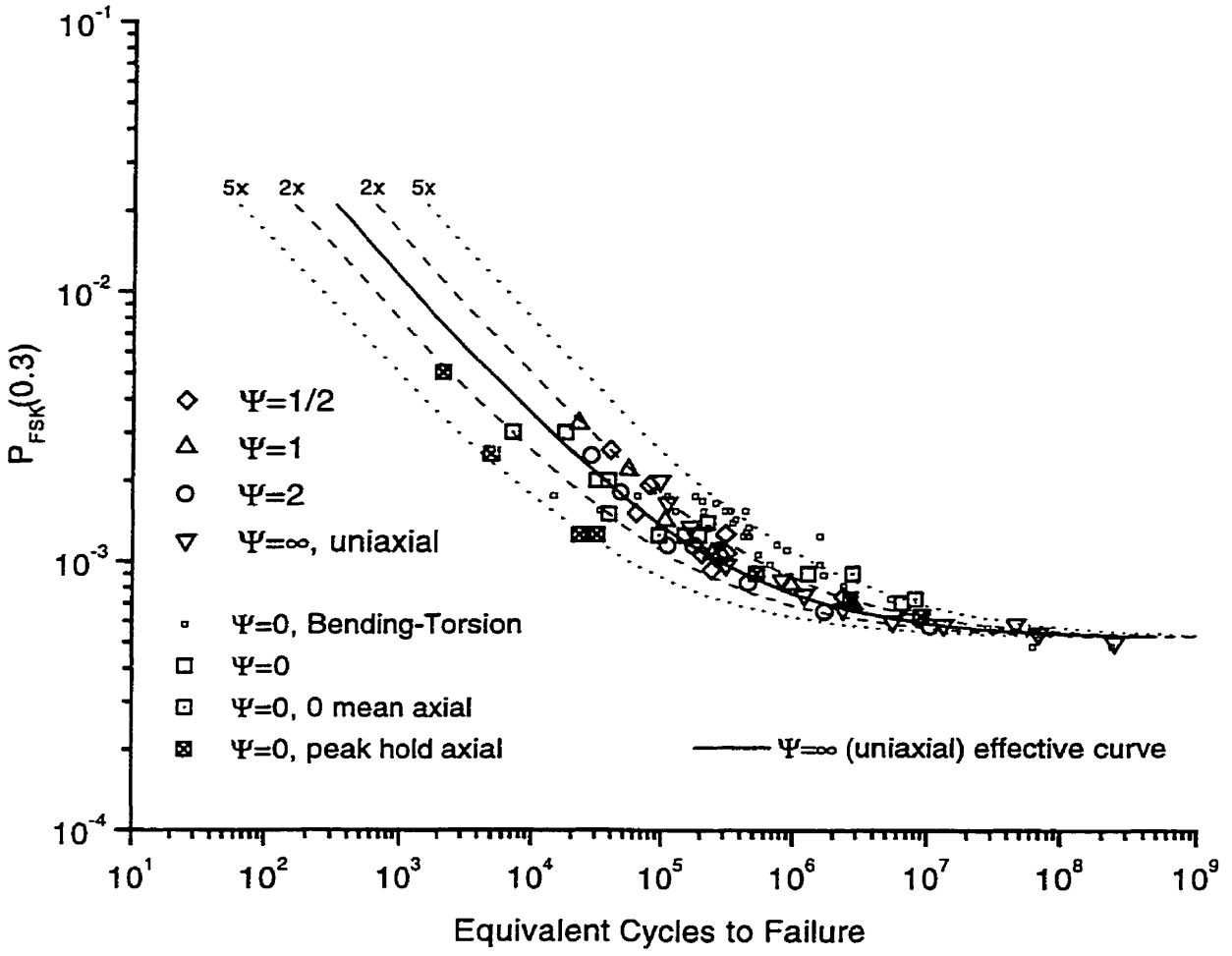

Figure 3.39: Fatemi-Socie-Kurath [30, 42] parameter-life plot for tension-torsion and bending-torsion overload tests.

The parameter-life plot for the Fatemi-Socie-Kurath parameter (equation 2.64), where K_F is taken to be 0.3, is presented in Figure 3.39. Under this parameter the data fall in much the same fashion as in Brown and Miller's parameter, except that this parameter was better at unifying the endurance limit data, the vertical spread for this parameter was about ±5%.

Energy based parameters The parameters which fall under this label are the Smith-Watson-Topper parameter [37] and Chu's parameter [43].

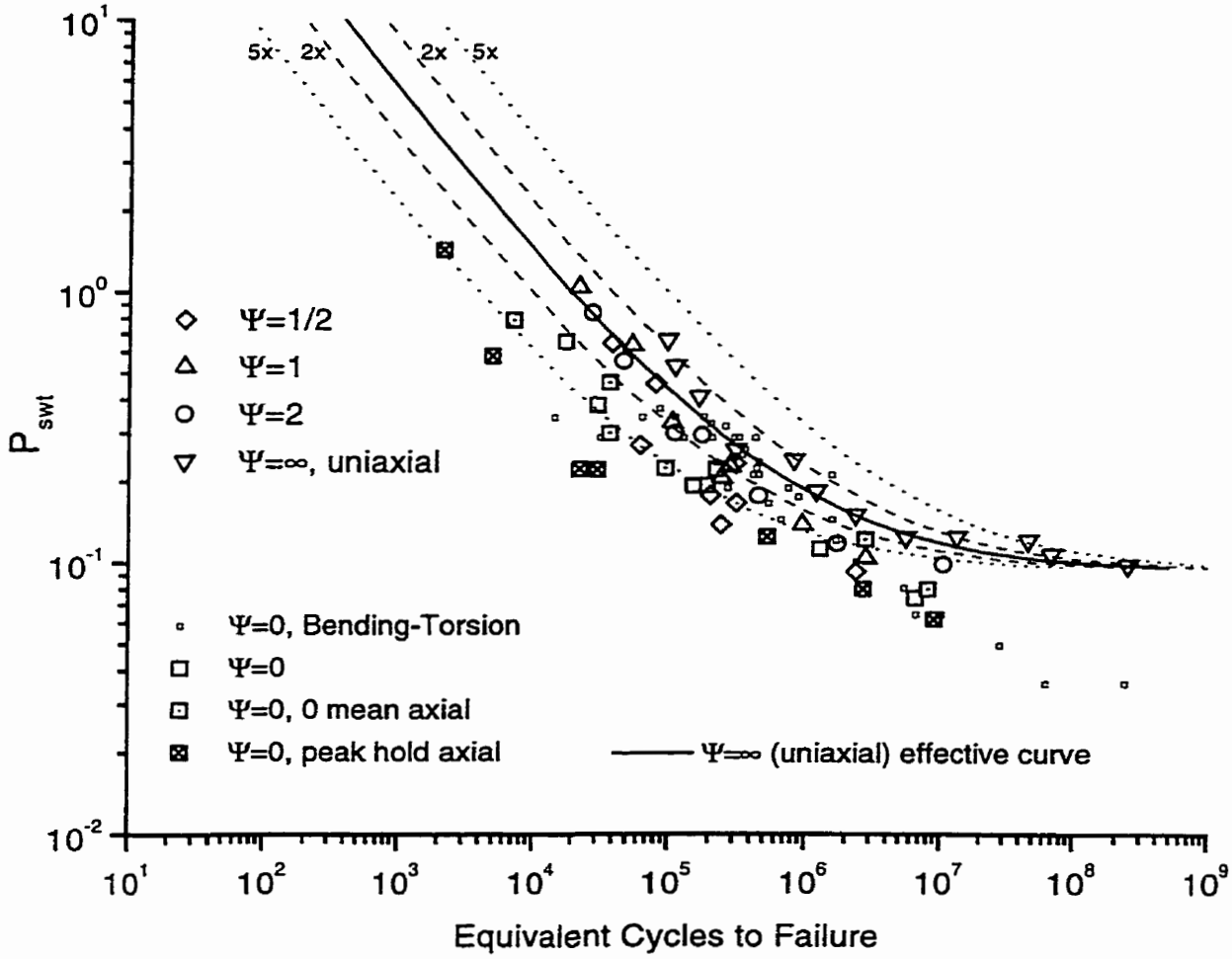

Figure 3.40: Smith-Watson-Topper [37] parameter-life plot for tension-torsion and bending-torsion overload tests.

Presented in Figure 3.40 is a plot created using the Smith-Watson-Topper parameter (equation 2.70). In this case, as mentioned in section 3.4.2.1, the maximum stress term was changed to a stress amplitude. The distribution of the data points is poor for this parameter. One-third of the data lies outside of the 5x bands, and it also does a poor job of consolidating the fatigue limit data. The vertical spread in the data at the fatigue limit is almost a factor four, and each experimental dataset exhibits a different endurance limit.

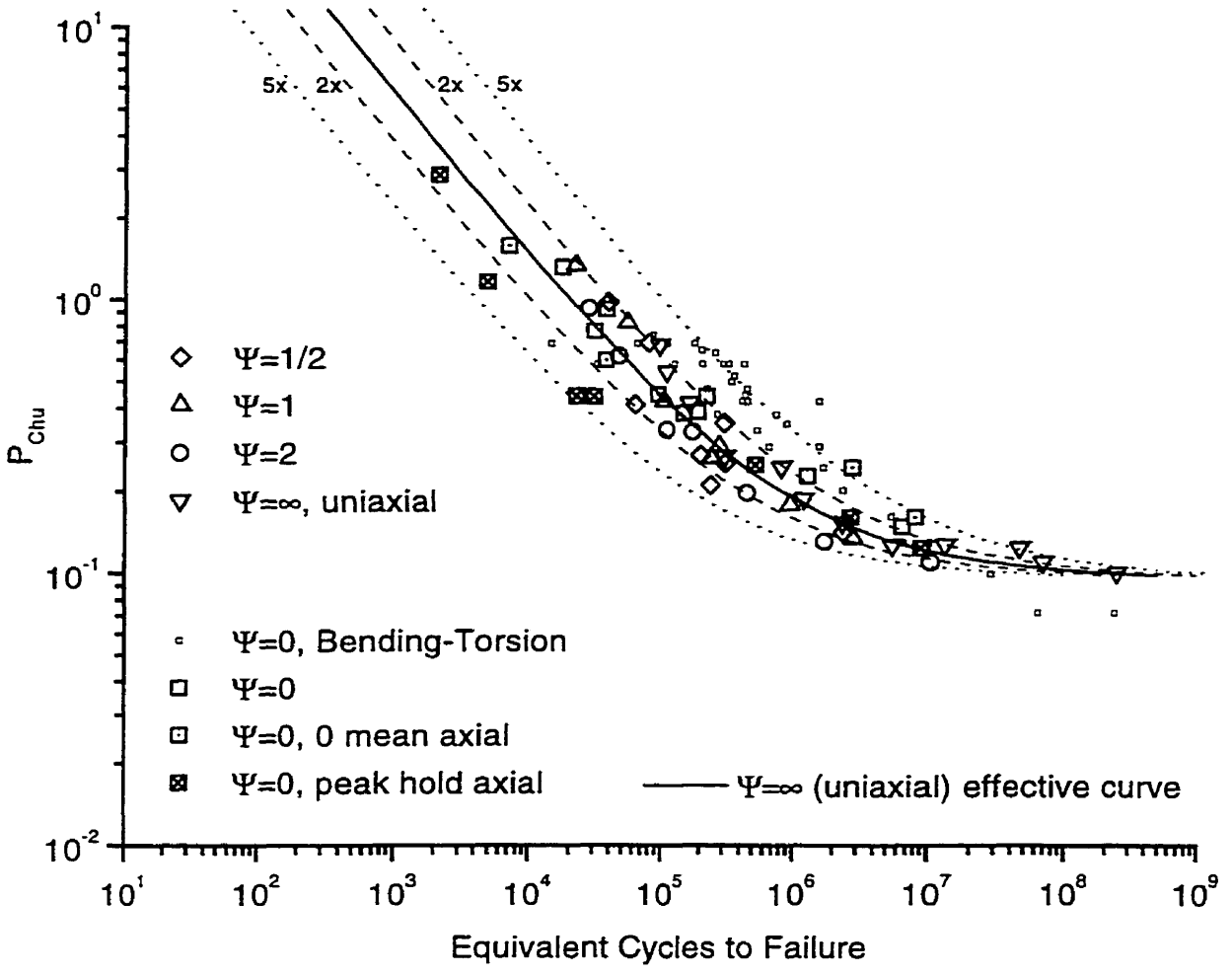

Figure 3.41: Parameter-life plot for Chu's [43] parameter for tension-torsion and bending-torsion overload tests.

Chu's parameter (equation 2.72) gives a reasonably good correlation of the data, as can be seen in Figure 3.41. This parameter, when small cycle amplitudes are substituted for the maximum stress components is similar to that proposed by Glinka, et al. [91]. Again, most of the tension-torsion and uniaxial test data fall within the 2x band, and the 5x band contains most of the the rest of data. About half of the bending-torsion data, however, falls outside the 5x bands, especially the two data point at the fatigue limit. The vertical spread at the fatigue limit is ±30%.

3.4.2.2 Initiation Plane Based Data Reduction

In section 3.4.1 it was demonstrated that plotting constant amplitude fatigue lives against the resolved shear strain on the initiation plane provided a good consolidation of the data. Plotting the data based on maximum shear strain amplitude also provided a suitable data reduction. Since there were no large differences in observed initiation behavior between constant amplitude and overload datasets these same techniques were used to generate Figure 3.42. In addition, a maximum shear strain plot is presented in Figure 3.43 (equation 2.68).

In viewing the graphs, it is apparent that the degree of success achieved with the constant amplitude data was not duplicated here. In both figures about one-half of the data falls within the 2x bands, and most of the data is contained by the 5x bands. In particular tests conducted under Ψ=0 fall outside of the 5x bands near the endurance limit. However, the maximum shear strain parameter does a reasonable job of reducing the endurance limit data, the vertical separation in the data is roughly $\pm$15%.

For all of the parameters the bending-torsion data points do not fit the trend of the rest of the data well at low and intermediate lifetimes, and this behavior is presumed to be either a result of inaccuracies inherent in employing a multiaxial Neuber analysis to generate local notch stress-strain data and/or a result of not having achieved fully crack face interference free crack growth in these tests. At lower strain levels where the the Neuber correction is small or nonexistent and where crack face interference is more easily removed by overloads, the bending-torsion data do follow the general overload trend. At the fatigue limit in many parameter plots the bending-torsion data falls above that of other tests.

The parameter-life diagram which demonstrates the least scatter is the Fatemi-Socie-Kurath parameter. However, the solution for this parameter is complex and the results from Brown and Miller's parameter, shear strain amplitude on the initiation plane, and maximum shear parameter provide very nearly as good of a consolidation of the data. As a result it is suggested that the maximum shear parameter be used since it is the simplest, and easily obtained uniaxial data may be used to make predictions with it.

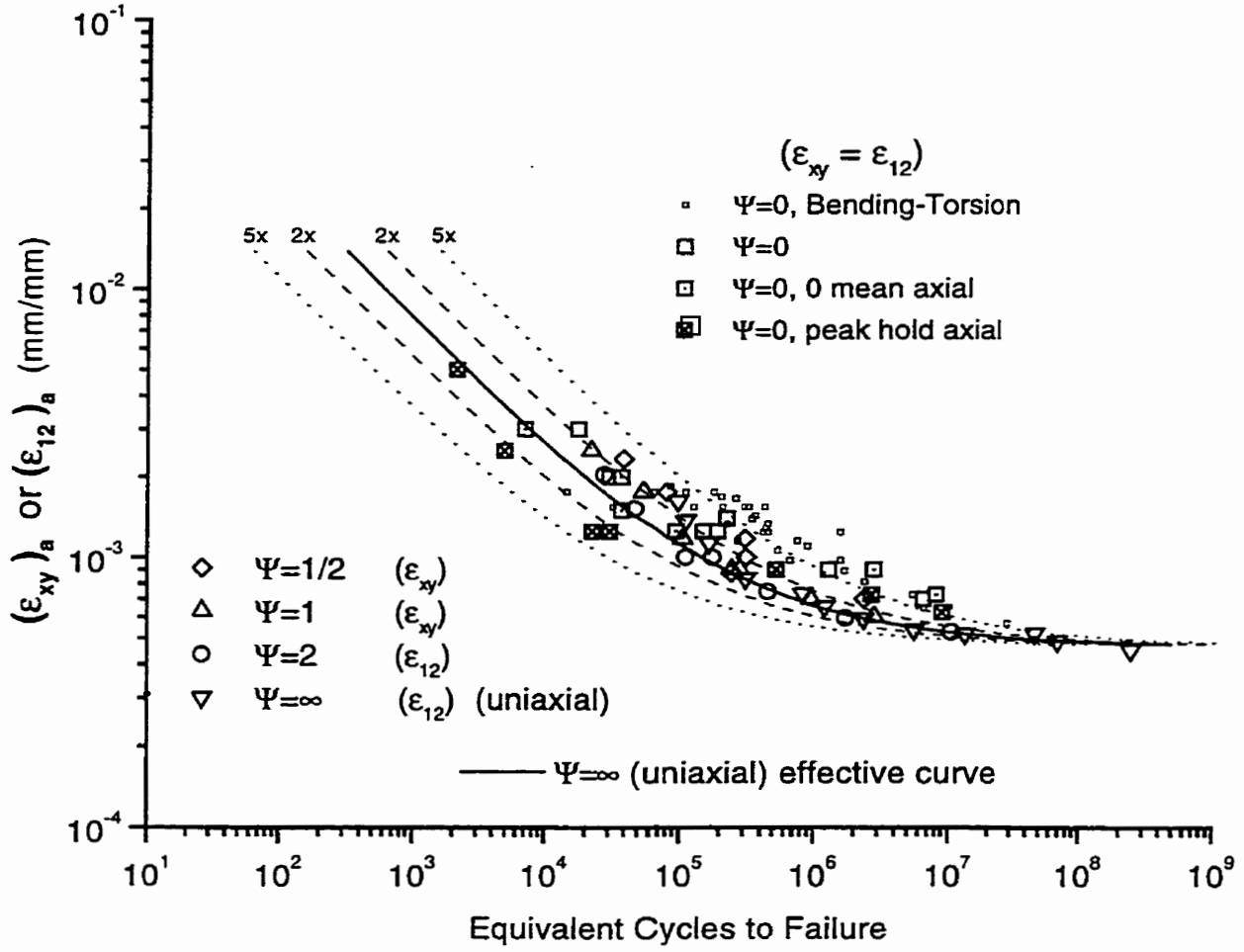

Figure 3.42: Shear strain plot of tension-torsion and bending-torsion overload tests (based on initiation plane).

3.5 Summary

The application of periodic overloads reduces crack face interference and shortens fatigue life for all strain ratios. On average the reduction in the 10^7 cycle endurance limit for overloads tests is close to one-half – regardless of the loading condition.

Uniaxial overload tests yielded a 10^7 cycle endurance limit reduction to a little under one-half of the constant amplitude fatigue limit, and this further dropped to 2/5 at 10^8 cycles. For those tests which were subjected to in-phase Ψ=0 loading

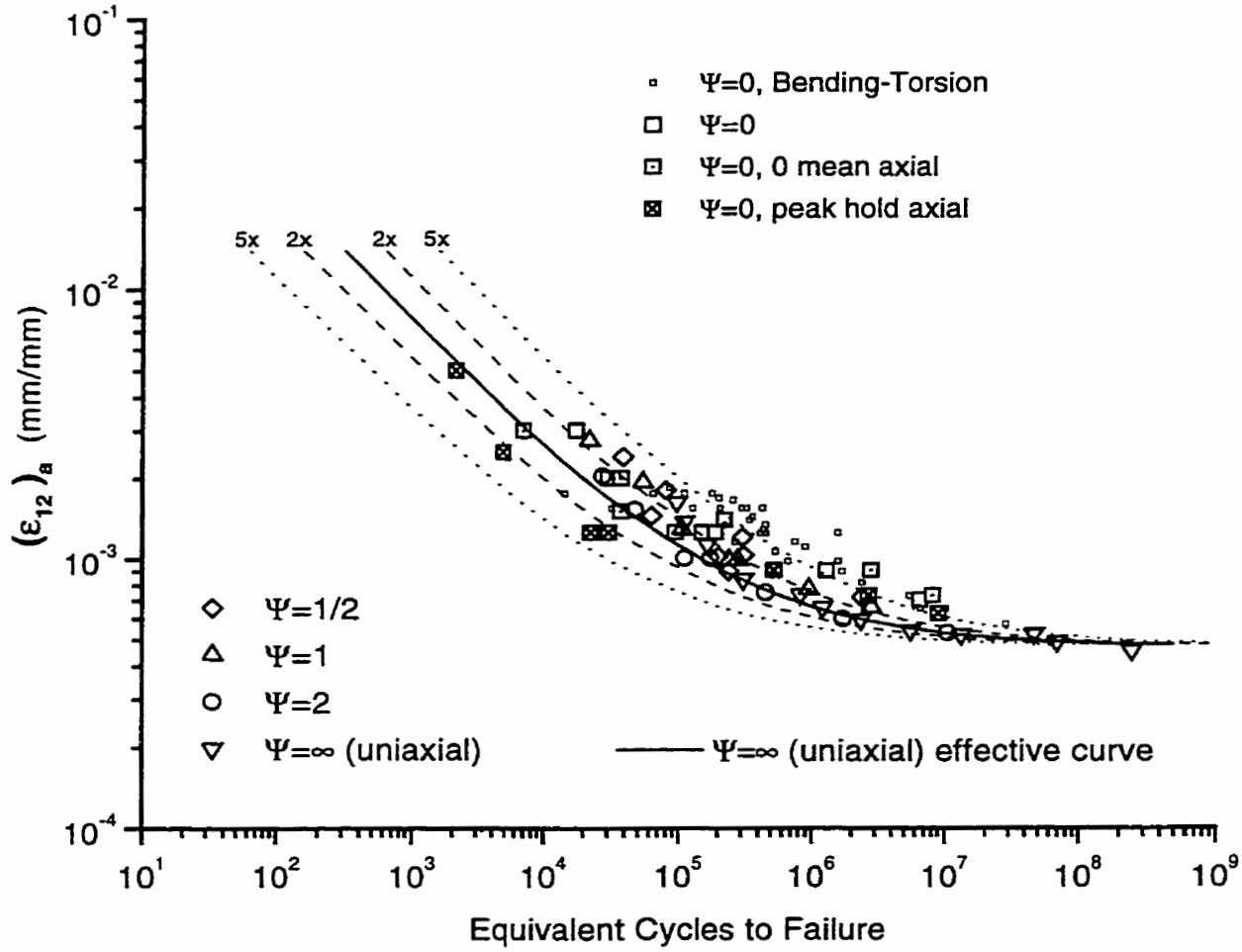

Figure 3.43: Maximum shear strain amplitude (ϵ_{12}) curves for tension-torsion and bending-torsion overload tests.

the endurance limit reduction was consistent between in-phase torsion overload and tension overload with zero mean tests at a reduction of a little under half of the Ψ=0 constant amplitude endurance limit. A reduction to 3/8 of the constant amplitude endurance limit was obtained for the peak-hold tension overload tests. In the bending-torsion tests there was a similar reduction – a factor of one-half at 10^7 cycles was obtained for both overload and peak-hold tests, which further reduced to 3/8 at 10^8 cycles. Finally, in stress ratios of $\Psi=\frac{1}{2}$, 1, and 2 periodic overload tests exhibited a 10^7 cycle endurance limit which was one-half of constant amplitude endurance limit.

Cracking behavior for the various stress ratios was also quite similar. Cracks formed on maximum shear planes and, with the exception of Ψ=2, also along longitudinal and circumferential directions. Because of the longitudinal banding of pearlite and ferrite grains in the microstructure, the longitudinal cracks propagated preferentially through ferrite rich regions to become failure cracks. Under Ψ=2 loading shear cracks initiated and grew only on planes of maximum shear strain amplitude. Cracks subjected to Ψ=0 loading with tension overloads were also an exception in that, instead of longitudinal cracks, circumferential cracks grew to failure.

However, once cracks had grown to roughly 1mm in length growth tended to move onto planes of maximum tensile stress, for stress ratios Ψ=1 and 2. However, some tensile growth was observed for all stress ratios at the lowest strain amplitudes. This behavior is similar to that described in [61]. Fash, however, attributed the tendency to initiate and grow in the longitudinal direction to the presence of stringers in his material.

Although a sliding motion is the most common crack face motion in these tests, the crack face interaction mechanisms which are believed to be in operation are fairly simple. Under in-phase Ψ=0 and Ψ=$\frac{1}{2}$, and 1 where longitudinal crack initiation is dominant, overloads remove asperities by simply pushing the asperities across one another until they are smeared and show less resistance to crack movement. Under Ψ=0 with axial overloads and Ψ=2 loading the overloads perform the same function by crushing the asperities in the same fashion as they are crushed under uniaxial loading. Fracture surfaces which had asperities with smear marks consistent with such processes were observed in each case.

The parameter which best reduces the constant amplitude and overload data from all of the tests for design purposed is the Fatemi-Socie-Kurath parameter. However, the maximum shear strain amplitude parameter is recommended because it provided nearly as good a data consolidation and has a simpler implementation.

Finally, the constant amplitude stress strain curve, when viewed with both constant amplitude and overload biaxial stress-strain data, provides a reasonable approximation to the response of the material to the various stress ratios.

Chapter 4

Crack Growth and Crack Growth Modelling

The observations made in Chapter 3 regarding cracking behavior are extended in this chapter to include the observation of cracks at longer crack lengths. Crack face interference-free crack growth curves are obtained for mode I and mode II crack growth.

The crack growth curves and observations of cracking are then combined with two models which predict changes in crack growth behavior. The models used were based on crack area increment and strain energy release rate criteria. Both of these models underpredict the shear crack length at which crack growth mode changes, but they do predict the general trends observed in the data in terms of changes in crack growth mode as a function of strain amplitude and load ratio.

Several different crack growth predictions were made. These included baseline predictions wherein the strain concentration profile [50] (described in section 1.2.2.1), is determined separately for each load ratio. Predictions were then made using the crack area increment and strain energy release rate criteria. First, the strain concentration profiles for shear and tensile crack growth were independently determined. They were then placed into the area and energy models, and these models were used to predict strain life curves for all of the stress ratios. The area and energy models gave good predictions of the experimental lives for all of the stress ratios, but the best predictions were provided by the baseline predictions.

4.1 Crack Growth Measurements and Crack Mode Observations

In this section mode I and mode II crack growth measurements are presented as are observations made of specimen cracking behavior during strain-life experiments.

4.1.1 Mode I Crack Growth Experiments

Four single edge notched uniaxial crack growth specimens (see Figure 2.9) were used to produce the effective ΔK versus crack growth rate curve shown in Figure 4.1. The geometry factor used to calculate K for this specimen is that for a single edge cracked panel [92] and is given in more detail in Appendix B, section B.1.1. The tests were conducted as discussed in section 2.2.4. In order to ensure fully open crack growth, observations of the crack tip were made to determine if the crack was open throughout the loading cycle. A check was made for each data point. This technique has been used in the past [86, 51] to determine whether the crack was growing under fully open conditions.

Data from four different specimens were used to construct Figure 4.1. For each specimen shown in the figure, the scatter was about $\pm 20\%$ in crack growth rate. However, growth rates varied between specimens by a factor of 2. More scatter (up to an order of magnitude) is found in the near-threshold region where the local microstructure at the crack tip can influence the growth rate, and a lower scatter (a factor of 2) is encountered in the Paris-law region where larger crack growth increments reduce the influence of the local microstructure.

As-received 1045 steel is similar to the normalized 1045 steel used in this study and researchers have recently obtained both long [84] and short [4] crack growth data for this material. These results are combined with data for the present normalized 1045 steel in Figure 4.2. All of the data, including short crack data, fall into a single band, and the trend line depicted in this figure was later used as the mode I crack growth curve during modelling.

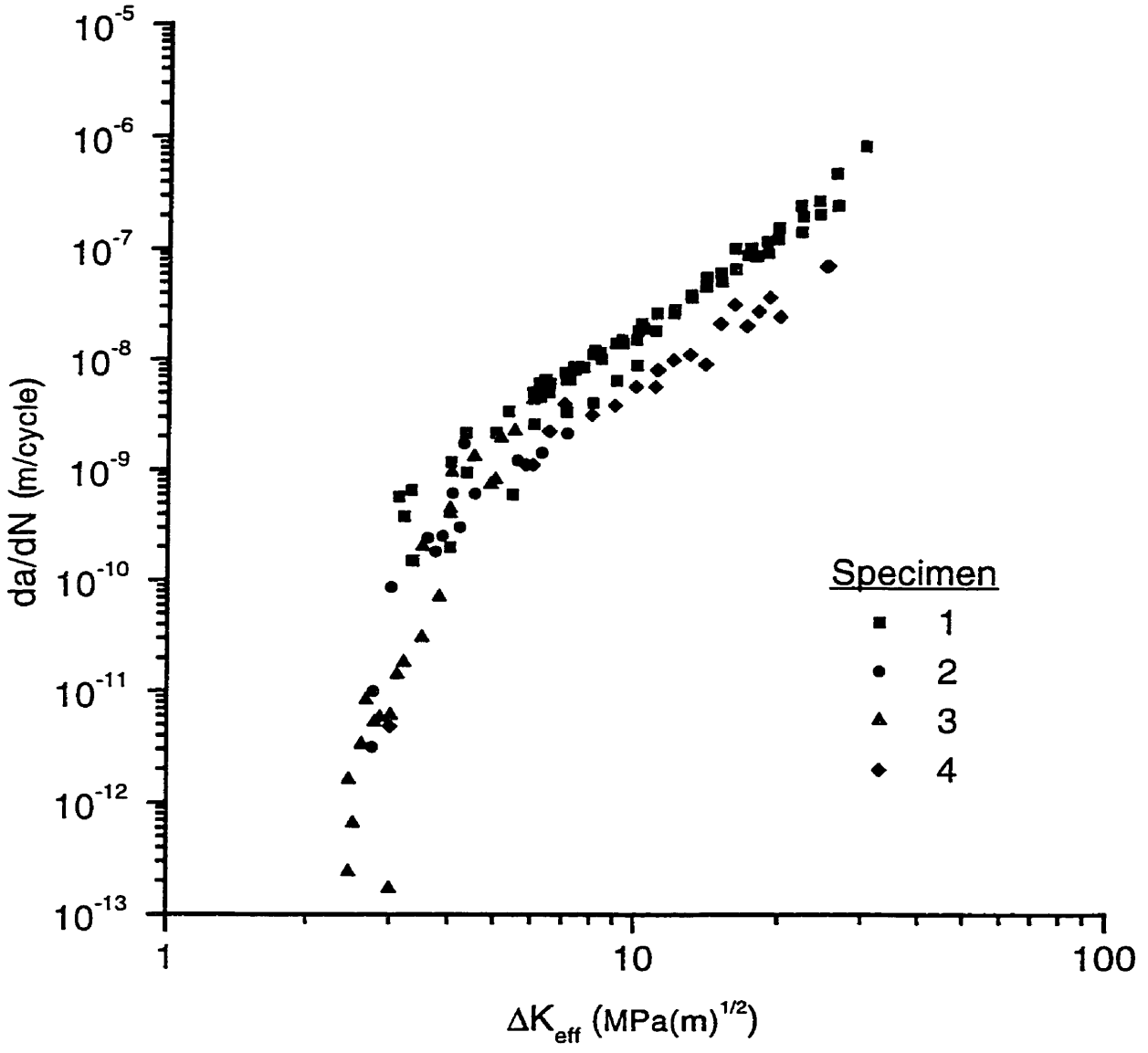

Figure 4.1: Effective crack growth curve for normalized 1045 steel.

4.1.2 Mode II Crack Growth Experiments

Long crack experiments were performed on the tubular specimens and, since the long cracks were also through cracks, the crack growth data extracted from the experiments was for growth under mode II loading. This mode II long crack growth data was obtained from two notched tube specimens (Figure 2.24) and are presented in

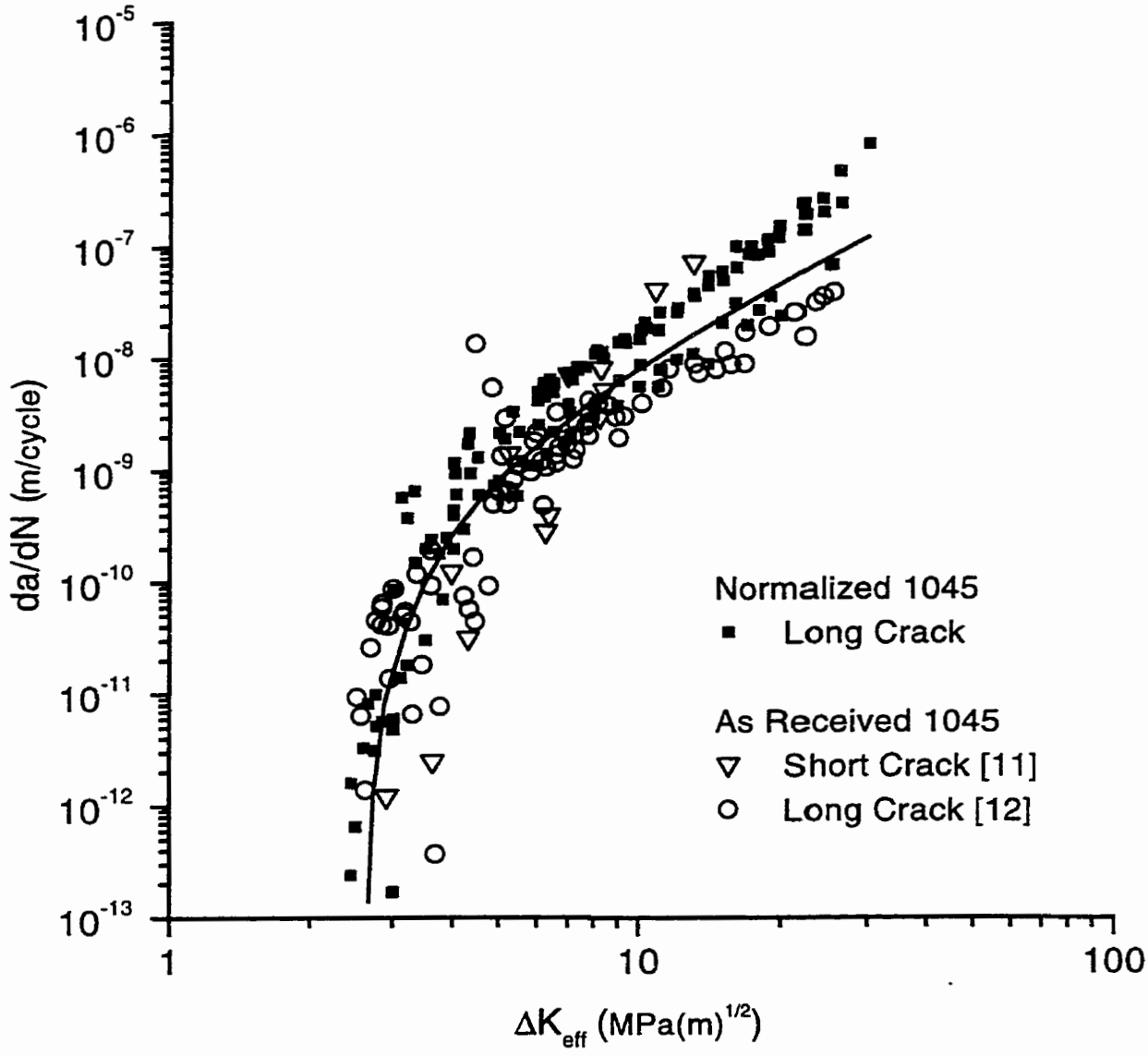

Figure 4.2: Effective crack growth curve for normalized 1045 and for as-received 1045 for short [4] and long cracks [84].

Figure 4.3. The geometry factor used to derive the stress intensity values was taken from reference [93], and is presented in Appendix B, section B.2.1. The tests were conducted as described in section 2.3.2.2.

Identifying crack face interference-free crack growth behavior was more compli-

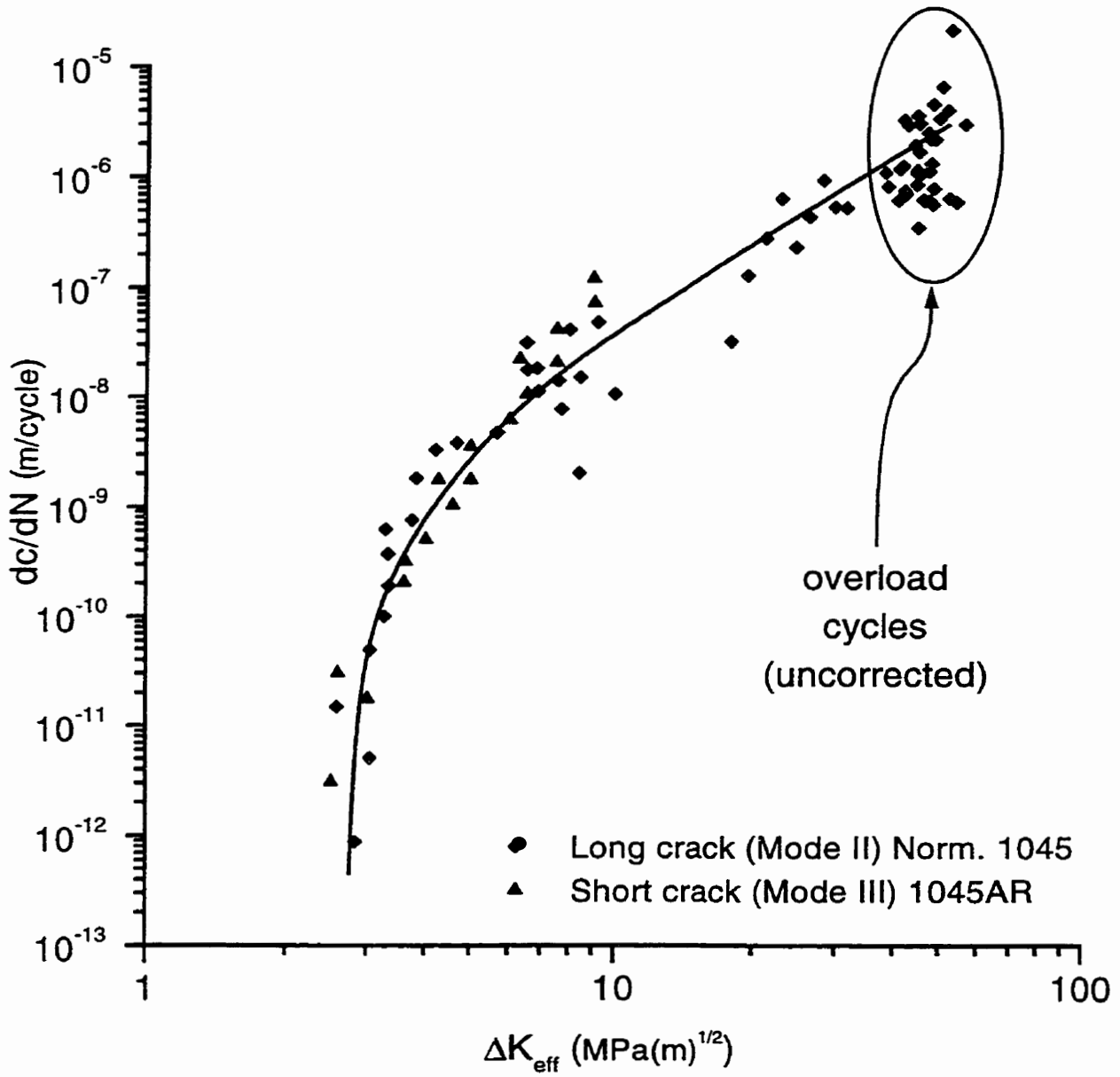

Figure 4.3: Mode II effective crack growth curve for normalized 1045 steel. Effective crack growth data for small cracks in as-received 1045 steel (from [4]).

cated in these tests since the crack faces were observed to slide back and forth rather than together and apart as observed in mode I loading. In this case an overload level

and η, the number of small cycles between overload applications, that caused growth during the smaller cycles to take place under fully interference-free conditions was determined in the following manner. For a given overload level and η, small cycle growth rates were recorded, and a second test was run with the same small cycle size and η, but with a much higher overload amplitude level. If the second small cycle crack growth rate was the same as the first, the first overload level was presumed to have resulted in crack face interference-free crack growth for this small cycle amplitude. It is also assumed that other lower small cycle amplitudes would also be crack face interference-free for the first overload level and η. As the small cycle size decreased, the number of small cycles between overloads (η) was periodically increased. At each increase in η, an extra crack length measurement was made at $\eta/2$. If the crack growth extension was the same for the first and second halves of the small cycle block then the cycle was assumed to still be crack face interference-free for that η.

Locating the crack tip in these tests was more difficult than in the mode I tests. Although a mode II crack is clearly visible typically to within $50\mu m$ of the tip (largely due to fretting debris), beyond this point the crack path and especially the crack tip become exceedingly difficult to identify. In mode I tests the crack tip is obvious since the crack visibly opens all the way to the tip at the peak tension level. The primary method of locating a mode II crack tip was through observation of the sliding crack faces along the crack path and the deformation field around the crack tip. In addition on the specimen surface there are dark areas of intense local deformation into which the crack occasionally grows, making precise observations difficult. Finally, many measurements were discarded when the crack bifurcated. In this case the crack was grown away from the bifurcation and crack growth measurements were started anew. These problems were exacerbated near the threshold (below about $4\text{MPa}\sqrt{\text{m}}$) because the deformation field, and hence the crack tip, became less distinct. It is estimated that the growth rate scatter in the Paris region is roughly one order of magnitude and in the threshold region (below $4\text{MPa}\sqrt{\text{m}}$), it is up to two orders of magnitude.

Presented together with the mode II data for normalized 1045 steel in Figure 4.3 is mode III small crack data from Varvani-Farahani [4] for as-received 1045 steel. These data and the normalized 1045 steel data fall into the same scatter band. The trend line drawn on Figure 4.3 is the curve used for predictions of mode II and mode III crack growth in following sections.

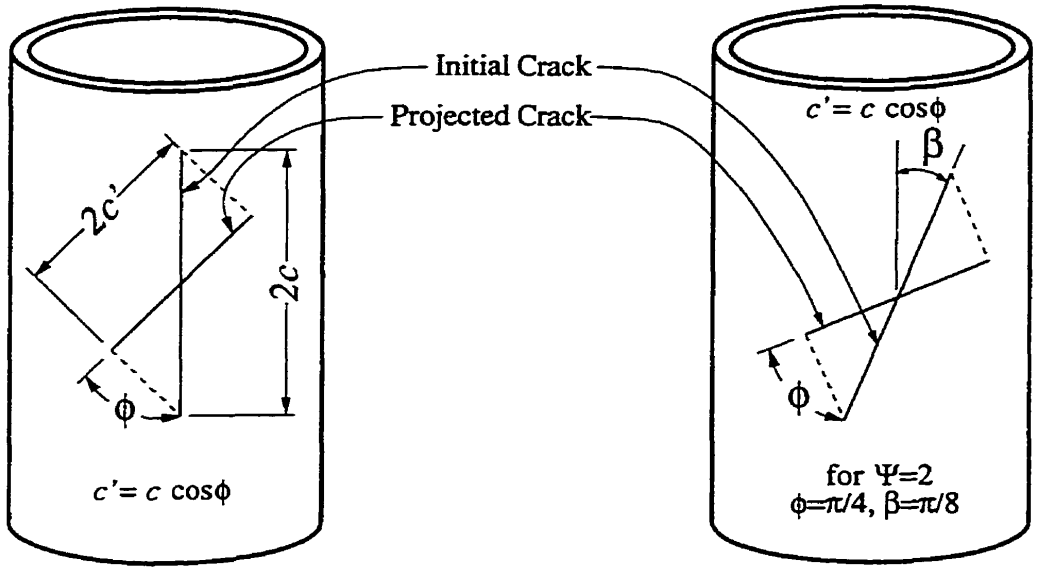

Figure 4.4: Definition of angles β and ϕ, and and examples of crack length projection onto principle stress plane.

4.1.3 Crack Growth Mode Observations

As previously described in section 3.2, the planes of both crack initiation and subsequent growth were observed and recorded. These observations are summarized in Table 4.1. The crack initiation planes for Ψ=0, 1/2 and 1 were found to be aligned with the longitudinal (x-axis as defined previously in Figure 2.26), and the angles β and ϕ presented in the table are defined in Figure 4.4. However, Ψ=2 loading was an exception in that the initiation plane was close to the maximum shear plane. No observations were made for uniaxial loading, but observations of uniaxial crack growth from other work on 1045 steel [87] have been placed in the table. At longer crack lengths, cracks were frequently observed to grow on planes of maximum tensile strain. Both the angle the initiation plane makes with the x-axis, β, and the angle the initiation plane makes with the tensile cracking plane, ϕ, are given in the table.

There was three different types of cracking behavior observed in the tests. The first type of cracking was termed shear dominated (SD) cracking, and specimens which exhibited this behavior had a crack which initiated and grew in shear until the crack spanned the entire gage length of the specimen. The second type of behavior

Table 4.1: Initiation and propagation angles (with respect to the x-axis) for normalized 1045.

Ψ	β	ϕ
0	0°	45°
$\frac{1}{2}$	0°	52°
1	0°	57°
2	22.5°	45°
∞	45°	45°

observed was termed extended shear (ES) cracking in which a crack initiated and grew anywhere in shear to between a fraction of millimeter and several millimeters in length, after which crack growth switched to maximum tensile planes. This distance the shear crack grows before the transition to tensile cracking is termed the initial shear crack length (ISCL). In several tests a crack initiated and grew a very short distance in shear before tensile cracking began; this behavior was termed shear initiated (SI) cracking.

Table 4.2 presents ISCL observations made of Ψ=0 specimens. Also given in this table are predictions of ISCL, but these are discussed later. Specimens subjected to intermediate and high torsional strain levels demonstrated SD behavior, and this is indicated in the table by an entry indicating the specimen gage length, c_{gl}. Two specimens were tested at a strain level of 0.000125, as indicated by the "2@" in the table. At strain levels below 0.00125, ES behavior was observed. An entry with a "-" indicates that no specimens were tested at this strain amplitude. SI behavior was not observed in tests conducted at this load ratio.

Observations made for specimens subjected to Ψ=1/2 loading can be found in Table 4.3, and these observations are similar to those for torsion. This table clearly shows the stochastic nature of the experimental cracking – there is no definite demarcation between one type of behavior and another, hence in the descriptions of cracking behavior overlapping bands are employed. At larger strain amplitudes (roughly above 0.0014), SD behavior dominated, and for strain amplitudes which ranged from 0.0018 down to 0.0009 ES behavior was prevalent. At a strain amplitude of 0.0007 the only

Table 4.2: Observed and predicted initial shear crack lengths (ISCL) for Ψ=0 loading.

$(\epsilon_{xy}^{sc})_a$ (mm/mm)	Observed c (μm)	Predicted (area) (μm)	Predicted (energy) (μm)
0.0007	450	80.4	81.9
0.0008	-	153.0	106.4
0.0009	240	c_{gl}	118.1
0.0011	-	c_{gl}	180.4
0.0013	2@c_{gl}	c_{gl}	c_{gl}
0.0014	c_{gl}	c_{gl}	c_{gl}
0.0018	c_{gl}	c_{gl}	c_{gl}
0.0020	c_{gl}	c_{gl}	c_{gl}
0.0030	c_{gl}	c_{gl}	c_{gl}

$2c_{gl} = 30mm$

Table 4.3: Observed and predicted initial shear crack lengths (ISCL) for $\Psi=\frac{1}{2}$ loading.

$(\epsilon_{xy}^{sc})_a$ (mm/mm)	Observed c (μm)	Predicted (area) (μm)	Predicted (energy) (μm))
0.0007	<50	71.9	68.4
0.0009	c_{gl}	117.5	80.3
0.00092	-	c_{gl}	82.0
0.0010	900/500	c_{gl}	85.2
0.0012	200	c_{gl}	94.6
0.0014	c_{gl}	c_{gl}	132.0
0.0017	-	c_{gl}	c_{gl}
0.0018	3300	c_{gl}	c_{gl}
0.0023	c_{gl}	c_{gl}	c_{gl}

$2c_{gl} = 30mm$

instance of SI behavior was observed for this stress ratio (as indicated by "<50μm"). The designation "<50μm" indicates that, although a shear crack was visible at the initiation site, the size of the crack was at or slightly less than the resolution of the

technique used to determine the crack size, $50\mu m$.

Table 4.4 contains the observations made for the Ψ=1 load ratio. In this case, SI behavior was dominant for strain amplitudes up to 0.001, ES behavior existed between strain amplitudes of roughly 0.001 and 0.0025 and SD behavior was only observed at strain amplitudes above 0.0018.

Table 4.4: Observed and predicted initial shear crack lengths (ISCL) for Ψ=1 loading.

$(\epsilon_{xy}^{sc})_a$ (mm/mm)	Observed c (μm)	Predicted (area) (μm)	Predicted (energy) (μm)
0.0006	50	50*	50*
0.00065	-	50.1	50.02
0.0007	<50	53.5	51.5
0.0009	2@<50	84.0	62.6
0.0011	-	c_{gl}	71.5
0.0012	100	c_{gl}	74.6
0.0018	c_{gl}	c_{gl}	112.2
0.0025	2500	$c_{gl}^{\ddagger}$	163.9‡
0.003	-	$c_{gl}^{\ddagger}$	$c_{gl}^{\ddagger}$

$2c_{gl} = 30mm$, $^*c_o = 50\mu m$, ‡out-of-bounds prediction

The last table, Table 4.5, contains the observations from specimens subjected to Ψ=2 loading. SI behavior was dominant for strain amplitudes up to about 0.00075. At and above this level ES behavior was observed, and SD behavior was not observed at all.

Two distinct trends are observable in the data presented in Tables 4.2-4.5. The first trend is that, as the strain amplitude is increased, the initial shear crack length increases and the behavior moves from SI to ES to SD. The second trend is that, as Ψ is increased from 0 to 2, the initial shear crack lengths (ISCL) generally shortened and SI and ES behavior became more dominant.

What is not documented in the tables is that, while they initially followed ES behavior, cracks in several specimens at Ψ=1/2 and 1 oscillated between shear and tensile cracking, while at Ψ=0 and 2 cracks tended to stay in the same mode to failure.

Table 4.5: Observed and predicted initial shear crack lengths (ISCL) for Ψ=2 loading.

$(\epsilon_{xy}^{sc})_a$ (mm/mm)	Observed c (μm)	Predicted (area) (μm)	Predicted (energy) (μm)
0.0004	<50	$50^{*\dagger}$	$50^{*\dagger}$
0.00045	<50	50^{*}	50^{*}
0.00049	-	50.2	50.1
0.00056	<50	59.9	56.1
0.00075	700,<50	78.1	64.3
0.001	-	c_{gl}	76.4
0.0011	100	c_{gl}	82.1
0.0015	200	c_{gl}	96.8

$2c_{gl} = 30mm$, $^{*}c_o = 50\mu m$, †non-propagating crack

4.2 Predictions of Cracking Behavior

Using two pre-existing criteria for selecting crack growth directions, two models were developed to predict the initial shear crack length. The crack angles listed in Table 4.1 were used to define the allowable cracking planes in the models, and the models assume an initial shear crack and use a criterion to determine whether a crack is likely to continue growing in shear or to switch to growth on tensile planes. The ISCL is defined as the length at which the switch takes place. Predictions, given in the following two sections, are made for semi-elliptical cracks on the exterior surface of the tubes and for through cracks in tubes. The purpose of the former prediction is to model the ISCL, and the purpose of the latter is to model frequent switching observed at longer crack lengths between shear and tensile crack growth under Ψ=1/2 and 1 loading.

4.2.1 Crack Area Increment Criterion

This criterion is based on observations made by Hourlier and Pineau [20] and is further supported by work in reference [57]. Hourlier and Pineau stated that a crack will grow in the direction for which the crack growth rate is the greatest.

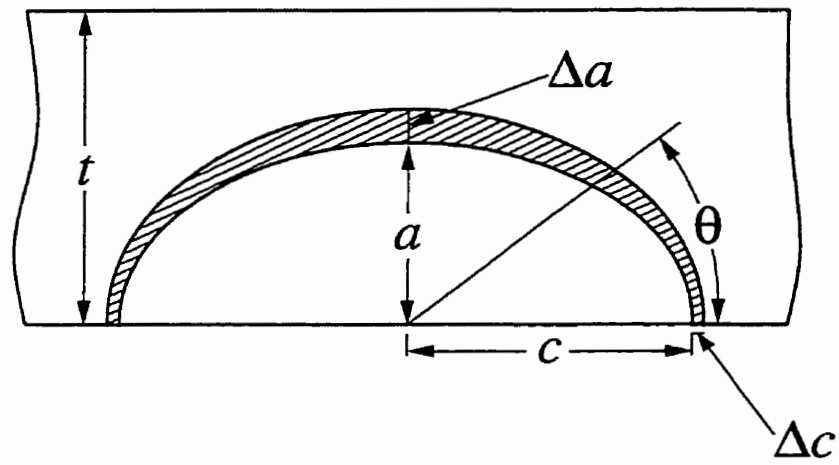

Figure 4.5: Definition of terms for a semi-elliptical crack.

However, since the crack front in this model is elliptical and the increment in each direction is not the same, the criterion was changed from crack length increment per cycle to crack area increment per cycle. In other words, the criterion as used in this thesis is restated as follows; the crack will grow in the direction in which the increment in crack growth area is greatest.

Using the terms defined in Figure 4.5, the crack area increment in a given direction may be obtained from the equation for the area of an ellipse (πac) and is given by

$$\Delta A = \frac{\pi}{2}(c\Delta a + a\Delta c). \tag{4.1}$$

For the purposes of presentation (and programming) the ratio of the tensile to the shear area increment, ξ, is defined as

$$\xi = \frac{\Delta A_t}{\Delta A_s} = \frac{c_t \Delta a_t + a\Delta c_t}{c_s \Delta a_s + a\Delta c_s}, \tag{4.2}$$

where the subscript "t" refers to the tensile (or mode I) growth increment and the subscript "s" denotes the shear crack increment. The ratio, ξ, is evaluated over a series of shear crack lengths, and at each increment the shear crack length is projected onto the tensile crack plane and an equivalent surface crack length, c_t, is calculated as in Figure 4.4. The new surface crack length is calculated by

$$c_t = c_s \cos\phi. \tag{4.3}$$

Since the cracks grow straight into the surface, the value of crack depth, a, does not change when projected as shown in Figure 4.4. These crack lengths are used to calculate the stress intensities, which are in turn used to obtain the growth rates to calculate ξ.

Using this criterion a value of ξ which is less than unity indicates that a crack will continue growing in shear while a value of ξ which exceeds unity indicates that the crack will switch into tensile growth.

The results of crack transition predictions made using this model can be found in Tables 4.2 through 4.5 labelled as "area." These results will be discussed after the following model has been introduced.

4.2.2 The Strain-Energy Release Rate Criterion

Another theory which has been used to predict crack growth transitions is supported by several researchers [59, 60, 47]. It proposes that a crack will grow in the direction of the maximum strain energy release rate.

In general terms, the strain energy release rate may be expressed as

$$G_c = \frac{K^2}{E} = \frac{(F\Delta\sigma)^2\pi a}{E}. \tag{4.4}$$

Substituting a strain intensity factor [45, 46] in place of the stress intensity factor gives

$$G_c = \frac{(FE\Delta\epsilon)^2\pi a}{E}, \tag{4.5}$$

This may be expressed as the energy released for a given crack increment, δa, as

$$\delta G_c = (F\Delta\epsilon)^2 E\pi\delta a, \tag{4.6}$$

where F is the crack geometry factor. Under mode I loading F can be taken as F_I^e from Irwin's solution [55] for an elliptical edge crack.

Previous multiaxial studies [47, 52, 4] found that surface (edge) cracks in tubes are elliptical (although the ellipticity changes throughout the test from nearly zero to

nearly one). Thus, for a semi-elliptical crack with the line of shear directed along the major axis, the mode III incremental strain energy release rate can be expressed as

$$\delta G_{c,III} = \frac{(1+\nu)}{E}\Delta K_{III}^2 = 2(F_{III}^e \Delta e_{xy})^2 G\pi\delta a_s \sin\theta, \tag{4.7}$$

where E is the elastic modulus, G is the shear modulus, ν is Poisson's ratio, and F^e are the elliptical crack geometry factors found in Appendix B. The mode II incremental strain energy release rate is

$$\delta G_{c,II} = \frac{\Delta K_{II}^2}{E} = \frac{2(F_{II}^e \Delta e_{xy})^2 Gk\pi}{1+\nu}\delta c_s \cos\theta, \tag{4.8}$$

where k is the crack eccentricity, $\frac{a}{c}$, and θ is the crack parametric angle. Figure 4.5 shows how these terms are defined for an elliptical crack.

The strain energy release rate increment for a semi-elliptical crack subjected to shear can be integrated across the entire crack front to yield the energy released per cycle for the whole crack,

$$\delta G_c^s = 2G\Delta e_{xy}^2 \pi((F_{III}^e)^2\delta a_s + \frac{(F_{II}^e)^2 k}{1+\nu}\delta c_s). \tag{4.9}$$

For a crack under mode I (or tensile) loading, the energy released is

$$\delta G_c^t = E\Delta e_{xx}^2 \pi\left((F_I^e)^2\delta a_t + (F_I^e)^2 k\delta c_t\right). \tag{4.10}$$

The ratio of the energies, defined as

$$\chi = \delta G_c^t / \delta G_c^s, \tag{4.11}$$

can then be used to determine when the transition from shear growth to normal growth occurs. Once χ exceeds unity, the crack growth is assumed to switch from the shear growth plane onto the maximum principal (normal) strain plane.

Calculation of χ is performed in the same fashion as ξ. The results of crack transition predictions made using this model can be found in Tables 4.2 through 4.5.

4.2.3 Discussion of Crack Transition Predictions for a Semi-Elliptical Crack

As can be seen from Table 4.2, the Ψ=0 experiments demonstrate extensive shear cracking (ES) behavior for strains up to and including $(\epsilon_{xy}^{sc})_a$=0.0009; above this level the experiments demonstrated shear dominated (SD) cracking behavior. The crack area increment (area) criterion places the change from ES to SD behavior just below $(\epsilon_{xy}^{sc})_a$=0.0009, whereas the strain energy release (energy) criterion puts it just above $(\epsilon_{xy}^{sc})_a$=0.0011. While the energy criterion successfully predicted the ES-SD behavior change and the area criterion underpredicted it in this case, the stochastic nature of specimen cracking must be considered – no firm conclusions may be drawn from the small amount of data available for this or other strain ratios.

The actual initial shear crack lengths (ISCL's) observed for Ψ=0 are much longer than the predictions made with either criterion. Both criteria underpredicted the ISCL at $(\epsilon_{xy}^{sc})_a$=0.0007 by a factor of 5, and at $(\epsilon_{xy}^{sc})_a$=0.0009 the ISCL was only predicted by the energy model, and it underpredicted the length by a factor of 2.

Table 4.3 contains the observations and predictions for Ψ=1/2 loading. The experimental data point at $(\epsilon_{xy}^{sc})_a$=0.0007 demonstrated shear initiated (SI) behavior, but neither criterion predicted this behavior for Ψ=1/2 loading. In using the prediction models, the models SI behavior is defined when the crack switches to tensile growth before there is any significant surface crack growth over and above its initial value ($c = c_o$). This predicted behavior, when it occurs (Tables 4.4 and 4.5), is indicated by an asterisk (*). The change in the experimental data between ES and SD behavior was set at approximately 0.0014, and the predictions for this change were $(\epsilon_{xy}^{sc})_a$=0.00092 and 0.00167 for the area and energy criteria, respectively. The area criterion tends to underpredict the ES-SD behavior change and the energy tends to overpredict it.

In the range of strain amplitudes where the experimental ES regime overlaps with those of the models, the ISCL's predicted by the models are, again, much less than the observed lengths – the differences range from a factor of 2 to an order of magnitude.

The results for Ψ=1 are presented in Table 4.4, and the change between SI and ES behavior occurs for the experimental data at roughly $(\epsilon_{xy}^{sc})_a$=0.001. Both models underpredict the the SI-ES behavior change and they both predict it at the same strain amplitude – $(\epsilon_{xy}^{sc})_a$=0.00065. In the experimental data the change between ES and SD behavior lies approximately the range of $(\epsilon_{xy}^{sc})_a$=0.0015 to 0.0025, and the area criterion sets the ES-SD behavior change at 0.0011 and the energy criterion sets it at 0.003. The ISCL's predicted by the energy criterion for this load ratio are again less than the observed lengths, but for $(\epsilon_{xy}^{sc})_a$=0.0012 the prediction is within 30% of the observed value. The area criterion predicted SD behavior for all of the specimens which exhibited ES behavior.

Finally, the results for Ψ=2 are presented in Table 4.5. From the experimental evidence the SI-ES behavior change can be set at $(\epsilon_{xy}^{sc})_a$=0.00075, while an ES-SD behavior change is not observed – ES behavior dominates. Both models predict the SI-ES behavior change to be at $(\epsilon_{xy}^{sc})_a$=0.000485 – this is roughly 2/3 of the observed value. The area criterion sets the ES-SD behavior change at $(\epsilon_{xy}^{sc})_a$=0.001 while the energy criterion predicts no transition into SD behavior for the strain amplitudes listed in the table. The ISCL's predicted by both models are substantially shorter than the experimental ISCL, and the differences between the experimental and predicted ISCL's are similar to those found for the other load ratios.

No predictions are given for uniaxial loading ($\Psi = \infty$) since no experimental observations were made.

The trend of the predictions follows the trend of the experimental observations. At low strain levels in the ES region the transition length is fairly short, and, as the strain amplitude increases, increased initial shear crack lengths (ISCL's) are predicted until shear cracks are predicted to continue until they span the entire gage length. However, both models substantially underpredict the real transition length.

The area criterion underpredicts the strain amplitudes at which the change between ES and SD behavior occurs and the energy criterion overpredicts this strain amplitude. However, both criteria underpredict the strain amplitude at which the change between SI and ES behavior occurs.

4.2.4 Crack Transition Predictions for Through Cracks

The same techniques used in the preceding sections were applied to through cracks in tubes to see if similar predictions might be made for longer length cracks. In these models the through-crack geometry factors, F^t from Appendix B, were used to calculate χ and ξ. In the models shear crack length, c, is incremented from $30\mu m$ to 15mm, and χ is calculated at each increment. Through crack surface crack lengths of less than the tube wall thickness are unlikely because the surface length is normally greater than 2.5mm ($\frac{a}{c} \leq 1$) once the crack penetrates the inner diameter of the tube. The crack projection takes place as pictured in Figure 4.4, but with a through crack rather than a semi-elliptical one. In a fashion similar to that discussed in section 4.2, the equivalent crack length is projected onto the principal stress plane, and that crack length is used to calculate the energy released by cracking on that plane. The energy to continue cracking in a shear mode is also calculated. The former is divided by the latter to yield χ (and through a similar method ξ), and the results of these calculations are presented in Figures 4.6 and 4.7.

In each figure stress ratios of 0, 1/2, 1 and 2 are shown, and within each stress ratio either ξ or χ calculations are provided for a high, an intermediate, and a fatigue limit strain. Also marked on each graph is the tube wall thickness designated by t (a rough indication of the minimum through-crack length), the region where tensile cracking is predicted ($\xi > 1$ or $\chi > 1$) and where continued shear growth is expected ($\xi < 1$ or $\chi < 1$). All simulations were stopped when K_{max} exceeded K_c.

The models predict that, regardless of strain amplitude, all shear cracks will eventually switch to cracking on tensile planes, but this change was not always observed experimentally, especially for Ψ=0 loading. Figures 4.6a and 4.7a indicate that this will happen under Ψ=0 loading. An observation like this was made only during the mode II crack growth tests (Ψ=0) it was observed that the maximum shear crack length was approximately 7mm before the crack switched permanently to tensile growth. The two specimens which switched to tensile growth in this load ratio did so before the elliptical fatigue crack had reached the inner wall of the tube and become a through crack. The rest of the specimens had cracks which grew in shear until failure.

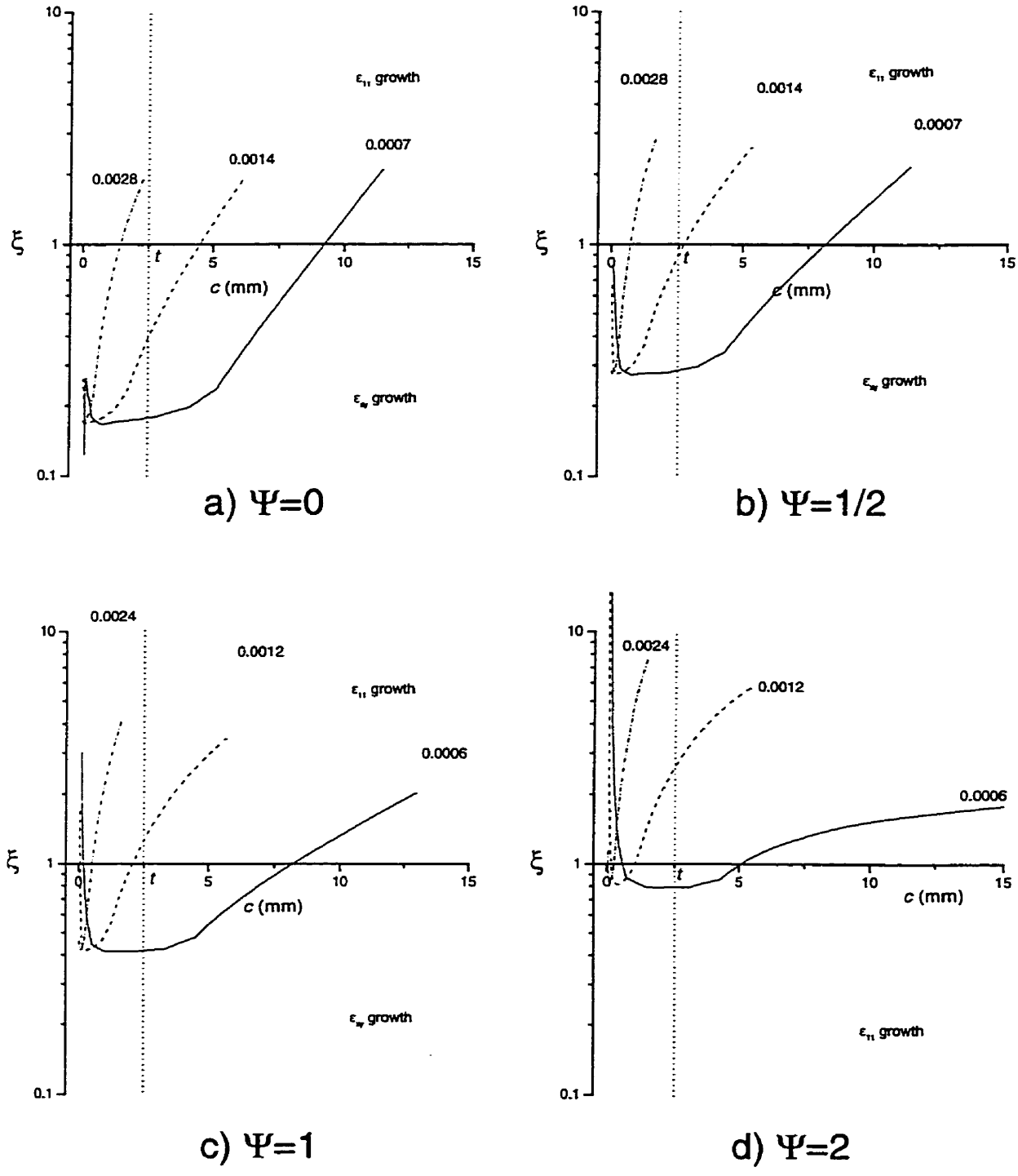

Figure 4.6: Shear crack to tensile crack transition predictions for the area model (ξ) for (a) $\Psi = \frac{\sigma_{xx}}{\sigma_{xy}}$=0, (b) Ψ=$\frac{1}{2}$, (c) Ψ=1 and (d)Ψ=2.

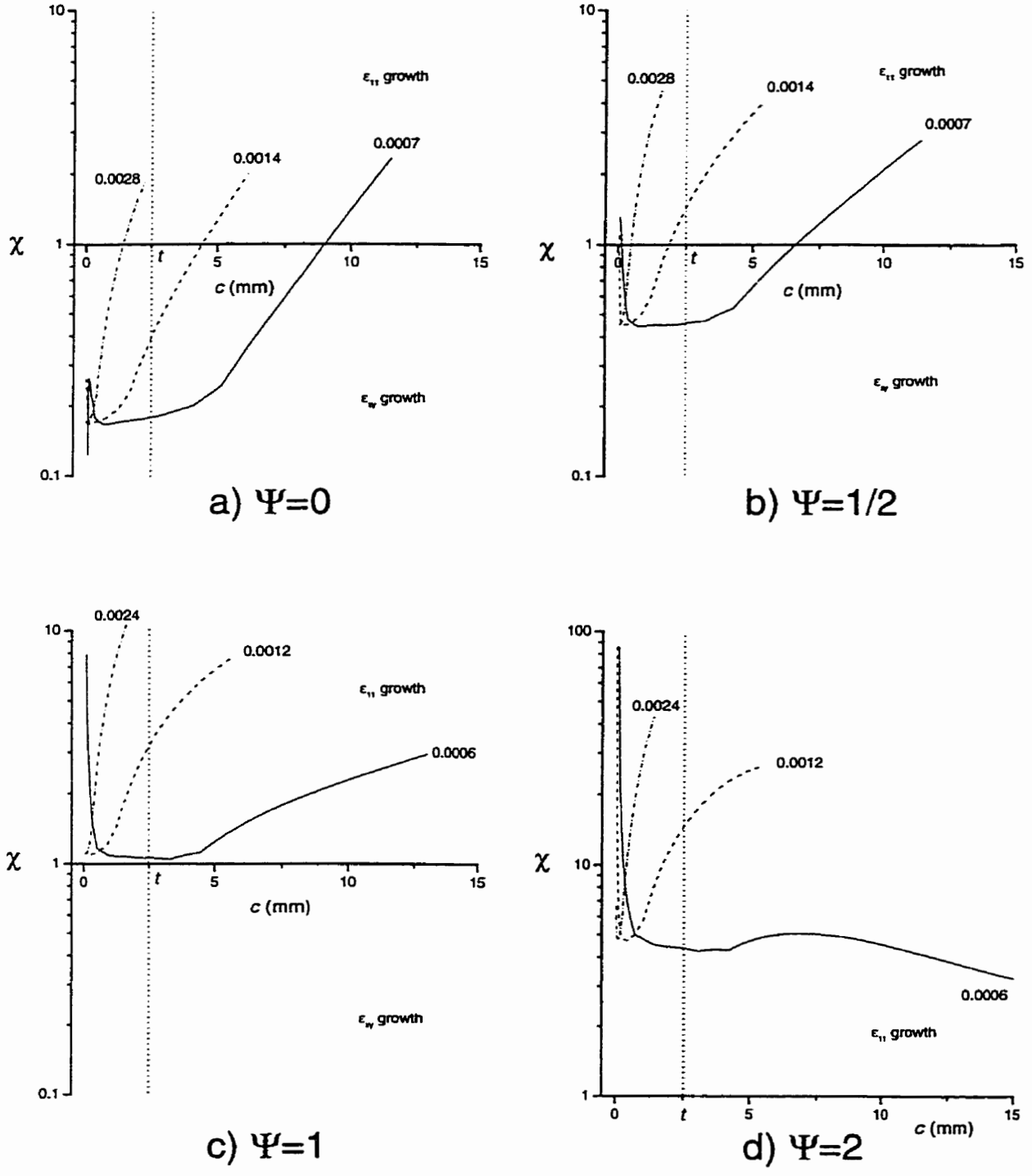

Figure 4.7: Shear crack to tensile crack transition predictions for the energy model (χ) for (a) $\Psi = \frac{\sigma_{xx}}{\sigma_{xy}}$=0, (b) Ψ=$\frac{1}{2}$, (c) Ψ=1 and d)Ψ=2.

For the other stress ratio (Figures 4.6b-d) the results are similar to those reported for Ψ=0. However, as the stress ratio increases to Ψ=0, 1/2, 1, and eventually to 2, each higher load ratio exhibits higher minimum values of ξ. This trend in ξ implies that tensile cracking becomes dominant as the load ratio increases, and this observation is supported by experimental observations – as the load ratio increased larger amounts of tensile crack growth were observed in the specimens. Over one-half of the Ψ=1/2 specimens exhibited some tensile crack growth; all but one of the Ψ=1 specimens exhibited a significant amount of tensile cracking (most also exhibited significant sections of shear crack growth); and at Ψ=2 all of the specimens had a significant amount of tensile cracking with very little shear cracking observed.

The trends predicted by the energy model (χ) are similar to those of the area model (ξ). However, for a given load ratio the energy model predicts a change to tensile crack growth before the area model will predict it. This is evident for Ψ=2 loading where the χ-diagram (Figure 4.7d) indicates only tensile growth while the ξ-diagram (Figure 4.6d) indicates that some shear growth will occur. However, the results of predictions for Ψ=0 loading are the same for the two models.

Another set of predictions were made using the same criteria to determine whether a tensile crack would change back into a shear crack, as observed in specimens subjected to Ψ=1/2 and 1 loading. Smooth tubular specimens subjected to these load ratios initially exhibited ES behavior, but subsequent cracking oscillated back and forth between tensile and shear planes. The model used for this prediction includes the same crack projection technique described in section 4.2.1 and Figure 4.4. The predictions are shown in Figures 4.8 and 4.9, where the ordinates are plotted as $1/\xi$ and $1/\chi$, respectively, so that, if a shear crack is favored, it appears above the abscissa.

The results of predictions are almost the same for the area and energy models. Only for Ψ=0 is there a predicted return to shear crack growth, but in only one specimen did the tensile crack return to shear cracking (after about 5mm of tensile cracking). The return to shear cracking after tensile cracking was commonly observed under Ψ=1/2 and 1, but neither model predicted it for these load ratios. The models were accurate in predicting no return to shear crack growth for Ψ=2 loading.

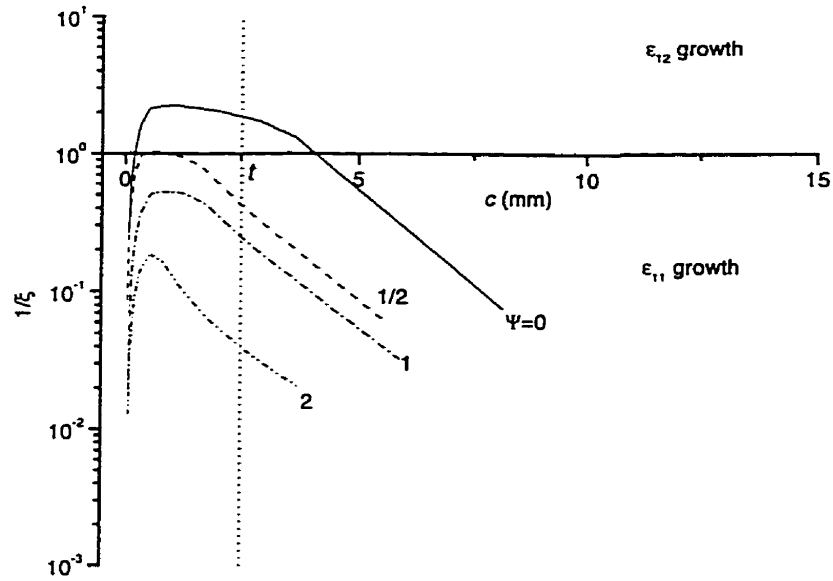

Figure 4.8: Tensile crack to shear crack transition prediction for ξ for tests at $\Delta\epsilon_{xy}$=0.0007 under $\Psi = \frac{\sigma_{xx}}{\sigma_{xy}}$=0, $\frac{1}{2}$, 1 and 2.

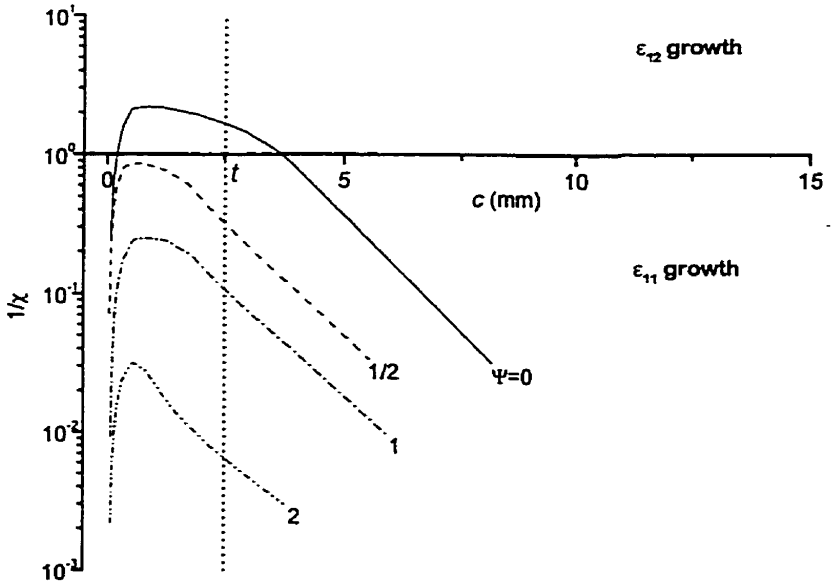

Figure 4.9: Tensile crack to shear crack transition prediction for ξ for tests at $\Delta\epsilon_{xy}$=0.0007 under Ψ=d, $\frac{1}{2}$, 1 and 2.

4.3 Crack Growth Life Predictions

Crack growth based life predictions were made to determine whether crack growth data and a strain based crack growth model would accurately predict fatigue lives for crack face interference-free crack growth. A series of baseline predictions for each stress ratio are first presented wherein the surface strain concentration profile for the crack [50] (described in section 1.2.2.1) is separately determined for that stress ratio. Subsequently, Ψ=0 and Ψ=∞ fatigue life curves were used to determine the surface strain concentration profiles for shear and tensile crack growth respectively. These surface strain profiles were used along with the crack area increment and strain energy release rate criteria to create life prediction models, and predictions were made for all of the load ratios.

Since the overload strain-life curves presented in Chapter 3 were presumed to be crack face interference-free (by virtue of the increased overload amplitude companion experiments) no attempt to model the interference process has been attempted. Hence in all of these models it is assumed that the applied strain is fully effective. In addition, since crack face interference-free crack growth data has been generated by removing the propagation due to the overload cycle from the crack growth curves (see sections 4.1.1 and 4.1.2) and the overload damage from the fatigue life curves (see section 3.1.2), the overloads are not modelled in the crack growth predictions.

4.3.1 Baseline Life Predictions

In Chapter 3 it was observed that the maximum shear strain criterion coupled with the uniaxial fatigue data would provide safe but not unreasonably conservative estimates of fatigue life for all of the load ratios. For this method the maximum shear strain is taken as the crack growth driving parameter, and it is coupled with the mode I fatigue data for the purpose of making life predictions.

The maximum shear strain criterion ($(\epsilon_{12})_{max}$) was transformed into a crack driving parameter

$$\Delta K(\epsilon) = 2Q_{\epsilon}\Delta\epsilon_{12}GF^{e}\sqrt{\pi a}, \tag{4.12}$$

where a is the crack length, F^e is the crack geometry factor, G is the shear modulus, $\Delta\epsilon_{12}$ is the maximum shear strain range, and Q_ϵ is the surface strain concentration factor [50].

The geometry factor used in the baseline life prediction is that of a semi-elliptical crack in a solid, F^e as given in Appendix B, section B.2.2. Because this geometry factor is strongly influenced by the ellipticity of the the crack ($\frac{a}{c}$), both crack growth into the specimen (a dimension and negative z-direction) and crack growth along the surface of the specimen (c dimension) must be modelled. Since, when using the prediction it is assumed that the crack is loaded in a shear mode, the crack growth into the specimen (mode III) and along its surface (mode II) are then modelled by

$$\Delta K_{III}(\epsilon) = 2Q_\epsilon \Delta\epsilon_{12} G F^e_{III}\sqrt{\pi a} \qquad \text{and} \tag{4.13}$$

$$\Delta K_{II}(\epsilon) = 2Q_\epsilon \Delta\epsilon_{12} G F^e_{II}\sqrt{\pi a}, \tag{4.14}$$

respectively. Once the crack grows through the wall of the specimen the geometry factor is changed to that of a through crack in a tube, F^t_{II}, as given in Appendix B, section B.2.1. In this case the crack driving equation becomes

$$\Delta K_{II}(\epsilon) = 2\Delta\epsilon_{12} G F^t_{II}\sqrt{\pi c}. \tag{4.15}$$

The transition from an elliptical crack of surface crack length c tangent to the inner diameter of the tube (in the a dimension) to a through crack of crack length c is assumed to be instantaneous. Under mode I loading, this assumption is reasonable since, at the point of intersection, the crack geometry factor has been estimated to be quite large [94, 95] and, as a result, the uncracked ligament is cracked in a relatively small number of cycles. Under shear loading (mode II/III) it is assumed that a similar process takes place. Finally, the error introduced by this assumption is in part offset by the lack of a back face correction in the analysis – a correction for the inner wall of the tube which raises stress intensity values for the crack and shortens the number of cycles predicted for the crack to reach the inner diameter of the specimen. The assumption of an instantaneous transition also helps to offset the lack of a back face correction by shortening the total predicted number cycles to failure.

The function Q_ϵ, proposed by Abdel-Raouf et al. [50], is given by

$$Q_\epsilon = \frac{\Delta\epsilon}{\Delta e} = 1 + qe^{-\frac{a}{D}a}. \tag{4.16}$$

As discussed in the introduction, this term estimates the strain concentration for a short crack in a favorably oriented grain. The value of q is usually taken as 5.3, and $\frac{a}{D}$ is usually calculated using the stress intensity threshold, ΔK_{th}, and the closure free fatigue limit strain range, Δe_{th}, and the following equation

$$\Delta e_{th} = \frac{\Delta K_{th}}{Q_\epsilon EF\sqrt{\pi a}}. \tag{4.17}$$

The value of $\frac{a}{D}$ is adjusted until the value of the peak of the curve produced by equation 4.17 matches the experimentally observed Δe_{th}. This calculation technique may be used in situations where the geometry factor is stable for the range of crack lengths where where Q_ϵ has an influence (approximately five grain diameters). However, the geometry factor selected for these models is highly sensitive to crack ellipticity ($\frac{a}{c}$). Both the crack growth simulations in this thesis and experimental observations elsewhere [4] have indicated that the surface crack length remains unchanged while the crack grows in depth thus changing ellipticity greatly from nearly 0 to nearly 1 within the five grain diameters of depth. As a result, it was necessary to estimate $\frac{a}{D}$ independently by iterating the entire model until the fatigue limit in the life predictions matched the experimental fatigue limit data. This iterating was performed separately for each stress ratio.

The initial crack depth, a_o, was set at the length of a slip band crack, $3\mu m$. The initial surface crack length, based on specimen surface crack length observations, was set at $2c_o = 100\mu m$. One failure criterion for the model was defined as the point at which the current crack length reached the final crack length, c_f, and this was set at the specimen gage length, $2c_f = 30mm$, because most cracks reached this length before the specimen was removed. Another failure criteria was set at the point where K_{max} reached K_c. The critical stress intensity was taken to be $64\text{MPa}\sqrt{\text{m}}$ [96].

The crack growth data used in the baseline modelling were the mode I crack growth data, converted to shear using the formulae presented in section 2.4.1. The

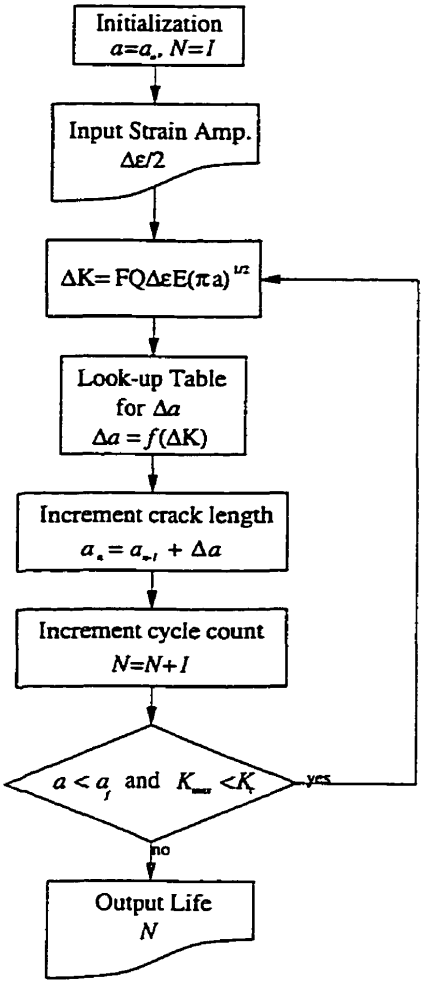

Figure 4.10: Typical algorithm for crack growth life prediction.

experimental crack growth data did not extend to K_c, and when growth rates exceeded experimental values the curve representing the crack growth data was extrapolated to K_c. Predictions in which more than one-third of the cycles were spent in this region were discarded. This cutoff was applied to all predictions, whether they used mode I or mode II growth curves.

A flow chart typical of a generic crack growth calculation algorithm is presented in Figure 4.10. A more specific flowchart is introduced later for the energy (area) crack growth model.

The results of baseline crack growth predictions for Ψ=0, 1/2, 1, 2, and ∞ are

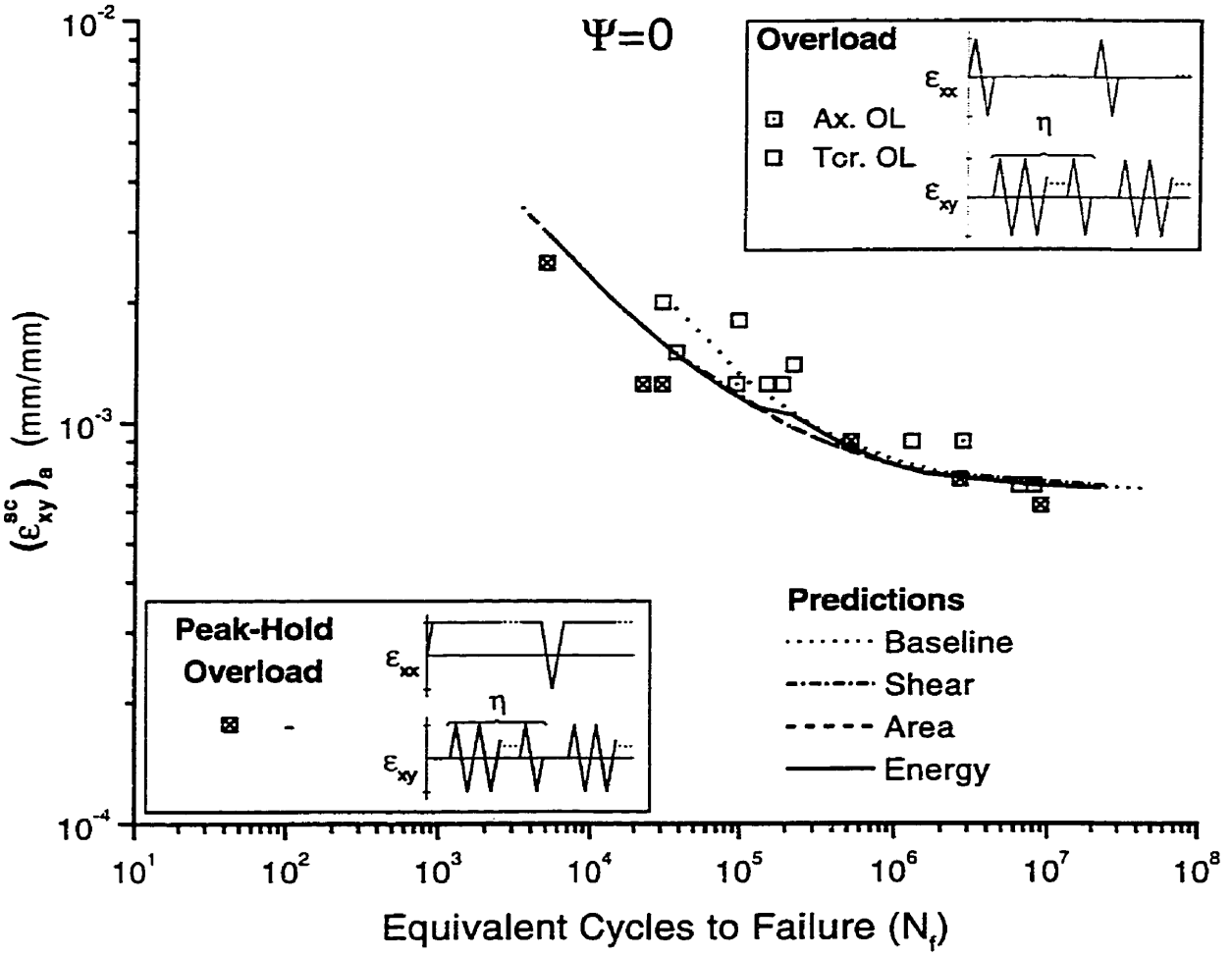

Figure 4.11: Crack growth predictions for $\Psi = \frac{\sigma_{xx}}{\sigma_{xy}}$=0 tubular overload experiments.

presented in Figures 4.11 through 4.15, respectively. The heavy dotted line in these figures represents the baseline prediction. In general, the baseline predictions give good predictions of the overload data for all of the stress ratios. A detailed discussion of the predictions of this and subsequent models will be presented later.

4.3.2 Shear and Tensile $\frac{\alpha}{D}$ Estimates (and Predictions)

In order to use the crack area increment and strain energy release rate criteria, it was necessary to estimate the value of the $\frac{\alpha}{D}$ parameter (from Q_ϵ) for shear and tensile

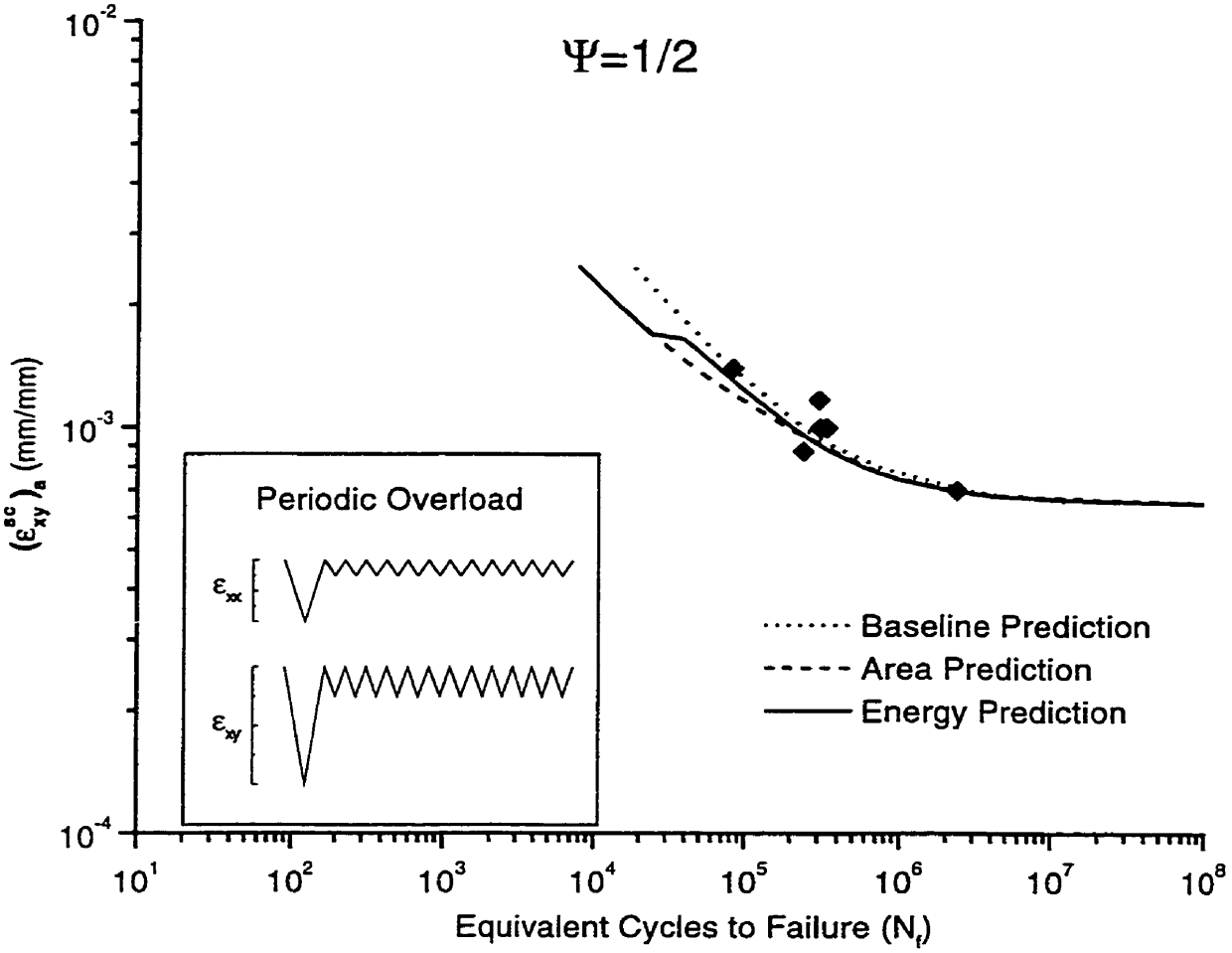

Figure 4.12: Crack growth prediction for $\Psi = \frac{\sigma_{xx}}{\sigma_{xy}} = \frac{1}{2}$ tubular overload experiments.

crack growth. As in the previous section, the estimates of $\frac{a}{D}$ for shear and tensile crack growth were determined by using the entire crack growth model and matching the predicted fatigue limit with that observed in the experimental data for Ψ=0 and Ψ=∞, respectively.

The determination for shear was carried out with a model very similar to that discussed in the previous section. The only difference was that the mode II shear crack growth curve was employed rather than the modified mode I curve. The value for $\frac{a}{D}$ was estimated to be 105,000. The shear prediction is represented as the dash-

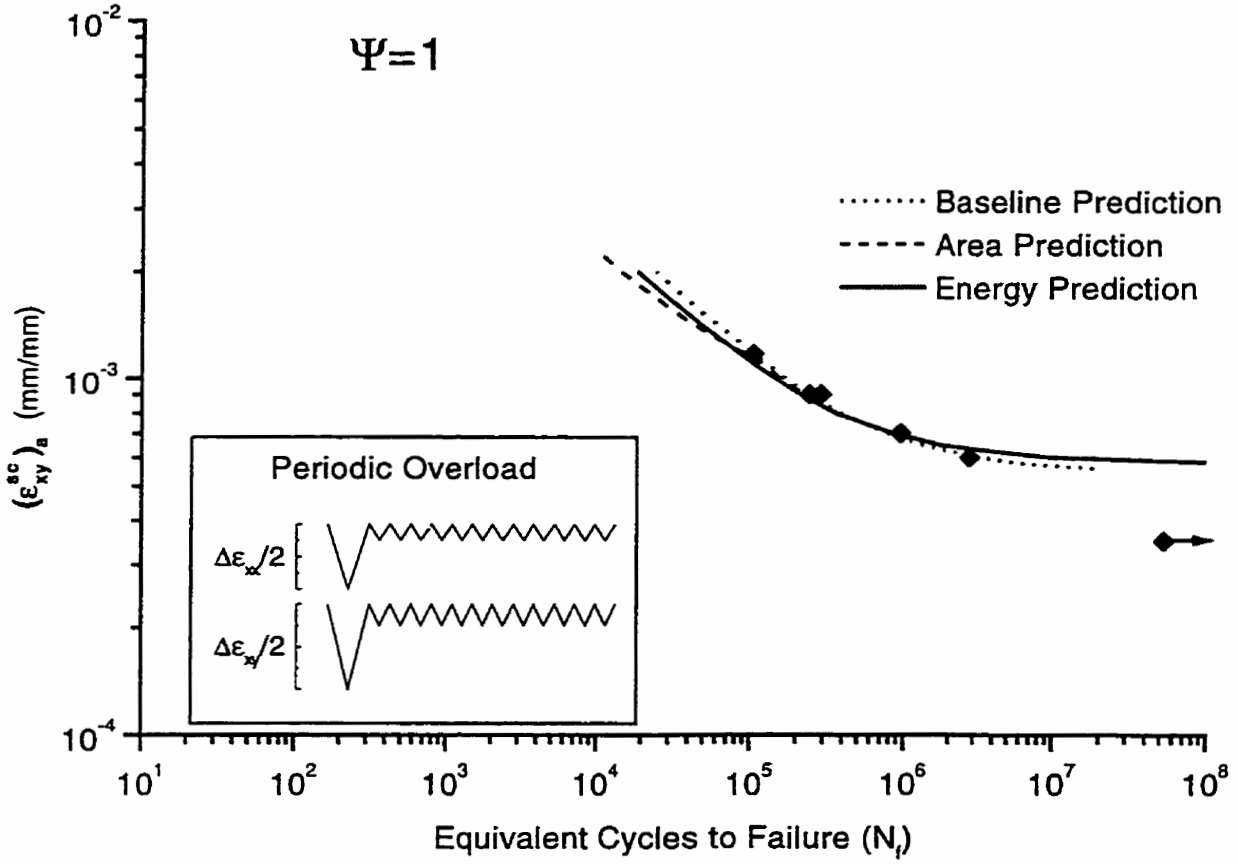

Figure 4.13: Crack growth prediction for $\Psi = \frac{\sigma_{xx}}{\sigma_{xy}}$=1 tubular overload experiments.

dot curve in Figure 4.11. This curve is partially obscured by the curve labelled "Area" because the "Area" curve inherited the same crack growth model and $\frac{a}{D}$ value from the shear prediction model.

The tensile growth prediction was carried out using the Ψ=∞ overload data and the mode I crack growth data. The crack growth model used an entirely different geometry factor – an elliptical crack in a circular cross section under tensile loading. While the model used the same general algorithm as used in the previous section, the stress intesity equation was replaced by

$$\Delta K_I(\epsilon) = Q_\epsilon \Delta\epsilon_{11} E F_I^{ss} \sqrt{\pi a}, \tag{4.18}$$

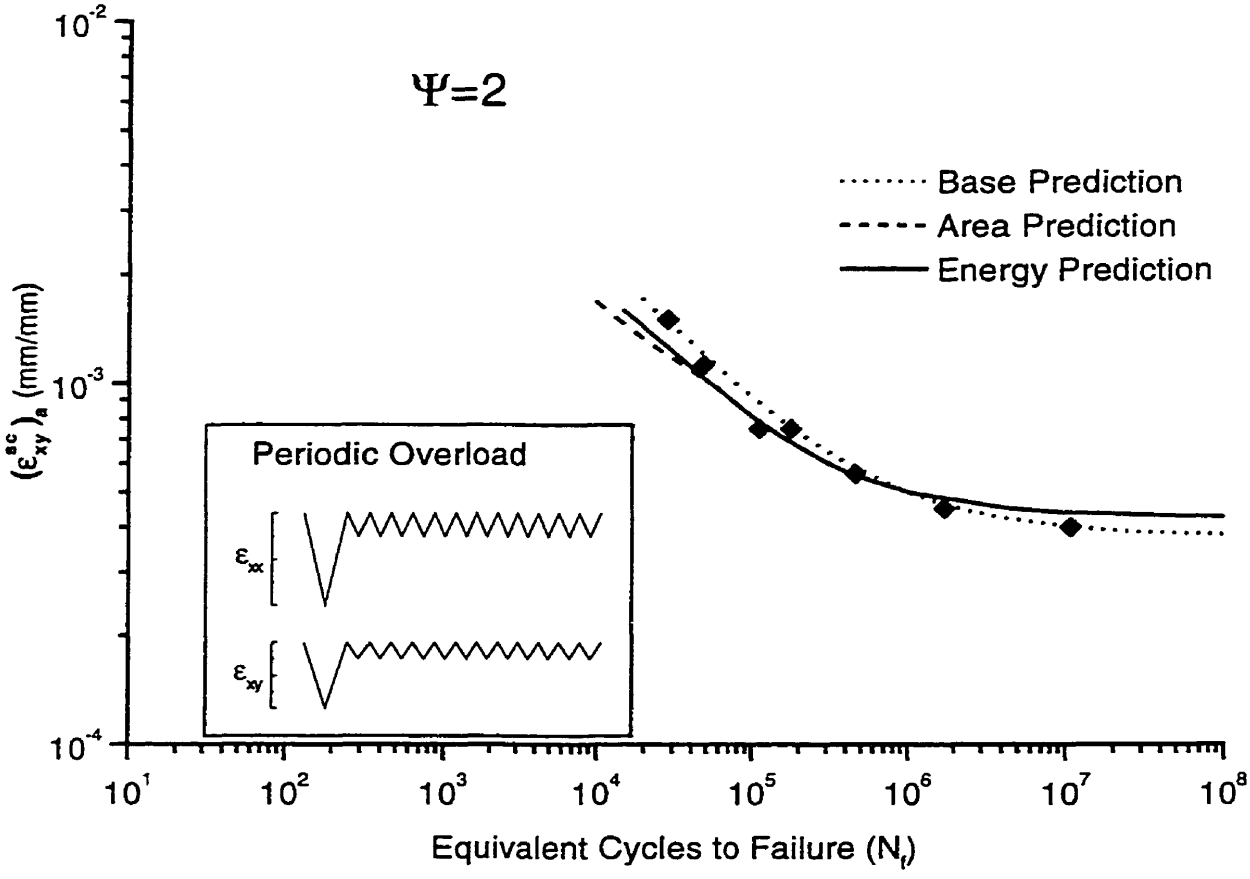

Figure 4.14: Crack growth prediction for $\Psi = \frac{\sigma_{xx}}{\sigma_{xy}}$=2 tubular overload experiments.

where $\Delta\epsilon_{11}$ is the maximum principal strain range, and F_I^{ss} is the geometry factor, presented in Appendix B, section B.1.2, for an elliptical crack in a circular cross section under tensile loading. This geometry factor was used because it best models the uniaxial specimen geometry. Further, no modelling of the surface crack length was performed, as the model made calculations for the a dimension only. Since the geometry factor was stable, the value of $\frac{a}{D}$ could be calculated by matching the peak of the curve determined from

$$(\Delta\epsilon_{11})_{th} = \frac{\Delta K_I(\epsilon)}{Q_\epsilon E F_I^{ss}\sqrt{\pi a}}, \tag{4.19}$$

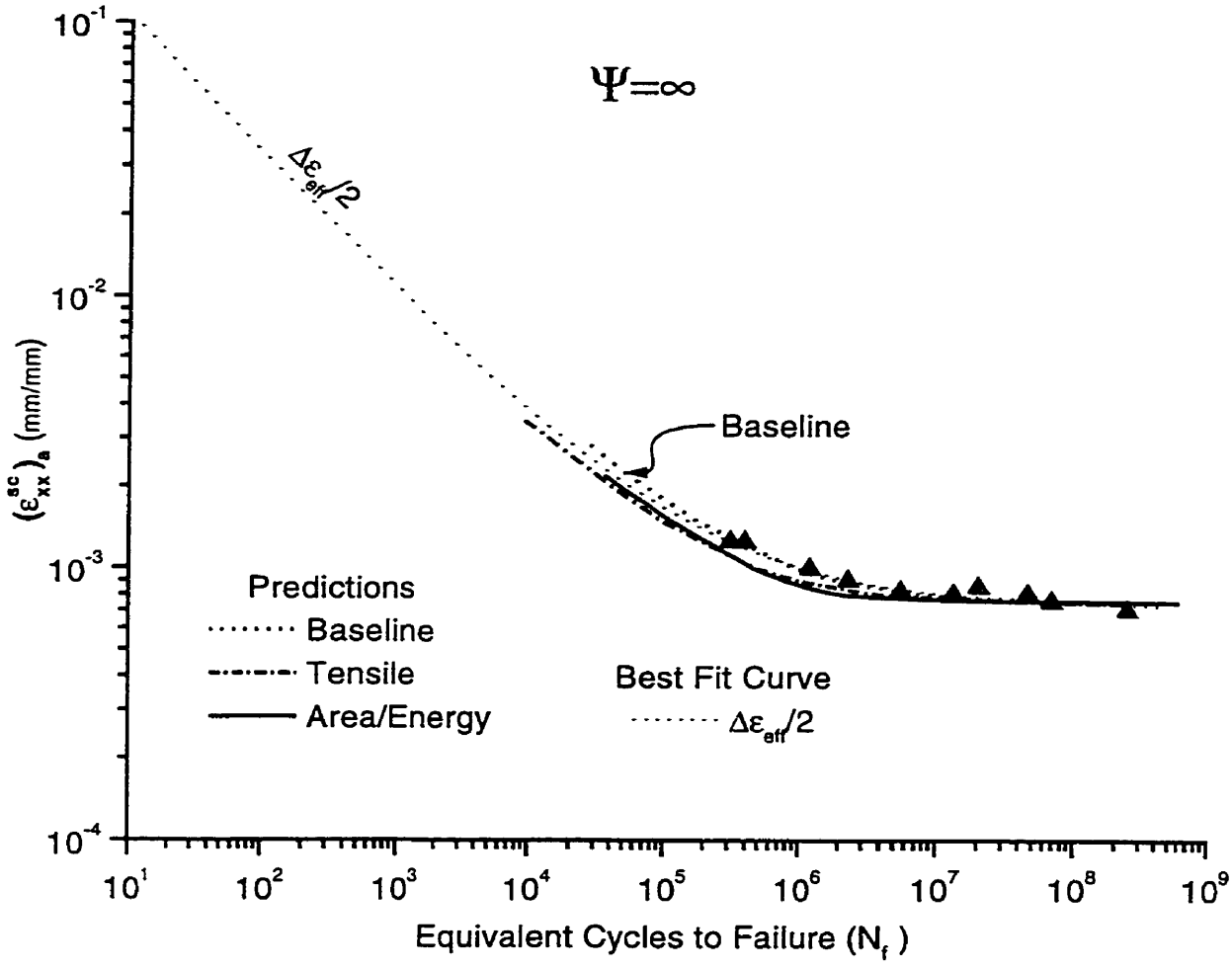

Figure 4.15: Crack growth prediction for $\Psi = \frac{\sigma_{xx}}{\sigma_{xy}} = \infty$ uniaxial overload experiments.

with the observed threshold strain range from experiments. This value was calculated to be 45,000.

Two failure criteria for this model were used. These were the exceedence of the final crack length, $a \geq a_f$ ($a_f = 5.08mm$), or the critical stress intensity, $K_{max} \geq K_{Ic}$.

The results of these crack propagation calculations, labelled "tensile prediction," are presented as the dash-dot line in Figure 4.15 along with both the mode I overload fatigue life data and the effective strain-life curve originally presented in section 3.1.2.

4.3.3 Crack Area Increment and Strain Energy Release Rate Growth Models

In this portion of the modelling the shear and tensile $\frac{a}{D}$ values calculated in the previous section were used to predict both fatigue life and crack growth mode changes observed for all of the stress ratios.

The crack growth models are similar to the one used in predicting the baseline fatigue curves in section 4.3.1, but modified to allow the model to predict tensile growth. As reported in section 4.1.3, cracks in tests of tubular specimens initiated on shear planes and either continued to propagate in shear or switched to tensile crack growth. For biaxial loading ratios Ψ=0, $\frac{1}{2}$, and 1 shear cracks initiated on longitudinal shear planes, and for Ψ=2 shear cracks initiated on the maximum shear strain plane.

Hence, in modelling crack growth, all cracks are started in shear on the experimentally observed initiation plane. In addition, cracks are constrained to grow to a depth of at least one grain diameter ($25\mu m$) on this plane. This constraint is imposed based upon observations made by Varvani-Farahani [4]. He observed that shear cracks started out with a shallow depth and a long surface crack length (very low $\frac{a}{c}$), and most of the specimen life was spent while these cracks deepened without appreciable surface propagation until $\frac{a}{c}$ reached roughly one. He determined that this transition depth was of the order of a few grain diameters.

Once a shear crack has grown to a depth of one grain diameter, the model was then allowed to choose between continued growth on a shear plane, or to switch to growth on a principal stress plane. In each of the models one of two criteria are used to make this decision: these are the crack area increment criterion (discussed in section 4.2.1), or the strain energy release rate criterion (discussed in section 4.2.2).

The techniques discussed in section 4.2.1 for projecting equivalent tensile crack lengths from the original shear crack are used in these models. The transition to a tensile crack is assumed to be instantaneous. The crack depth, a, is not modified when the switch to tensile crack growth is made, and once the crack depth reaches the tube wall thickness, 2.5mm, the crack growth geometry factor is switched to a through-crack of length $2c$ in a tube – these geometry factors are detailed in Appendix B,

section B.2.1. The crack growth mode (shear or tensile) that the crack is in when it reaches the wall is maintained until failure ($2c$=30mm).

Figure 4.16 gives a flow chart which details the operation of the program. The full program code for crack predictions under the energy criterion is provided in Appendix C, and the predictions for both criteria are given in Figures 4.11 through Figures 4.15. In these figures the dashed line represents predictions made with the crack area increment criterion and the solid line indicates predictions made using the strain energy release rate criterion.

4.3.4 Discussion of Predictions

The predictions for Ψ=0 are presented in Figure 4.11, together with all of the fully effective torsional data. Since the mode II crack growth data was produced using torsional overloads combined with torsional small cycles it was expected that it would give good predictions for the strain life curve for fatigue life tests subjected to the same loading (data marked by open squares). In fact, for strain amplitudes above the fatigue limit all of the predictions are conservative for this data. The baseline prediction which gives the best fit to this data lies at the leftmost edge of the test data. The rest of the predictions are even more conservative. The crack growth predictions fall closer to the out-of-phase torsional tests. There are two possible reasons for the conservative predictions for axial and torsional overload tests and for those tests having longer lives than the peak-hold overload tests.

Firstly, although results from the high overload strain amplitude companion test discussed in section 3.2.1.1 indicated that the fatigue cracks in these experiments grew crack face interference-free, it is possible that fatigue cracks in the in-phase Ψ=0 fatigue life tests did not grow entirely free of crack face interference. The presence of interference would cause the experimental lives to shift to higher values.

The discrepancy may also be due in part to the way in which the mode II crack growth data was prepared. When crack bifurcation took place, the crack growth rate slowed considerably when compared with the growth rate when the crack growth was along a single line. Crack growth data obtained when bifurcation occurred were

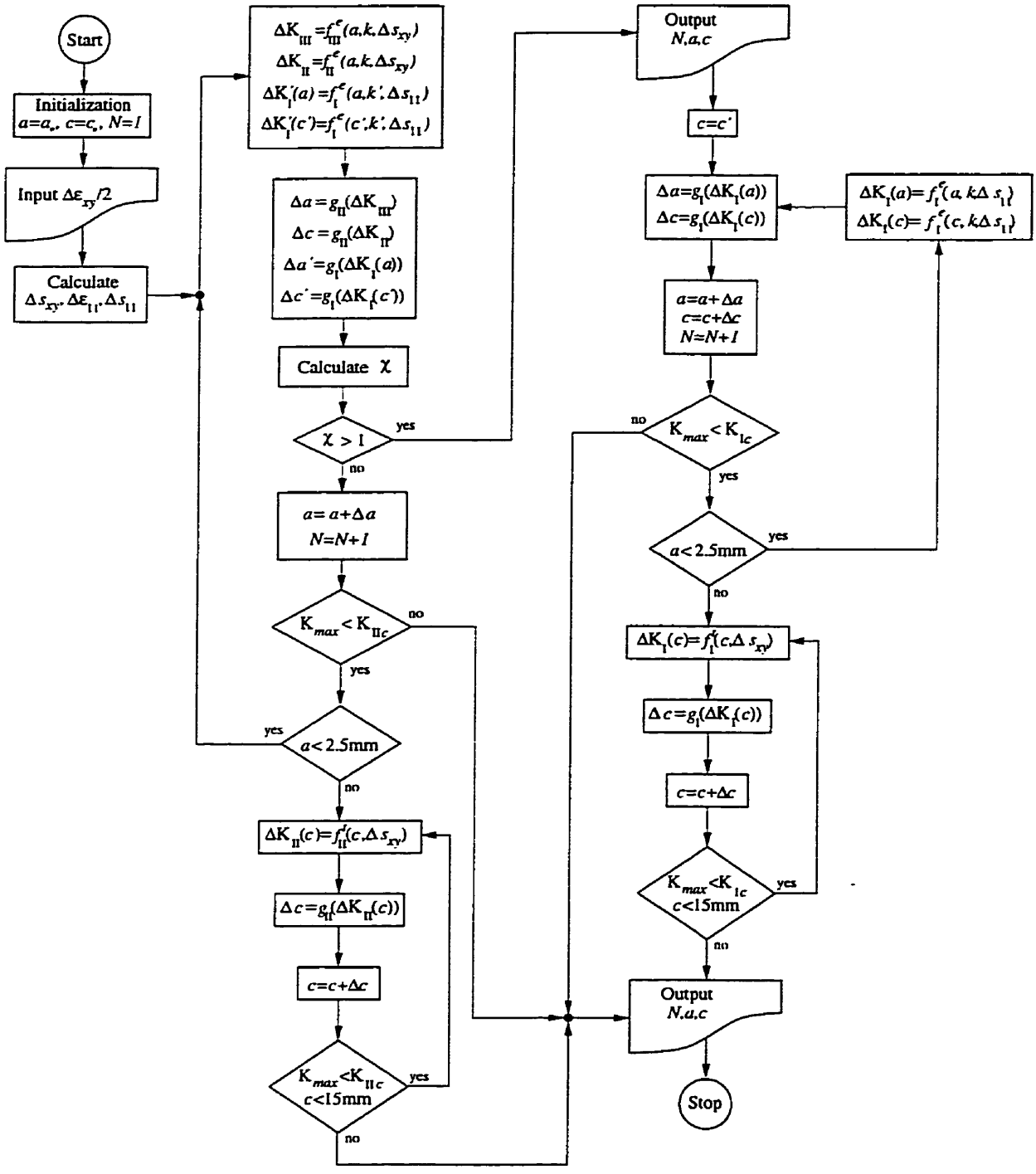

Figure 4.16: Flow chart for strain energy release rate crack prediction program.

eliminated in order to obtain the most conservative crack growth curve. However, since bifurcation occurred frequently throughout the torsional overload tests, it is probable that the crack growth data is unduly conservative. Differences in the amount of bifurcation may also explain the discrepancy at higher strain levels between the three different types of overloads. The axial peak-hold overload tests exhibited the least crack bifurcation (as well as promoting crack growth on the circumferential shear plane) and the shortest fatigue lives.

The second possible source of error may come from the assumption originally proposed in section 1.2.2.1, where it was postulated that the mode II shear crack growth data could be used for mode III crack growth modelling. If this assumption is incorrect, then an error may have been introduced in the crack growth predictions. However, in section 4.1.2 the mode II data generated in this research was compared with mode III short crack growth data from another source and the combined data formed a common band. Hence, if an error arises from this assumption it is believed to be small.

The dashed and solid lines in Figure 4.11 represent the predictions made with models which used the area criterion and energy criterion for switching crack growth mode, respectively. At all strain amplitude levels the predictions of the area model match those of the "shear" prediction curve, which is indicated by the dash-dot line. Since these tests are dominated by shear crack growth and this criterion tends to predict shear crack growth, this behavior is not surprising. At the fatigue limit the energy criterion based crack growth model initially falls along the shear calibration curve, but above $(\epsilon_{xy}^{sc})_a$=0.0008 it falls at longer lives. It follows this trend up to roughly $(\epsilon_{xy}^{sc})_a$=0.001 where it abruptly shifts back to the "shear" prediction curve. Although both the area and energy criteria predict a shift to tensile growth near the fatigue limit, the energy criterion continues to predict tensile mode cracking for strains up to $(\epsilon_{xy}^{sc})_a$=0.001. Since the shear growth curve at the shift point is a factor of two lower in life, a discontinuity arises in the predicted curve. This kind of discontinuity will not arise in the area predictions because this criterion switches growth behavior where the tensile and shear growth curves cross.

Results of life predictions for $\Psi=\frac{1}{2}$ are given as curves in Figure 4.12 along with experimental overload data. As in $\Psi=0$ loading the best prediction is given by the baseline (dotted) curve, and the predictions for the area (dashed curve) and energy models (solid line) are again more conservative. For strain amplitudes up to $(\epsilon_{xy}^{sc})_a=0.001$ both models predict the same curve, but above this level the curves diverge with the area model providing the more conservative estimate. The energy curve rejoins the area curve at $(\epsilon_{xy}^{sc})_a=0.0018$. The energy model provides a better prediction than the area model, but it shows the discontinuity discussed above.

Figure 4.13 shows crack growth predictions for $\Psi=1$. Once again, the baseline prediction (dotted line) provides the best fit to the overload data. The area (dashed line) and energy (solid line) criteria provide the same predictions up to strain amplitudes of $(\epsilon_{xy}^{sc})_a=0.0012$. Above this amplitude, the area model predicts somewhat shorter lives than the energy criterion. The same shift as before in the energy criterion curve in fact does occur, but it is above the strain level where the predictions are cut off. In terms of a comparison with the experimental data, neither criterion can be said to be better – the experimental data is insufficient to make an assessment.

The prediction for $\Psi=2$ are shown in Figure 4.14. In comparison with experimental data the energy model is slightly better than the area model in predicting the life of the highest data point. Again, the best prediction of the experimental data is given by the baseline model – the prediction line runs through nearly every data point.

However, the area and energy models are 7% unconservative in predicting the $\Psi=2$ fatigue limit strain – they predict $\Delta\epsilon_{xy}=0.0043$ at 10^7 cycles to failure rather than the actual value of 0.0040. The reason that the area and energy models do not predict the fatigue limit is that the model predicts incorrectly the location of the crack length at which the maximum in the threshold stress for crack growth occurs. This is apparent in Figure 4.17, which plots threshold of the applied torsional strain range ($(\Delta\epsilon_{xy})_{th}$) for shear and tensile growth versus crack length. These two curves were calculated using two crack growth models – one for shear and the other for tensile crack growth. Both used the elliptical crack geometry factor employed in both the area and energy crack growth models. Various strain amplitude levels (and crack

lengths for the negatively sloped portions of the diagrams) were input into each model, the crack was grown, and the crack length at arrest was recorded. When plotted, a boundary between the region in which cracks will grow and not grow results. In the figure tests with a strain range below the peak of the lower of the tensile (dashed curve) or shear (solid curve) resistance curves will have fatigue cracks which arrest. The experimental fatigue limit is given in Figure 4.17 by a horizontal dashed line. A dashed line indicates tensile crack growth and a solid line indicates shear crack growth. Although it is known that cracks in the experiments started as shear cracks, exact data is lacking for these experiments regarding the crack length at switch over into tensile growth – it is, however, believed to be less than $50\mu m$. The fatigue limit for both crack growth models is also drawn as a horizontal line in Figure 4.17, and in this case the crack growth models predict shear crack growth out to $32\mu m$ at which point they switch to tensile crack growth (as indicated by the dashed line) which continues to failure.

A threshold diagram for Ψ=1 loading is shown in Figure 4.18. In this case the crack growth models correctly predicted the experimental threshold – in the models the crack grows in shear until it reaches approximately the peak of the tensile curve ($30\mu m$) and then switches to tensile growth and grows to failure.

The final set of predictions is given in Figure 4.15 for uniaxial loading ($\Psi = \infty$). Along with the predictions is plotted the effective strain curve (thin dotted line) which was independently developed in section 3.1.2. The role of the predictions and the effective strain curves are similar – they are both estimates of the fully open strain-life curve. All of the predictions, including the baseline (heavy dotted line), calibration (dash-dot line), and the area and energy (solid line), fall into a narrow band of less than a factor of two. The best prediction is again given by the baseline model. The area and energy models predict the same curve for uniaxial loading. Unlike the behavior observed for Ψ=0 loading where the area and energy model predictions overlayed that of the "shear" model, the single curve for the area and energy models and the curve for the "tensile" model differ slightly for $\Psi = \infty$ because these two curves were predicted using two different geometry factors (as discussed earlier).

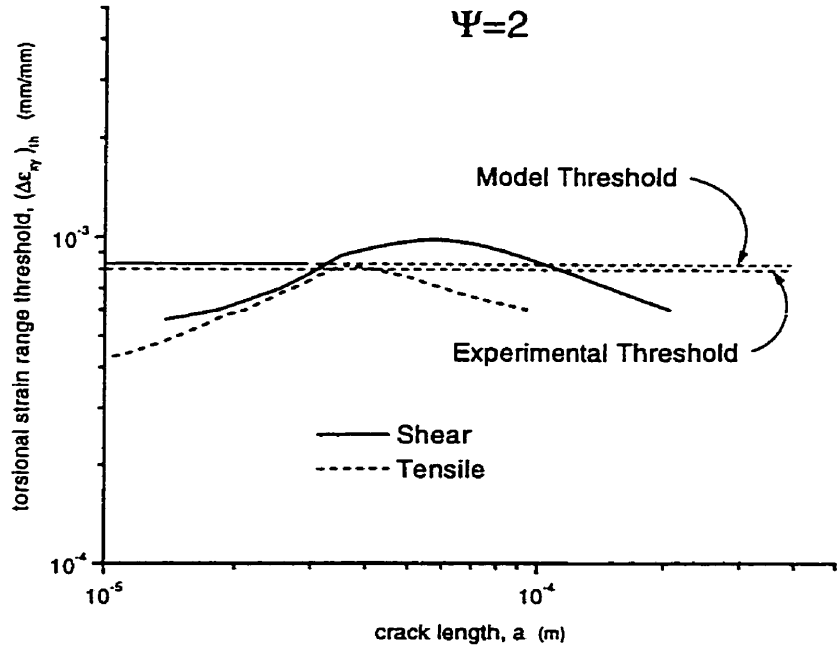

Figure 4.17: Threshold conditions for shear and tensile growth for Ψ=2.

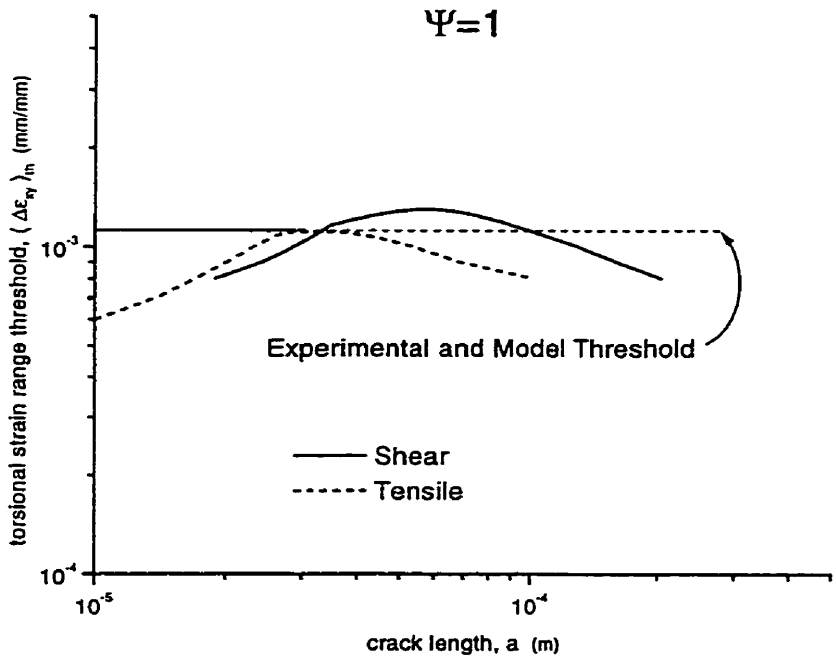

Figure 4.18: Threshold conditions for shear and tensile growth for Ψ=1.

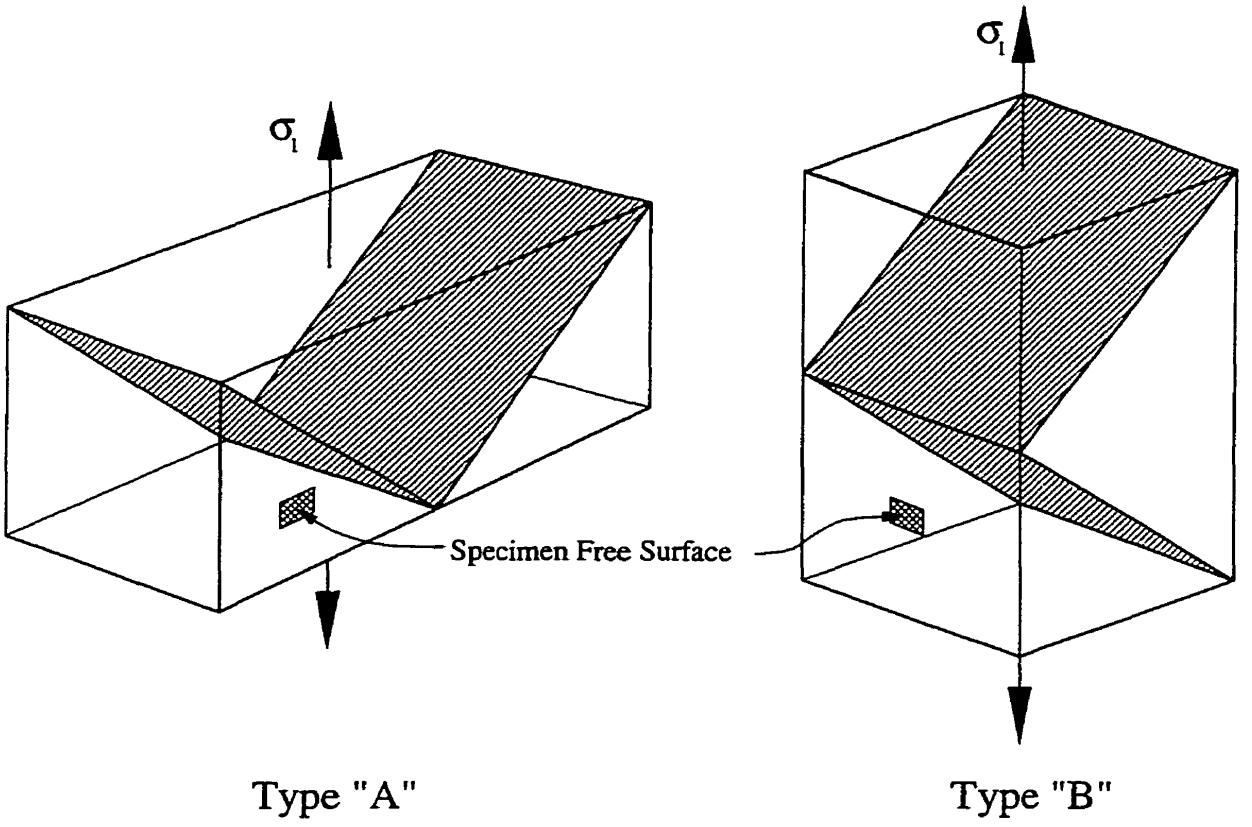

Figure 4.19: Crack initiation types from [38].

A small difference exists between the crack growth model used for the uniaxial predictions and the models used for the other load ratios. Because the plane on which the shear crack propagates is substantially different for uniaxial loading, the projection algorithm for uniaxial loading was changed. The difference is depicted in Figure 4.19 where the shear crack types are presented as defined by Brown and Miller [38]. The crack growth models for Ψ=0 through Ψ=2 assume type A shear crack growth because all of the tube tests exhibited this behavior. However, uniaxial cracks initiate as type B [87], and the tensile crack growth models were modified to reflect this difference. This difference affects only the crack projection technique, where, for type A cracks a shorter c-dimension is projected and for type B cracks a shortened a-dimension is projected. See section 4.1.3 for the discussion on crack projection.

4.4 Summary

Further observations from and analysis of the tube test data of Chapter 3 have been presented. It was noted that tubes initially cracked in shear for all of the load ratios and that often these shear cracks eventually made a transition to a tensile plane. For all stress ratios it was observed that a transition to tensile cracking occurred at fatigue limit strain amplitudes. As strain amplitudes increased, the length of the initial shear crack increased, and at the highest strain amplitudes the initial shear crack continued growing until it reached the specimen gage length. Superimposed on this trend was another in which, as the load ratio increased, tensile cracking occurred at shorter initial shear crack lengths. Three regions of behavior were identified; in the first region (SI) the initial shear crack growth region was small before the switch to tensile growth, in the second region (ES) there was extensive shear crack growth before a transition to tensile growth, and in the last region (SD) the shear crack grew to failure without changing to a tensile growth mode.

A fully effective mode I crack growth curve and a crack face interference-free mode II curve were obtained for normalized 1045 steel, These curves were combined with a crack area increment and a strain energy release rate model to predict the length at which the transition from shear cracking to tensile cracking occurred – the initial shear crack length. Both models substantially underpredicted these shear crack lengths, although in a few cases the predictions came within 30% of the actual observed transition crack lengths. It was noted that the change in mode of cracking in these tubes was of a stochastic nature – there were frequent examples of tubes which did not follow the general trend. The crack area increment and strain energy release rate models also provided estimates of the range of strain amplitudes for which shear and tensile crack growth should occur. The crack area increment model overpredicted the strain amplitudes at which the transition between ES and SD behavior occurred. In contrast, the strain energy release model underpredicted the strain amplitudes at which the transition occurred from ES to SD behavior. However, both models predicted the trends observed in the experimental data; these were (1) as the strain

amplitudes increased initial shear crack lengths increased, and (2) as the load ratio increased the initial shear crack lengths decreased.

Predictions were made using the mode I and mode II crack growth curves developed earlier. The first set of predictions, which were termed the baseline predictions, were the most successful in predicting the strain-life curves for all load ratios. These predictions were created by taking the shear strain amplitude criterion of the previous chapter and combining it with mode I closure free crack growth data. The shear strain amplitude criterion was changed to a crack growth parameter and the mode I data converted to shear crack growth data. These were successfully combined with a semi-elliptical shear crack geometry factor to make the predictions. For each load ratio the value of the parameter $\frac{a}{D}$, which determines the surface strain concentration profile and hence the fatigue limit strain amplitude, was separately determined. This was done for a given load ratio by iterating the prediction of the fatigue limit strain until it matched that observed experimentally for that load ratio.

Another set of predictions were made which allowed the crack to change crack mode using one of two criteria. The crack growth (area) increment and strain energy release rate models discussed above were used to make fatigue life prediction. Each criterion was used in a separate prediction model to predict the fatigue life. The models were allowed to predict either shear crack or tensile crack growth, and in order to do this the values of $\frac{a}{D}$ parameter for the surface strain concentration profile (as discussed above) for shear crack growth and tensile crack growth were determined from tensile dominated ($\Psi = \infty$) and for shear dominated (Ψ=0) datasets. The shear and tensile $\frac{a}{D}$ were then inserted into the crack growth models, and the models were used to make predictions for all of the load ratios. The predictions provided by both the area and energy models were safe but not overly conservative. For lower load ratios (Ψ=0 and 1/2) the energy model predicted a discontinuity in the strain life curve which arose from the transition from ES behavior to predicting SD behavior. With the exception of Ψ=2 loading, the model adequately predicted the fatigue limits of all of the load ratios.

Chapter 5

Summary and Conclusions

The purpose of this investigation was to observe the effect of overloads in multiaxial fatigue. In-phase strain controlled constant amplitude and periodic overload tests were conducted on tubular specimens, and the tension-torsion strain ratio was selected such that the stress ratios at the overload loop tips were Ψ=0, 1/2, 1, 2, and ∞. In in-phase tests both the overloads and small cycles shared the same strain ratio.

- Periodic overloads reduced the 10^7 cycle endurance limit of normalized SAE 1045 steel to one-half for all load ratios. Further tests conducted on a notched shaft under Ψ=0 loading exhibited similar results. Experiments in which cycling was continued out to 10^8 cycles (Ψ=0 and ∞) exhibited a further endurance limit reduction to 2/5 of the constant amplitude value. A final set of experiments were performed in which axial periodic overloads were combined with torsional (Ψ=0) small cycles and in these experiments the 10^7 cycle endurance limit was also reduced to one-half of the constant amplitude level.

- Companion tests with overloads higher than those used in the test series were performed on one specimen at each stress ratio in order to determine whether the overload level used in the regular tests was large enough to produce crack-face interference free conditions. These tests indicated that the overloads used did produce a maximum fatigue life reduction, and it should follow that for small cycle amplitudes below that employed in the companion test, the fatigue cracks would grow under crack face interference free conditions. Simple models,

supported by fractographic evidence, were used to describe the nature of crack face interference and explain how it was reduced by overloads.

- Von Mises equivalent stresses and strains suitably consolidated the in-phase constant amplitude and periodic overload stress-strain data into a single curve. Uniaxial data and the von Mises equivalence equations can reasonably be used to model stress-strain behavior for other load ratios.

- A series of multiaxial damage parameters were examined in order to determine which best correlated fatigue data for different strain ratios. In the case of the constant amplitude data it was found that plotting the resolved shear strain from the initiation plane against fatigue life provided a good data consolidation. Maximum shear strain also gave a good consolidation of the constant amplitude data. For the periodic overload fatigue data the Fatemi-Socie-Kurath style parameter gave the best consolidation. However, the maximum shear strain parameter also provided a good consolidation of the data and is simpler to implement.

- The cracking behavior of tubes was observed and recorded for the various tests. The observed initiation planes were coincident with the maximum shear strain plane. However, in load ratios Ψ=0, 1/2, and 1 it was noted that cracks also initiated along the longitudinal axis of the specimen and that for these ratios it was these longitudinal cracks which grew to failure. It was determined that this cracking direction was coincident with the direction of the banding of pearlite and ferrite grains in the microstructure and it appeared that the ferrite bands provided channels in which cracking occurred more easily than in the adjacent pearlite rich bands.

  A tendency was observed for the initial shear crack to switch to growth on maximum tensile planes as the load ratio increased. This tendency decreased with increasing strain amplitude. The length of the initial shear crack also was observed to change as the inverse of the same variables. This length increased as the load ratio decreased or the strain amplitude increased. Tensile cracking was observed at all stress ratios.

- Crack growth behavior in the periodic overload experiments was modelled using mode I and mode II crack face interference free crack growth curves. Two parameters, ξ and χ, were used in the crack growth modelling. They are based on earlier investigations which, respectively, stated that the crack will grow in the direction in which: (1) the crack growth (area) increment is maximized or (2) the strain energy release is greatest. The results of the modelling indicated that neither theory accurately predicted the crack length at which the change to tensile crack growth occurred in the experiments. The first, or area theory, underpredicted this shear crack length and the second, or energy theory, overpredicted it. However, both of these models correctly predicted the cracking behavior trends discussed in the preceding paragraph – increased shear crack lengths was observed with increasing strain amplitudes and with decreasing load ratio.

- Several different crack growth life predictions were made for the periodic overload experiments. The first of these used maximum shear strain amplitude as a crack driving parameter. The surface strain concentration profile was determined separately for each stress ratio in these predictions, and they fell within 50% of the experimental fatigue life.

  Two series of predictions employed the parameters ξ and χ, and, since these models could choose between shear or tensile crack growth, a separate surface strain concentration profiles were determined for shear and tensile crack growth. Both models gave conservative predictions of experimental fatigue life but were usually within a factor of two of the observed fatigue life. They correctly predicted the change in the endurance limit as a function of load ratio. Finally, the energy criterion predicted, for Ψ=0 and 1/2, a discontinuity in the strain-life curve which occurred at the transition in the model between predicting tensile cracking to failure and predicting shear cracking to failure. This discontinuity arose from the difference at that strain amplitude between the shear and tensile crack growth curves. The area criterion predicted no such discontinuity because the basis of area criterion is to select the intersection of the two growth rate curves. This leads to a continuous global growth rate function which produces a continuous life prediction.

Appendix A

Chu's Modified Mróz Plasticity Model

This appendix is taken from reference [43].

Although the method presented here is general enough to be applied to any three-dimensional problem, the equations are specifically derived for surface elements in which plane stress conditions prevail and where surface strains are given by strain gage measurements. As sketched in Figure A.1, for an element on the top surface of an axle shaft adopting the x-y-z coordinate system, the plane stress conditions are

$$\sigma_{iz} \equiv 0 \qquad i = x, y, z \tag{A.1}$$

$$\epsilon_{\alpha z} \equiv 0 \qquad \alpha = x, y. \tag{A.2}$$

Given a time history of rosette strains, $e_1(t), e_2(t), e_3(t)$, the history of surface strains can be derived by

$$\epsilon_{xx}(t) = e_2(t) \tag{A.3}$$

$$\epsilon_{xy}(t) = \frac{1}{2}[-e_1(t) + e_3(t)] \tag{A.4}$$

$$\epsilon_{yy}(t) = e_1(t) - e_2(t) + e_3(t) \tag{A.5}$$

An isotropic-kinematic hardening model generalized from Mróz's yield surface field concept [78, 76, 97] is adopted to follow the strain history and calculate the corresponding stress history. The material model, utilizing two commonly adopted

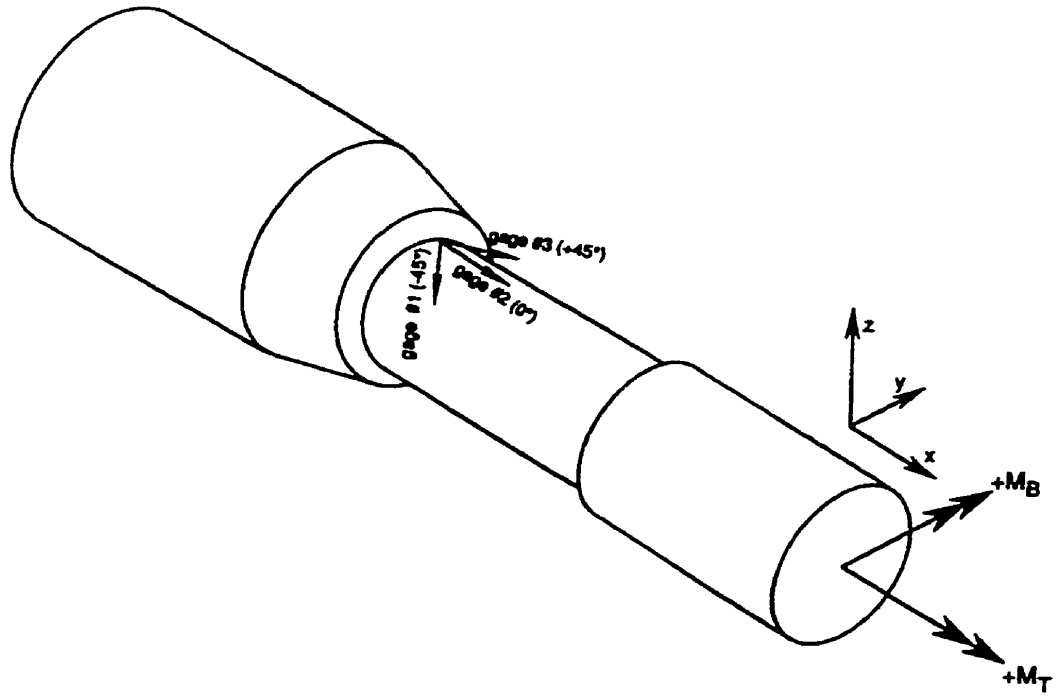

Figure A.1: Definition of strain gage coordinates.

assumptions that (a) during an elastic-plastic deformation the total strain increment is the sum of the elastic and the plastic increment and (b) the plastic strain increment obeys the normality rule, can be summarized here by the following set of equations describing the incremental stress - incremental strain relationship.

$$d\sigma_{ij} = L_{ijkl} d\epsilon_{kl} \tag{A.6}$$

$$= \frac{E}{1+\nu}\left(d\epsilon_{ij} + \frac{\nu}{1-2\nu}\delta_{ij} d\epsilon_{kk} - H\frac{\tau_{ij}\tau_{kl}}{\overline{\sigma}^2} d\epsilon_{kl}\right) \tag{A.7}$$

with

$$\tau_{ij} = s_{ij} - \alpha_{ij} = (\sigma_{ij} - \frac{1}{3}\delta_{ij}\sigma_{kk}) - \alpha_{ij} \tag{A.8}$$

$$\overline{\sigma}^2 = \frac{3}{2}\tau_{ij}\tau_{ij} \tag{A.9}$$

$$H = \begin{cases} 0 & \text{if } \overline{\sigma} \leq \overline{\sigma}_y \\ \frac{3}{2}\left(\frac{2(1+\nu)}{3(E/E_t(\overline{\sigma})-1)} + 1\right)^{-1} & \text{if } \overline{\sigma} > \overline{\sigma}_y. \end{cases} \tag{A.10}$$

In equations A.6 through A.10, L is used to denote the instantaneous modulus tensor, E is Young's modulus, ν is Poisson's ratio, δ_{ij} is the Kronecker delta, $E_t(\overline{\sigma})$ is the instantaneous tangent modulus at equivalent stress level $\overline{\sigma}$, and $\overline{\sigma}_y$ denotes the initial yield stress which is a material constant. The center of the active yield surface in the deviatoric stress (s_{ij}) space is denoted by α_{ij}, which during a plastic loading process moves in a direction toward the center of the previously active yield surface at the last load reversal. In the above equations and hereafter, Roman scalar subscripts i through l take values that range from x to z and Greek scalar subscripts α through δ take values that range from x to y. Repetition of these subscripts implies summation.

The plane stress conditions mentioned earlier can be expressed by

$$d\sigma_{iz} = L_{iz\alpha\beta}d\epsilon_{\alpha\beta} + L_{izzz}d\epsilon_{zz} \equiv 0 \tag{A.11}$$

which can be used with equations A.6 through A.10 to give the incremental stress - strain relationship on the x-y plane

$$d\sigma_{\alpha\beta} = L_{\alpha\beta\gamma\delta}d\epsilon_{\gamma\delta} + L_{\alpha\beta zz}d\epsilon_{zz} \tag{A.12}$$

$$= \left(L_{\alpha\beta\gamma\delta} - \frac{L_{\alpha\beta zz}L_{zz\gamma\delta}}{L_{zzzz}}\right)d\epsilon_{\gamma\delta}. \tag{A.13}$$

The basic equivalent stress-strain equation of the material used in this analysis is a modified power-law type

$$\overline{\epsilon} = \begin{cases} \overline{\sigma}/E \quad (= \overline{\epsilon}_y\overline{\sigma}/\overline{\sigma}_y) & \text{if } \overline{\sigma} \le \overline{\sigma}_y \\ \overline{\epsilon}_y\left(n'(\overline{\sigma}/\overline{\sigma}_y)^{\frac{1}{n'}} - n' + 1\right) & \text{if } \overline{\sigma} > \overline{\sigma}_y \end{cases} \tag{A.14}$$

The function of tangent modulus used in equation A.10, $E/E_t(\overline{\sigma})$, is then obtained as

$$\frac{E}{E_t} = \frac{E}{d\overline{\sigma}/d\overline{\epsilon}} = \begin{cases} 1 & \text{if } \overline{\sigma} \le \overline{\sigma}_y \\ (\overline{\sigma}/\overline{\sigma}_y)^{\frac{1}{n'}-1} & \text{if } \overline{\sigma} > \overline{\sigma}_y \end{cases} \tag{A.15}$$

Here n' is the strain hardening exponent of the material. It is important to note that the material constants, n' and $\overline{\sigma}_y$, should be determined from fitting the above stress

- strain relation to the cyclically stabilized stress - strain data instead of the initial monotonic curve. The present initial yield stress, $\overline{\sigma}_y$, corresponds more to a cyclic proportional limit than the 0.2% offset yield stress of the material. The modified power law, equation A.14, is used mainly to give a smooth curve with continuous slope change at the yield point, $\overline{\sigma} = \overline{\sigma}_y$.

Appendix B

Crack Growth Geometry Factors

B.1 Correction Factors for Uniaxial Specimens

B.1.1 Single Edge Crack With Backface Correction

This correction is taken from Brown and Srawley [92], and was used to calculate ΔK for data taken from mode I crack growth specimens (Figure 2.9). The geometry factor, F_{cgI}, is approximated by

$$F_{cgI}\left(\frac{a}{W}\right) = 1.12 - 0.231\left(\frac{a}{W}\right) + 10.55\left(\frac{a}{W}\right)^2 - 21.72\left(\frac{a}{W}\right)^3 + 30.39\left(\frac{a}{W}\right)^4. \tag{B.1}$$

The geometry factor is a function of the ratio of crack length (a) to plate width, W, as shown in Figure B.1.

B.1.2 Elliptical Surface Crack in a Solid Bar Under Tension

This geometry factor, used to model mode I crack growth in smooth uniaxial specimens (see Figure 2.6), was taken from Raju and Newman [98]. Through inspection of the fracture surfaces of uniaxial specimens it was determined that the average ellipticity ($\frac{a}{c}$) of the crack was roughly 0.8 throughout most of the life of the specimen. This $\frac{a}{c}$ value falls within the stable range determined by Raju and Newman. The terms a, c and D are defined in Figure B.2. The geometry factor used in this research for the solid smooth specimens, F_{ssI}, was approximated by

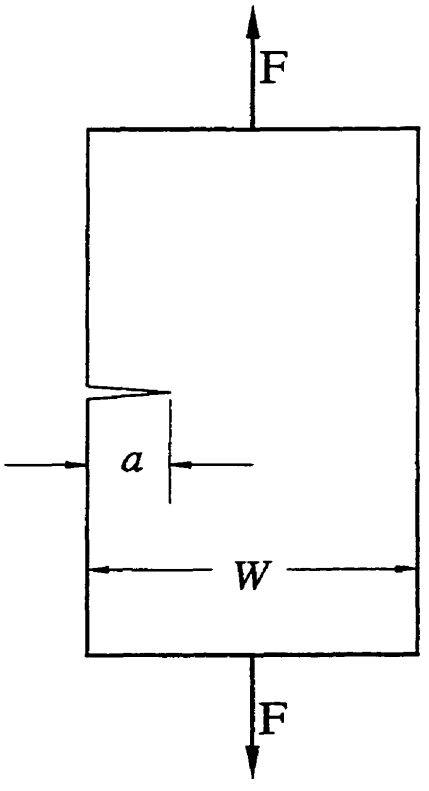

Figure B.1: Definitions of a and W in a single edge cracked plate.

$$F_I^{ss}(\frac{a}{D}) = 0.739 + 0.107(\frac{a}{D}) - 0.684(\frac{a}{D})^2 + 6.804(\frac{a}{D})^3. \quad \text{(B.2)}$$

B.2 Integrated Mode I, Mode II and Mode III Geometry Factors

B.2.1 Mode I and II Stress Intensity Solutions for a Through Crack in a Tube

Lakshminarayana and Murthy [93] developed a solution for an arbitrarily oriented through-crack in a tube. Reduced for an axial-torsional specimen and relative to the coordinate system in Figure 2.26, they become,

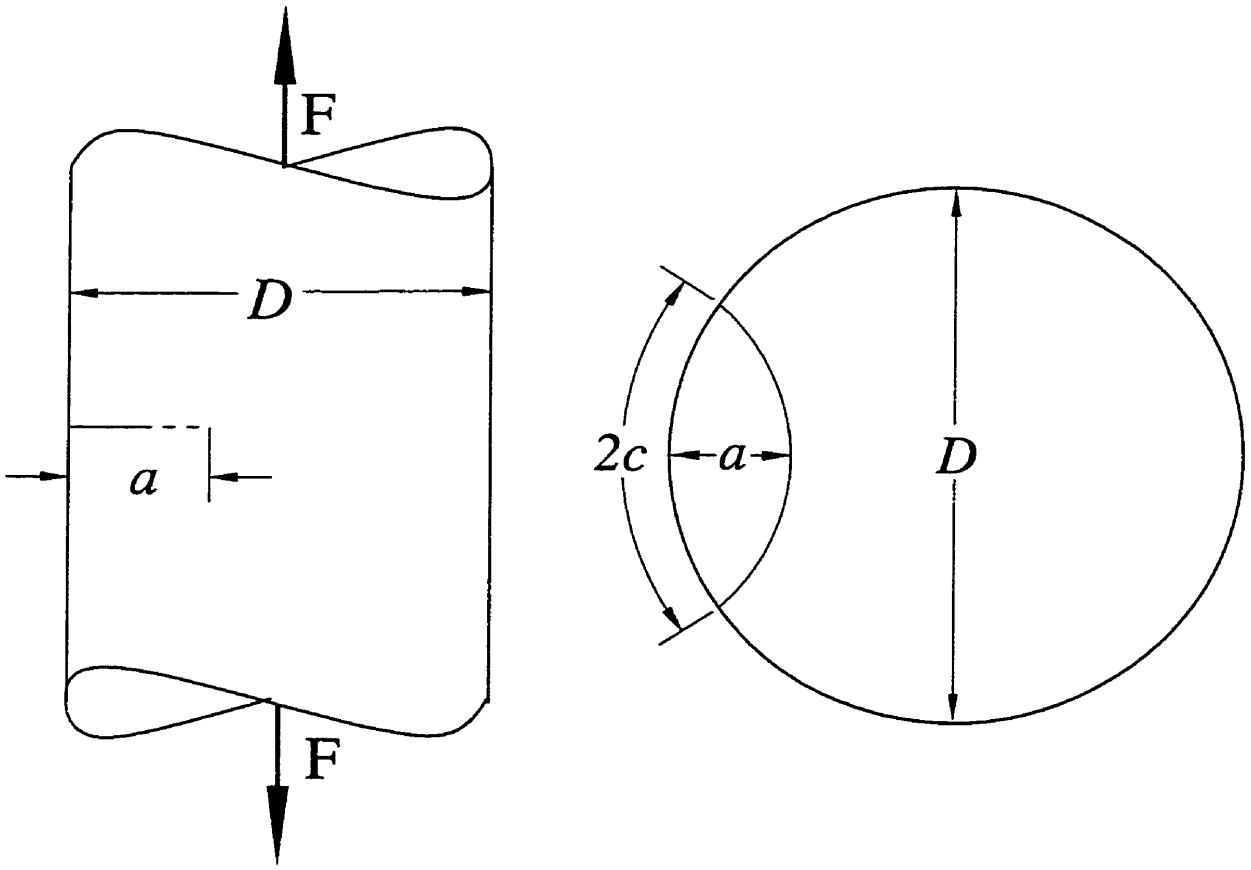

Figure B.2: Definitions of a, c and W for an ellipical crack in a rod under tension.

$$K_I^t = \sigma_{xx}\sqrt{\pi c}\left[\sin^2\beta + \frac{\pi\rho^2}{32}(3 - 2\cos 2\beta - \cos 4\beta)\right] + \sigma_{xy}\sqrt{\pi c}\left[\sin 2\beta + \frac{\pi\rho^2}{32}(9\sin 2\beta + 2\sin 4\beta)\right] \quad \text{(B.3)}$$

$$K_{II}^t = \sigma_{xx}\sqrt{\pi c}\left[\frac{1}{2}\sin 2\beta + \frac{\pi\rho^2}{32}\sin 4\beta\right] + \sigma_{xy}\sqrt{\pi c}\left[\cos 2\beta - \frac{\pi\rho^2}{16}(1 - 2\cos 2\beta - \cos 4\beta)\right] \quad \text{(B.4)}$$

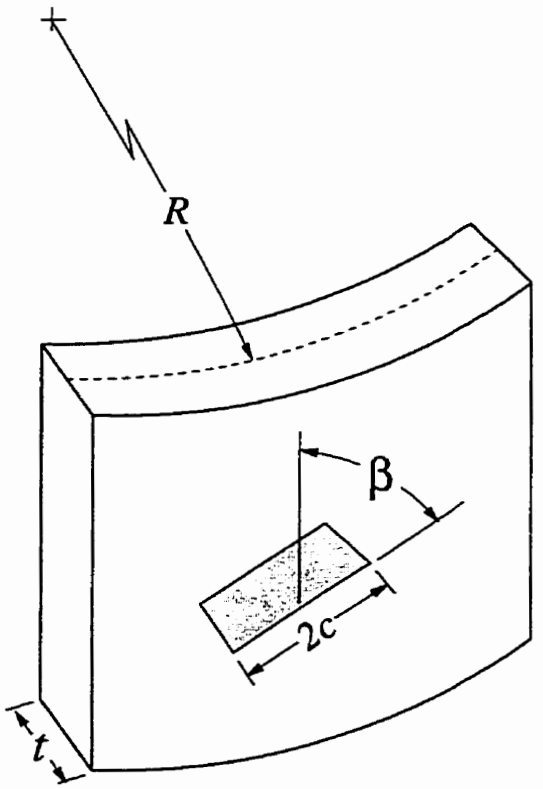

Figure B.3: Definitions of c, t, R, and β for an arbitrarily oriented through-crack in a tube.

where

$$\rho^2 = \frac{\sqrt{12(1-\nu^2)}c^2}{8Rt}. \tag{B.5}$$

Figure B.3 shows the definitions of the terms c, β, R, and t.

B.2.2 Elliptical Surface Crack in a Tube

Irwin [55] developed a stress intensity solution for an embedded elliptical crack in an elastic solid under tension from earlier work by Green and Sneddon [99]. Socie, et al. [47] suggested using this solution as an elliptical surface crack in a tube with a multiplier of 1.12 to account for the free surface. Irwin's solution then becomes

$$F_I^e = 1.12 * \frac{\Theta(k,\theta)}{E(k)} \tag{B.6}$$

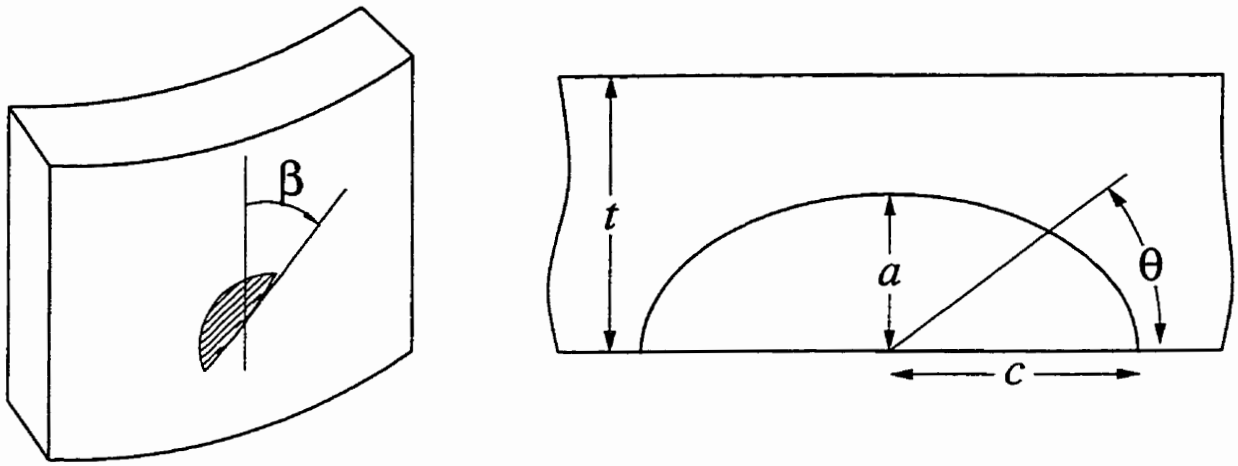

Figure B.4: Definitions of a, c, t, θ, and β for an arbitrarily oriented ellipical crack in a tube.

where

$$\Theta(k,\theta) = \sqrt[4]{\sin^2\theta + k^2\cos^2\theta} \tag{B.7}$$

$$E(k) = \int_0^{\frac{\pi}{2}} \sqrt{1-(k')^2\sin^2\theta}\,d\theta \tag{B.8}$$

$$k = \frac{a}{c} \tag{B.9}$$

$$k' = \sqrt{1-k^2}. \tag{B.10}$$

The terms a, c, and θ are defined in Figure B.4.

Kassir and Sih [56] extended Irwin's solution for an embedded elliptical crack to include shear loading. The specific solution for a shear applied in the plane of the crack and in the direction of the major axis of the crack is

$$F^e_{II} = 1.12\frac{k(k')^2\cos\theta}{\Theta(k,\theta)B(k,\nu)} \tag{B.11}$$

$$F^e_{III} = \frac{(1-\nu)(k')^2\sin\theta}{\Theta(k,\theta)B(k,\nu)} \tag{B.12}$$

where

$$B(k,\nu) = ((k')^2 - \nu)E(k) + \nu^2 F(k), \tag{B.13}$$

$$F(k) = \int_0^{\frac{\pi}{2}} \frac{d\theta}{\sqrt{1-(k')^2\sin^2\theta}}. \tag{B.14}$$

Equations B.8 and B.14 are elliptical integrals of the second and first kinds, respectively. These integrals were approximated by

$$(E(k))^2 = 1 + 1.464k^{1.65} \tag{B.15}$$

$$(F(k))^2 = \frac{34.05}{(1+22.77*k)^{0.684}} - 1.432. \tag{B.16}$$

Appendix C

Crack Propagation Program

This program calculates crack growth and life for Ψ=1 loading.

```
      real beta, betb, ka, kc, k, squarek
      real anglea, angleb, sigma, tau, ratio
      real pi,divvy,stress
      real delki(100),dadni(100)
      real delkii(100),dadnii(100)
      real*8 daa, dac, ndaa, ndac, rate
      real qa, qt, bfa, bfc
      real bf,kic,kiic,Y
      real alpha, alpht, fa, fc, nfa, nfc
      real enera, eners
      real*8 alen,clen,clast,len,nclen
      real straini,stressi,strainn,stressn
      real nstrain,nstress
      integer*4 cycles
      logical*4 once,once2,once3,oncek
      integer lasti,lastii
      logical sheargrow,thresha,threshc,penny

      common/logic/once,once2,once3,oncek,cycles,sheargrow,
```

```
     & thresha,threshc
      common/grate/pi,divvy,delki,dadni,delkii,dadnii,
     & kic,alpha,alpht,nstress,lasti,lastii,nfa,nfc

C Initialize variable
      once=.true.
      once2=.true.
      once3=.true.
      oncek=.true.
      sheargrow=.true.
      thresha=.false.
      threshc=.false.
      penny=.false.
      pi=3.141592654
      cos58=cos(58.28*pi/180.)
      alpht=45000.
      alpha=105000.
C read(5,*)alpht
      alen=3.0e-6
      clen=50.0e-6
      clast=2.5e-3
      Y=203000.0
      G=Y/1.29
      kic=64.0
      kiic=1.29*kic

C input strain level
      read(5,*)atstrain
C calculate elastic stress
      atstress=atstrain*G*2.0
```

```
C read in mode I and mode II crack growth data
      open(10,FILE="axialgrowth.dat",status="OLD")
      open(20,FILE="sheargrowth.dat",status="OLD")
      do 10 i=1,100
       read(10,*,err=100)delki(i),dadni(i)
       delki(i)=log10(delki(i))
       dadni(i)=log10(dadni(i))
10            lasti=i
100     close(10)
      do 20 j=1,100
       read(20,*,err=200)delkii(j),dadnii(j)
       delkii(j)=log10(delkii(j))
       dadnii(j)=log10(dadnii(j))
20            lastii=j
200     close(20)
C read in stress strain curve
      open(30,FILE="sr1ss.tor",status="OLD")
235     read(30,*)strainn,stressn
      if(atstrain.gt.strainn)then
       straini=strainn
       stressi=stressn
       goto 235
       endif
      close(30)

C calculate actual stress
      rstress=(atstrain-straini)/(strainn-straini)*(stressn-stressi)+
     &              stressi
C calculate applied axial strain
```

```
      anstrain=2.0*atstrain/3.0
C calculate effective poisson ratio
      poisseff=0.5-0.21*rstress/(G*atstrain)
C calculate max shear strain
      sstrain=sqrt(atstrain**2+((anstrain*(1.+poisseff))**2)/4.0)
      center=(1.0-poisseff)*anstrain/2.0
C calculate max normal strain
      nstrain=center+sstrain
C calculate max normal stress
      nstress=nstrain*Y*2.0

C constant for Lakshmi
      divvy=8.0*0.01173*0.00254/sqrt(12*(1-poisseff**2))
C start crack calc with semi-elliptic shear crack
125      psia = 1.0
      aoc=alen/clen
      qc=1.0 + 5.3*exp(-alpht*clen)
      qa=1.0 + 5.3*exp(-alpht*alen)
C check to see if transition to penny crack
      if(aoc.gt.0.995.and.(.not.penny))then
       print *,"penny shaped crack at"
       write(6,23)cycles,alen,ka,daa,clen,kc,dac
       penny=.true.
       endif
C check to see if transition back to elliptical crack
      if(aoc.lt.0.995.and.penny)then
       print *,"elliptical shaped crack at"
       write(6,23)cycles,alen,ka,daa,clen,kc,dac
       penny=.false.
       endif
```

```
      if(penny)then
C calculate geom fac's for penny crack
        fa=4.0*(1.0-poisseff)/(pi*(2.0-poisseff))*qa*atstress
        fc=1.12*4.0/(pi*(2.0-poisseff))*qc*atstress
      else
C otherwise calc geom fac's for elliptical crack
        psic = sqrt(aoc)
        squarek= 1.0-aoc*aoc
        k=sqrt(squarek)
          E=sqrt(1.0+1.464*(aoc**1.65))
        F=sqrt((34.05337/(1.0+22.76638*aoc)**0.684453)-1.43264)
        b=(squarek-poisseff)*E+poisseff*aoc*aoc*F
C geom term for a direction
        fa=(1.0-poisseff)*squarek/(psia*b)*qa*atstress
C geom term for c direction
        fc=1.12*aoc*squarek/(psic*b)*qc*atstress
      endif
C calc K in each direction
      ka=fa*sqrt(pi*alen)
      kc=fc*sqrt(pi*alen)

C get crack growth rate in shear, a direction and check
C for threshold condition
      call getdadn(ka,delkii,dadnii,daa,lastii)
      if(daa.lt.1.0e-15)then
       thresha=.true.
      else
       thresha=.false.
      endif
```

```
C get crack growth rate in shear, c direction and check
C for threshold condition
      call getdadn(kc,delkii,dadnii,dac,lastii)
      if(dac.lt.1.0e-15)then
       threshc=.true.
      else
       threshc=.false.
      endif

C project crack onto tensile plane
      nclen=clen*cos58
C calc k's and growth rates for a possible tensile crack
      call checknormal(alen,nclen,ndaa,ndac)

C calculate energy release
      eners=(fa**2)*(1.0+poisseff)*daa + (fc**2)*aoc*dac
      enera=(nfa**2)*ndaa + (nfc**2)*alen/clen*ndac
C calculate chi
      ratener=enera/eners

C check chi and crack depth
      if(ratener.gt.1.0.and.aoc.gt.0.5)then
C growth in normal strain is indicated
       sheargrow=.false.
       goto 525
       endif


C check to see if crack is completely in threshold
      if(thresha.and.threshc)then
```

```
C crack in threshold so output crack state and stop
       write(6,23)cycles,alen,ka,daa,clen,kc,dac
       print *,ndaa,ndac
       stop "stage 1 threshold"
       endif
C crack to see in which direction growth is fastest
      rate=dmax1(daa,dac)
C increment crack lengths and cycle count
      if(rate.ge.1.0e-9)then
       alen=alen+daa
       clen=clen+dac
       cycles=cycles+1
C accelerate calculation because of threshold growth
      else if(rate.gt.1.0e-10)then
       alen=alen+10.d0*daa
       clen=clen+10.d0*dac
       cycles=cycles+10
      else if(rate.gt.1.0e-11)then
       alen=alen+100.d0*daa
       clen=clen+100.d0*dac
       cycles=cycles+100
C print *,"here 1e-11"
       once=.true.
       once2=.true.
       once3=.true.
      else if(rate.gt.1.0e-12)then
       alen=alen+1000.d0*daa
       clen=clen+1000.d0*dac
       cycles=cycles+1000
       if(once)then
```

```
      print *,"here 1e-12"
      once=.false.
      once2=.true.
      once3=.true.
      endif
     else if(rate.gt.1.0e-13)then
      alen=alen+10000.d0*daa
      clen=clen+10000.d0*dac
      cycles=cycles+10000
      if(once2)then
      print *,"here 1e-13"
      once2=.false.
      once3=.true.
      once=.true.
      endif
     else if(rate.gt.1.0e-14)then
      alen=alen+100000.d0*daa
      clen=clen+100000.d0*dac
      cycles=cycles+100000
      if(once3)then
      print *,"here 1e-14"
      once3=.false.
      once2=.true.
      once=.true.
      endif
     else if(rate.ge.1.0e-15)then
      alen=alen+1000000.d0*daa
      clen=clen+1000000.d0*dac
      cycles=cycles+1000000
     else if(rate.lt.1.0e-15)then
```

```
        print *,cycles,alen,10**ka,daa
        stop "definitely in threshold"
       endif
C check to see if through crack and high k, if not, repeat
      if(alen.lt.0.00254.and.ka.lt.kiic)goto 125
      if(alen.ge.0.00254)then
C through shear crack - go to through crack growth
       sheargrow=.true.
       goto 220
       endif
      if(ka.ge.kiic)then
C K exceeds max stop calc.
       write(6,23)cycles,alen,ka,daa,clen,kc,dac
       stop "specimen failed in shear stage I"
       endif
C switch to growing an elliptical crack on tensile plane
525      print *,"switch to max normal strain"
      print *,eners,enera,enera/eners,clen,aoc
      write(6,23)cycles,alen,clen
23      format(x,i10,2x,6(e9.3,x))
      sheargrow=.false.
      clen = clen*cos58
C account for a/c greater than 1
425      if(alen.gt.clen)then
       aoc=clen/alen
       psia = sqrt(aoc)
       psic = 1.0
       len=clen
      else
       aoc=alen/clen
```

```
        psia = 1.0
        psic = sqrt(aoc)
        len=alen
       endif
       squarek= 1.0-aoc*aoc
       k=sqrt(squarek)
C calculate q
       qc=1.0 + 5.3*exp(-alpha*clen)
       qa=1.0 + 5.3*exp(-alpha*alen)
C calculate elliptic integrals
         E=sqrt(1.0+1.464*(aoc**1.65))
C calculate geometry factor in a direction
       fa=1.12*psia/E
C calculate K in a direction
       ka=qa*fa*nstress*sqrt(pi*len)
C calculate geometry factor in a direction
       fc=1.12*psic/E
C calculate K in c direction
       kc=qc*fc*nstress*sqrt(pi*len)
C get growth rates for a and c directions
       call getdadn(ka,delki,dadni,daa,lasti)
       call getdadn(kc,delki,dadni,dac,lasti)
C find the faster of the two growth rates
       rate=dmax1(daa,dac)
C increment crack lengths and cycle count
       if(rate.ge.1.0e-9)then
        alen=alen+daa
        clen=clen+dac
        cycles=cycles+1
C accelerate crack growth in threshold
```

```
      else if(rate.gt.1.0e-10)then
       alen=alen+10.d0*daa
       clen=clen+10.d0*dac
       cycles=cycles+10
      else if(rate.gt.1.0e-11)then
       alen=alen+100.d0*daa
       clen=clen+100.d0*dac
       cycles=cycles+100
C print *,"here 1e-11"
       once=.true.
       once2=.true.
       once3=.true.
      else if(rate.gt.1.0e-12)then
       alen=alen+1000.d0*daa
       clen=clen+1000.d0*dac
       cycles=cycles+1000
       if(once)then
       print *,"here 1e-12"
       once=.false.
       once2=.true.
       once3=.true.
       endif
      else if(rate.gt.1.0e-13)then
       alen=alen+10000.d0*daa
       clen=clen+10000.d0*dac
       cycles=cycles+10000
       if(once2)then
       print *,"here 1e-13"
       once2=.false.
       once3=.true.
```

```
        once=.true.
        endif
       else if(rate.gt.1.0e-14)then
        alen=alen+100000.d0*daa
        clen=clen+100000.d0*dac
        cycles=cycles+100000
        if(once3)then
        print *,"here 1e-14"
        once3=.false.
        once2=.true.
        once=.true.
        endif
       else if(rate.ge.1.0e-15)then
        alen=alen+100000.d0*daa
        clen=clen+100000.d0*dac
        cycles=cycles+100000
       else if(rate.lt.1.0e-15)then
C crack in threshold so stop
        print *,cycles,alen,10**ka,daa
        stop "definitely in threshold"
       endif
C check to see if crack a through crack and if K exceeds critical
      if(alen.lt.0.00254.and.ka.lt.kic)goto 425
C Now crack is a through tensile crack
220       print *,"switch to through crack"
      write(6,23)cycles,alen,ka,daa,clen,kc,dac
C Grow through crack
225       beta=clen*clen/divvy
C calculate K based on whether shear or tensile crack
      if(sheargrow)then
```

```
        kc=(1.+0.39270*beta)*sqrt(pi*clen)*atstress
        call getdadn(kc,delkii,dadnii,dac,lastii)
       else
        kc=(1.61804+1.07445*beta)*sqrt(pi*clen)*atstress
        call getdadn(kc,delki,dadni,dac,lasti)
       endif
C increment crack length and cycle count
       clen=clen+dac
       cycles=cycles+1
C check for endpoint and for max k, depending on crack
       if(.not.sheargrow.and.clen.lt.0.015.and.kc.lt.kic)goto 225
       if(sheargrow.and.clen.lt.0.015.and.kc.lt.kiic)goto 225
C crack exceeded cmax or kcritical
       write(6,23)cycles,alen,ka,daa,clen,kc,dac
       end

C subroutine to calculate crack growth rates
       subroutine getdadn(k,delk,dadn,daa,lastj)
       real k,ka
       real dadn(100),delk(100)
       real*8 daa
       integer j, lastj
       integer*4 cycles
       logical once,once2,once3,oncek
       common/logic/once,once2,once3,oncek,cycles,sheargrow,
      & thresha,threshc
       j=1
C interpolate growth in log-log coordinates
       ka=log10(k)
       if(ka.lt.delk(1))then
```

```
        daa=(ka-delk(1))/(delk(2)-delk(1))*
     & (dadn(2)-dadn(1))+dadn(1)
C daa=0.0
       else
        do 300 while(ka.gt.delk(j))
        j=j+1
        if(j.gt.lastj) then
C check for exceedence of curve
        if(oncek)then
        print *,"K=",10**ka," out of range at ",cycles
        oncek=.false.
        endif
        j=lastj
        goto 305
        endif
300             continue
305             daa=(ka-delk(j-1))/(delk(j)-delk(j-1))*
     & (dadn(j)-dadn(j-1))+dadn(j-1)
       endif
       daa=10.0**daa
       return
       end

C routine to calc tensile crack parameters for use in energy calc
       subroutine checknormal(alen,clen,daa,dac)
       real beta, betb, ka, kc, k, squarek
       real anglea, angleb, sigma, tau, ratio
       real pi,divvy,stress
       real delki(100),dadni(100)
       real delkii(100),dadnii(100)
```

```
      real*8 daa, dac, ndaa, ndac
      real qa, qt, bfa, bfc
      real bf,kic,Y
      real alpha, alpht, nfa, nfc
      real*8 alen,clen,clast,len,nclen
      real straini,stressi,strainn,stressn
      real nstrain,nstress
      integer*4 cycles
      logical*4 once,once2,once3,oncek
      integer lasti,lastii
      logical sheargrow,thresha,threshc
      common/logic/once,once2,once3,oncek,cycles,sheargrow,
     & thresha,threshc
      common/grate/pi,divvy,delki,dadni,delkii,dadnii,
     & kic,alpha,alpht,nstress,lasti,lastii,nfa,nfc

C account for a/c > 1
425      if(alen.gt.clen)then
       aoc=clen/alen
       psia = sqrt(aoc)
       psic = 1.0
       len=clen
      else
       aoc=alen/clen
       psia = 1.0
       psic = sqrt(aoc)
       len=alen
      endif
      squarek= 1.0-aoc*aoc
      k=sqrt(squarek)
```

```
C calc Q
      qc=1.0 + 5.3*exp(-alpha*clen)
      qa=1.0 + 5.3*exp(-alpha*alen)
C calc elliptical integral
        E=sqrt(1.0+1.464*(aoc**1.65))
C calc geometry factor in c direction
      fa=1.12*psia/E*qa*nstress
      nfa=fa
C calc K in a direction
      ka=fa*sqrt(pi*len)
C calc geometry factor in c direction
      fc=1.12*psic/E*qc*nstress
      nfc=fc
C calc K in a direction
      kc=fc*sqrt(pi*len)
C calc crack growth rates in a and c directions
      call getdadn(ka,delki,dadni,daa,lasti)
      call getdadn(kc,delki,dadni,dac,lasti)
      return
      end
```

Bibliography

[1] C.-C. Chu and A. Hübner. Personal communication, 1997.

[2] J.A. Bannantine, J.J Comer, and J.L. Handrock. *Fundamentals of Metal Fatigue Analysis.* Prentice-Hall, 1990.

[3] D.L. DuQuesnay. *Fatigue Damage Accumulation in Metals Subjected to High Mean Stress and Overload Cycles.* PhD thesis, University of Waterloo, Waterloo, Ontario, 1991.

[4] A. Varvani-Farahani. *Biaxial Fatigue Crack Growth and Crack Closure under Constant Amplitude and Periodic Compressive Overload Histories in 1045 Steel.* PhD thesis, University of Waterloo, Waterloo, Ontario, 1998.

[5] J. Schijve. Fatigue crack closure: Observations and technical significance. In *Mechanics of Fatigue Crack Closure*, ASTM STP 982, pages 5–34, Philadelphia, 1988. American Society for the Testing of Materials.

[6] O. Vosikovski. The effect of stress ratio on fatigue crack growth rates in steels. *Engineering Fracture Mechanics*, 11:595–602, 1979.

[7] M.T. Yu and T.H. Topper. The effects of material strength, stress ratio and compressive overloads on the threshold behavior of a SAE 1045 steel. *Journal of Engineering Materials and Technology*, 107:19–25, 1985.

[8] W. Elber. Fatigue crack closure under cyclic tension. *Engineering Fracture Mechanics*, 2(1):37–45, 1970.

[9] W. Elber. The significance of fatigue crack closure. In *Damage Tolerance in Aircraft Structures*, ASTM STP 486, pages 230–242, Philadelphia, 1971. American Society for the Testing of Materials.

[10] A.J. McEvily and K. Minikawa. On the effect of microstructure on crack closure in the near threshold region. In *7th International Conference on the Strength of Metals and Alloys*, pages 1385–1392, 1985. .

[11] R.O. Ritchie and S. Suresh. Some considerations on fatigue crack closure at near-threshold stress intensities due to fracture surface morphology. *Metallurgical Transactions, A*, 13A:937–940, 1982.

[12] S. Suresh and R.O. Ritchie. A geometric model for fatigue crack closure induced by fracture surface roughness. *Metallurgical Transactions, A*, 13A:1627–1631, 1982.

[13] K. Endo, K. Komai, and K. Ohnishi. Effects of stress history and corrosive environment on fatigue crack propagation. Faculty of engineering memo, Kyoto University, Kyoto, Japan, 1969. vol. 31.

[14] J. Schijve. Fatigue crack propagation in light alloy sheet material and structures. Technical Report MP 195, National Luchtvaart Laboratorium, Amsterdam, August 1960. .

[15] R.I. Stephens, D.K. Chen, and B.W. Hom. Fatigue crack growth with negative stress ratio following single overloads in 2024-T3 and 7075-T6 aluminum alloys. In *Fatigue Crack Growth Under Spectrum Loads* [100], pages 27–40.

[16] R. Jurcevic, D.L. DuQuesnay, T.H. Topper, and M.A. Pompetzki. Fatigue damage accumulation in 2024-T351 aluminium subjected to periodic reversed overloads. *International Journal of Fatigue*, 12(4):259–266, 1990.

[17] T.H. Topper, D.L. DuQuesnay, and M.A Pompetzki. Crack closure, damage and short crack growth under variable amplitude loading. In *Theoretical Concepts and Numerical Analysis of Fatigue*, pages 201–235, University of Birmingham, U.K., 1992. Chameleon Press.

[18] D.L. DuQuesnay, T.H. Topper, and R. Jurcevic. A new fatigue life prediction model for variable amplitude loading. In *Localized Damage II: Fatigue and Fracture Mechanics*, volume 1, Southampton, U.K., July 1-3 1992. Computer and Mechanical Publishers.

[19] C.D. Hopper and K.J. Miller. Fatigue crack propagation in biaxial stress fields. *Journal of Strain Analysis*, 12(1):23–28, 1977.

[20] F. Hourlier and A. Pineau. Fatigue crack propagation behavior under complex mode loading. In *Advances in Fracture Research*, pages 1833–1840. Pergamon Press, 1981.

[21] M.W. Brown and K.J. Miller. Mode I fatigue crack growth under biaxial stress at room and elevated temperature. In *Multiaxial Fatigue* [101], pages 135–152.

[22] H. Youshi, M.W. Brown, and K.J. Miller. Fatigue crack growth from a circular notch under high levels of biaxial stress. *Fatigue and Fracture of Engineering Materials and Structures*, 15(12):1185–1197, 1992.

[23] E.W. Smith and K.J. Pascoe. Fatigue crack initiation and growth in a high-strength ductile steel subject to in-plane biaxial loading. In *Multiaxial Fatigue* [101], pages 111–134.

[24] D. Socie. Critical plane approaches for multiaxial fatigue damage assessment. In *Advances in Multiaxial Fatigue* [102], pages 7–36.

[25] E.K. Tschegg. Sliding mode crack closure and mode III fatigue crack growth in mild steel. *Acta Metallurgica*, 31(9):1323–1330, 1983.

[26] C.H. Wang and K.J. Miller. The effect of mean shear stress on torsional fatigue behaviour. *Fatigue and Fracture of Engineering Materials and Structures*, 14(2/3):293–307, 1991.

[27] C.H. Wang and K.J. Miller. The effects of mean and alternating shear stresses on short fatigue crack growth rates. *Fatigue and Fracture of Engineering Materials and Structures*, 15(12):1223–1236, 1992.

[28] M.W. Brown, E. Hay, and K.J. Miller. Fatigue at notches subjected to reversed torsion and static axial loads. *Fatigue and Fracture of Engineering Materials and Structures*, 8(3):243–258, 1985.

[29] A. Fatemi and D. Socie. A critical plane approach to multiaxial fatigue damage including out-of-phase loading. *Fatigue and Fracture of Engineering Materials and Structures*, 11(3):149–169, 1988.

[30] A. Fatemi and P. Kurath. Multiaxial fatigue life predictions under the influence of mean-stresses. *Journal of Engineering Materials and Technology*, 110:380–388, October 1988.

[31] R.O. Ritchie, F.A. McClintock, E.K. Tschegg, and H. Nayeb-Hashemi. Mode III fatigue crack growth under combined torsional and axial loading. In *Multiaxial Fatigue* [101], pages 203–227.

[32] K.-H. Trautmann, E. Maldfeld, and H. Nowack. Crack propagation in cruciform IMI 834 specimens under variable biaxial loading. In *Multiaxial Fatigue and Deformation Testing Techniques*, ASTM STP 1280, pages 290–309, Philadelphia, 1997. American Society for the Testing of Materials.

[33] L.E. Tucker. Cumulative damage analysis. Technical Paper #820686, Society of Automotive Engineers, 1982.

[34] A. Palmgren. Die Lebensdauer von Kugellagern (Fatigue life of ball bearings). *ZDVDI*, 68(14):339–341, 1924. In German.

[35] M.A. Miner. Cumulative damage in fatigue. *Journal of Applied Mechanics*, 67:A159–A164, September 1945.

[36] T.H. Topper and C.V.B. Gowda. Local stress-strain approach to fatigue analysis and design. Technical Digest 70-DE-24, ASME, 1970. Presented at the ASME Design Engineering Conference & Show in Chicago, Ill., May 1970.

[37] R.N. Smith, P. Watson, and T.H. Topper. A stress strain function for the fatigue of metals. *Journal of Materials, JMSLA*, 5(4):767–778, 1970.

[38] M.W Brown and K.J. Miller. A theory for fatigue failure under multiaxial stress-strain conditions. *The Institution of Mechanical Engineers Proceedings*, 187(65):745–755, 1973.

[39] C.-C. Chu. Fatigue damage calculation using the critical plane approach. *Journal of Engineering Materials and Technology*, 117:41–49, 1995.

[40] C.-C. Chu. Critical plane fatigue analysis of various constant amplitude tests for SAE 1045 steels. Technical Paper #940246, Society of Automotive Engineers, 1994.

[41] W.N. Findley. A theory for the effect of mean stress on fatigue of metals under combined torsion and axial loading or bending. *Journal of Engineering for Industry*, pages 301–306, 1959.

[42] D.F. Socie, L.A. Waill, and D.F. Dittmer. Biaxial fatigue of Inconel 718 including mean stress effects. In *Multiaxial Fatigue* [101], pages 463–481.

[43] C.-C. Chu, F.A. Conle, and J.J.F. Bonnen. Multiaxial stress-strain modeling and fatigue life prediction of SAE axle shafts. In *Advances in Multiaxial Fatigue* [102], pages 37–54.

[44] P.C. Paris, M.P. Gomez, and W.E. Anderson. *The Trend in Engineering*, 13:9–14, 1961.

[45] A.J. McEvily. Fatigue crack growth and the strain intensity factor. In *Air Force Conference on Fatigue and Fracture of Aircraft Structures and Materials*, AFFDL-TR 70-144, pages 451–456, 1970. .

[46] M.H. El Haddad, K.N. Smith, and T.H. Topper. Fatigue crack propagation of short fatigue cracks. *Journal of Engineering Materials and Technology*, 10:42–46, 1979.

[47] D.F. Socie, C.T. Hua, and D.W. Worthem. Mixed mode small crack growth. *Fatigue and Fracture of Engineering Materials and Structures*, 10(1):1–16, 1987.

[48] H. Kitigawa, S. Takahashi, C.M. Suh, and S. Miyashita. Quantitative analysis of fatigue process – microcracks and slip lines under cyclic strains. In *Fatigue Mechanisms* [100], pages 420–449.

[49] Y. Imai and T. Matake. Surface crack growth during push-pull fatigue of smooth specimens. *Zairyo: Journal of the Society of Materials Science, Japan*, 32:1157–1161, 1983. In Japanese.

[50] H. Abdel-Raouf, T.H. Topper, and A. Plumtree. A short fatigue crack model based on the nature of the free surface and its microstructure. *Scripta Metallurgica et. Materialia*, 25:587–602, 1991.

[51] A.A. Dabayeh and T.H. Topper. Changes in crack opening stress after overloads in 2024-T351 aluminum alloy. *International Journal of Fatigue*, 17(4):261–269, 1995.

[52] H Sehitoglu, D.F. Socie, and D. Worthem. Crack growth studies in biaxial fatigue. In *Basic Questions in Fatigue*, volume I of *STP 924*, pages 120–135. American Society for the Testing of Materials, American Society for the Testing of Materials, 1988.

[53] S.Z. Wang, K.J. Miller, M.W. Brown, and E.R. de los Rios. A statistical analysis of short fatigue crack growth. *Fatigue and Fracture of Engineering Materials and Structures*, 14(2/3):351–368, 1991.

[54] C.H. Wang and K.J. Miller. Short fatigue crack growth under mean stress uniaxial loading. *Fatigue and Fracture of Engineering Materials and Structures*, 16(2):181–198, 1993.

[55] G.R. Irwin. Crack-extension force for a part-through crack in a plate. *Journal of Applied Mechanics, ASME*, 29:651–654, 1962.

[56] M.H. Kassir and G.C. Sih. Three-dimensional stress distribution around an elliptical crack under arbitrary loadings. *Journal of Applied Mechanics, ASME*, 33:601–611, 1966.

[57] E.K. Tschegg. Mode III and mode I fatigue crack propagation behaviour under torsional loading. *Journal of Materials Science*, 18:1604–1614, 1983.

[58] A.A. Griffith. The phenomena of rupture and flow in solids. *Philosophical Transactions of the Royal Society (London)*, A221:163–198, 1920.

[59] K. Palaniswamy. *Crack Propagation under General In-Plane Loading.* PhD thesis, California Institute of Technology, Pasadena, California, 1972.

[60] R.J. Nuismer. An energy release rate criterion for mixed mode fracture. *International Journal of Fracture*, 11:245–250, 1975.

[61] J.W. Fash. *An Evaluation of Damage Development During Multiaxial Fatigue of Smooth and Notched Specimens.* PhD thesis, University of Illinois, Urbana-Champaign, Illinois, August 1985. UIUC Report No. 123/UILU-ENG 85-3607.

[62] P. Kurath, S.D. Downing, and D.R. Galliart. Summary of non-hardened notched shaft round robin program. In Socie and Leese [68], chapter 2, pages 13–31.

[63] Standard practice for strain-controlled fatigue testing. In *Annual Book of ASTM Standards*, volume 03.01, chapter E606-92, pages 525–539. ASTM, 1995.

[64] J.J.F. Bonnen and F.A. Conle. An adaptable, multichannel, multiaxial control system. Technical Paper #950703, Society of Automotive Engineers, 1995. Also in *Recent Developments in Fatigue Technology*, SAE PT-67, 1997.

[65] M.A. Pompetzki, R.H. Saper, and T.H. Topper. Software for high frequency control of variable amplitude fatigue tests. *Canadian Metallurgy Quarterly*, 25(181), 1986.

[66] P. Kurath. Personal communication, 1994.

[67] C.-C. Chu and J.J.F. Bonnen. Determining the material fatigue curve using the critical plane approach. In T. Cordes and S. Tipton, editors, *Multiaxial Fatigue: Analysis and Experiment*, AE-??, chapter ?, pages ??–?? Society of Automotive Engineers, 1998. To be published in 1998.

[68] D. Socie and G.E. Leese, editors. *Multiaxial Fatigue: Analysis and Experiment.* AE-14. Society of Automotive Engineers, 1989.

[69] W.D. Pilkey. *Peterson's Stress Concentration Factors.* J. Wiley and Sons, 1997.

[70] H. Neuber. Theory of stress concentration for shear strained prismatical bodies with arbitrary nonlinear stress-strain law. *Journal of Applied Mechanics*, pages 544–550, December 1961.

[71] T. T. Topper, R. Wetzel, and J.D. Morrow. Neuber's rule applied to fatigue of notched specimens. *Journal of Materials*, 4(1):200–209, March 1969.

[72] S. Tipton. A review of the development and use of Neuber's rule for fatigue analysis. Technical Paper #910165, Society of Automotive Engineers, 1991.

[73] G. Glinka. Energy density approach to calculation of inelastic stress-strain near notches. *Engineering Fracture Mechanics*, 22(3):485–, 1985.

[74] C.-C. Chu and F.A. Conle. Multiaxial Neuber-type of elastic to elastic-plastic stress-strain correction. In *Fourth International Conference on Biaxial/Multiaxial Fatigue*, Paris, May 31 - June 3 1994.

[75] C.-C. Chu. Incremental multiaxial Neuber correction for fatigue analysis. Technical Paper #950705, Society of Automotive Engineers, 1995.

[76] C.-C. Chu. A three-dimensional model of anisotropic hardening in metals and its application to the analysis of sheet metal formability. *Journal of the Mechanics and Physics of Solids*, 32:197–212, 1984.

[77] C.-C. Chu. Programming of a multiaxial stress-strain model for fatigue analysis. Technical Paper #920662, Society of Automotive Engineers, 1992.

[78] Z. Mróz. A three-dimensional model of anisotropic hardening in metals and its application to the analysis of sheet metal formability. *Journal of the Mechanics and Physics of Solids*, 15:163–175, 1967.

[79] H. Nowack. Biharmonische Beanspruchungsabläufe zur Beurteilung der Schädigung unregelmässiger Beanspruchungen (Biharmonic load cases for determination of damage due to irregular loading). *VDI-Z Fortschritt Berichte*, 5(7), April 1969.

[80] F.A. Conle. *An Examination of Variable Amplitude Histories in Fatigue*. PhD thesis, University of Waterloo, Waterloo, Ontario, 1978.

[81] D. L. DuQuesnay. Fatigue life prediction for variable amplitude strain histories. Technical Paper #930400, Society of Automotive Engineers, 1993.

[82] D.L. DuQuesnay, H. Abdel-Raouf, T.H. Topper, and A. Plumtree. A modified fracture mechanics approach to metal fatigue. *Fatigue and Fracture of Engineering Materials and Structures*, 15(10):973–993, 1992.

[83] R.A. Chernenkoff. Constant amplitude behavior of Phase II normalized SAE 1045 steel. 1993.

[84] C. MacDougall. The effect of periodic overloads on the notch fatigue behaviour of 1045 steel. Master's thesis, University of Waterloo, Waterloo, Ontario, 1996.

[85] T.H. Topper and T.S. Lam. Effective-strain fatigue life data for variable amplitude fatigue. *International Journal of Fatigue*, 19(supplement no. 1):S137–S143, 1997.

[86] M. Vormvald and T. Seeger. The consequences of short crack closure on fatigue crack growth under variable amplitude loading. *Fatigue and Fracture of Engineering Materials and Structures*, 14(2/3):205–225, 1991.

[87] A. Varvani-Farahani, T.H. Topper, and A. Plumtree. Confocal scanning laser microscopy measurements of the growth and morphology of microstructurally short fatigue cracks in Al 2024-T351 alloy. *Fatigue and Fracture of Engineering Materials and Structures*, 19(9):1153–1159, 1996.

[88] M. Hill. Fatigue properties of Republic X-50-W and Maxi-Form 50 steels. Research Report #TR 12,036-4, Republic Steel Corp., November 1972.

[89] J.M. Holt and B.K. Stewart. Variability of strain-controlled fatigue properties of USS Dual Phase 80. Technical Paper #801400, Society of Automotive Engineers, 1980.

[90] N.E. Dowling. Fatigue life and inelastic strain response under complex histories for an alloy steel. *Journal of Testing and Evaluation*, 1(4):271–287, July 1973.

[91] G. Glinka, G. Shen, and A. Plumtree. A multiaxial fatigue strain energy density parameter related to the critical fracture plane. *Fatigue and Fracture of Engineering Materials and Structures*, 18(1):37–46, 1995.

[92] W.F. Brown, Jr. and J.E. Srawley. In *Plane Strain Crack Toughness Testing of High Strength Metallic Materials*, STP 410, page 12. American Society for the Testing of Materials, 1966.

[93] H.V. Lakshminarayana and M.V.V. Murthy. On stresses around an arbitrarily oriented crack in a cylindrical shell. *International Journal of Fracture*, 12:547–566, 1976.

[94] T. Miyoshi, K. Ishii, and S. Yoshida. Database of stress intensity factors for surface cracks in pre/post penetration. *Transactions of the Japan Society of Mechanical Engineers*, 56(527):1563–1569, 1990.

[95] T. Miyoshi and S. Yoshida. Analysis of stress intensity factors for surface cracks in pre/post penetration. *Transactions of the Japan Society of Mechanical Engineers*, 54(505):1771–1777, 1988.

[96] H.-Y. Zhang. *Fatigue Crack Growth Behavior of Induction Hardened Shafts Under the Effects of Residual and Applied Bending Stresses.* PhD thesis, University of Iowa, Iowa City, Iowa, 1998.

[97] C.-C. Chu. The analysis of multiaxial cyclic loading with an anisotropic hardening model. *International Journal of Solids and Structures*, 23(5):569–579, 1987.

[98] I.S. Raju and J.S. Newman. Stress-intensity factors for circumferential surface cracks in pipes and rods under tension and bending loads. In *Fracture Mechanics: Seventeenth Volume*, ASTM STP 905, pages 789–805. American Society for the Testing of Materials, 1986.

[99] A.E Green and I.N. Sneddon. The distribution of stress in the neighbourhood of a flat elliptical crack in an elastic solid. *Proceedings of the Cambridge Philosophical Society*, 46:159–164, 1950.

[100] American Society for the Testing of Materials. *Fatigue Crack Growth Under Spectrum Loads*, ASTM STP 595, Philadelphia, 1976.

[101] American Society for the Testing of Materials. *Multiaxial Fatigue*, ASTM STP 853, 1985.

[102] American Society for the Testing of Materials. *Advances in Multiaxial Fatigue*, ASTM STP 1191, 1993.